UNIVERSIDADE DE SANTIAGO DE COMPOSTELA
Departamento de Física de Partículas
Instituto Galego de Física de Altas Enerxías

TESE DE DOUTORAMENTO

Study of the penguin-dominated decay $B_s^o \to K^{*o}\overline{K}^{*o}$ at LHCb

Presentada por Paula Álvarez Cartelle

Dirixida por Prof. Bernardo Adeva Andany
e Prof. Abraham Antonio Gallas Torreira

Santiago de Compostela, Setembro de 2014

Study of the penguin-dominated decay $B_s^0 \to K^{*0}\overline{K}^{*0}$ at LHCb
Author: Paula Álvarez Cartelle
Advisor: Bernardo Adeva Andany
Advisor: Abraham Antonio Gallas Torreira

Up-to-date information about this dissertation and related topics can be found at
`http://fpmac116.usc.es/twiki/bin/view/Main/PaulaAlvarezCartelle`

Picture: *The decay of a Λ^0 particle in the 32 cm hydrogen bubble chamber*, CERN, 1960. Retrieved from CERN Document Server, CERN-EX-11465.

Text printed in Santiago de Compostela
First edition, September 2014
Second edition, March 2015

D. BERNARDO ADEVA ANDANY, Catedrático de Física Atómica, Molecular e Nuclear da Universidade de Santiago de Compostela e D. ABRAHAM ANTONIO GALLAS TORREIRA, Profesor Contratado Doutor de Física Atómica, Molecular e Nuclear da Universidade de Santiago de Compostela, informan:

Que a memoria titulada "*Study of the penguin-dominated decay* $B_s^0 \to K^{*0}\overline{K}^{*0}$ *at LHCb*" foi realizada por Paula Álvarez Cartelle baixo a súa dirección e que constitúe a Tese que presenta para optar ao Grado de Doutora en Física.

Santiago de Compostela, a 1 de Setembro de 2014.

Asdo. Bernardo Adeva Andany

Asdo. Abraham Antonio Gallas Torreira

Asdo. Paula Álvarez Cartelle

Acknowledgements

First of all, I would like to thank my supervisors, Bernardo Adeva and Abraham Gallas, for their support and time dedicated to my learning. Without them this thesis would not have been possible.

My special gratitude goes to Diego Martínez, for teaching me lots of things about LHCb and data analysis in general, and for trusting my work from the first day. To him and Xabier Cid, I also thank their support and friendship during these years.

I want to show my gratitude to the people involved in the analysis of $B_s^0 \to K^{*0}\overline{K}^{*0}$: Laurence Carson, Xabier Cid, Álvaro Dosil, Diego Martínez, Antonio Romero, Juan Saborido, Brais Sanmartín, Cibrán Santamarina and, specially, to Celestino Rodríguez, for opening the path and making possible the discovery. Thanks to Robert Fleischer, Joaquim Matías, David London and Alakabha Datta for useful conversations about this study and to my colleagues in the *BnoC Working Group*, in particular to Stephane Monteil and Marc Grabalosa. I would also like to acknowledge the work of all the members of the LHCb and LHC collaborations for making possible this thesis.

I want to express my gratitude to Guy Wilkinson, Tim Gershon, Joaquim Matías, Diego Martínez and Jose Ángel Hernando for kindly accepting to be members of my thesis jury.

I thank the financial support provided by the "Programa de Formación de Personal Investigador" of the "Ministerio de Ciencia e Innovación".

Finally, I would like to thank all of the people with whom I had the pleasure to work with at the University of Santiago. A special word for my fellow PhD students during these years: Álvaro, Brais, Carlos and Víctor, and those who already passed on to a "better life": Diego, Lucas, Xabier and Pablo. Thanks to Marcos, for his useful advice in so many different subjects, to Eliseo for his emergency seminar about silicon detectors, to Máximo for letting me give good marks to all of his students, and to the rest of the members: Jose Ángel, Pablo, Antonio, María and Julián. It was a pleasure to work with such an excellent group of people.

Nun ámbito máis persoal, quero agradecer a todos os amigos que me aturaron durante estes anos e me animaron a seguir, en especial a Jacobo e Marta, por apoiarme sempre. Aos compañeiros de Santiago, en particular a Daniel, Ricardo e Jose, por alegrar a vida do doutorando. A Jorge, por seguir aí.

Gracias a meus pais, María Rita e Efrén, á miña irmá Marta, á miña avoa Lola, á miña *Tata* (María del Mar), á miña *Pepa* (María José), a Vito e a Ester polo seu amor e apoio incondicionais, sen os cales non tería chegado ata aquí. Gracias a Daniel, pola súa paciencia e axuda, e por facerme sorrir cada día.

Por último gustaríame dedicar esta tese á memoria de Antonio Cartelle Rodríguez, de quen valentía e bondade teño sempre presentes.

Paula

"Now, if you'll only attend and not talk so much, I'll tell you all my ideas about Looking-glass House. First, there's the room you can see through the glass –that's just the same as our drawing room, only the things go the other way. I can see all of it when I get upon a chair –all but the bit behind the fireplace. Oh! I do so wish I could see that bit!"

Through the looking-glass, and what Alice found there,
Lewis Carroll

Abstract

This thesis is devoted to the search for and subsequent analysis of the decay channel $B_s^0 \to K^{*0}\overline{K}^{*0}$, using the first data acquired by LHCb during 2010 and 2011 from the LHC proton-proton collisions at a centre-of-mass energy $\sqrt{s} = 7$ TeV, corresponding to an integrated luminosity of 37 pb^{-1} and 1.0 fb^{-1} respectively.

As a result of the work presented here, the first observation of the $B_s^0 \to K^{*0}\overline{K}^{*0}$ decay was performed. With the extended data sample collected in 2011, a combined angular and mass analysis was carried out, in order to assess the longitudinal polarisation fractions of the K^{*0}, obtaining $f_L = 0.201 \pm 0.057(\text{stat.}) \pm 0.040(\text{syst.})$. The branching fraction for this decay was also measured to be $\mathcal{B}(B_s^0 \to K^{*0}\overline{K}^{*0}) = (10.6 \pm 1.8(\text{stat.}) \pm 1.0(\text{syst.}) \pm 0.6\ (f_d/f_s)) \times 10^{-6}$, in agreement with the Standard Model prediction.

All of the triple product and *CP* direct asymmetries measurable in the time-integrated and flavour-untagged analysis of $B_s^0 \to (K^+\pi^-)(K^-\pi^+)$ were also determined. No signs of *CP*-violation were found, in agreement with the Standard Model expectation.

Limiar

Esta tese está dedicada á procura e subsecuente análise do canal de decaemento $B_s^0 \to K^{*0}\overline{K}^{*0}$, baseados nos primeiros datos acumulados polo LHCb durante os anos 2010 e 2011 a partires das colisións protón-protón a una enerxía no centro de masas de $\sqrt{s} = 7$ TeV proporcionadas polo LHC, correspondentes a unha luminosidade integrada de 37 pb^{-1} e 1.0 fb^{-1} respectivamente.

Como resultado do traballo aquí presentado, a desintegración $B_s^0 \to K^{*0}\overline{K}^{*0}$ foi observada por vez primeira. Coa maior mostra de datos, recollida no ano 2011, levouse a cabo unha análise combinada da distribución angular e na masa invariante co obxectivo de determinar a fracción de polarización lonxitudinal do mesón K^{*0}, obténdose $f_L = 0.201 \pm 0.057(\text{stat.}) \pm 0.040(\text{syst.})$. Tamén se determinou a fracción de desintegración para este proceso. O valor medido $\mathcal{B}(B_s^0 \to K^{*0}\overline{K}^{*0}) = (10.6 \pm 1.8(\text{stat.}) \pm 1.0(\text{syst.}) \pm 0.6(f_d/f_s)) \times 10^{-6}$ é compatible coa predición do Modelo Estándar.

Determináronse ademais todas as asimetrías de CP directas e asimetrías asociadas a productos triples accesibles ó decaemento $B_s^0 \to (K^+\pi^-)(K^-\pi^+)$ nun estudo independente do tempo e do sabor do meson B_s^0. Nestas medidas non se atoparon sinais de violación CP, tal e como predí o Modelo Estándar.

Contents

1

Introduction

The Standard Model (SM) of Particle Physics is the most successful theory to explain the elementary particles composing the universe and the interactions among them, with the exception of gravity. Based on three fundamental interactions, weak, strong and electromagnetic, the SM is able to describe most of the phenomena observed in Nature. However, there are still questions it can not give an answer to. It fails to explain, for example, the nature of Dark Matter, which from cosmological observations [1] is known to account for a large fraction of the visible universe. It can neither provide a explanation for the matter-antimatter unbalance or neutrino oscillation. Due to these issues, together with its lack of description of gravity, the SM is considered an effective theory of a more general picture which different High Energy Physics (HEP) experiments attempt to probe.

Currently, some of the most important experiments trying to discover physics beyond the SM are located at CERN, as part of the Large Hadron Collider (LHC) complex. The LHC collides protons at a nominal centre-of-mass energy of $\sqrt{s} = 14$ TeV ($\sqrt{s} = 7$ TeV during 2010 and 2011). These collisions are analysed by the four main experiments, ATLAS, CMS, LHCb and ALICE. The work of this thesis has been developed within the LHCb experiment, specialised in rare decays and CP-violation in the context of B-physics. ALICE is mainly devoted to the study of quark-gluon plasma in heavy ion collisions delivered by the LHC in special runs. ATLAS and CMS, are general purpose detectors, that, among other measurements, have performed the discovery of the last particle of the SM that remained unobserved, the Higgs boson.

Some of the most remarkable LHCb results so far are in the context of CP-violation. Understanding the origin and mechanism of CP-violation is a key question in Particle Physics. In the SM, it is described by the CKM mechanism, which, although successful in explaining the current experimental data, is known to generate insufficient CP-violation to originate the baryon asymmetry of the Universe. In the study of CP violation, Flavour Changing Neutral Current (FCNC) processes are of special interest, since new particles beyond the SM may enter the loops mediating them. In the context of B-physics two types of $b \to q$ FCNC transitions are commonly studied: neutral B meson mixing and loop-mediated B decays.

$B_s^0 \to K^{*0}\overline{K}^{*0}$ is one of the later processes. This decay into two light vector mesons (V) proceeds solely through penguin $b \to s$ diagrams in the SM. $B \to V_1 V_2$ transitions are actually three different decays, since the two vector mesons can have orbital angular momentum $l = 0, 1, 2$ in the final state. The $B_s^0 \to K^{*0}\overline{K}^{*0}$ partial width arises, thus, from three helicity amplitudes that are mainly determined by the chiral structure of the quark operators, both in the electroweak and QCD sectors, assuming no additional contributions from New Physics (NP). The interplay between the various penguin contributions has been studied in QCD, and predictions in the framework of QCD factorisation from [2] are $(9.1^{+11.3}_{-6.8}) \times 10^{-6}$ for the branching ratio and $f_L = 0.63^{+0.42}_{-0.29}$ for the fraction of the total amplitude which is longitudinally polarised. According to the same paper, predictions improve to $(7.9^{+4.3}_{-3.9}) \times 10^{-6}$ and $f_L = 0.72^{+0.16}_{-0.21}$, respectively, when experimental input is used (mainly from $B \to K^*\phi$).

The interest in $B^0_s \to K^{*0}\overline{K}^{*0}$ for precision CP-violation studies has been analysed by several authors [3–6]. The main advantage of this decay stems from the fact that its exact U-spin rotated channel $B^0 \to K^{*0}\overline{K}^{*0}$ $(b \to d)$ is also accesible to LHCb with identical experimental properties. This potentially allows full assesment of all relevant SM penguin amplitudes at lowest order and next-to-leading order, as a first step to carry out precision investigation of the CP-violating electroweak phase, $\phi_s^{b\to sd\bar{d}}$ [6,7]. Moreover, even with an untagged and time integrated analysis of $B^0_s \to K^{*0}\overline{K}^{*0}$, CP-violation and T-violation may arise from four triple products asymmetries and four direct-like asymmetries measurable from the terms corresponding to the interference among the different amplitudes [8].

The goal of this thesis is the study of $B^0_s \to K^{*0}\overline{K}^{*0}$ with the first two years of data taken by the LHCb experiment at the LHC. The structure of the thesis is the following. Chapter 2 overviews the most important theory aspects for the search and further study of this process. These include a brief explanation of the SM and its predictions on $B^0_s \to K^{*0}\overline{K}^{*0}$. The LHCb experiment is presented in Chapter 3, where the detector and the experimental conditions during 2010 and 2011 are described. A detailed explanation on how to obtain the decay rate as a function of the decay angles and the K^{*0} masses for the transition $B^0_s \to K^{*0}\overline{K}^{*0}$ (and the scalar final state contributions in $B^0_s \to (K^+\pi^-)(K^-\pi^+)$) is given in Chapter 4. Chapter 5 describes the analysis that led to the discovery of the decay with the first 37 pb^{-1} of data recorded by LHCb in 2010. The analysis of 2011 data is presented in Chapter 6, where the higher statistics (1.0 fb^{-1}) allowed a precise determination of the polarisation fractions of the decay to be performed through a mass-dependent angular analysis. This chapter also includes the search for NP perfromed by measuring the eight CP-violating quantities accessible to the untagged sample. The $\mathcal{B}(B^0_s \to K^{*0}\overline{K}^{*0})$ measurement is also reported. Finally, conclusions are drawn in Chapter 7.

2

Theory overview

2.1 Standard Model

The Standard Model (SM) is a quantum field theory (QFT) based on strong and electroweak (EW) interactions. The SM structure is described in this section following [9–11]. The strong interactions are described by Quantum Chromodynamics (QCD) corresponding to the symmetry group $SU(3)_C$ of color (C), while the EW interaction is described by the group $SU(2)_T \otimes U(1)_Y$ of weak-isospin (T) and hypercharge(Y), being then $SU(3)_C \otimes SU(2)_T \otimes U(1)_Y$ the full group of gauge symmetry for the SM.

$$G_{SM} = SU(3)_C \otimes SU(2)_T \otimes U(1)_Y \tag{2.1}$$

This symmetry is spontaneously broken into $SU(3)_C \otimes U(1)_{EM}$ by the vacuum expectation value (VEV) of (the neutral component of) a scalar isospin doublet, with hypercharge 1/2, called the Higgs

$$G_{SM} \xrightarrow{Higgs(1,2)_{1/2}} SU(3)_C \otimes U(1)_{EM}$$

As a result of the interaction with the Higgs field, EW bosons combine into the massive particles $W^{\pm}$ and Z^0 and the massless photon. The interaction with the Higgs field gives also masses to the elenmentary fermions. Each fermion generation, out of a total of three, has five representations of the SM gauge symmetry

$$Q_{L,i}(3,2)_{+1/6} \quad U_{R,i}(3,1)_{+2/3} \quad D_{R,i}(3,1)_{+1/3} \quad L_{L,i}(1,2)_{-1/2} \quad E_{R,i}(1,1)_{-1}$$

The subscript number is the hypercharge, and the numbers in parenthesis indicate if it acts as a triplet or singlet in $SU(3)_C$ and as a doublet or singlet in $SU(2)_T$. The subscript i = 1,2,3 indicates fermion generation. The EW symmetry breaking (EWSB) and the effects induced by the Higgs field such as CP violation and flavor depending processes are explained in Sect. 2.1.1. The fermion and boson content of SM is explained in more detail in Sect. 2.1.2.

Thus, the SM Lagrangian can be decomposed into three parts

$$\mathcal{L} = \mathcal{L}_{Kin} + \mathcal{L}_{Higgs} + \mathcal{L}_{Yuk} \tag{2.2}$$

where the kinetic part includes the corresponding covariant derivative to preserve the gauge invariance, the Higgs part includes Higgs self interactions and the Yukawa part includes Higgs-fermion interactions.

2.1.1 Mass generations and eigenstates

A Lagrangian containing only the terms of the gauge symmetry is not enough to build a model where the particles are massive. The gauge bosons are massless if the symmetry is unbroken, and masses for the fermions as self-interactions such like $\overline{\Psi}_L \Psi_R$ (Dirac mass) or $\Psi_L \Psi_L$ (Majorana mass) would explicitly break the SU(2) symmetry. Non-abelian broken gauge theories are not renormalisable, thus in the SM the masses of the EW gauge bosons and the fermions are generated via spontaneous symmetry breaking.

2.1.1.1 Boson masses and EWSM

The spontaneous symmetry breaking is achieved by the introduction of the Higgs, a scalar isospin doublet with hypercharge +1/2,

$$\phi = \begin{pmatrix} \phi^+ \\ \phi^0 \end{pmatrix} \tag{2.3}$$

This doublet has a self interaction of the form

$$\mathcal{L}_{Higgs} = \mu^2 \phi^\dagger \phi - \lambda (\phi^\dagger \phi)^2 \tag{2.4}$$

The first term is similar to a mass one, but with opposite sign. Such a quadratic potential does not minimise at 0 (see example in Fig. 2.1), and thus acquires a VEV $\nu = \mu/\lambda$.

$$\langle \phi \rangle_0 = \frac{1}{\sqrt{2}} \begin{pmatrix} 0 \\ \nu \end{pmatrix} \tag{2.5}$$

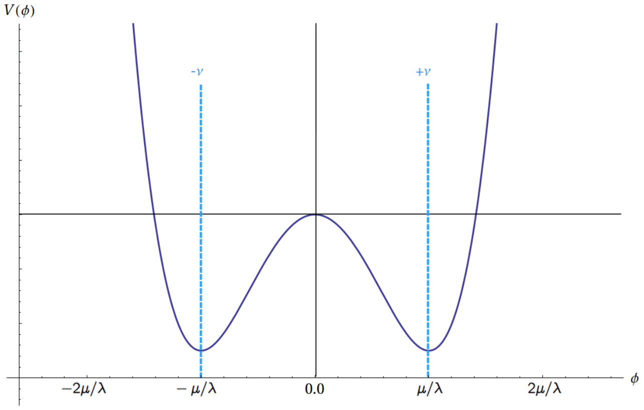

Figure 2.1: Higgs-like potential. The minimum is not at 0, and therefore the potential has a VEV.

The VEV gives masses, through the Higgs kinetic term plus the Higgs self-interaction Lagrangian, to the following boson combinations:

$$\begin{aligned} W^\pm_\mu &= \frac{1}{\sqrt{2}} \left(W^{(1)}_\mu \mp W^{(2)}_\mu \right) \rightarrow M_W = g \cdot \frac{\nu}{2}\,, \\ Z^0_\mu &= \frac{1}{\sqrt{g^2 + g'^2}} \left(g W^{(3)}_\mu - g' B^{(2)}_\mu \right) \rightarrow M_Z = \sqrt{g^2 + g'^2} \cdot \frac{\nu}{2} \end{aligned} \tag{2.6}$$

From the degrees of freedom of the original Higgs field,

$$\phi = \begin{pmatrix} \phi^+ \\ \phi^0 \end{pmatrix} = \frac{1}{\sqrt{2}} \begin{pmatrix} G_1^+ + iG_2^+ \\ \nu + (H^0 + iG_3^0) \end{pmatrix} \tag{2.7}$$

H^0 will be a massive scalar particle, having the massless Goldstone bosons G_i "eaten" by the gauge bosons $W^\pm$ and Z^0 , giving rise to their longitudinal polarisations and masses. The Higgs boson, H^0, the last particle in the SM to be observed, has recently been discovered at the LHC with a mass of around 125 GeV [12, 13].

2.1.1.2 Fermion masses and CKM matrix

In order to give masses to the fermions, the corresponding couplings between them and the Higgs field are added, while keeping the Lagrangian $SU(2)$ invariant. For example, for a single generation

$$\Delta\mathcal{L} = -\lambda_e \bar{E}_L \phi E_R - \lambda_d \bar{Q}_L \phi D_R - \lambda_u \epsilon^{ab} \bar{Q}_{La} \phi_b^\dagger U_R + h.c. \tag{2.8}$$

Substituting the VEV, the fermion masses have the form

$$m_e = \frac{\nu \cdot \lambda_e}{\sqrt{2}} \quad m_u = \frac{\nu \cdot \lambda_u}{\sqrt{2}} \quad m_d = \frac{\nu \cdot \lambda_d}{\sqrt{2}} \ . \tag{2.9}$$

These λ_i are inputs to the SM and thus allow having very different masses for different fermions. When the three fermion generations are added to the theory, additional terms mixing quarks of different generations are possible. Alternatively, it is possible to diagonalise the Higgs couplings by switching to a different basis for the quark fields. Writing the Lagrangian in this alternative basis (hereinafter referred to as "mass basis" or "physical basis") will of course simplify $\mathcal{L}_{Yuk}$ but with the cost of causing a complication in the gauge side. Calling q the interaction eigenstates and q' the mass eigenstates, both bases are related through the unitary relations

$$u_L^i = U_u^{ij} u'^j_L \quad d_L^i = U_d^{ij} d'^j_L \tag{2.10}$$

and thus the weak current $\bar{u}_L^i \gamma^\mu d_L^i$ transforms to $\overline{u'}^i_L \gamma^\mu (U_u^\dagger U_d)_{ij} d'^i_L \equiv \overline{u'}^i_L \gamma^\mu V_{ij}^{CKM} d'^i_L$. V^{CKM} is called the CKM matrix [14, 15] (from Cabibbo-Kobayashi-Maskawa). Its coefficients are usually written as

$$V^{CKM} = \begin{pmatrix} V_{ud} & V_{us} & V_{ub} \\ V_{cd} & V_{cs} & V_{cb} \\ V_{td} & V_{ts} & V_{tb} \end{pmatrix} \tag{2.11}$$

V^{CKM} is not diagonal (the experimental values of the coefficients can be found in [16]) and such structure allows transitions between the different quark generations, giving rise to processes in which quarks change flavour without changing its electric charge. These processes are called Flavour Changing Neutral Currents (FCNC) and in particular include the decay $B_s^0 \to K^{*0}\overline{K}^{*0}$. CP violation (CPV) also arises from the non-diagonal structure of V^{CKM}, requiring, in addition, the presence of three different generations (see Sect. 2.2.4). Equivalently, if V^{CKM} were the identity matrix CP violation and FCNCs would not exist within the SM.

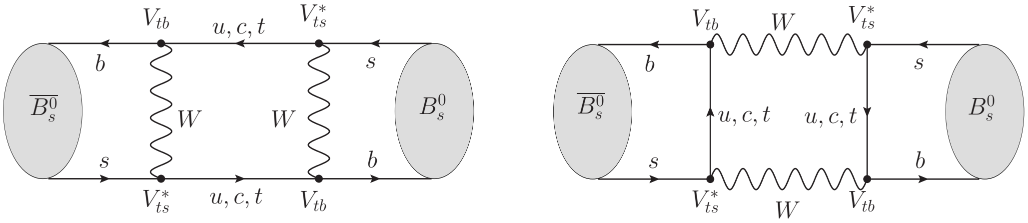

Figure 2.2: Diagrams contributing to B_s^0- $\overline{B}_s^0$ oscillation.

Another particular but very important example of process arising from the fact that V^{CKM} is different from the identity matrix is the oscillation of neutral mesons composed by quarks of different generations. The off-diagonal terms of CKM matrix allow particles such like D^0, K^0, B^0 or B_s^0 to perform particle-antiparticle oscillations (see Fig. 2.2 for examples of diagrams involving Bs oscillation). Neutral mesons oscillation will be explained in more detail in Sect. 2.2.1.

2.1.2 Elementary particles

2.1.2.1 Fermions

The Standard Model fermions can be divided in two groups, depending on whether they are affected by strong interaction (quarks) or not (leptons). Each quark has three possible color states and (at low energy) only exists in bound states of color singlets, called hadrons. Hadrons are then composed of quarks (and gluons, the gauge bosons of QCD), being the most common states quark - antiquark (mesons), and three quarks (baryons). Due to spin addition, baryons are also fermions, while mesons are bosons. Leptons are e, μ, τ and a neutrino (ν) for each one. In the SM neutrinos are massless particles so that their helicity becomes equivalent to chirality. This means that there are no right-handed neutrinos in the SM and, equivalently, there are no left-handed antineutrinos[1].

2.1.2.2 Bosons

Apart from mesons, the SM contains the gauge bosons corresponding to strong and EW interactions, and Higgs (H^0) boson, responsible for the masses of SM particles. The gauge bosons of QCD are massless particles of spin 1, called gluons, and have eight possible color states. QCD couplings have the property of becoming small at high energies (or small distances); this effect is known as "asymptotic freedom".

The gauge bosons corresponding to $SU(2)_T \otimes U(1)_Y$ are W_μ^i ($i = 1, 2, 3$) and B_μ , for $SU(2)$ and $U(1)$ respectively, and the four should be massless in order to conserve the gauge symmetry. However, the symmetry breaking induced by the Higgs field changes them into W^+, W^-, Z^0 and photon (A^μ), where only the photon is massless. All of them have spin 1.

---

[1] It is now known experimentally that neutrinos undergo flavour oscillations, which means they are not massless. This behaviour can be fitted into the SM with small modifications to it.

Table 2.1: SM fermions.

		T	T_3	Y	Q
Leptons	ν_e, ν_μ, ν_τ	$\frac{1}{2}$	$\frac{1}{2}$	-1	0
	e_L, μ_L, τ_L	$\frac{1}{2}$	$-\frac{1}{2}$	-1	-1
	e_R, μ_R, τ_R	0	0	-2	-1
Quarks	u'_L, c'_L, t'_L	$\frac{1}{2}$	$\frac{1}{2}$	$\frac{1}{3}$	$\frac{2}{3}$
	u'_R, c'_R, t'_R	0	0	$\frac{4}{3}$	$\frac{2}{3}$
	d'_L, s'_L, b'_L	$\frac{1}{2}$	$-\frac{1}{2}$	$\frac{1}{3}$	$-\frac{1}{3}$
	d'_R, s'_R, b'_R	0	0	$-\frac{2}{3}$	$-\frac{1}{3}$

2.2 *CP* violation and neutral meson decays

The *CP* transformation combines charge conjugation C with parity P, which means this operation changes particles into anti-particles. If *CP* were an exact symmetry, the laws of Nature would be the same for matter and for antimatter. It is observed that most phenomena are indeed *CP*-symmetric. In particular, this symmetry is respected by electromagnetic and strong interactions. The weak interactions, on the other hand, violate *C*, *P* and also *CP*. *CP* violation was first discovered in neutral *K* decays in 1964 [17]. Today we have more evidences of *CP* violation in the B^0-system, measured at the *B*-factories at the turn of the 2000's [18, 19], and the recently observation of CPV in the B^0_s-system by LHCb [20].

CP symmetry is broken in the SM by complex phases in the Yukawa couplings, through a single *CP*-violating parameter in the CKM matrix. This description of *CP* violation, known as the Kobayashi-Maskawa (KM) mechanism, agrees with all measurements to date. However, the current level of experimental accuracy and the theoretical uncertainties involved in the interpretation of the various observations leave room for additional (beyond the SM) sources of *CP* violation. Moreover, the observed baryon asymmetry of the universe, *i.e.*, the fact that there is much more matter than antimatter in the observed universe, could only be generated from an initial situation in which the amounts of matter and antimatter would be equal if there is *CP* violation. This fact was first shown by Andrei Sakharov in 1967 [21], who pointed out that baryon-number violation, *C* and *CP* violation, and a departure from thermal equilibrium, are all necessary in order for it to be possible to generate a net baryon asymmetry in the early universe. Despite the phenomenological success of the KM mechanism, it seems to fail to accommodate the observed baryon asymmetry [22]. On the other hand, many extensions of the SM provide new sources of *CP* violation, so the search for physics beyond the SM is much in contact with the study of CP violation [23].

Experimentally, a natural place to search for *CP* violation is meson decays. In particular, the study of neutral meson systems provides a lot of information about the nature of *CP* violation, to the extent that much can be learned about *CP* violation in the SM even from *CP*-conserving processes. In this section, the formalism and basic physics that are relevant to the measurements of *CP* violation in neutral meson system are explained.

2.2.1 Neutral mesons systems

2.2.1.1 The effective Hamiltonian: Weisskopf-Wigner approximation

Let P^0 refer to any neutral meson: K^0, D^0, B^0 or B_s^0. P^0 and $\overline{P^0}$ have an opposite internal quantum number (flavour quantum number) F, which is conserved by strong and electromagnetic interactions, $\Delta F = 0$, and not conserved by the weak interaction, $\Delta F \neq 0$. If only strong and electromagnetic interactions existed, P^0 and $\overline{P^0}$ would be a stable particle-antiparticle pair with common mass m_0. Because of the weak interaction, P^0 and $\overline{P^0}$ decay. Moreover, $P^0 \leftrightarrow \overline{P^0}$ transitions are also possible as a one-step process ($\Delta F = 2$) or through an intermediate state (second order $\Delta F = 1$). The full Hamiltonian for this system can be written as

$$H = H_0 + H_W, \tag{2.12}$$

where H_0 is the flavour invariant Hamiltonian and H_W, treated as a perturbation, contains the weak interaction.

Consider an inicial state which is a mixure of a P^0 and a $\overline{P^0}$,

$$|\psi(t=0)\rangle = c|P^0\rangle + \bar{c}|\overline{P^0}\rangle. \tag{2.13}$$

At $t > 0$ this state will evolve in two different ways: oscillation between P^0 and $\overline{P^0}$ and decays into lighter particles. The evolved state can be described by

$$|\psi(t)\rangle = c(t)|P^0\rangle + \bar{c}(t)|\overline{P^0}\rangle + \sum_n c_n(t)|n\rangle \tag{2.14}$$

where $|n\rangle$ represents any decay mode of the original mesons and t is the time measured in the P^0-$\overline{P^0}$ rest frame. It is possible to simplify the resolution of this problem if

- only the values of $c(t)$ and $\bar{c}(t)$ are of interest, *i.e.*, if only the time evolution of the projection of the full state, $|\psi(t)\rangle$, on the two-dimensional subspace of the P^0-$\overline{P^0}$ system is desired,
- the considered times t are much larger than the typical strong-interaction scale.

Under these assumptions, known as the Weisskopf-Wigner approximation, the system can be described by a Schrödinger-like equation [24]

$$i\frac{d}{dt}\begin{pmatrix}|c(t)\rangle \\ |\bar{c}(t)\rangle\end{pmatrix} = H_{eff}\begin{pmatrix}|c(t)\rangle \\ |\bar{c}(t)\rangle\end{pmatrix} \tag{2.15}$$

where the effective Hamiltonian H_{eff} is not Hermitian, else the mesons would just oscillate, they would not decay[1] . It is given by

$$H_{eff} = \begin{pmatrix}\langle P^0|H_{eff}|P^0\rangle & \langle P^0|H_{eff}|\overline{P^0}\rangle \\ \langle\overline{P^0}|H_{eff}|P^0\rangle & \langle\overline{P^0}|H_{eff}|\overline{P^0}\rangle\end{pmatrix} = \boldsymbol{M} - \frac{i}{2}\boldsymbol{\Gamma} = \begin{pmatrix}M_{11} - \frac{i}{2}\Gamma_{11} & M_{12} - \frac{i}{2}\Gamma_{12} \\ M_{12}^* - \frac{i}{2}\Gamma_{12}^* & M_{22} - \frac{i}{2}\Gamma_{22}\end{pmatrix}. \tag{2.17}$$

---

[1] Since H_{eff} is not Hermitian, the probability to observe either P^0 or $\overline{P^0}$ is not conserved, but goes down with time,

$$\frac{d}{dt}\left(|c(t)|^2 + |\bar{c}(t)|^2\right) = -\left(c(t)^* \;\; \bar{c}(t)^*\right)\boldsymbol{\Gamma}\begin{pmatrix}c(t) \\ \bar{c}(t)\end{pmatrix} \tag{2.16}$$

where $\boldsymbol{M}$ and $\boldsymbol{\Gamma}$ are 2×2 Hermitian matrices. The explicit matrix elements for $\boldsymbol{M}$ and $\boldsymbol{\Gamma}$ are given, in second-order perturbation theory by [25] $(i, j = 1, 2)$

$$\begin{aligned} M_{ij} &= m_0 \delta_{ij} + \langle i | H_W^{(\Delta F=2)} | j \rangle + \sum_n \mathcal{P} \left[\frac{\langle i | H_W^{(\Delta F=1)} | n \rangle \langle n | H_W^{(\Delta F=1)} | j \rangle}{m_0 - E_n} \right], \\ \Gamma_{ij} &= 2\pi \sum_n \langle i | H_W^{(\Delta F=1)} | n \rangle \langle n | H_W^{(\Delta F=1)} | j \rangle \delta(m_0 - E_n) \end{aligned} \tag{2.18}$$

where $\mathcal{P}$ stands for the principal part prescription, and the sum runs over all intermediate states n. m_0 and E_n are the energies in the centre-of-mass frame defined as $H_0|P^0\rangle = m_0|P^0\rangle$, $H_0|\overline{P^0}\rangle = m_0|\overline{P^0}\rangle$ and $H_0|n\rangle = E_n|n\rangle$.

Assuming CPT as a symmetry of H_W leads to the following relations

$$M_{11} = M_{22} \equiv M \qquad \Gamma_{11} = \Gamma_{22} \equiv \Gamma \tag{2.19}$$

The states $|P^0\rangle$ and $|\overline{P^0}\rangle$ are eigenstates of H_0 but not of H_W. Therefore these are not physical states (or mass eigenstates) with the corresponding consequence of mixing and decay. A new basis $\{P_L, P_H\}$ which diagonalizes H_{eff} defines two fields that do not oscillate, just decay. As H_{eff} is not herminian, its eigenstates will not be ortogonal.

Using the shorthand notation $B = \sqrt{(M_{12} - \frac{i}{2}\Gamma_{12})(M_{12}^* - \frac{i}{2}\Gamma_{12}^*)}$, the eigenvalues of H_{eff} can be shown to be

$$H_{eff}|P_L\rangle = (M - \frac{i}{2}\Gamma + B)|P_L\rangle \equiv (M_L - \frac{i}{2}\Gamma_L)|P_L\rangle \tag{2.20}$$

$$H_{eff}|P_H\rangle = (M - \frac{i}{2}\Gamma - B)|P_H\rangle \equiv (M_H - \frac{i}{2}\Gamma_H)|P_H\rangle \tag{2.21}$$

where the real and imaginary parts have been grouped in the definition of M_L, M_H, Γ_L and Γ_H respectively. The corresponding eigenstates are

$$\begin{aligned} |P_L\rangle = p|P^0\rangle + q|\overline{P^0}\rangle \\ |P_H\rangle = p|P^0\rangle - q|\overline{P^0}\rangle \end{aligned} \tag{2.22}$$

with

$$\frac{q}{p} = \pm\sqrt{\frac{M_{12}^* - \frac{i}{2}\Gamma_{12}^*}{M_{12} - \frac{i}{2}\Gamma_{12}}} \tag{2.23}$$

The state $|P_L\rangle$ is the mass eigenstate with mass M_L and inverse-lifetime Γ_L. Similarly the mass M_H and the inverse-lifetime Γ_H are defined for state $|P_H\rangle$. The sign of q/p determines whether $|P_L\rangle$ or $|P_H\rangle$ is heavier. It is useful to define

$$\begin{aligned} \Delta m &\equiv M_H - M_L = 2\Re(B) \\ \Delta\Gamma &\equiv \Gamma_L - \Gamma_H = 4\Im(B) \end{aligned} \tag{2.24}$$

The common convention is the choice $\Delta m > 0$[1], wich implies the positive sign in (2.23). Note that this choice does not imply anything for the sign of $\Delta\Gamma$.

---

[1] This choice gives also meanig to the notation of H and L to denote the "heavy" and "light" eigenstate

2.2.1.2 Time evolution

Let $|P^0(t)\rangle$ denote the state at time t that at $t = 0$ was a pure $|P^0\rangle$. The time evolution of the flavour states, P^0 and $\overline{P^0}$, is complicated: the states $|P^0(t)\rangle$ and $|\overline{P^0}(t)\rangle$ will be superpositions of P^0 and $\overline{P^0}$ at $t > 0$. However, the time evolution of the mass eigenstates will be given by the simple expression

$$|P_{H,L}(t)\rangle = e^{-(iM_{H,L}+\Gamma_{H,L}/2)t}|P_{H,L}\rangle \tag{2.25}$$

as they diagonalize the effective Hamiltonian. By inversion of (2.22) the time evolution of the states P^0 and $\overline{P^0}$ can be expressed as

$$\begin{array}{rcccc} |P^0(t)\rangle & = & g_+(t)|P^0\rangle & + & \dfrac{q}{p}g_-(t)|\overline{P^0}\rangle \\ |\overline{P^0}(t)\rangle & = & \dfrac{p}{q}g_-(t)|P^0\rangle & + & g_+(t)|\overline{P^0}\rangle \end{array} \tag{2.26}$$

where

$$g_\pm(t) = \frac{1}{2}\left(e^{-iM_Lt}e^{-\frac{1}{2}\Gamma_Lt} \pm e^{-iM_Ht}e^{-\frac{1}{2}\Gamma_Ht}\right). \tag{2.27}$$

Considering decays from a initial state B_s^0 or $\overline{B}_s^0$ to a final state $|f\rangle$ or to its *CP* conjugate $|\bar{f}\rangle$, the following amplitudes can be defined

$$\begin{array}{ll} A_f = \langle f|H_W^{(\Delta F=1)}|P^0\rangle & A_{\bar{f}} = \langle \bar{f}|H_W^{(\Delta F=1)}|P^0\rangle \\ \bar{A}_f = \langle f|H_W^{(\Delta F=1)}|\overline{P^0}\rangle & \bar{A}_{\bar{f}} = \langle \bar{f}|H_W^{(\Delta F=1)}|\overline{P^0}\rangle. \end{array} \tag{2.28}$$

The decay rates are proportional to the square of the time-dependent decay amplitudes, the proportionality factor given by a phase space factor f_{PS},

$$\begin{aligned} \Gamma(P^0(t) \to f) \;=\;& f_{PS}|A_f|^2e^{\Gamma t}\Big[\left(1+|\lambda_f|^2\right)\cosh\left(\frac{\Delta\Gamma t}{2}\right) - 2\Re\lambda_f\sinh\left(\frac{\Delta\Gamma t}{2}\right) \\ &+ \left(1-|\lambda_f|^2\right)\cos(\Delta mt) - 2\Im\lambda_f\sin(\Delta mt)\Big] \end{aligned} \tag{2.29}$$

$$\begin{aligned} \Gamma(P^0(t) \to \bar{f}) \;=\;& f_{PS}|\bar{A}_{\bar{f}}|^2e^{\Gamma t}\left|\frac{q}{p}\right|^2\Big[\left(1+|\bar{\lambda}_{\bar{f}}|^2\right)\cosh\left(\frac{\Delta\Gamma t}{2}\right) - \Re\bar{\lambda}_{\bar{f}}\sinh\left(\frac{\Delta\Gamma t}{2}\right) \\ &- \left(1-|\bar{\lambda}_{\bar{f}}|^2\right)\cos(\Delta mt) + 2\Im\bar{\lambda}_{\bar{f}}\sin(\Delta mt)\Big] \end{aligned} \tag{2.30}$$

$$\begin{aligned} \Gamma(\overline{P^0}(t) \to f) \;=\;& f_{PS}|A_f|^2e^{\Gamma t}\left|\frac{p}{q}\right|^2\Big[\cosh\left(\frac{\Delta\Gamma t}{2}\right) - \Re\lambda_f\sinh\left(\frac{\Delta\Gamma t}{2}\right) \\ &- \left(1-|\lambda_f|^2\right)\cos(\Delta mt) + 2\Im\lambda_f\sin(\Delta mt)\Big] \end{aligned} \tag{2.31}$$

$$\begin{aligned} \Gamma(\overline{P^0}(t) \to \bar{f}) \;=\;& f_{PS}|\bar{A}_{\bar{f}}|^2e^{\Gamma t}\Big[\left(1+|\bar{\lambda}_{\bar{f}}|^2\right)\cosh\left(\frac{\Delta\Gamma t}{2}\right) - 2\Re\bar{\lambda}_{\bar{f}}\sinh\left(\frac{\Delta\Gamma t}{2}\right) \\ &+ \left(1-|\bar{\lambda}_{\bar{f}}|^2\right)\cos(\Delta mt) - 2\Im\bar{\lambda}_{\bar{f}}\sin(\Delta mt)\Big] \end{aligned} \tag{2.32}$$

where the complex quantities λ_f have been defined as:

$$\lambda_f = \frac{q}{p}\frac{\bar{A}_f}{A_f} \qquad \bar{\lambda}_{\bar{f}} = \frac{p}{q}\frac{A_{\bar{f}}}{\bar{A}_{\bar{f}}} \tag{2.33}$$

and also

$$\Gamma = \frac{\Gamma_L + \Gamma_H}{2}. \tag{2.34}$$

2.2.2 *CP* violation in the neutral meson system

In order to determine whether a symmetry is conserved or violated, it is necessary to compare processes related by that symmetry. In the case of *CP* symmetry, it is interesting to study pairs of processes related by a *CP* transformation. Let $|f\rangle$ and $|\bar{f}\rangle$ be two *CP* conjugated final states,

$$CP|f\rangle = e^{i\alpha_f}|\bar{f}\rangle, \qquad CP|\bar{f}\rangle = e^{-i\alpha_f}|f\rangle. \tag{2.35}$$

The flavour states P^0 and $\overline{P^0}$ are also related by a *CP* transformation

$$CP|P^0\rangle = e^{i\alpha_P}|\overline{P^0}\rangle \tag{2.36}$$

In these expressions, the phases α_f and α_P are convention-dependent and hence unphysical. Additionally, if $|f\rangle$ is a *CP* eigenstate then $e^{i\alpha_f} = \eta_f = \pm 1$, according to whether $|f\rangle$ is *CP*-odd or *CP*-even. The amplitudes A_f and $\bar{A}_{\bar{f}}$ describe the *CP* conjugated processes $P^0 \to f$ and $\overline{P^0} \to \bar{f}$

$$\begin{aligned} A_f &= \langle f|H|P^0\rangle & (2.37)\\ \bar{A}_{\bar{f}} &= \langle \bar{f}|H|\overline{P^0}\rangle \\ &= \langle \bar{f}|CP^\dagger(CPHCP^\dagger)CP|\overline{P^0}\rangle \\ &= e^{-i(\alpha_P-\alpha_f)}\langle f|H_{CP}|P^0\rangle. & (2.38) \end{aligned}$$

There are three main independent ways in which *CP* is broken in meson decays:

- *CP*-violation in the decay or direct *CP*-violation. This type of *CP*-violation occurs when the decay rates for $P^0 \to f$ and $\overline{P^0} \to \bar{f}$ are different. This is the only *CP*-violation possible in $\Delta F = 1$ processes.
- *CP*-violation in the mixing or indirect *CP*-violation. It implies that the oscillation $P^0 \to \overline{P^0}$ is different from $\overline{P^0} \to P^0$, so it manifests itself in $\Delta F = 2$ processes.
- *CP*-violation in the interference between mixing and decay. When the final state is accesible from P^0 and $\overline{P^0}$, this type of *CP*-violation can be observed in the interference between the amplitudes with and without mixing.

Before entering upon the explanation on the different types of *CP*-violation, an important remark about the structure of the amplitudes is interesting. Consider a decay process and its *CP* conjugate. If *CP* is not conserved, the two amplitudes do not need to be correlated and can be completely different in modulus and phase. Two arbitrary complex numbers A_f and $\bar{A}_{\bar{f}}$ can always be decomposed in the following way

$$\begin{aligned} A_f &= \sum_j |A_j|e^{i\delta_j}e^{i\phi_j} \\ \bar{A}_{\bar{f}} &= \sum_j |A_j|e^{i\delta_j}e^{-i\phi_j}. & (2.39) \end{aligned}$$

The amount of *CP* violation can be this way encoded iside the so called *CP-violating* phases, ϕ_j, which arise from the *CP*-violating terms of the Lagrangian and change sign under *CP*. In the SM, these terms appear only in the weak sector (through Yukawa couplings, see Sect. 2.1.1.2), so these phases are usually called *weak* phases.

The *CP*-conserving phases, δ_j, arise in the amplitudes even if the Lagrangian is invariant under *CP*. In the SM they are normally related with the strong interaction, and are commonly referred to as *strong* phases.

The descomposition (2.39) is particularly explicit in the SM, where the different terms can be associated to contributions with the same CKM content.

CP-violation in the decay

Consider the situation in which no oscillation occurs, *i.e.*, $B = 0$ or $\Delta M = \Delta\Gamma = 0$. Then, following the master equations (2.32), it can be shown that

$$\begin{aligned} \Gamma(P^0(t) \to f) &= f_{PS} e^{-\Gamma t} |A_f|^2 \\ \Gamma(\overline{P^0}(t) \to \bar{f}) &= f_{PS} e^{-\Gamma t} |\bar{A}_{\bar{f}}|^2 \end{aligned} \tag{2.40}$$

CP is violated if these two decay rates are different, $\Gamma(P^0(t) \to f) \neq \Gamma(\overline{P^0}(t) \to \bar{f})$, which will happen if

$$\left| \frac{\bar{A}_{\bar{f}}}{A_f} \right| \neq 1 \tag{2.41}$$

Note that this type of *CP* violation requires at least two terms in (2.39) with different weak and strong phases,

$$|A_f|^2 - |\bar{A}_{\bar{f}}|^2 = -2 \sum_{i,j} |A_i||A_j| \sin(\phi_i - \phi_j) \sin(\delta_i - \delta_j). \tag{2.42}$$

This type of *CP* violation is the only possible one in charged meson (and baryon) decays, where mixing effects are absent.

CP-violation in the mixing

Consider now a final state f that can only come from P^0, but not from $\overline{P^0}$, and its *CP* analogue, that is

$$A_{\bar{f}} = \bar{A}_f = \lambda_f = \bar{\lambda}_{\bar{f}} = 0 \tag{2.43}$$

These processes are normally referred to as *flavour-specific* decays. The transitions $P^0(t) \to \bar{f}$ and $\overline{P^0}(t) \to f$ can only procceed through mixing. According to (2.32),

$$\begin{aligned} \Gamma(P^0(t) \to f) &= f_{PS} |\bar{A}_{\bar{f}}|^2 \left| \frac{q}{p} \right|^2 \left[\cosh\left(\frac{\Delta\Gamma t}{2} \right) - \cos(\Delta m t) \right] \\ \Gamma(\overline{P^0}(t) \to \bar{f}) &= f_{PS} |A_f|^2 \left| \frac{p}{q} \right|^2 \left[\cosh\left(\frac{\Delta\Gamma t}{2} \right) - \cos(\Delta m t) \right] \end{aligned} \tag{2.44}$$

Considering also that there is not *CP*-violation in the decay ($|A_f| = |\bar{A}_{\bar{f}}|$), the two decay rates can still be different if

$$\left| \frac{q}{p} \right| \neq 1. \tag{2.45}$$

In such case, *CP* is violated in the mixing between P^0 and $\overline{P^0}$.

It is interesting to note that in case of *CP* conservation the mass eigenstates (P_L and P_H) are also *CP* eigenstates, as can be shown from (2.22) and (2.36).

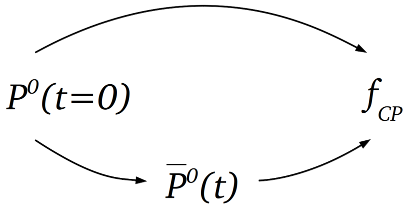

Figure 2.3: Interference between the direct decay $P^0 \rightarrow f_{CP}$ and the decay after mixing $P^0 \rightarrow \overline{P^0} \rightarrow f_{CP}$, at time t, from an initial P^0 meson.

CP-violation in the interference between mixing and decay

Consider, finally, the case where a final state f can be reached from both P^0 and $\overline{P^0}$. In particular, if the final state f is a *CP* eigenstate the process falls in this category. In the following, the case of a final *CP* eigenstate is treated. For examples of non-*CP* eigenstates see [26, 27].

As $f = \bar{f} \equiv f_{CP}$, two amplitudes interfere in the process,

$$A(P^0(t) \rightarrow f_{CP}) \sim A(P^0 \rightarrow f_{CP}) + A(P^0 \rightarrow \overline{P^0} \rightarrow f_{CP}) \tag{2.46}$$

as it is sketched in Fig. 2.3. Even if neither the decay itself nor the mixing introduce *CP*-violation, the interference between these two decay channels can produce a nonzero *CP* asymmetry. In this situation, (2.32) can be simplified to

$$\begin{aligned}
\Gamma(P^0(t) \rightarrow f) &= f_{PS}|A_{f_{CP}}|^2 e^{\Gamma t}\Big[\left(1 + |\lambda_{f_{CP}}|^2\right)\cosh\left(\frac{\Delta\Gamma t}{2}\right) - 2\Re\lambda_{f_{CP}}\sinh\left(\frac{\Delta\Gamma t}{2}\right) \\
&\quad + \left(1 - |\lambda_{f_{CP}}|^2\right)\cos(\Delta m t) - 2\Im\lambda_{f_{CP}}\sin(\Delta m t)\Big] \qquad (2.47) \\
\Gamma(\overline{P^0}(t) \rightarrow f) &= f_{PS}|A_{f_{CP}}|^2 e^{\Gamma t}\left|\frac{p}{q}\right|^2\Big[\cosh\left(\frac{\Delta\Gamma t}{2}\right) - \Re\lambda_{f_{CP}}\sinh\left(\frac{\Delta\Gamma t}{2}\right) \\
&\quad - \left(1 - |\lambda_{f_{CP}}|^2\right)\cos(\Delta m t) + 2\Im\lambda_{f_{CP}}\sin(\Delta m t)\Big] \qquad (2.48) \\
& \qquad (2.49)
\end{aligned}$$

and the following time-dependent *CP* asymmetry can be defined

$$\begin{aligned}
\mathcal{A}_{CP}(t) &= \frac{\Gamma(\overline{P^0}(t) \rightarrow f_{CP}) - \Gamma(P^0(t) \rightarrow f_{CP})}{\Gamma(\overline{P^0}(t) \rightarrow f_{CP}) + \Gamma(P^0(t) \rightarrow f_{CP})} \\
&= \frac{\left(|\lambda_f|^2 - 1\right)\cos(\Delta m t) + 2\Im\lambda_f\sin(\Delta m t)}{(1 + |\lambda_f|^2)\cosh\left(\frac{\Delta\Gamma t}{2}\right) - 2\Re\lambda_f\sinh\left(\frac{\Delta\Gamma t}{2}\right)}.
\end{aligned} \tag{2.50}$$

From the later expresion it is clear that even if neither the decay itself nor the mixing introduce *CP* violation, *i.e.* $|\lambda_{f_{CP}}| = 1$, the interference between the two decay amplitudes can produce a nonzero *CP* asymmetry whenever

$$\Im\lambda_{f_{CP}} \neq 0 \tag{2.51}$$

and only in the presence of P^0-$\overline{P^0}$ oscillation ($\Delta M \neq 0$). In this particular situation, where $\lambda_{f_{CP}}$ is a pure phase, it is common to use the notation

$$\lambda_{f_{CP}} = e^{-i(\phi_M + \phi_D)} \tag{2.52}$$

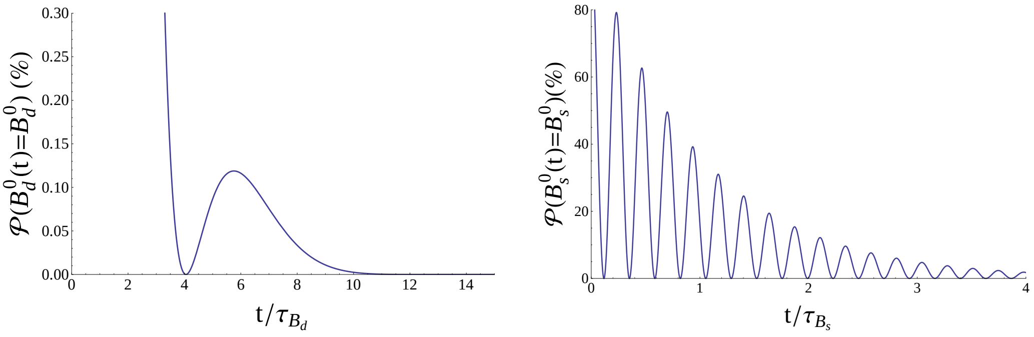

Figure 2.4: Oscillation probabilities for B^0 and B_s^0 mesons. The time is given in units of the meson lifetime.

where the *mixing angle*, ϕ_M, and the *decay angle*, ϕ_D, have been defined as

$$\phi_M \equiv \arg(p/q)\,, \qquad \phi_D \equiv \arg\left(A_f/\bar{A}_f\right)\,. \tag{2.53}$$

Note that these two phases are convention dependent, and consequently non physical. The only measurable phase is $\arg(\lambda_{f_{CP}})$.

The interpretation of the different types of *CP* violation in terms of CKM parameters is in general non trivial, since the hadronic quantities, A_i and δ_i are usually afected by large uncertainties. There are, however, some particular cases where this calculation turns cleaner. As it will be explainded in Sect. 2.3.2.3, a B decay into a *CP*-eigenstates which is dominated by a *single* amplitude, like $B_s^0 \rightarrow K^{*0}\overline{K}^{*0}$, is an example of this kind of processes.

2.2.3 *B*-meson systems

The discussion about *CP* violation in the previous sections describes all meson systems of different families, K, D, B^0 and B_s. In this section, the characteristic features of B decays are reviewed.

There are two neutral B meson systems, B^0-$\overline{B}^0$ and B_s^0-$\overline{B}_s^0$, with a good measure of similarities and differences. The mass differences for both systems are [28, 29]

$$\begin{aligned} \Delta M_d &= 0.510 \pm 0.004\text{ps}^{-1} \\ \Delta M_s &= 17.69 \pm 0.08\text{ps}^{-1} \end{aligned} \tag{2.54}$$

This means that while the B^0 meson oscillates relatively slowly, the oscillations of the B_s^0 meson are very fast: ~ 25 oscillations before the decay, on average. In fact from (2.26), the probability of finding a P^0 at time t from an original P^0 is given by

$$\mathcal{P}(P^0(t) = P^0) = |g_+(t)|^2 \simeq \frac{1}{2}e^{-\Gamma t}\left(1 + \cos(\Delta M t)\right) \tag{2.55}$$

where Γ is the average width and the approximation is valid if $\Delta\Gamma \ll \Gamma$. Then, B_s^0 mesons oscillate about 35 times faster than B^0 mesons, as it is shown in Fig. 2.4.

The width difference in the B^0 system is found to be small. While an initial beam of K^0 and $\overline{K}^0$ turns into a practically pure K_L beam, this does not happen with $B^0/\overline{B}^0$

beams. For the B_s^0 system $\Delta\Gamma$ is also sizable and should be taken into account. Measured values for these width differences can be found in [30], which average to

$$\begin{aligned}\Delta\Gamma_d/\Gamma_d &= 0.015 \pm 0.018 \\ \Delta\Gamma_s/\Gamma_s &= 0.123 \pm 0.017\end{aligned} \tag{2.56}$$

Bounds on *CP* violation in B mixing have been measured using semileptonic decays. A semileptonically decaying b-quark proceeds as $b \to l^- \bar{\nu} X$, whereas the $\bar{b}$-quark decays as $\bar{b} \to l^+ \nu X$. At the B-factories (BaBar, Belle experiments), B and $\bar{B}$ mesons are produced simultaneously through $e^+e^- \to \Upsilon \to B^0\bar{B}^0$. Two same-sign leptons in the final state characterise the events where mixing has taken place, so the following asymmetry can be determined

$$\mathcal{A}_{sl} = \frac{N^{++} - N^{--}}{N^{++} + N^{--}} = \frac{\Gamma(P^0 \to \overline{P^0}) - \Gamma(\overline{P^0} \to P^0)}{\Gamma(P^0 \to \overline{P^0}) + \Gamma(\overline{P^0} \to P^0)} = \frac{1 - |q/p|^4}{1 + |q/p|^4} \tag{2.57}$$

from where $|q/p|$ can be extracted. An average of all measurements performed at B factories yields [31]

$$\left|\frac{q}{p}\right|_d = 1.0002 \pm 0.0028. \tag{2.58}$$

Since the energy at the B-factories is not large enough to produce B_s^0 mesons, the measurement of $|q/p|$ for B_s^0 system comes from the Tevatron experiments D0 and CDF [31]

$$\left|\frac{q}{p}\right|_s = 1.0048 \pm 0.0033. \tag{2.59}$$

These results are compatible with *CP* conservation in B^0 and B_s^0 mixing, as well as with the small predicitions of the SM for these values (see Sect. 2.2.4).

The D0 collaboration has reported the evidence for a large decay asymmetry A_{sl}^b in a mixture of B^0 and B_s^0 semileptonic decays [32], which shows tension with the SM prediction at the level of 3.6 standard deviations. If the measure of A_{sl}^b is confirmed, this would demonstrate the presence of physics beyond the SM in the quark sector. The most precise results for the separate asymmetries in B_s^0 and B^0 come from LHCb [33, 34] and the B-factories [31], and are in good agreement with the SM. Fig. 2.5 shows all of these measurements and the SM prediction.

2.2.4 *CP*-violation in the SM

The *CP*-violation in the Standard Model comes from the electroweak sector, in particular, from the Yukawa couplings. As explained in Sect. 2.1.1.2, the spontaneous breaking of the gauge symmetry in EW theory provides masses for the quarks and introduces flavour mixing, through the CKM matrix. Since this matrix is complex, it also allows the possibility of *CP* violation.

The SM makes no predictions for the values of the CKM matrix elements, aside from the unitarity relation $V^{CKM}(V^{CKM})^\dagger = \mathbf{1}$. To see how *CP* violation arises in this picture consider first the case of 2 fermion families. The most general 2×2 unitary matrix can be parameterised by one angle and three phases. However, three of those phases can be

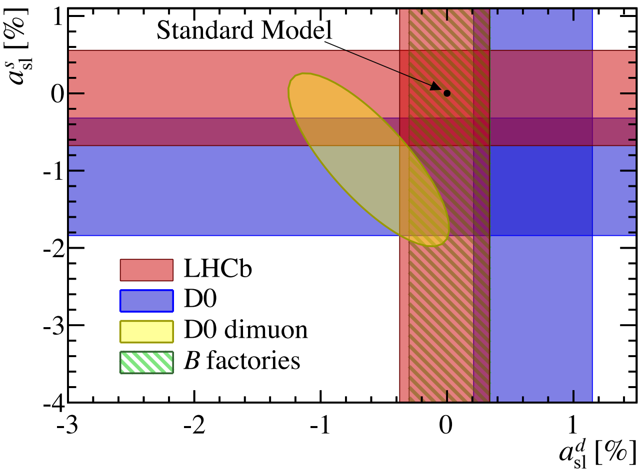

Figure 2.5: Measurement of semileptonic B decay asymmetries. The bands correspond to the central values ±1 standard deviation.

absorbed by rephasing the four quark fields. This means that for 2 fermion families, the CKM matrix can always be chosen to be real.

$$V_C = \begin{pmatrix} \cos\theta_C & \sin\theta_C \\ \sin\theta_C & \cos\theta_C \end{pmatrix} \tag{2.60}$$

where θ_C is the Cabibbo angle [14]. The conclusion is that with only two families, the SM can not account for *CP* violation. This argument led to the prediction of the third family of quarks, once *CP* violation was observed.

For three generations of quarks, unitarity reduces the number of independent parametres from 18 to 9[1], by applying the set of constraints

$$\sum_{k=1}^{3} V^*_{ki} V_{kj} = \delta_{ij}. \tag{2.61}$$

These constraints are usually pictured as triangles in the complex plane, the *unitarity triangles*. For example, the first and the third columns of the CKM matrix, *i.e.*, the b and d sectors, can be used to build the unitarity relation

$$V^*_{ud}V_{ub} + V^*_{cd}V_{cb} + V_{td} * V_{tb} = 0, \tag{2.62}$$

which can be represented as the triangle shown in Fig. 2.6, with its sides normalised to $V^*_{cd}V_{cb}$.

From the remaining independent parameters of V^{CKM}, five of them can be absorbed in the redefinition of the quark fields. The resulting four free parameters are tree rotation angles, the quark mixing angles θ_{ij}, and one complex phase δ. Therefore, the SM with three families predicts *CP* violation provided this phase is not zero. In terms of these

---

[1] A $n \times n$ complex matrix, $U_{n\times n}$, contains $2n^2$ parameters. If the matrix is unitary, the number of independent parameters decreases to n^2.

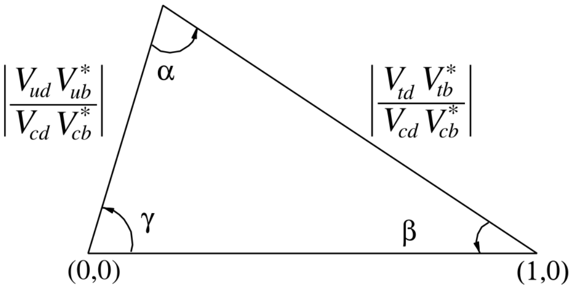

Figure 2.6: Unitarity triangle defined by (2.62).

parameters,

$$V^{CKM} = \begin{pmatrix} c_{12}c_{23} & s_{12}c_{13} & s_{13}e^{-i\delta} \\ -s_{12}c_{23} - c_{12}s_{23}s_{13}e^{i\delta} & c_{12}c_{23} - s_{12}s_{23}s_{13}e^{i\delta} & s_{23}c_{13} \\ s_{12}s_{23} - c_{12}c_{23}s_{13}e^{i\delta} & -c_{12}s_{23} - s_{12}c_{23}s_{13}e^{i\delta} & c_{23}c_{13} \end{pmatrix}, \tag{2.63}$$

where $s_{ij} = \sin\theta_{ij}$ and $c_{ij} = \cos\theta_{ij}$. The interactions between quarks of different generations are scaled by the appropriate CKM matrix elements, which means that a certain quark transition is more or less favorable depending on the value of the CKM element involved. To clearly show this hierarchy, it is useful to use the Wolfenstein parametrisation [16], which allows to write the CKM matrix as an expansion on $s_{12} \simeq 0.22$,

$$V^{CKM} = \begin{pmatrix} 1-\frac{\lambda^2}{2} & \lambda & A\lambda^3(\rho - i\eta) \\ -\lambda & 1-\frac{\lambda^2}{2} & A\lambda^2 \\ A\lambda^3(1-\rho-i\eta) & -A\lambda^2 & 1 \end{pmatrix} + \mathcal{O}(\lambda^4), \tag{2.64}$$

with λ, A, ρ and η defined by

$$s_{12} = \lambda = \frac{|V_{us}|}{\sqrt{|V_{ud}|^2 + |V_{us}|^2}}, \qquad s_{23} = A\lambda^2 = \lambda\left|\frac{V_{cb}}{V_{us}}\right|, \qquad s_{13}e^{i\delta} = A\lambda^3(\rho + i\eta) = V_{ub}^*. \tag{2.65}$$

In this parameterisation, the complex *CP* violating phase is

$$\gamma \equiv \arg\left(\frac{V_{ud}^*V_{ub}}{V_{cd}^*V_{cb}}\right) = \arg(\rho + i\eta) + \mathcal{O}(\lambda^4) \tag{2.66}$$

which up to $\mathcal{O}(\lambda^4)$ is localized in $V_{ub} = |V_{ub}|e^{-i\gamma}$ and $V_{td} = |V_{td}|e^{-i\beta}$, and the rest of the entries are real. β is defined as

$$\beta \equiv \arg\left(\frac{V_{cd}^*V_{cb}}{V_{td}^*V_{tb}}\right) = \arg(1 - \rho + i\eta) + \mathcal{O}(\lambda^4), \tag{2.67}$$

and it is zero if γ is zero. Therefore, *CP* is not conserved in the SM provided $\gamma \neq 0$, and the size of this violation in related to the area of the triangle shown in Fig. 2.6.

Experimentally, the sides and angles of this triangle (and analog triangles corresponding to different unitarity relations) can be determined by measuring the decay rates and *CP*-violating asymmetries of processes involving those CKM elements. Fig. 2.7 shows the current experimental situation for the unitarity triangle defined by (2.62), from [35].

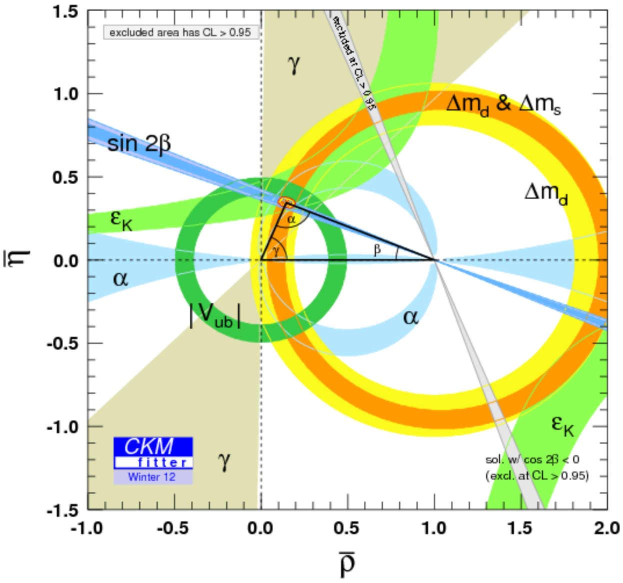

Figure 2.7: Current best fit for the unitarity triangle defined by (2.62) by the CKM-fitter collaboration.

2.2.4.1 Predictions for $B_{d,s}$ mixing angles in the SM

As it has been discussed in a previous section, the experimental data reveal that $\Delta\Gamma \ll \Delta M$ for both B meson systems. This result implies[1] that also $|\Gamma_{12}| \ll |M_{12}|$, and then

$$\frac{q}{p} = \sqrt{\frac{M_{12}^* - \frac{1}{2}\Gamma_{12}^*}{M_{12} - \frac{1}{2}\Gamma_{12}}} \simeq \sqrt{\frac{M_{12}^*}{M_{12}}} \equiv e^{-i\phi_M} \tag{2.68}$$

This means that in order to compute the mixing angles and the mass differences, it is enough to compute the mixing parameters $M_{12}^{d,s}$. As stated in Sect. 2.2.1.1, M_{12} contains contributions from $H_W^{(\Delta F=2)}$ and also from transitions with intermediate on-shell states at second order in $H_W^{(\Delta F=1)}$. Fortunately, in the SM the mixing of B mesons is dominated by the $\Delta F = 2$ box diagrams with a top quark in the loop, shown in Fig. 2.2 for the B_s^0 system (equivalen diagrams for B^0 system, exchanging each s-quark by a d-quark).

The CKM structure of these contributions is

$$\begin{aligned} (M_{12}^d)^* &\propto (V_{td}V_{tb}^*)^2 \\ (M_{12}^s)^* &\propto (V_{ts}V_{tb}^*)^2 \,. \end{aligned}$$

Consequently, it is easy to see that the B^0-$\overline{B}^0$ mixing angle in the SM is given by

$$\phi_d^{SM} = 2\beta + \mathcal{O}(\lambda^4). \tag{2.69}$$

---

[1] From (2.24) and the definition of B, it can be shown that

$$\begin{aligned} (\Delta M)^2 - \frac{1}{4}(\Delta\Gamma)^2 &= 4|M_{12}|^2 - |\Gamma_{12}|^2 \\ \Delta M \cdot \Delta\Gamma &= 4\Re(M_{12}\Gamma_{12}^*) \end{aligned}$$

The analogous angle for the B_s^0-system, ϕ_s^{SM}, is zero at this level of approximation, which means that enters in terms which are suppressed by at least λ^4. However, the phase itself is $\mathcal{O}(\lambda^2)$. The angle β_s is defined as

$$\beta_s \equiv -\arg\left(-\frac{V_{ts}V_{tb}^*}{V_{cs}V_{cb}^*}\right). \tag{2.70}$$

Up to $\mathcal{O}(\lambda^6)$, only V_{ts} acquires a phase, so $V_{ts} = -|V_{ts}|e^{-1\beta_s}$. In fact, $\beta_S \simeq -\lambda^2\eta$. Then, the B_s^0-$\bar{B}_s^0$ mixing angle in the SM is given by

$$\phi_s^{SM} = 2\beta_s + \mathcal{O}(\lambda^6). \tag{2.71}$$

This is the way in which the mixing angles are related to the angles of the unitarity triangles in the Standard Model.

2.3 The $B_s^0 \to K^{*0}\bar{K}^{*0}$ decay

The $B_s^0 \to K^{*0}\bar{K}^{*0}$ decay proceeds through a flavour changing neutral current (FCNC). In particular, in this process a *b* quark transforms into a *s* quark. These kind of processes do not arise at tree level in the SM. The reason is that in the SM, the couplings of the quarks to the neutral Z^0 boson are flavour-diagonal (the terms with the neutral boson have the form $\bar{u}_L\gamma^\mu u_L Z_\mu$), and the FCNC transitions can only occur at higher orders in perturbation theory, in loop processes, such as *penguin* and *box* diagrams, see Fig. 2.8.

These processes allow physics at high energies to be probed through the virtual particles entering the loops. This feature makes them suitable for searching for physics beyond the SM, which may introduce new heavy particles that affect the observables related to these transitions.

In particular, time-dependent *CP* asymmetries in $b \to s$ modes, like $B_s^0 \to K^{*0}\bar{K}^{*0}$, are considered a very sensitive probe of New Physics (NP) [5]. The study of $B^0 \to \phi K_s^0$, for example, has already shown tensions with the SM predictions[1] [36, 37]. However, the lack of a model-independent evaluation of the theoretical error is a strong limitation for a complete and meaningful test of the SM. This is not the case of the $B_s^0 \to K^{*0}\bar{K}^{*0}$, where the theoretical error can be controlled with high accuracy by using the U-spin mirror channel $B^0 \to K^{*0}\bar{K}^{*0}$ [3].

In the next section, a brief introduction on the main theoretical tools used in the study of *B* physics is given. Specific predictions for the $B_s^0 \to K^{*0}\bar{K}^{*0}$ mode based in these approaches are given in the following sections.

2.3.1 Factorisation and Effective field theories

In general, the term "*B* physics" refers to the study of weak decays of *b* quarks. However, the confinement properties of QCD forbids quark level transitions, such as $b \to s$, to be measured directly. Instead, the decays of *B* mesons (or baryons) will be observed experimentally. This means that an undersanding of the conection between quark and hadron properties is required in order to determine the parameters of the weak sector

---

[1] *CP* mixing asymmetry has been measured to be $S(B_d \to \phi K^0) = 0.39 \pm 0.18$, show some tension with the theoretical prediction $sin(2\beta) = 0.675 \pm 0.026$

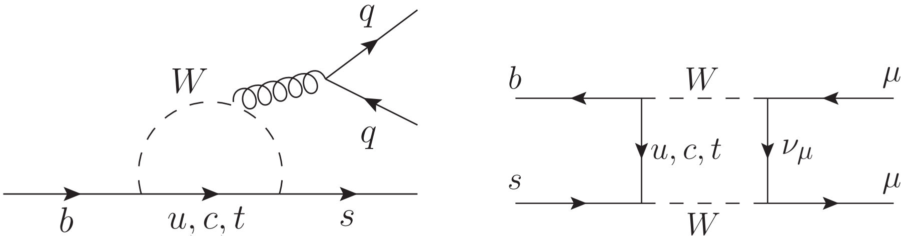

(a) $b \to s q\bar{q}$ penguin diagram.

(b) $B_s^0 \to \mu^+\mu^-$ box diagram

Figure 2.8: Effective flavour-changing neutral current processes.

of the SM. Equivalently, (at least) two different energy scales become relevant to the problem: the scale of weak interactions, given by the mass of the W boson, M_W, and the hadronic scale Λ_{QCD}.

Fortunately, in this kind of physical process, where contributions come from two (or more) widely separated energy scales, it is possible to study the low-energy (long-distance) phenomena independently of the details of the high-energy (short-distance) interactions. At this point it is also useful to introduce a simpler description of the relevant features of the full theory at a given energy scale in the form of an *effective theory*.

In the case of B decays, the large scale of weak interactions with respect to the mass of the B mesons ($m_B \ll M_W$) motivates the use of the *weak effective Hamiltonian*. Additional intermediate scales can also be considered. For example, the large mass of the B meson compared with the low scale of the strong interaction inside hadrons allows the definition of the Heavy Quark Effective Theory [38].

2.3.1.1 The weak effective Hamiltonian

Effective field theories [39] are used to express a full, complete theory as an effective Hamiltonian constructed from a set of local operators O_i in which the high energy degrees of freedom, defined with respect to a mass scale Λ, have been integrated out. The weak effective Hamiltonian describes weak interactions at low energy, below M_W, and is defined so that the amplitude of a weak process $i \to f$ is expressed as a sum of local operator amplitudes,

$$A(i \to f) = \langle f|\mathcal{H}_e ff|i\rangle = \frac{G_F}{\sqrt{2}}\sum_i V_i C_i(\mu)\langle f|O_i|i\rangle \tag{2.72}$$

where G_F is the Fermi constant characterizing the strength of the underlying weak processes, V_i are the suitable CKM matrix elements for the quark transition and O_i are the local operators forming a complete set for a given transition. The coeficients associated with the local operators, C_i, are called *Wilson coefficients* and include the effects of interactions at scales higher than μ. The choice of μ is arbitrary, usually chosen to be $\mathcal{O}(m_b)$ when dealing with B decays. The long distance interactions, on the other hand, are contained in the matrix elements of the local operators.

Wilson coefficients are calculated by *matching* the prediction of the effective theory with the assumed full theory at high mass scale, $\mu \sim M_W$; at this scale the relevant diagrams and their QCD corrections can be calculated perturbatively and evolved down to the relevant energy scale ($\mu \sim m_b$) by making use of the renormalisation-group equations.

After renormalisation, the local operators O_i can be identified within the full calculation and their corresponding Wilson coefficients can be extracted.

2.3.1.2 Hadronic Matrix elements

The Wilson coefficients of the effective weak Hamiltonian are process-independent and can be used directly in the description of exclusive models. The theoretical precision is thus limited by the difficulty of evaluating the, intrinsically non-perturvative, hadronic matrix elements between initial and final state, $\langle f|O_k|i\rangle$.

The concept of *factorisation* of matrix elements has been used to face this problem [40]. The idea being to reduce the matrix elements to products of process-independent form factors and decay constants that could be extracted from data or calculated using non-perturvatibe techniques, such as lattice simulation.

In the case of B decays, this factorisation can be understood in terms of the *heavy quark approximation* [38, 39]. The dynamical simplifications which occur in the heavy-mass limit are usually ilustrated by considering a hadron composed of a heavy quark, Q, and other light constituents. The quarks confined inside hadrons exchange momentum of magnitude $\sim \Lambda_{QCD}$. The mass of the heavy quark in the hadron is, by definition, $M_Q \gg \Lambda_{QCD}$ and its Compton wavelength $\lambda_Q \sim 1/M_Q$ is much smaller than the hadronic size $R_{had} \sim 1/\Lambda_{QCD}$. To resolve the quantum numbers of the heavy quark a hard probe, $q^2 \gtrsim M_Q^2$, is required. However, the soft gluons coupled to the light constituents of the hadron can only resolve larger distances of order R_{had} and are thus blind to the flavour and spin orientation of the heavy quark, feeling only its colour field . Therefore, in the infinite M_Q limit, the properties of the *heavy-light* hadrons are independent of the mass and spin of the heavy source of colour. Based on this limit, a whole effective theory can be constructed as an expansion in powers of Λ_{QCD}/m, with m the mass of the heavy quark. This effective theory is known as the Heavy Quark Effective Theory.

A complementary approach to B decay phenomenology relies on the approximate flavour symmetries of QCD in order to find relations between observables of different processes. Both approaches are usually combined, specially in the study of non-leptonic B decays.

2.3.2 The decay $B_s^0 \to K^{*0}\overline{K}^{*0}$ in the Standard Model

The decay of a B_s^0 meson into two light K^{*0} vector mesons proceeds dominantly in the SM through the penguin diagrams shown Fig. 2.9. This process has been studied in the framework of QCD factorisation, and SM predictions of its expected branching ratio ($\mathcal{B}$) and longitudinal polarisation fraction (f_L, defined in the following section) have been provided [2]. Additionally, the use of flavour symmetries has been proposed in order to relate this decay to its B^0 counterpart for the study of CP-violation [4, 5]. The next sections summarize the theoretical work related to $B_s^0 \to K^{*0}\overline{K}^{*0}$.

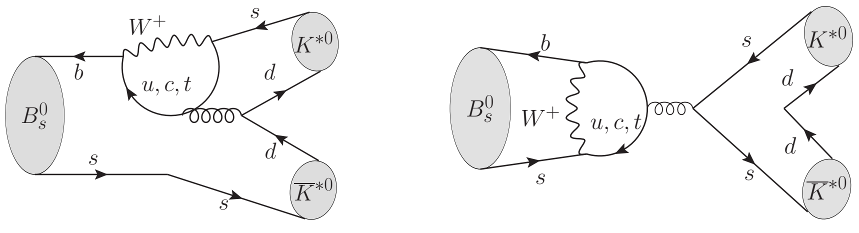

Figure 2.9: Diagrams contributing to the decay $B_s^0 \to K^{*0}\overline{K}^{*0}$ in the SM. Left: The colour-suppressed penguin diagram, which is expected to be the dominant contribution. Right: Penguin anihilation contribution.

2.3.2.1 $B \to VV$ decays: Amplitudes and Observables

The amplitude of a B meson decaying into two vector mesons V_1 and V_2 can be written, using the notation $B(p) \to V_1(k_1, \epsilon_1)V_2(k_2, \epsilon_2)$, as [41]

$$\mathcal{A}_{B\to VV} = \boldsymbol{a}\ \varepsilon_1^* \cdot \varepsilon_2^* + \frac{\boldsymbol{b}}{m_B^2}(p \cdot \varepsilon_1^*)(p \cdot \varepsilon_2^*) + i\frac{\boldsymbol{c}}{m_B^2}\epsilon_{\mu\nu\rho\sigma}p^\mu q^\nu \varepsilon_1^{*\rho}\varepsilon_2^{*\sigma} \tag{2.73}$$

where $k_{1,2}$ and $\varepsilon_{1,2}$ are the momentum and polarisation for the vector meson 1 and 2 respectively and $q \equiv k_1 - k_2$. The amplitudes $\boldsymbol{a}$ and $\boldsymbol{b}$ are linear combinations of the amplitudes describing final states with relative angular momentum between V_1 and V_2 of $L = 0, 2$. The amplitude $\boldsymbol{c}$ corresponds to $L = 1$.

Alternatively, a basis of amplitudes describing decays to final state particles with definite helicity is given by

$$A_0 = \frac{k_1 \cdot k_2}{m_1 m_2}\left(-\boldsymbol{a} + \boldsymbol{b}\frac{p^2}{k_1 \cdot k_2}\right) \qquad A_\pm = \boldsymbol{a} \pm 2\frac{p}{m_B}\boldsymbol{c}. \tag{2.74}$$

In experimental analyses, the transversity basis, where $A_\pm$ are replaced by $A_\parallel = (A_+ + A_-)/\sqrt{2}$ and $A_\perp = (A_+ - A_-)/\sqrt{2}$, corresponding to linearly polarised final states, is preferably used .

Experimentally, the magnitudes and relative phases of the various amplitudes can be extracted from the analysis of the angular distributions of the vector resonances' decay products. The full angular dependence of the cascade where both vector mesons decay into a pair of pseudoscalar particles will be given in Chapter 4. The decay rate can be written as

$$\frac{d\Gamma}{d\Omega} \propto \left|A_0 F_0(\Omega) + A_\parallel F_\parallel(\Omega) + A_\perp F_\perp(\Omega)\right|^2 \tag{2.75}$$

where $F_i(\Omega)$ are functions describing the angular distribution of the B daughters. Therefore, a given $B \to VV$ decay allows the definition of five observables corresponding to the three magnitudes and two relative phases of the helicity amplitudes or the five angular coefficients obtained from the expansion of (2.75). A typical set of observables consist of the branching fraction, two out of the three polarisation fractions f_L, $f_\parallel$, $f_\perp$, and two phases $\delta_\parallel$, $\delta_\perp$, where

$$f_{L,\parallel,\perp} = \frac{|A_{0,\parallel,\perp}|^2}{|A_0|^2 + |A_\parallel|^2 + |A_\perp|^2}, \qquad \delta_{\parallel,\perp} = \arg\frac{A_{\parallel,\perp}}{A_0} \tag{2.76}$$

It is conventional to combine the five observables of the $B \to VV$ decay with those of its CP conjugate $\bar{B}$ decay. Denoting the $\bar{B}$ decay helicity amplitudes as $\bar{A}_h$ and the corresponding transversity amplitudes as $\bar{A}_{\parallel,\perp} = (\bar{A}_+ \pm \bar{A}_-)/\sqrt{2}$, the equality $A_{\parallel,\perp} = \bar{A}_{\parallel,\perp}$ is true in the absence of CP violation. The CP average observables and asymmetries are thus given by

$$f_h = \frac{1}{2}(f_h^B + f_h^{\bar{B}}), \qquad \mathcal{A}_{CP}^h = \frac{f_h^{\bar{B}} - f_h^B}{f_h^{\bar{B}} + f_h^B} \tag{2.77}$$

($h = L, \parallel, \perp$) for the polarisation fractions and

$$\delta_h = \delta_h^{\bar{B}} - \Delta\delta_h = \delta_h^B + \Delta\delta_h \tag{2.78}$$

for the phase observables.

2.3.2.2 The $B_s^0 \to K^{*0}\bar{K}^{*0}$ amplitude

Following the convention by Beneke, Rohrer and Yang [2], the SM weak effective Hamiltonian mediating $B_s^0 \to K^{*0}\bar{K}^{*0}$ transitions is given by

$$\mathcal{H}_{eff} = \frac{G_F}{\sqrt{2}} \sum_{p=u,c} V_{pb}V_{ps}^* \left\{ C_1 O_1^p + C_2 O_2^p + \sum_{i=3,\ldots 10,7\gamma,8g} C_i O_i \right\} + h.c. \tag{2.79}$$

where $O_{1,2}^p$ are the left-handed current-current operators arising from W-boson exchange, $O_{3,\ldots 6}$ and $O_{7,\ldots 10}$ are QCD and electroweak penguin operators, and $O_{7\gamma}$ and Q_{8g} are the electromagnetic and chromomagnetic dipole operators. They are given by

$$\begin{array}{ll}
O_1^p = (\bar{p}b)_{V-A}(\bar{s}p)_{V-A}, & O_2^p = (\bar{p}_i b_j)_{V-A}(\bar{s}_j p_i)_{V-A}, \\
O_3 = (\bar{s}b)_{V-A} \sum_q (\bar{q}q)_{V-A}, & O_4 = (\bar{s}_i b_j)_{V-A} \sum_q (\bar{q}_j q_i)_{V-A}, \\
O_5 = (\bar{s}b)_{V-A} \sum_q (\bar{q}q)_{V+A}, & O_6 = (\bar{s}_i b_j)_{V-A} \sum_q (\bar{q}_j q_i)_{V+A}, \\
O_7 = (\bar{s}b)_{V-A} \sum_q \frac{3}{2} e_q (\bar{q}q)_{V+A}, & O_8 = (\bar{s}_i b_j)_{V-A} \sum_q \frac{3}{2} e_q (\bar{q}_j q_i)_{V+A}, \\
O_9 = (\bar{s}b)_{V-A} \sum_q \frac{3}{2} e_q (\bar{q}q)_{V-A}, & O_{10} = (\bar{s}_i b_j)_{V-A} \sum_q \frac{3}{2} e_q (\bar{q}_j q_i)_{V-A}, \\
O_{7\gamma} = \frac{-e}{8\pi^2} m_b \bar{s}\sigma_{\mu\nu}(1+\gamma_5)F^{\mu\nu} b, & O_{8g} = \frac{-g_s}{8\pi^2} m_b \bar{s}\sigma_{\mu\nu}(1+\gamma_5)G^{\mu\nu} b
\end{array} \tag{2.80}$$

where $(\bar{q}_1 q_2)_{V\pm A} = \bar{q}_1 \gamma_\mu (1 \pm \gamma_5) q_2$, i, j are colour indices, e_q are the electric charges of the quarks in units of $|e|$, and the sum runs over all active quark flavours in the effective theory, i.e. $q = u, d, s, c, b$.

In general, the matrix elements $\langle V_1 V_2 | O_i | \bar{B} \rangle$, can be calculated using the QCD factorisation approach [2, 42]. In this framework they can be expressed, at leading order in the Λ_{QCD}/m_b expansion, as

$$\langle V_1 V_2 | O_i | \bar{B} \rangle = \left(F^{B \to V_1} T_i^I * f_{V_2} \Phi_{V_2} + [V_1 \leftrightarrow V_2] \right) + T_i^{II} * f_B \Phi_B * f_{V_1} \Phi_{V_1} * f_{V_2} \Phi_{V_2}, \tag{2.81}$$

where non-perturbative effects are cotained in the form factors $F^{B \to V_i}$, the decay constants f_{V_i} and the meson light-cone distribution amplitudes, Φ (the star products imply an integration over light-cone momentum fractions of the constituent quarks inside the meson). The hard scattering kernels $T_i^{I,II}$ include only short distance effects and can

Table 2.2: *CP*-averaged branching fraction and longitudinal polarisation fraction calculated in the framework of QCD factorisation [2]. Using experimental input from $B^0 \to \phi K^{*0}$ decays the column labeled "$\hat{\alpha}_4^{c,-}$ f. d." is obtained. The first uncertainty is the uncertainty associated with the CKM parameters and the second one is the theoretical uncertainty.

Decay	$\mathcal{B}/10^{-6}$		$f_L/\%$	
	default	$\hat{\alpha}_4^{c,-}$ f. d.	default	$\hat{\alpha}_4^{c,-}$ f. d
$B_s^0 \to K^{*0}\overline{K}^{*0}$	$9.1^{+0.5+11.3}_{-0.4-6.8}$	$7.9^{+0.4+4.3}_{-0.4-3.9}$	63^{+0+42}_{-0-29}	72^{+0+16}_{-0-21}
$B^0 \to K^{*0}\overline{K}^{*0}$	$0.6^{+0.1+0.5}_{-0.1-0.3}$	$0.6^{+0.1+0.3}_{-0.1-0.2}$	69^{+1+34}_{-1-27}	69^{+1+16}_{-1-20}

be calculated through perturbation theory. The result of computing this hard-scattering kernels for the various operators in the effective weak Hamiltonian is usually presented in terms of "factorised operators" $A([\bar{q}_{V_1} q_{V_1}][\bar{q}_{V_1} q_{V_1}])$ with coefficients $\alpha_i^p(V_1, V_2)$ [42]. The coeficients α_i^p contain all dynamical information, while the arguments of A_i encode the flavour composition of the final state ($V_1 V_2$) to which a given term can contribute. The matrix elements of the factorised operators, $A_{V_1 V_2}$, are simply proportional to a form factor times a decay constant.

The decay amplitude for the $B_s^0 \to K^{*0}\overline{K}^{*0}$ decay, can thus be written as ($h = 0, +, -$)

$$A^h_{B_s^0 \to K^{*0}\overline{K}^{*0}} = \sum_{p=u,c} V_{pb} V_{ps}^* \left\{ A^h_{K^{*0}\overline{K}^{*0}} \beta_4^{p,h} + A^h_{\overline{K}^{*0}K^{*0}} [\hat{\alpha}_4^{p,h} + \beta_4^{p,h}] \right\} \tag{2.82}$$

where $\beta_i^{p,h}$ are the coefficients corresponding to a second set of factorised operators describing weak annihilation amplitudes. From this expression, predictions for the branching ratio, $\mathcal{B}$, and the longitudinal polarisation fraction, f_L of $B_s^0 \to K^{*0}\overline{K}^{*0}$ have been provided [2]. These results are summarized in Table 2.2, together with the equivalent results for $B^0 \to K^{*0}\overline{K}^{*0}$.

2.3.2.3 *CP* violation in $B_s^0 \to K^{*0}\overline{K}^{*0}$

Consider the formalism presented in Sect. 2.2 for B_s^0 mesons, with $f = K^*\bar{K}^*$. As the final state is a mixture of *CP* eigenstates, this decay is sensitive to the three types of *CP* violation. The decay amplitude for a certain helicity (or polarisation) in the final state can be expressed as [40]

$$A(B_s^0 \to K^{*0}\overline{K}^{*0}) = -V_{tb}^* V_{ts} P_s - V_{ub}^* V_{us} P_s^{GIM}. \tag{2.83}$$

where P_s contains the hadronic matrix elements corresponding to $b \to s$ penguins containing a t-quark loop, and P_s^{GIM} represents the GIM-suppressed difference of contributions coming from charm and up quarks loops.

Neglecting the contribution of P_s^{GIM} [5], the decay $B_s^0 \to K^{*0}\overline{K}^{*0}$ is mediated by a single amplitude, so that under this asumption no *CP* violation in the decay can be produced,

$$\frac{\bar{A}}{A} = \frac{V_{tb} V_{ts}^*}{V_{tb}^* V_{ts}} = e^{-i\phi_D} \quad \text{with} \quad \phi_D = -2\beta_s. \tag{2.84}$$

As was explained in Sect. 2.2.4.1, within the SM, *CP* violation in mixing is not expected at a measurable level for the B_s^0-system,

$$\frac{q}{p} = e^{-i(2\beta_s)}. \tag{2.85}$$

Consequently, the only source of *CP* violation in this process is expected to be the interference between mixing and decay. However, according to Eqs. 2.84 and 2.85, there is a cancellation between the phases arising from mixing and decay[1], and the total *CP*-violating weak phase, $\phi_s^{B_s^0 \to K^{*0}\overline{K}^{*0}}$, is negligibly small in the SM for this channel, as

$$\lambda(B_s^0 \to K^{*0}\overline{K}^{*0}) = \frac{q}{p}\frac{A(\overline{B}_s^0 \to K^{*0}\overline{K}^{*0})}{A(B_s^0 \to K^{*0}\overline{K}^{*0})} = e^{-i\phi_s^{B_s^0 \to K^{*0}\overline{K}^{*0}}} = 1. \tag{2.86}$$

The study of *CP*-violation in this decay is then a null test of the SM. This is already a very attractive feature in favour of $B_s^0 \to K^{*0}\overline{K}^{*0}$, but there is another one. As the precision in the measurement of the *CP*-violation parameters will increase, an estimate of the error induced by neglecting P_s^{GIM} will be needed. However, the polluting contribution, P_s^{GIM}, is an hadronic object, in general, difficult to compute. The advantage of this mode is the possibility of calculating the theoretical error in a model independent way extracting the size of P_s^{GIM} from the analysis of $B^0 \to K^{*0}\overline{K}^{*0}$. This will be explained with more detail in the following section.

2.3.2.4 U-spin symmetry

The prediction given in the previous section for $\phi_s^{B_s^0 \to K^{*0}\overline{K}^{*0}}$ relies on the fact that the second amplitude P_s^{GIM} can be neglected to a good approximation. The theoretical error induced by this assumption has been studied by various authors [3, 5, 6, 43]. As already mentioned, the main advantage of $B_s^0 \to K^{*0}\overline{K}^{*0}$ over other decay modes is that the size of the polluting amplitude can be estimated from the study of the U-spin-conjugate process $B^0 \to K^{*0}\overline{K}^{*0}$. This is a pure $b \to d$ penguin decay, whose amplitude can be written as

$$A(B^0 \to K^{*0}\overline{K}^{*0}) = -V_{tb}^* V_{td} P_d - V_{ub}^* V_{ud} P_d^{GIM} \tag{2.87}$$

which is equivalent to (2.83), except that in this case the two combinations of CKM matrix elements are of the same order of magnitude. As a consequence, the sensitivity to the second amplitude, P_d^{GIM}, is maximal in this case.

Assuming that no new physics contributes in an appreciable way to $B^0 \to K^{*0}\overline{K}^{*0}$, the measurement of its branching fraction ($\mathcal{B}$) and time-dependent *CP* asymmetry, allows the determination $|P_d|$, $|P_d^{GIM}|$ and their relative strong phase, δ_d. In the SU(3)-symmetry limit, $P_d^{GIM} = P_s^{GIM}$ and $\delta_d = \delta_s$. Imposing these relations, introduces an error that is related to the size of the SU(3) breaking. Fig. 2.10 for example, shows the precision on the theoretical prediction expected when 100% SU(3) breaking effects are assumed [5]. In [4–6], different ways, both experimental and theoretical, of determining the size of the SU(3) breaking are proposed.

---

[1] Other authors [8] argue that if P^{GIM} is neglected, every $\mathcal{O}(\lambda^4)$ term needs to be neglected too. Since $\phi_M \propto \arg(V_{tb}^* V_{ts})$ and $\Im(V_{tb}^* V_{ts}) \sim \mathcal{O}(\lambda^4)$, ϕ_M and $\phi_s^{B_s^0 \to K^{*0}\overline{K}^{*0}}$ vanish in this approximation.

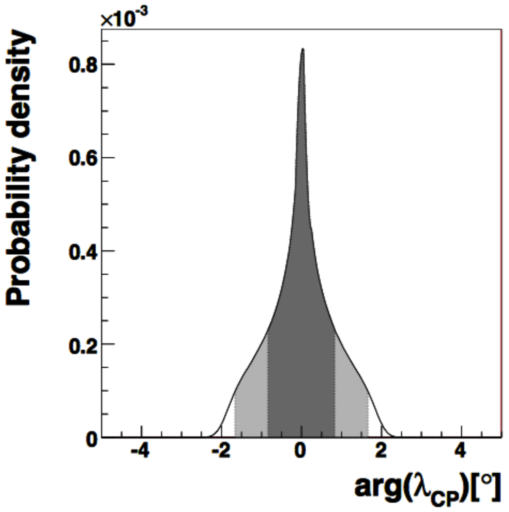

Figure 2.10: Probability density function for $\arg(\lambda_{CP}(B_s^0 \to K^{*0}\overline{K}^{*0}))$ obtained in [5] allowing 100% SU(3) breaking effects.

Additionally, calculations in the context of QCD-factorisation [44], provide SM predictions for the $B_s^0 \to K^{*0}\overline{K}^{*0}$ longitudinal observables[1] in terms of the corresponding observables for $B^0 \to K^{*0}\overline{K}^{*0}$. These predictions are summarized in Table 2.3.

Table 2.3: SM predictions for the longitudinal observables related to $B_s^0 \to K^{*0}\overline{K}^{*0}$ from [4, 44]. The SM value of the B_s^0 mixing phase $\phi_s = -2\beta_s = -2\,\text{deg}$ is used, and the $\mathcal{B}^{long}(B^0 \to K^{*0}\overline{K}^{*0})$ is assumed to be larger than 5×10^{-7}.

$$R_{sd}^{DMV} = \frac{\mathcal{B}^{long}(B_s^0 \to K^{*0}\overline{K}^{*0})}{\mathcal{B}^{long}(B^0 \to K^{*0}\overline{K}^{*0})} = 16.4 \pm 5.2$$

$$\mathcal{A}_{dir}^{long}(B_s^0 \to K^{*0}\overline{K}^{*0}) = \frac{1-|\lambda_0|^2}{1+|\lambda_0|^2} = 0.000 \pm 0.0014$$

$$\mathcal{A}_{mix}^{long}(B_s^0 \to K^{*0}\overline{K}^{*0}) = -2\frac{\Im\lambda_0}{1+|\lambda_0|^2} = 0.004 \pm 0.018$$

2.3.2.5 Triple product asymmetries in $B_s^0 \to K^{*0}\overline{K}^{*0}$

A powerful tool for the study of *CP*-violation is the investigation of *triple product asymmetries* [41, 45]. A four body decay gives rise to three independent final momenta in the rest frame of the decaying particle. It is possible to construct a T-odd observable out of these, *e.g.* $\vec{p}_1 \times (\vec{p}_2 \cdot \vec{p}_3)$. Equivalently, triple products (TP) of spin or polarisation vectors in particle decays are odd under time-reversal.The presence of a non-zero TP can be established by measuring a nonzero value of the asymmetry

$$\mathcal{A}_T \equiv \frac{\Gamma(\vec{p}_1 \times (\vec{p}_2 \cdot \vec{p}_3) > 0) - \Gamma(\vec{p}_1 \times (\vec{p}_2 \cdot \vec{p}_3) < 0)}{\Gamma(\vec{p}_1 \times (\vec{p}_2 \cdot \vec{p}_3) > 0) + \Gamma(\vec{p}_1 \times (\vec{p}_2 \cdot \vec{p}_3) < 0)} \quad , \tag{2.88}$$

---

[1] The longitudinal observables are those related to the longitudinal polarisation (where only A_0 occurs). These observables, free form positive- and negative-helicity components, can be predicted with much better accuracy than transverse ones [4].

this corresponding to the TP previously given as an example. This may be due to a T-violating phase, and hence, by the CPT theorem, be a sign of CP-violation. However, the nonzero value of such asymmetry could also be caused by a CP-conserving phase from final state interactions. Thus the TP asymmetry $\mathcal{A}_T$ is not a true T-violating observable. However, it is still possible to obtain a genuine T-violating (CP-violating) signal when comparing $\mathcal{A}_T$ and $\overline{\mathcal{A}}_T$, where $\overline{\mathcal{A}}_T$ is the TP asymmetry measured in the CP-conjugated process.

Consider B_s decays into two vector mesons V_1 and V_2, each decaying to a pair of pseudoscalars, P_1P_1' and P_2P_2', as in $B_s^0 \to K^{*0}(K^+\pi^-)\overline{K}^{*0}(K^-\pi^+)$. The most general Lorentz-covariant amplitude for the this kind of decays is given by (2.73). In $|\mathcal{M}|^2$, a triple product correlation arises from interference terms involving the $\boldsymbol{c}$ amplitude. In the rest frame of the B meson, it takes the form $q \cdot (\varepsilon_1^* \times \varepsilon_2^*)$. This TP will be present if $\Im(ac^*)$ or $\Im(bc^*)$ is nonzero. Since the three amplitudes contain, in general, both CP-conserving and CP-violating phases, the origin of these terms cannot be associated with a CP-violating effect.

Consider now the amplitude for the CP-conjugated process $\bar{B}(p) \to \bar{V}_1(k_1, \epsilon_1)\bar{V}_2(k_2, \epsilon_2)$,

$$\overline{\mathcal{M}} = \bar{\boldsymbol{a}}\ \varepsilon_1^* \cdot \varepsilon_2^* + \frac{\bar{\boldsymbol{b}}}{m_B^2}(p \cdot \varepsilon_1^*)(p \cdot \varepsilon_2^*) - i\frac{\bar{\boldsymbol{c}}}{m_B^2}\epsilon_{\mu\nu\rho\sigma}p^\mu q^\nu \varepsilon_1^{*\rho}\varepsilon_2^{*\sigma} \tag{2.89}$$

where $\bar{\boldsymbol{a}}$, $\bar{\boldsymbol{b}}$ and $\bar{\boldsymbol{c}}$ can be obtained from $\boldsymbol{a}$, $\boldsymbol{b}$ and $\boldsymbol{c}$ by changing the sign of the weak phases. If CP is conserved, $\bar{\boldsymbol{a}} = \boldsymbol{a}$, $\bar{\boldsymbol{b}} = \boldsymbol{b}$ and $\bar{\boldsymbol{c}} = \boldsymbol{c}$. Note that the term containing the amplitude $\boldsymbol{c}$ in $\overline{\mathcal{M}}$ changes sign relative to that in $\mathcal{M}$. This means the TP asymmetry in $|\overline{\mathcal{M}}|^2$ is opposite to the one in $|\mathcal{M}|^2$. Thus the *true* T-violating asymmetry is defined by the addition of the TP asymmetries in $|\mathcal{M}|^2$ and $|\bar{\mathcal{M}}|^2$,

$$\mathcal{A}_T^{true} \equiv \frac{1}{2}\left(\mathcal{A}_T + \bar{\mathcal{A}}_T\right). \tag{2.90}$$

In fact, considering the following parameterisation for the amplitudes

$$\begin{aligned}
\boldsymbol{a} &= \sum_i a_i e^{i\phi_i^a} e^{\delta_i^a}\ , \qquad & \bar{\boldsymbol{a}} &= \sum_i a_i e^{-i\phi_i^a} e^{\delta_i^a}\ , \\
\boldsymbol{b} &= \sum_i b_i e^{i\phi_i^b} e^{\delta_i^b}\ , \qquad & \bar{\boldsymbol{b}} &= \sum_i b_i e^{-i\phi_i^b} e^{\delta_i^b}\ , \\
\boldsymbol{c} &= \sum_i c_i e^{i\phi_i^c} e^{\delta_i^c}\ , \qquad & \bar{\boldsymbol{c}} &= \sum_i c_i e^{-i\phi_i^c} e^{\delta_i^c}\ ,
\end{aligned} \tag{2.91}$$

where $\phi_i^{a,b,c}$ ($\delta_i^{a,b,c}$) are weak (strong) phases, it can be shown that [8]

$$\frac{1}{2}\left[\Im(\boldsymbol{a}\boldsymbol{c}^*) - \Im(\bar{\boldsymbol{a}}\bar{\boldsymbol{c}}^*)\right] = \sum_{ij} a_i c_j \sin(\phi_i^a - \phi_j^c)\cos(\delta_i^a - \delta_j^c) \tag{2.92}$$

$$\frac{1}{2}\left[\Im(\boldsymbol{b}\boldsymbol{c}^*) - \Im(\bar{\boldsymbol{b}}\bar{\boldsymbol{c}}^*)\right] = \sum_{ij} b_i c_j \sin(\phi_i^b - \phi_j^c)\cos(\delta_i^b - \delta_j^c). \tag{2.93}$$

These observables are true CP-violating quantities even when the strong phase difference vanishes, provided that the weak phase difference between the two amplitudes is not zero. It is interesting to note that these CP-violating quantities occur in triple product asymmetries measured in *untagged* $B_{(s)}$ decays –no knowledge of the flavour of the $B_{(s)}$ meson is required to determine them.

In the case $\bar{B}_{(s)}$ can also decay to V_1V_2, the TP can be modified in time due to $B_{(s)}-\bar{B}_{(s)}$ mixing. As it will be shown in Sect. 4.2.1, the time dependence of the TP asymmetries for untagged decays is

$$\mathcal{A}_T^{true,ac}(t) \propto \sum_{ij} a_i c_i \cos(\delta_i^a - \delta_j^c) \quad e^{-\Gamma t} \quad \left[\sin(\phi_i^a - \phi_j^c)\cosh\left(\frac{\Delta\Gamma t}{2}\right) \right.$$
$$\left. - \sin(\phi_i^a + \phi_j^c + \phi_M)\sinh\left(\frac{\Delta\Gamma t}{2}\right)\right], \tag{2.94}$$

and equivalently for $\mathcal{A}_T^{true,bc}(t)$. Ocasionally, the time-independent factors multiplying $e^{-\Gamma t}\cdot\sinh(\Delta\Gamma t/2)$ are referred to as *mixing-induced TP asymmetries* while the factors before $e^{-\Gamma t}\cdot\cosh(\Delta\Gamma t/2)$ assume the name *TP asymmetry*. Therefore, the two time-integrated *true* TP asymmetries will be proportional to

$$\int_0^\infty \mathcal{A}_T^{true,ac}(t)dt \propto$$
$$\sum_{ij} a_i c_i \cos(\delta_i^a - \delta_j^c)\left[\sin(\phi_i^a - \phi_j^c) - \sin(\phi_i^a + \phi_j^c + \phi_M)\ \mathcal{O}\left(\frac{\Delta\Gamma}{2\Gamma}\right) + \mathcal{O}\left(\left(\frac{\Delta\Gamma}{2\Gamma}\right)^2\right)\right] \tag{2.95}$$

where ϕ_M is the $B_{(s)}-\bar{B}_{(s)}$ mixing phase. An equivalent expression can be written for the time-integrated $\mathcal{A}_T^{true,bc}(t)$.

Previously, it has been shown that $B_s^0 \to K^{*0}\overline{K}^{*0}$ is dominated in the SM by a single amplitude corresponding to the exchange of a t quark inside the loop. In this case, no *CP* violation can be produced, which implies the true TP asymmetries for this decay are expected to be very small, $\mathcal{O}(\lambda^2)$. Note that from the point of view of searching for New Physics, the precise predicted value of a given TP asymmetry is not particularly important. What is relevant is that they are very suppressed in the SM, and so the measurement of a large value for any TPA would point clearly towards the presence of physics beyond the SM.

In the analysis presented in this thesis, the decay $B_s^0 \to K^{*0}\overline{K}^{*0}$ is reconstructed from the final state $B_s^0 \to (K^+\pi^-)(K^-\pi^+)$. Consequently, an irreducible contribution from scalar resonances in the $K\pi$ system is present in the data. While this might be considered a disadvantage, the presence of these new amplitudes actually extends the reach of the study by introducing a new set of *CP*-violating observables (TPA's and direct *CP* asymmetries), described in greater detail in the Chapter 4.

2.3.3 $B_s^0 \to K^{*0}\overline{K}^{*0}$ beyond the Standard Model

In addition to establishing the presence of physics beyond the SM in a model-independent way, the study of *CP* violation in $B_s^0 \to K^{*0}\overline{K}^{*0}$ could reveal information about the nature of the underlying theory when a specific NP scenario is considered. In the time-integrated untagged sample, the sensitivity to mixing-induced NP effects is limited by $\mathcal{O}(\frac{\Delta\Gamma}{2\Gamma})$ as shown in (2.95), and so the most interesting possibility is that NP arises in the decay.

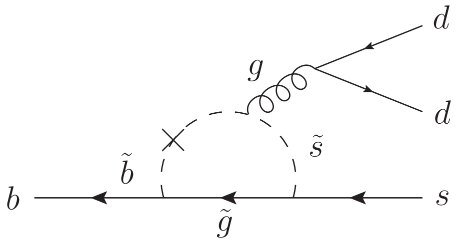

Figure 2.11: Gluino-squark penguin contribution to $b \to s d \bar{d}$ decay.

The case of an extended Higgs sector in which the neutral scalars have FCNC couplings has been studied in [8], assuming that the decay $b \to s d \bar{d}$ is mediated by the lowest-mass state[1]. The form of each helicity amplitude is obtained for different NP operators, in order to compute the *CP*-violating observables that appear in the untagged distribution. The pattern of measurement of these quantities would then give information about the kind of operators mediating the decay.

In the context of SuperSymmetry (SUSY), see [46] for a review, contributions from squark-gluino loops, like the one shown in Fig. 2.11, can be comparable to the penguin-dominated SM amplitudes. These contributions could account for an important enhancement of the direct *CP* asymmetries expected to be very small in $b \to s$ decays [40, 47]. As already mentioned, the presence of scalar resonances in the sample enables the measurement of direct *CP* asymmetries that could contribute in constraining the parameter space of multiple supersymmetric models.

---

[1] This state may be identified with the newly discovered particle of mass $m_H \sim 125$ GeV, in which case $B_s^0 \to K^{*0}\overline{K}^{*0}$ would have the potential to explore the coupling of this new scalar to light quarks.

3

The LHC beauty experiment

3.1 The Large Hadron Colider

The Large Hadron Collider (LHC) is a hadron accelerator and collider operating at CERN [48] since September 2008. It was installed in the 27 km long tunnel built to house the Large Electron Positron collider (LEP), between 45 m and 170 m underneath the surface, in the French and Swiss countryside near Geneva.

LHC was designed to collide proton beams with a centre-of-mass energy of $\sqrt{s} = 14$ TeV [49], providing a perfect enviroment to test the Standard Model and search for signals of physics beyond it. The discovery of the Higgs boson, the last particle in the SM to be observed, was a fundamental objective for the project. On July 2012, the ATLAS and CMS experiments announced they had observed a new particle in the mass region around 125 GeV [12, 13]. One year later, the Nobel prize in physics was awarded jointly to François Englert and Peter Higgs [50].

During 2010 and 2011, when the data used for this thesis were taken, proton-proton collisions took place at $\sqrt{s} = 7$ TeV. Currently, protons collide at $\sqrt{s} = 8$ TeV, and collisions at the $\sqrt{s} = 13$ TeV are expected early in 2015. Protons, obtained from hydrogen gas, pass through several pre-accelerators before reaching the LHC. There, each beam is accelerated to the final energy, from an injection energy of 450 GeV. Fig. 3.1 shows the CERN acceleration complex, including the LHC and all the pre-accelerators. At these energies, a very intense magnetic field (8.33 T at the nominal 7 TeV per beam [48]) is needed to keep the two proton beams in opposite orbits along the accelerator ring. This field is provided by superconducting magnets cooled to a temperature of 1.9 K, using super-fluid helium. The "two-in-one" design chosen, accommodates the windings for the two beam channels in a common yoke and cryostat, with magnetic flux circulating in the opposite sense through the two channels. Fig. 3.2 shows a schematical cross–section of a cryodipole.

Big experiments are placed at each of the four LHC interaction points. The two general–purpose experiments ATLAS [51] and CMS [52] are based on large central detectors, and are designed for the direct detection of new physics particles and processes, like the Higgs boson or SUSY particles. ALICE [53] is a dedicated heavy–ion experiment and studies quark-gluon plasma with data resulting from nucleus–nucleus collision. For the later, the LHC is filled in dedicated runs with heavy ions (e.g., Pb) instead of protons. Finally, LHCb [54] is designed for the study of CP violation and rare decays focusing on the physics of the beauty and charm quarks. Figure 3.3 shows pictures of these four experiments.

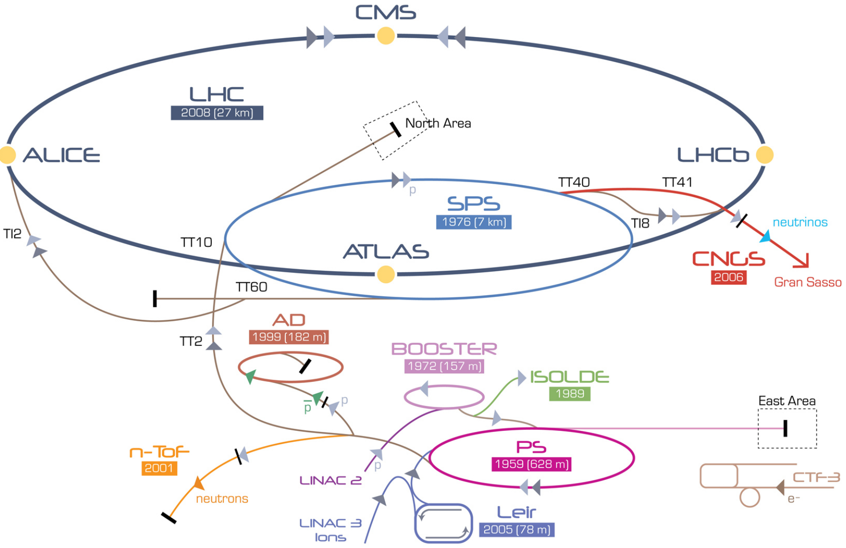

Figure 3.1: CERN accelerator complex with LHC at its end.

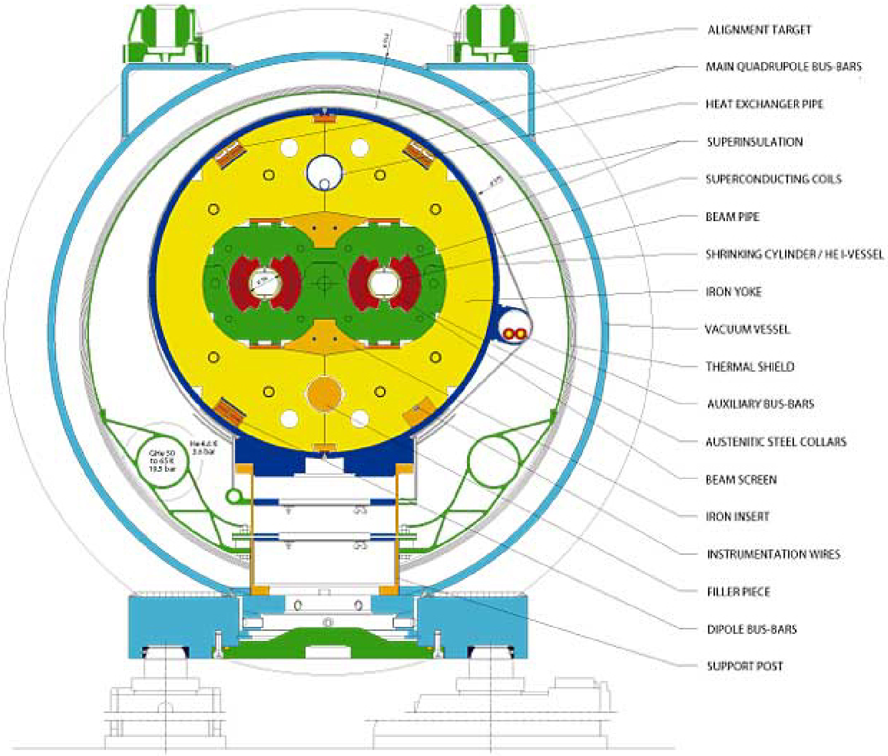

Figure 3.2: Cross–section of a LHC cryodipole.

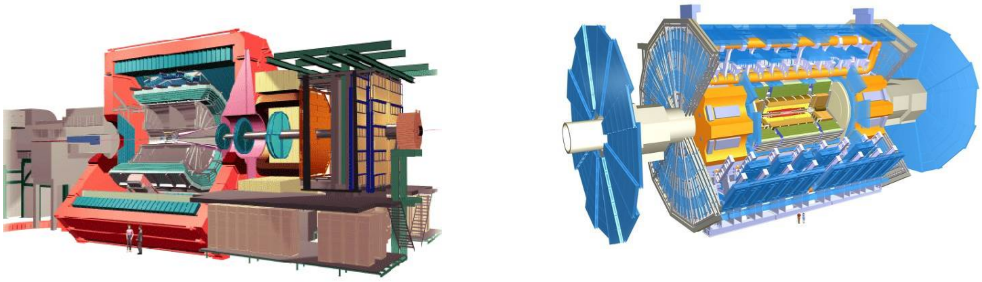

(a) ALICE (b) ATLAS

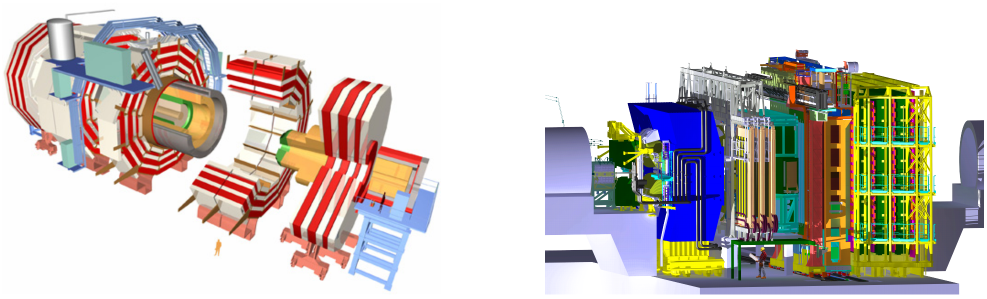

(c) CMS (d) LHCb

Figure 3.3: Four main detectors in LHC

3.2 The LHCb experiment

The Large Hadron Collider beauty (LHCb) experiment was designed to look for indirect evidence of physics beyond the SM in *CP*–violation and rare decays of beauty and charm hadrons [55].

The dedication to B physics constrained the design of the dectector and the choice of its work environment. The forward geometry of the detector takes advantage of the large $b\bar{b}$ cross–section at low angle at the considered energies, see Fig. 3.4. Another essencial requirement for the physics in the experiment is the ability to identify the point where the proton–proton collision took place (primary vertex or PV) and the point where other short–lived but flying particles decayed (secondary vertex or SV). In order to ease this task, LHCb was designed to work at an instantaneous luminosity of $2\text{–}5\times10^{32}$ $\text{cm}^{-2}\cdot\text{s}^{-1}$, smaller than LHC nominal value of 10^{34} $\text{cm}^{-2}\cdot\text{s}^{-1}$. This is achieved by changing the beam focus at the LHCb interaction point independently from the other interaction points.

The detector is located at Intersection Point 8 of the LHC, the former location of the LEP experiment DELPHI. A modification to the LHC optics, displacing the interaction point by 11.25 m from the centre, has permitted maximum use to be made of the existing cavern for the LHCb detector components [56]. In the following sections the LHCb detector and its different subdetectors are described in more detail.

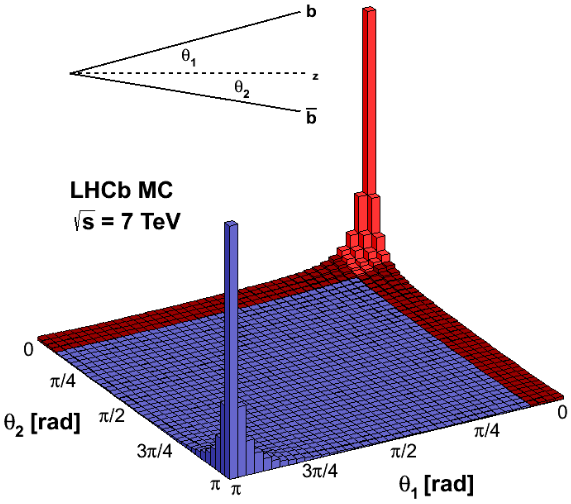

Figure 3.4: Angular distribution of $b\bar{b}$ pairs produced in pp collisions at $\sqrt{s} = 7$ TeV.

3.3 LHCb detector

The LHCb detector is a single–arm spectrometer with a forward angular coverage from approximately 10 mrad to 300 (250) mrad in the bending (non-bending) plane, with respect to the beam axis. In terms of pseudorapidity (η), the LHCb acceptance covers the range $2 < \eta < 5$.

Figure 3.5 shows the layout of the LHCb spectrometer and indicates the right–handed coordinate system adopted, which has the z axis along the beam and the y axis along the vertical. In the following sections, each of the LHCb subsystems will be described in detail.

3.3.1 Tracking System

An efficient and precise reconstruction of the trajectories of charged particles is of fundamental importance for LHCb. From a reconstructed track it is possible to determine the bending of the charged particle in the magnetic field and thus to measure its momentum and electric charge. Combinations of tracks allow one to define vertices, measuring their precise location and their charged track multiplicity. Moreover, a reconstructed track can be interpolated and extrapolated in space, permitting information to be gathered in different subdetectors to characterise the nature of the charged particle.

The LHCb tracking system consists of the Vertex Locator (VELO) and the Tracking Turicensis (TT) placed upstream of the dipole magnet, and the T1-T3 tracking stations downstream of the magnet.

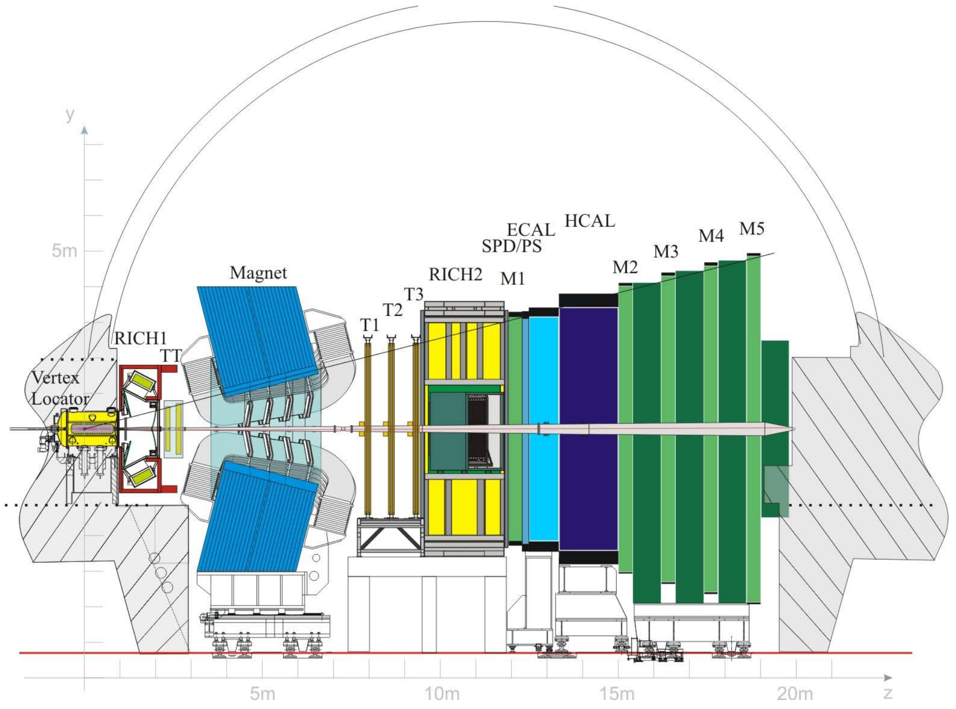

Figure 3.5: View of the LHCb detector.

3.3.1.1 Vertex Locator

The VELO [57] measures the coordinates of tracks close to the interaction point, allowing the decay vertex of the *b*- or *c*-hadron to be separated from the primary *pp* interaction. It is made of 2×21 stations arranged along and perpendicular to the beam direction. Each station contains two semicircular silicon strip sensors mounted back-to-back. One of them measures the *r* coordinate, with circular strips centred around the beam axis, and the other one measures the ϕ coordinate with straight, almost radial strips. Fig. 3.6 (right) shows one of the r-sensors. The minimum pitch in the sensors, at the innermost radius, is 38 μm, with a linear increase up to 101.6 μm, ensuring that the first points on the track are measured with the finest pitch available.

The VELO acceptance covers a pseudo–rapidity range of $1.6 < \eta < 4.9$ for particles coming from primary vertices in the range $-10.6 < z < 10.6$ cm. Two dedicated stations, containing only r–sensors, placed upstream the VELO constitute the *pile–up veto system* that was conceived to veto events with large number of primary vertices.

To improve the resolution on the primary vertex, the first measurement of the track should be as close to the primary interaction as possible. The sensitive area of the modules starts thus at 8mm from the beam axis. This radius is much smaller than the aperture required by the LHC during the injection. In order to prevent severe radiation damage in the detector, the sensors must be retracted by 3cm when LHC is being filled. Consequently, the VELO was designed so that the two halves of the detector can be moved away from the beam in the horizontal direction. Fig. 3.6 (left) shows the layout of one half of the VELO detector.

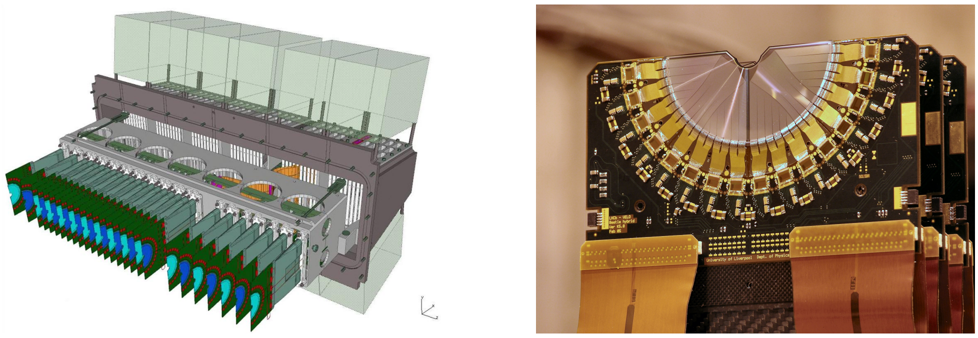

Figure 3.6: Left, layout of one half of the LHCb Vertex Locator. Right, one of r sensors.

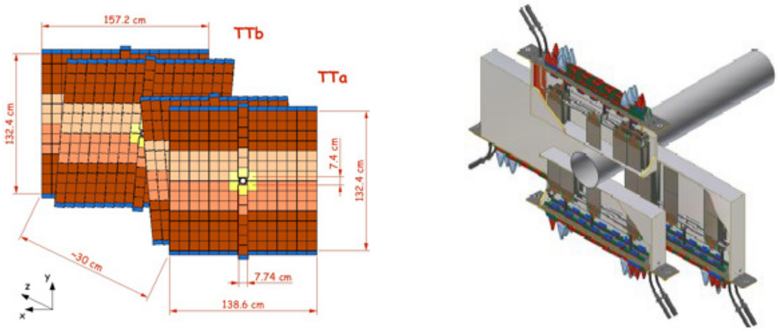

Figure 3.7: Left, layout of the four TT layers. Right, layout of one of the three IT stations.

3.3.1.2 TT and Tracking Stations

Together with the VELO, the LHCb tracking system is composed of the TT, just upstream of the magnet, and by the tree tracking stations between the magnet and RICH2. Two different technologies are employed in these detectors. The TT and the innermost region of the tracking stations, called usually Inner Tracker (IT), is covered by silicon microstrip detectors [58], for this reason the system TT-IT is also called Silicon Tracker (ST). The outer region of the tracking stations, or Outer Tracker (OT), is made of straw–tube drift chambers [59].

In order to get a 3D reconstruction, each of the ST stations consists of four detection layers with vertical strips in the first and last layers and strips rotated by +5º (-5º) for the second (third) layer. The strip pitch in this modules is 200 µm, which gives a single hit resolution of 50 µm. The TT covers the full acceptance of the detector. The IT covers a small cross–shaped region around the beam pipe that constitutes only the 1.3% of a tracking station. However, approximately 20% of the charged tracks produced close to the primary vertex and going through the tracking stations pass through its area. Fig. 3.7 shows the layout of TT and IT subdetectors.

The OT modules are arranged in three stations, each one consisting of four detection layers. As in the case of the ST, the first and the last layers are oriented vertically, while those in the centre are rotated by ±5° with respect to the others. A mixture of Argon and CO_2 is chosen as counting gas. It provides a drift–time below 50 ns and a drift–coordinate resolution of 200 µm.

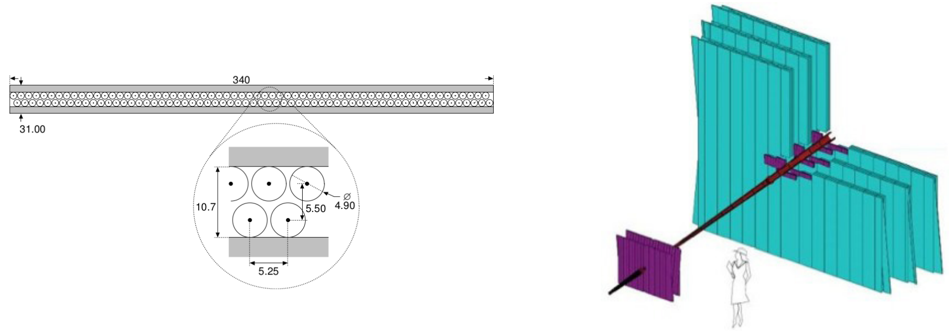

Figure 3.8: Left, cross section of one OT module. Right, TT, IT and OT systems layout.

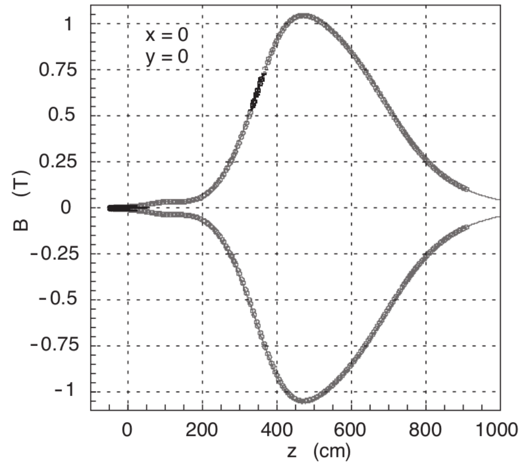

Figure 3.9: B_y component of the magnetic field as a function of the z coordinate.

3.3.1.3 Magnet

In order to measure the momentum of the charged particles produced in LHCb, the experiment uses a dipole magnet [60] that provides an integrated magnetic field of 4Tm. The measurement covers the forward acceptance of ±300 mrad horizontally (bending plane) and of ±250 mrad vertically.

The dipole is composed of two pure Al coils of conical saddle shape placed mirror–symmetrically to each other in a window–frame Fe yoke. The magnetic field provided by the dipole is measured with a precision of a few times 10^{-4} to achieve the required momentum resolution. Fig. 3.9 shows the measured magnetic field (B_y component) along the z axis.

The direction of the magnetic field is changed periodically, in order to reduce systematic uncertainties that might affect *CP* violation studies.

3.3.1.4 Tracking and Vertexing

Event reconstruction relies on the determination of the trajectories of all the charged particles (tracks) and the position where they were generated (vertices). Tracking algorithms combine hits in the VELO, TT and Tracking stations to reconstruct the tra-

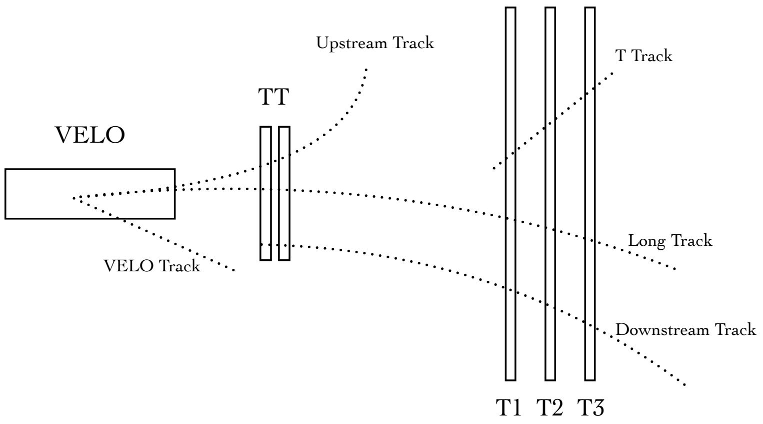

Figure 3.10: Illustration of the five different track types in LHCb.

jectory and measure the momentum of charged particles. Depending on the origin of the hits used to define the track, these can be classified as (see Fig. 3.10):

- **Long tracks:** traverse the full tracking system from the VELO to the T–stations. They provide the most precise momentum measurement, and therefore are the most important tracks in LHCb analyses.
- **Upstream tracks:** traverse only the VELO and the TT. They correspond in general to low momentum particles that were bent out of the detector acceptance by the magnetic field.
- **Downstream tracks:** go through the TT and T stations. They are usually produced by long-living particles decaying outside the VELO, such as K^0_S or Λ.
- **VELO tracks:** are just measured in the VELO. They are typically large angle or backward tracks, useful to reconstruct the primary vertex.
- **T tracks:** have only hits in the T–stations and are typically produced by particles generated in secondary interactions.

Different algorithms are used to reconstruct different types of tracks. In the case of long tracks, the algorithms look first for almost aligned track *seeds* in the VELO, where the magnetic field is low. These seeds are then complemented with hits from the other tracking subdetectors to form tracks [61]. Once the track is found, it is refitted using Kalman fitter algorithm [62], that accounts for multiple scattering and energy loss caused by crossed materials. This procedure provides also a χ^2 related with the probability that the track corresponds to a real particle instead of a mixture of hits left by different particles (ghosts). There is also the posibility of reconstructing the same track through different algorithms (clones); in this case only the best out of the two is kept.

The efficiency to reconstruct long tracks in LHCb has been evaluated using muons from J/ψ decays [63, 64]. The efficiency for 2011 data and and simulation as a function of momentum, rapidity and the number of primary vertices is shown in Fig. 3.11 The global efficiency is measured to be larger than 96%. Hadronic interactions not taken into account in this calculation are reflected in a larger systematic uncertainty.

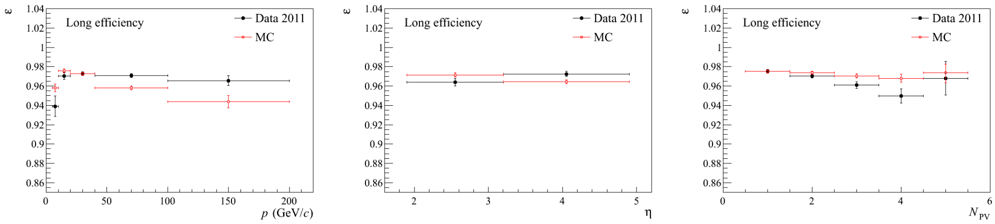

Figure 3.11: Tracking efficiency for the 2011 data and simulation as a function of the momentum, p (left), the pseudorapidity, η (centre) and the number of reconstructed primary vertices, N_{PV} (right).

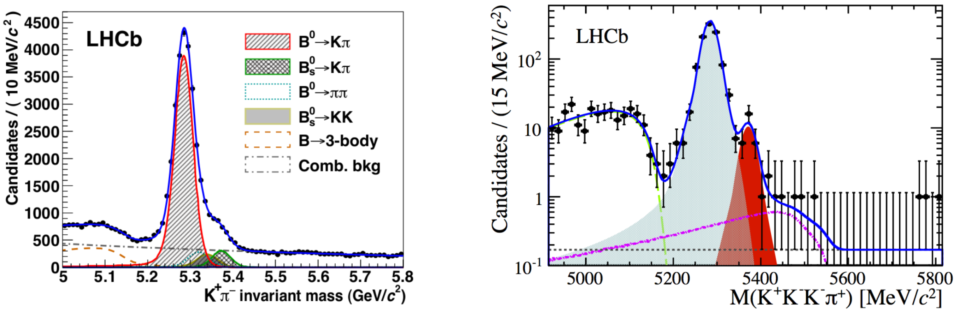

Figure 3.12: Invariant mass distribution of $K^+\pi^-$ [20] (left) and $K^+K^-K^-\pi^+$ [65] (right). The mass resolution is ~ 22 MeV/c^2 for the two body decay and ~ 15 MeV/c^2 for the four body decay.

The precision in the determination of the trajectory of the particle inside the magnetic field, is directly related with the momentum resolution, and a good momentum resolution translates into good mass resolution, a key ingredient for the physics in the experiment. LHCb momentum resolution goes from dp/p = 0.4% for tracks with $p_T = 5$ GeV/c to dp/p = 0.6% for tracks with $p_T = 100$ GeV/c. This results in a mass resolution of ~ 22 MeV/c^2 (~ 15 MeV/c^2) at the B–meson mass for two body (four body) B decays, see Fig. 3.12.

VELO tracks are used to reconstruct primary vertices [66]. The resolution improves significantly with the number of tracks used to reconstruct the vertex. This number ranges from 5 (minimum required) up to 100. Fig. 3.13 shows the PV resolution for the x, y and z coordinates in 2011 data, as a function of the number of tracks entering the PV reconstruction.

A distinctive feature of events containing B or D decays, is the existence of a secondary vertex (SV) separated from the PV, due to the large lifetime of these particles. Equivalently, particles created in these SV's will have a sizable impact parameter [1] (IP) with respect to the primary interaction. A natural way of showing the power of the LHCb track and vertex reconstruction is through the precision achieved in the determination of the IP and the proper–time. Fig. 3.14 shows the IPx (x projection of the IP) and IPy (y projection of the IP) resolutions as a function of $1/p_T$ for 2011 data and their comparison with those for MC simulation. The proper–time resolution is at the level of 50 fs. This

---

[1] The impact parameter is defined as the geometrical distance between a track and a certain vertex, normally the PV.

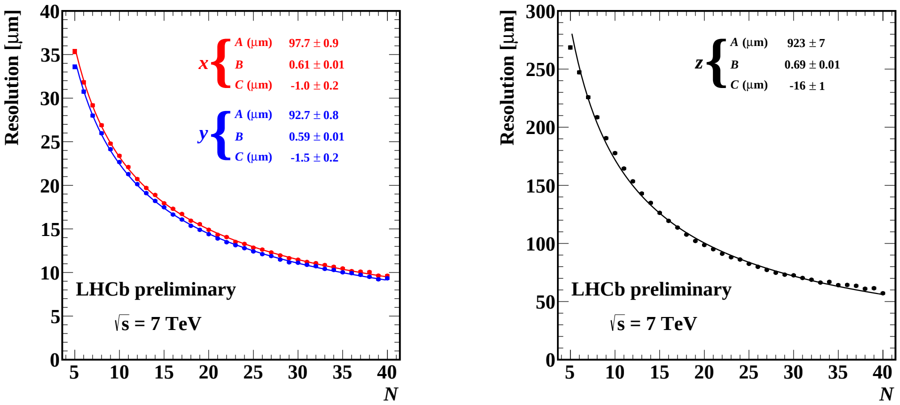

Figure 3.13: PV resolution in x, y (left) and z (right) coordinates in 2011 data as a fucntion of the number of tracks entering the PV reconstruction. Data points are fitted with the parameterisation: $Res = A/N^B + C$.

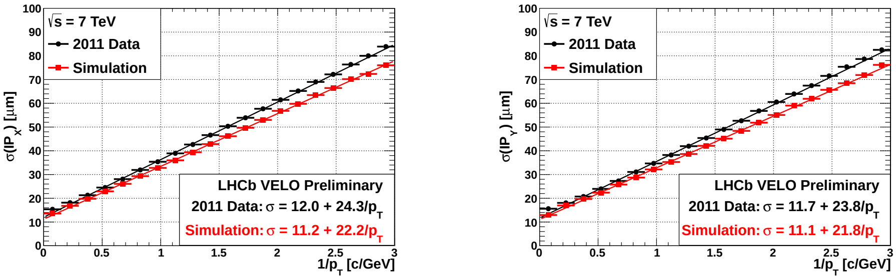

Figure 3.14: IPx (left) and IPy (right) resolution as a function of $1/p_{\mathrm{T}}$ for 2011 data and MC simulation. Data points have been fittes with a linear fucntion.

excellent precision allows the fast B_s^0–$\overline{B}_s^0$ oscillation to be resolved, with an oscillation frequency of $\Delta m_s = 17.768 \pm 0.023(\mathrm{stat}) \pm 0.006(\mathrm{syst})\mathrm{ps}^{-1}$, as measured by LHCb [67] (see Fig. 3.15).

3.3.2 Particle Identification Detectors

Key features for the physics at LHCb, such as the ability to tag the flavour of B mesons or to reject backgrounds that are kinetically and topologically similar to the signal, are only possible if particle identification is available. Distinction between different species of long lived particles is achieved at LHCb with

- two Ring Imaging Cherenkov (RICH) detectors, for K–π separation;
- the Calorimeter System, made of a Scintillator Pad Detector and Preshower (SPD/PS), and electromagnetic calorimeter (ECAL) and a hadronic calorimeter (HCAL), that provides identification of electrons, photons and hadrons with measurements of position and energy;
- the Muon detection System, made of five stations labelled M1 to M5, used to identify muons that have passed through the calorimeters.

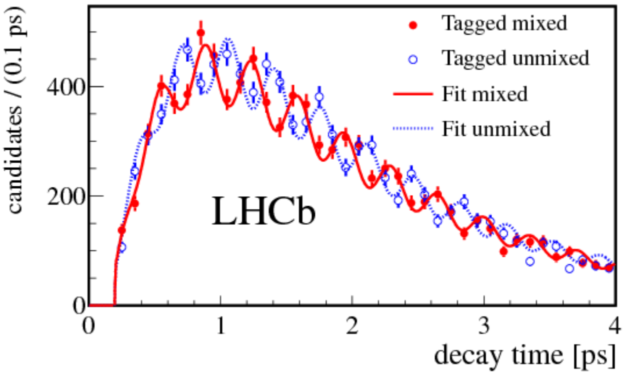

Figure 3.15: Decay time distribution for $B_s^0 \to D_s^- \pi^+$ candidates tagged as mixed (different flavour at decay and production; red, continous line) or unmixed (same flavour at decay and production; blue, dotted line), used in the LHCb measurement of Δm_s.

3.3.2.1 RICH detectors

LHCb has two RICH detectors, covering different momentum ranges. RICH1, located upstream of the dipole magnet, is optimised for low momentum particles, from 1 to 60 GeV/c, and uses aerogel and C_4F_{10} as radiators. RICH2, placed downstream of the tracking stations, covers larger momenta, from 15 up to and beyond 100 GeV/c, using a CF_4 radiator. RICH1 covers the full LHCb acceptance from ±25 mrad to ±300 mrad (horizontal) and ±250 mrad (vertical). RICH2 has a limited angular acceptance from ∼ ±15 mrad to ±120 mrad (horizontal) and ±100 mrad (vertical), where high momentum particles are abundant.

The Cherenkov light produced by particles traversing the radiators is reflected out of the spectrometer acceptance by a combination of spherical and flat mirrors. Hybrid Photon Detectors (HPDs) are used to detect Cherenkov photons in the wavelength range 200–600 nm. Fig. 3.16 shows the layout of both RICH detectors.

3.3.2.2 Calorimeter system

The calorimeter system is used to select transverse energy (E_T) hadron, electron and photon candidates for the first level of the trigger (L0) and to provide the identification of electrons, photons and hadrons as well as the measurement of their energies and positions.

LHCb uses an electromagnetic calorimeter (ECAL) followed by a hadron calorimeter (HCAL) to identify electromagnetic and hadronic showers, respectively. They are both sampling devices composed of alternating layers of scintillator and absorber, lead in the case of the ECAL and iron in the HCAL. Fig. 3.17 (right) shows, as an example, the internal structure of one HCAL cell. Longitudinal segmentation in the electromagnetic shower, needed to distinguish $e^{\pm}$ from the overwhelming background of neutral and charged pions, is achieved with the installation of a Scintillator Pad Detector (SPD) and a Preshower (PS) detector before the ECAL. A thin lead converter is installed between the PS and SPD. In all calorimeters scintillation light is transmitted to the Photo–Multipliers (PMTs) by wavelength–shifting (WLS) fibres.

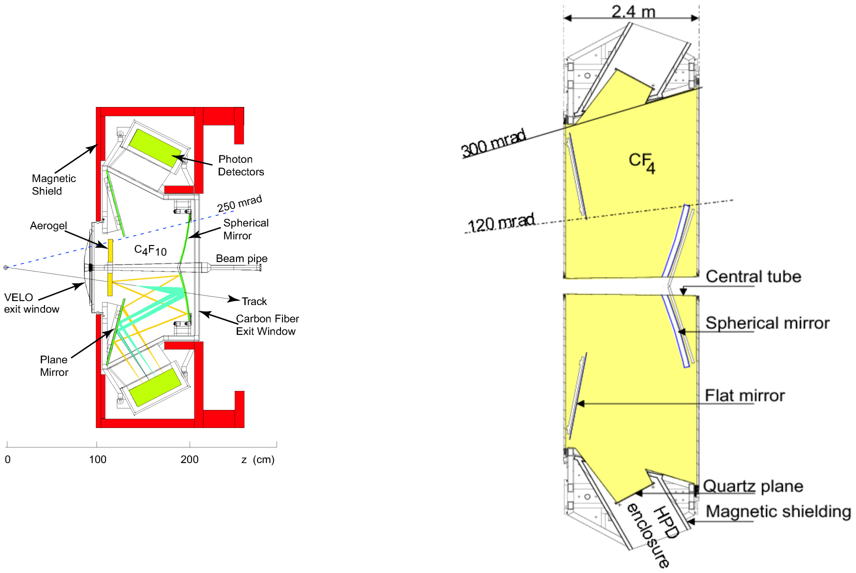

Figure 3.16: Left, RICH1 layout. Right, RICH2 layout.

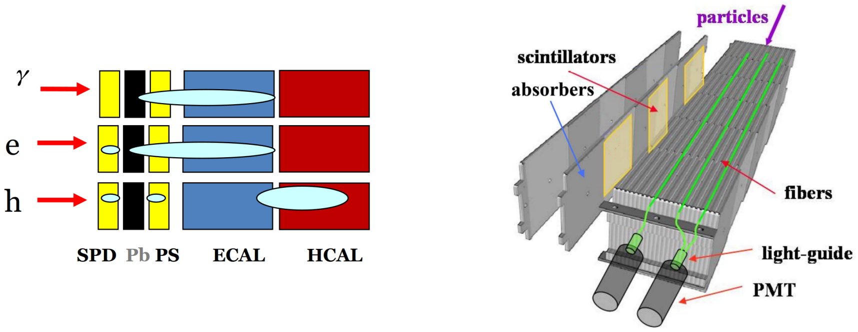

Figure 3.17: Left, Energy deposition pattern in the different subdetectors of the calorimeter system for photons, electrons/positrons and hadrons. Right, a schematic of the internal cell structure of a HCAL module.

The energy resolution of the ECAL is parameterised as

$$\frac{\sigma_E}{E} = \frac{a}{\sqrt{E}} \oplus b \oplus \frac{c}{E} \tag{3.1}$$

where a, b and c stand for the stochastic, constant and noise terms respectively. The stochastic and constant terms have been measured to be $8.5\% < a < 9.5\%$ and $b \sim 0.8\%$, in good agreement with the design resolution. For the HCAL the energy resolution has been determined to be $\sigma_E/E = (69 \pm 5)\%/\sqrt{(E)} \oplus (9 \pm 2)\%$ (E in GeV).

The Calorimeter PID makes use of the energy deposition along these detectors to identify the particles. Fig. 3.17 (left) shows a sketch of the energy loss in the SPD, PS, ECAL and HCAL for different particles.

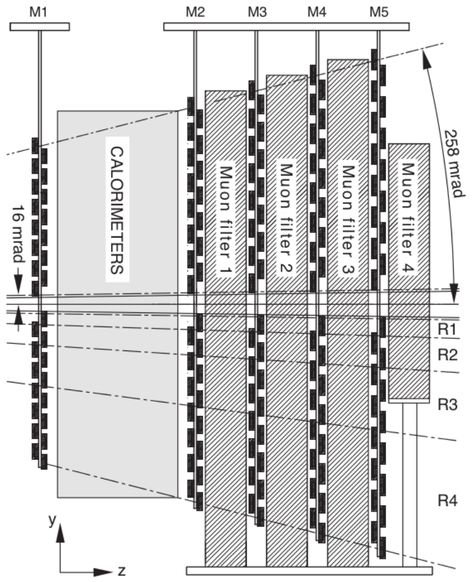

Figure 3.18: Side schematic of the muon system.

3.3.2.3 Muon system

The Muon System provides fast information for the high–p_{T} muon trigger at L0 and muon identification for the High Level Trigger (HLT) and offline analysis. It is composed of five stations labelled M1 to M5. M1 is placed in front of the calorimeter preshower, while M2 to M5 are located downstream of the HCAL, interleaved with three iron absorbers, see Fig. 3.18.

Multi–wire proportinal chambers (MWPC) are used in the five stations, with the exception of the inner region of station M1, where the high particle rate requires the use of triple gas electron multiplier (GEM) detector. M1-M3 have good resolution in the x coordinate (bending plane) in order to provide track direction and p_{T} measurement with $\sim 20\%$ precision. M4 and M5 are mainly designed to identify the most penetrating particles.

3.3.2.4 Particle Identification

Charged particles are identified using combined information from RICH detectors and calorimeters, while, neutrals (photons and neutral pions) are identified by just using energy deposits in the calorimeters.

RICH PID The main role of the RICH system is the identification of charged hadrons (π, K, p), although it also helps in the identification of e and μ. Cherenkov rings are predicted for each track under different particle hypotheses, and compared with the distribution of photons found on the photodetectors. Fig. 3.19 shows the display of a typical LHCb event in RICH1 and the reconstructed Cherenkov angle as a function of the particle momentum for isolated tracks selected in data.

An overall likelihood is computed for all the tracks in the event and minimised by changing the particle hypothesis for each track [68]. The final results of the particle

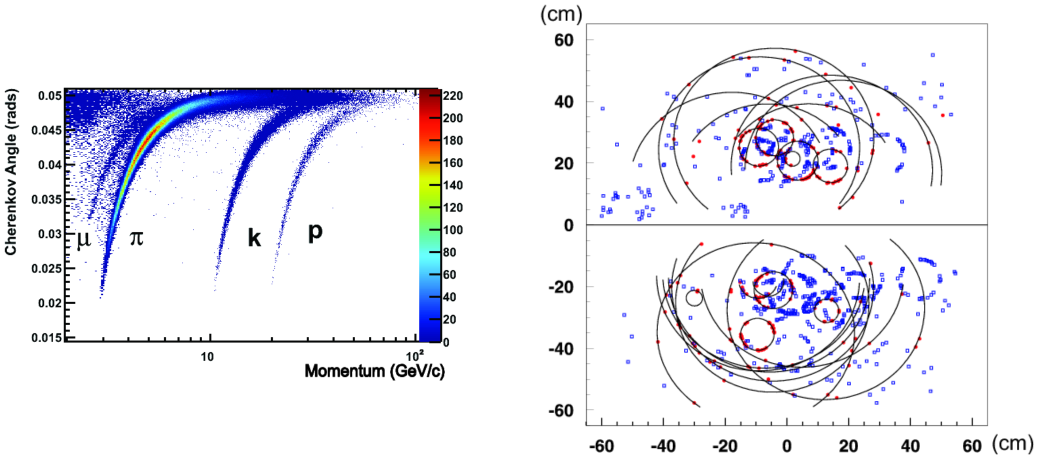

Figure 3.19: Reconstructed Cherenkov angle as a function of a track momentum in the C_4F_{10} radiator (left). Display of a simulated LHCb event in RICH1 (right).

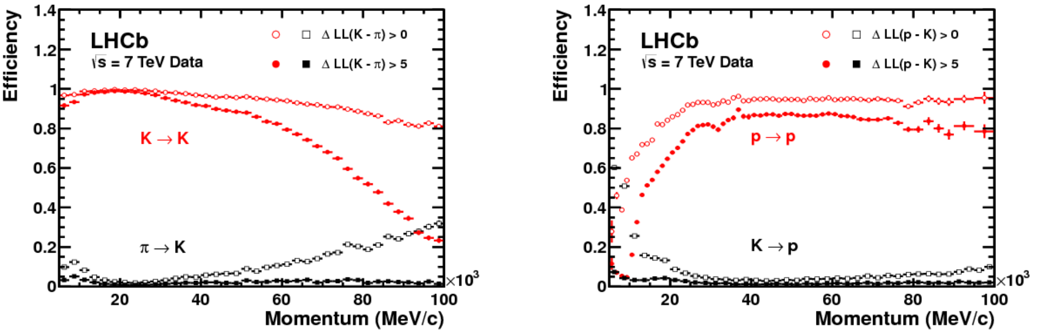

Figure 3.20: Left, kaon identification efficiency and pion misidentification rate measured on data as a function of track momentum, with two different cuts in $\Delta\log\mathcal{L}_{K/\pi}$. Right, proton efficiency and kaon misidentification fraction as a function of momentum with two different cuts in $\Delta\log\mathcal{L}_{p/K}$.

identification are differences in the log–likelihood values $\Delta\log\mathcal{L}$, which give for each track the change in the overall event log–likelihood when that track is changed from the pion hypothesis to each of the electron, muon, kaon and proton hypothesis. Fig. 3.20 left demonstrates the kaon efficiency (kaons identified as kaons) and pion misidentification (pions misidentified as kaons) as a function of particle momentum, obtained for different requirements in $\Delta\log\mathcal{L}_{K/\pi}$. The analogous plot for proton efficiency and kaon misidentification is shown in Fig. 3.20 right.

CALO PID As in the case of the RICH detectors, the discrimination of different species of particles (mainly photons, electrons and hadrons) in the CALO PID is achieved by means of a log–likelihood computed with the information of the energy deposits in the different regions of the calorimeters.

A description of the algorithms used in the calorimeter particle identification can be found in [69,70]. The electron ID performance was evaluated using $B^{\pm} \to J/\psi(e^+e^-)K^{\pm}$ candidates selected in 2011 data [71]. Fig. 3.21 shows the CALO electron ID efficiency and misidentification rate as a function of the momentum, for different cuts in

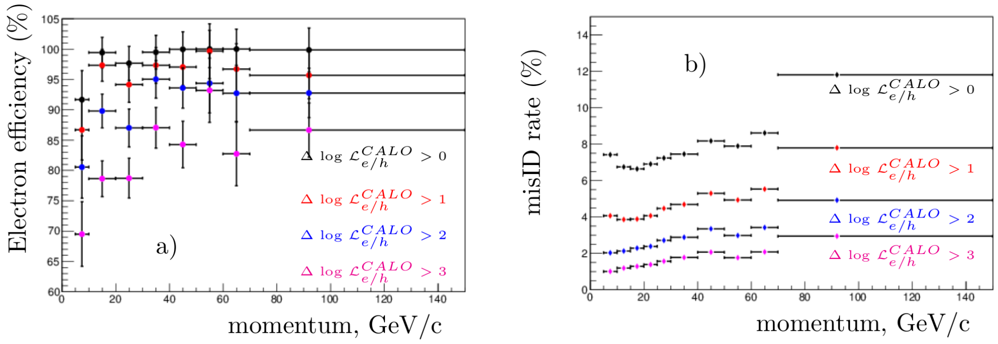

Figure 3.21: Performance of the Electron PID as a function of the momentum for several $\Delta\log\mathcal{L}_{e/h}$ cuts. Left, efficiency. Right, misidentification rate.

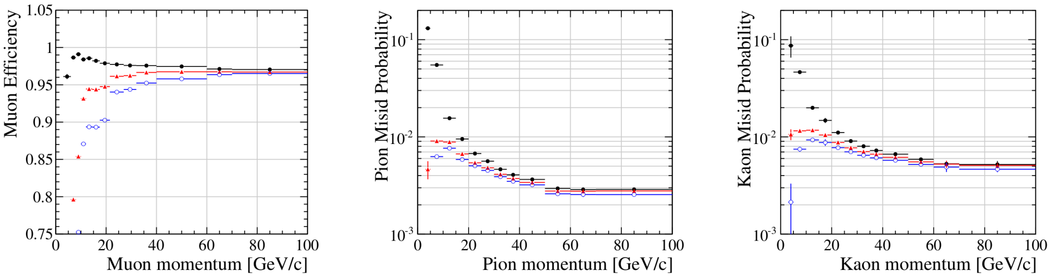

Figure 3.22: Muon ID performance for different cuts in the muon likelihood. Left, muon identification efficiency vs. momentum. Middle, pion misidentification rate vs pion momentum. Right, kaon misidentification rate vs. kaon momentum.

$\Delta\log\mathcal{L}_{e/h}$. The efficiency of reconstructing and selecting photons was also studied with 2011 data [72], comparing the yields of $B^+ \to J/\psi K^{*+}(K^+\pi^0)$ and $B^+ \to J/\psi K^+$ decays ($\pi^0 \to \gamma\gamma$).

Muon ID Muon ID is based in the fact that almost all particles able to go through the calorimeters and hit the muon stations are indeed muons. Trajectories reconstructed in the tracking system are extrapolated to the muon stations and hits are searched for in a certain field of interest around the extrapolation. A muon likelihood is then built with the identity and position of those hits and used to identify the muon candidates [73].

The Muon ID performance was studied with 2011 data [74]. Fig. 3.22 shows the muon identification efficiency and the pion and kaon misidentification rate as a function of the track momentum, for different requirements on the muon likelihood.

Combined PID Finally, for charged particles (e, μ, π, K, p), the information from the two RICH detectors, the calorimeters and the muon chambers is combined into a global log–likelihood difference between a given PID hypothesis, a, and the pion hypothesis,

$$\Delta\log\mathcal{L}_{a/\pi} = \log(\mathcal{L}_a) - \log(\mathcal{L}_\pi) = \log\left[\frac{\mathcal{L}_a}{\mathcal{L}_\pi}\right]. \tag{3.2}$$

Therefore, the log–likelihood difference between two particle hypothesis a and b is simply

$$\Delta\log\mathcal{L}_{a/b} = \Delta\log\mathcal{L}_{a/\pi} - \Delta\log\mathcal{L}_{b/\pi} = \log\left[\frac{\mathcal{L}_a}{\mathcal{L}_b}\right]. \tag{3.3}$$

Table 3.1: TCKs used during the 2011 data taking period and their the corresponding integrated luminosity.

TCK	Integrated Luminosity
0x5a0032	68 pb^{-1}
0x6d0032	100 pb^{-1}
0x730035	196 pb^{-1}
0x740036	5.2 pb^{-1}
0x760037	298.7 pb^{-1}
0x790037	39.3 pb^{-1}
0x790038	363.4 pb^{-1}

3.3.3 Trigger System

The amount of data generated by LHC collisions is too high to be directly stored. Therefore, a fast initial selection, or *trigger*, is needed to reduce it without discarding the events that are more interesting for the physics analyses. The LHCb trigger was designed to reduce the rate of visible interactions (those with at least two reconstructibe charged tracks) from the nominal $\sim$ 10 MHz, down to $\sim$ 3 kHz, the maximum allowed by the long term data storage resources [75]. Characteristic B or D mesons events contain tracks with non-zero impact parameter with respect to the PV and high transverse momenta (p_{T}) with respect to the beam axes. LHCb trigger exploits this signatures to enrich the proportion of interesting events in the recorded data.

The LHCb trigger is divided in two steps [76]: the Level-0 Trigger (L0) and the High Level Trigger (HLT). The L0 is a hardware trigger, implemented using custom made electronics, whereas the HLT is a software based trigger executed on a processor farm, called the Event Filter Farm (EFF), composed of several thousands CPUs. The 3 kHz HLT output rate is saved for permanent storage and offline analysis.

The combination of all the selections implemented in HLT, together with the L0 configuration, form a unique trigger with its associated Trigger Configuration Key (TCK), an hexadecimal label used to identify the trigger configuration used in a specific run. This label is stored for each event together with the information about the trigger lines that selected it. Table 3.1 shows the different TCKs used during 2011 data taking period.

3.3.3.1 Level-0 Trigger

The function of L0 is to reduce the input data rate to 1 MHz, at which value the entire detector can be read out. The L0 decision is taken by the Decision Unit (DU), based on the information collected, syncronously with the 40 MHz clock, from selected subdetectors:

- transverse energy (E_{T}) of calorimeter clusters produced by electrons, photons, neutral pions or charged hadrons (L0Calo).
- p_{T} of the muon or dimuon candidates in the muon system (L0Muon).
- Multiplicities in the SPD.

The L0Calo [77] computes the transverse energy deposited in clusters of 2 × 2 cells. The transverse energy of a cluster is defined as

$$E_T = \sum_{1=1}^{4} E_i \sin\theta_i \tag{3.4}$$

where E_i is the energy deposited in cell i and θ_i is the polar angle, relative to the z-axis, of the position of the centre of cell i. The identification of the particles producing the clusters relies on the energy deposits across the calorimeter (see Fig. 3.17 left). Additionally, the total E_T is also computed to reject crossings without visible interactions and to veto triggers from muons of the beam halo.

The L0 muon trigger [78] makes use of a fast stand–alone muon reconstruction. The muon candidates are built searching for hits on a straight line in the five muon stations pointing towards the interaction point. The p_T of the track can be also measured with a resolution of 20%. The two largest p_T muon candidates are selected for the decision.

The total number of cells of the SPD which have a hit is used to evaluate the charged track multiplicity and to reject high occupancy envents.

All this information is collected by the L0 DU and combined with calibration and random triggers into one decision per crossing, with a maximum latency of 4 μs. This decision is passed to the front-end electronics of all subdetectors, which pick-up the data from the relevant events from buffers and send them to the EFF.

3.3.3.2 High Level Trigger

The HLT is a C++ application which runs on every node of the EFF [56]. All calorimeter clusters and μ tracks selected by the L0 trigger are passed to the HLT as different kinds of L0 objects. The HLT is subdivided into two stages. The first stage (HLT1) uses a partial event reconstruction to reduce the 1 MHz L0 output rate to 43 KHz. This rate is sufficiently low to perform a complete event reconstruction in the second stage (HLT2).

The possible primary vertices are calculated from full 3D reconstructed VELO tracks. The offline pattern recognition in the tracking stations is then applied to those VELO tracks that have a larger probability to belong to a signal event, in different HLT1 *lines*. A fast muon identification is performed on the events triggered by muon candidates at L0. Requirements on the IP of the tracks with respect to any PV reduces the rate of the non–muonic trigger lines. Minimum momentum and transverse momentum requirements are then applied.

After the rate reduction achieved by the first stage of the HLT, a full reconstruction of the event is possible (see Sect. 3.3.1.4). In HLT2, the different tracks are combined to form composite particles ($J/\psi \to \mu^+\mu^-$, $K^{*0} \to K^+\pi^-$, ...) used as input to the different *inclusive* and *exclusive* selection. Inclusive selections, based on the topology of b–hadrons decays, form a large share of the HLT2 output rate of 3 KHz. These require at least two charged tracks in the final state and a displaced secondary vertex [79]. Exclusive selections require all the decay products in a specific decay chain to be reconstructed. After HLT2 50% of the rate consists of inclusive hadronic triggers, 25% are triggers on leptons and the remaining rate comes from exclusive triggers.

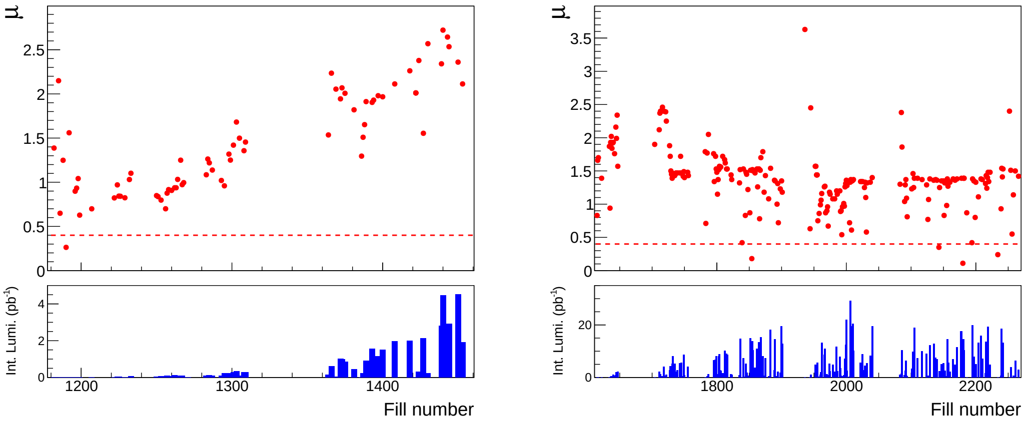

Figure 3.23: Average number of visible *pp* interaccions as a function of the fill number during 2010 (left) and 2011 (right), compared with the design value (red dashed line).

3.3.3.3 Trigger performance

The LHCb trigger was able to cope remarkably well with the non–standard conditions imposed by the LHC machine during 2010 and 2011, when the average number of visible *pp* interactions per bunch crossing was ~ 2.5 and ~ 1.5 respectively. The trigger efficiency for several representative physics channels was calculated using 2011 data [80].

LHCb is planning to upgrade the detector in 2018 [81, 82]. This upgraded detector will feature a fully software based trigger.

3.4 LHCb running conditions during 2010 and 2011

The study presented in this thesis is based on the data recorded by LHCb during 2010 and 2011 from the proton-proton collisions at a centre-of-mass energy of $\sqrt{s} = 7$ TeV provided by the LHC.

The first data taking period, during 2010, was devoted to comissioning and establishing confidence in the operation of the LHC, and so the running conditions changed continuously. A total integrated luminosity of 37 pb^{-1} was delivered during this period. Furthermore, although the LHC operated with only 10% of the nominal number of bunches per beam, $\sim 80\%$ of the design instantaneous luminosity was achieved at LHCb by changing the focussing of the beams at the interaction point. This led to an increase in the average number of visible interactions per bunch crossing, μ, with respect to the nominal number, see Fig. 3.23. A higher μ implies a rise of the readout rate per bunch crossing, the event size and the processing time. LHCb, and in particular its trigger system, showed great flexibility to cope with this continuously changing and non-standard running conditions.

In 2011, the LHC running conditions were more stable. During the early data taking period, the number of bunches colliding at LHCb steadily increased from 180 to 1296, which is about half of the final design number of bunches in the LHC machine. From then on, peak luminosities at LHCb were leveled in order not to exceed 3-3.5 $\times\, 10^{32}$ $\text{cm}^{-2}\text{s}^{-1}$, which corresponds to an average $\mu \sim 1.5$, almost a factor four higher than

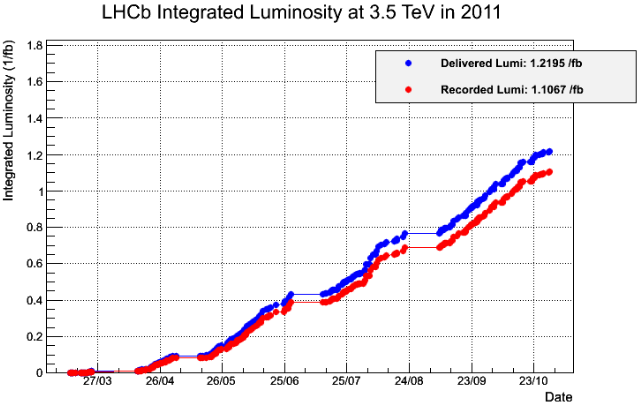

Figure 3.24: Integrated luminosity as a function of time during 2011.

design. Fig. 3.24 shows the integrated luminosity as a function of time for the 2011 data taking period, during which a total integrated luminosity of 1.0 fb^{-1} was collected by LHCb.

During both periods, luminosity leveling allowed LHCb to mantain constant the instantaneous luminosity during each fill, see Fig. 3.25. The orientation of the magnetic field was also frequently changed, in order to record approximately the same amount of data with positive ($B_y > 0$) and negative ($B_y < 0$) magnet polarity. This procedure minimises the impact of detection asymmetries of oppositely charged particles in the final measurements.

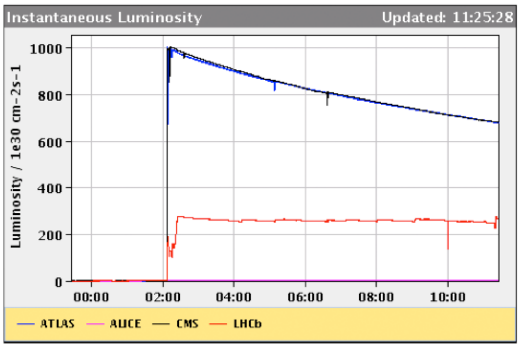

Figure 3.25: Instantaneous luminosity at ATLAS, CMS and LHCb vs. time during a typical LHC fill. The luminosity leveling yields a constant luminosity for LHCb.

4

Phenomenology of $B_s^0 \to K^{*0}(K^+\pi^-)K^{*0}(K^-\pi^+)$

Among the numerous two-body charmless decays of the B_s^0 mesons, the decay $B_s^0 \to K^{*0}\overline{K}^{*0}$ is of special interest. On one hand, the final state of this decay is a *CP*-eigenstate, which makes it particularly suitable for the study of *CP*-violation. On the other hand, the presence of two vector resonances in the final state means that this process in fact represents three different decays, one for each of the three possible helicities of the vector mesons. Therefore, a larger number of observables are available compared to the decays into PP or PV final states ($P \equiv$ pseudo-scalar, $V \equiv$ vector).

Moreover, when a neutral vector meson is detected via its decay $V \to PP'$, there is usually an indistinguishable contribution coming from the decay of a scalar resonace $S \to PP'$ or from scalar non-resonant PP' production [83,84]. It is necessary thus to take into account these additional contributions, which in the case of $B_s^0 \to K^{*0}\overline{K}^{*0}$ extend the total number of amplitudes to six [1]. These configurations, commonly referred to as "*S–wave* amplitudes", will be shown to be also linear combinations of *CP*-eigenstates, able to generate additional *CP*-violating quantities in the interference with the "*P–wave* amplitudes". This *CP*-violating observables can be measured without knowledge of the decay time or flavour (B_s^0 or $\overline{B}_s^0$) of the decaying B_s^0 meson, and can thus always be determined, even from samples with modest statistics.

4.1 The $B \to VV$ angular distribution

Consider the B meson decay into two neutral vector mesons, $B \to V_1V_2$, where V_1 and V_2 undergo two-body strong decays into pseudoscalar particles: $V_1 \to h_1H_1$ and $V_2 \to h_2H_2$. As already mentioned, this process is usually described by three helicity amplitudes according to the three possible helicity configuration of the vectors in the final state. Using the helicity formalism [85], the total amplitude can be written as

$$\mathcal{M}(B \to V_1V_2) \propto \sum_{\lambda=0,\pm1} A_\lambda(m_1, m_2)e^{i\lambda\phi}d^1_{\lambda,0}(\theta_1)d^1_{-\lambda,0}(\theta_2) \tag{4.1}$$

where λ is the helicity of V_1 and $A_\lambda(m_1, m_2)$ is a helicity amplitude depending on the mass of the two vectors: $m_1 \equiv M(h_1, H_1)$ and $m_2 \equiv M(h_2, H_2)$. The angles describing

---

[1] Other $B_s^0 \to$ VV decays might not need as many new amplitudes. For example, in $B^0 \to \phi\phi$ the most general description is achieved with only five amplitudes due to the presence of identical particles in the final state [8]

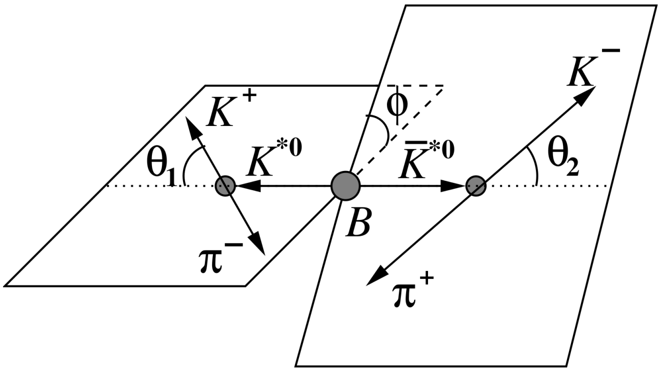

Figure 4.1: Definition of the angles involved in the analysis for the $B_s^0 \to K^{*0}\overline{K}^{*0}$.

the decay are shown in Fig. 4.1, $\theta_{1(2)}$ is the angle between the direction of $h_{1(2)}$ and the direction opposite to the B meson momentum in the rest frame of $V_{1(2)}$ and φ is the angle between the decay planes of the two vectors in the B rest frame. The *Wigner d-matrix* elements involved can be expressed as

$$d^l_{m,0}(\theta) = \sqrt{\frac{(l-m)!}{(l+m)!}} P^m_l(\cos\theta) \tag{4.2}$$

with $P^m_l(\cos\theta)$ representing the *Associated Legendre Polinomials*. It is useful to rewrite the total amplitude in terms of the transversity amplitudes,

$$A_0 = A_0, \qquad A_{\parallel} = \frac{1}{\sqrt{2}}(A_+ + A_-), \qquad A_{\perp} = \frac{1}{\sqrt{2}}(A_+ - A_-), \tag{4.3}$$

since they correspond to final states with definite CP-eigenvalue ($\eta_{\parallel} = \eta_0 = 1$ and $\eta_{\perp} = -1$).

In the particular case of $B_s^0 \to K^{*0}(892)\overline{K}^{*0}(892)$ ($V_1 \equiv K^{*0}$ and $V_2 \equiv \overline{K}^{*0}$), with $h_1 = K^+, H_1 = \pi^-, h_2 = K^-, H_2 = \pi^+$. However, the $K\pi$ mass spectrum does not correspond to only a $K^{*0}(892)$ meson. Instead, the spectrum is a mixture of resonances with different spin ($J = 0, 1, 2$), their interferences and nonresonant production. To take these contributions into account, additional amplitudes should be included in (4.1).

In the next section, the decay rate for $B_s^0 \to (K^+\pi^-)_{J_1}(K^-\pi^+)_{J_2}$ is calculated. Since the contribution from $J = 2$ resonances in the mass region of the $K^{*0}(892)$ is expected to be very small, only the contributions with $J_{1,2} = 0, 1$ will be considered.

4.2 The $B_s^0 \to (K^+\pi^-)(K^-\pi^+)$ model

The most general description of the decay $B_s \to (K^+\pi^-)_{J_1}(K^-\pi^+)_{J_2}$ when the $K\pi$ pairs are required to be in a narrow mass region around the $K^{*0}(892)$, i.e. only the *S–wave* ($J_i = 0$) and *P–wave* ($J_i = 1$) production of the $K\pi$ pairs are considered, is given by six decay amplitudes. In addition to the usual three amplitudes corresponding to the decay into two vectors – commonly called *P–wave* amplitudes –, the *S–wave* amplitudes:

$$\begin{aligned}
A_{VS} &: \ B \to \quad V_1 \quad (h_2H_2)_0 \\
A_{SV} &: \ B \to (h_1H_1)_0 \quad V_2 \\
A_{SS} &: \ B \to (h_1H_1)_0\,(h_2H_2)_0,
\end{aligned}$$

need to be taken into account [1]. Extending (4.1) to include these contributions and using the transversity amplitudes to describe the *P–wave* component, the differential decay rate can be expressed as

$$\begin{aligned}
\frac{\mathrm{d}^5\Gamma}{\mathrm{d}\Omega\mathrm{d}m_1\mathrm{d}m_2\mathrm{d}t} = N\Big| \; & \Big(A_0(t)\cos\theta_1\cos\theta_2 + \frac{A_\parallel(t)}{\sqrt{2}}\sin\theta_1\sin\theta_2\cos\varphi \\
& \quad + i\,\frac{A_\perp(t)}{\sqrt{2}}\sin\theta_1\sin\theta_2\sin\varphi \Big)\mathcal{M}_1(m_1)\mathcal{M}_1(m_2) \\
& - \frac{A_{VS}(t)}{\sqrt{3}}\cos\theta_1\mathcal{M}_1(m_1)\mathcal{M}_0(m_2) \\
& + \frac{A_{SV}(t)}{\sqrt{3}}\cos\theta_2\mathcal{M}_0(m_1)\mathcal{M}_1(m_2) \\
& - \frac{A_{SS}(t)}{3}\mathcal{M}_0(m_1)\mathcal{M}_0(m_2) \Big|^2
\end{aligned} \tag{4.4}$$

where the dependence of each amplitude with the two body effective masses $m_i \equiv M(h_iH_i)$ has been made explicit in terms of the *P–wave* and *S–wave* mass propagators, $\mathcal{M}_{1,0}(m)$. These propagators will be described in more detail in Sect. 4.3.1.1. The time evolution induced by B_s^0-$\overline{B}_s^0$ mixing is encoded in the time-dependence of the amplitudes $A_k(t)$.

Note that, unlike the $K^{*0}\overline{K}^{*0}$ final state, the S-wave configurations SV and VS defined in (4.4) do not build *CP*-eigenstates. Nevertheless, one may consider the following quantum final states:

$$\begin{aligned}
|s^+\rangle &= \frac{1}{\sqrt{2}}\left(|K^{*0}(K^-\pi^+)_0\rangle + |(K^+\pi^-)_0\overline{K}^{*0}\rangle\right) \\
|s^-\rangle &= \frac{1}{\sqrt{2}}\left(|K^{*0}(K^-\pi^+)_0\rangle - |(K^+\pi^-)_0\overline{K}^{*0}\rangle\right)
\end{aligned} \tag{4.5}$$

which are indeed *CP*-eigenstates with opposite *CP*-parities ($\eta_+ = -1$ and $\eta_- = +1$). Therefore, by introducing

$$A_s^+ = \frac{1}{\sqrt{2}}\left(A_{VS} + A_{SV}\right), \quad A_s^- = \frac{1}{\sqrt{2}}\left(A_{VS} - A_{SV}\right), \tag{4.6}$$

the decay rate (4.4) can be reformulated in terms of *CP*-odd and *CP*-even amplitudes

---

[1] The subscript $(\ )_J$ denotes the relative orbital angular momentum, J, of the pair.

(the SS final configuration is a CP-eigenstate with $\eta_{SS} = 1$) as follows,

$$\begin{aligned}
\frac{\mathrm{d}^5\Gamma}{\Gamma \mathrm{d}\Omega \mathrm{d}m_1 \mathrm{d}m_2 \mathrm{d}t} &= N \Bigg| \Big(A_0(t)\cos\theta_1\cos\theta_2 + \frac{A_\parallel(t)}{\sqrt{2}}\sin\theta_1\sin\theta_2\cos\varphi \\
&\qquad + i\,\frac{A_\perp(t)}{\sqrt{2}}\sin\theta_1\sin\theta_2\sin\varphi\Big)\mathcal{M}_1(m_1)\mathcal{M}_1(m_2) \\
&\qquad - \frac{A_s^+(t)}{\sqrt{6}}(\cos\theta_1\mathcal{M}_1(m_1)\mathcal{M}_0(m_2) - \cos\theta_2\mathcal{M}_0(m_1)\mathcal{M}_1(m_2)) \\
&\qquad - \frac{A_s^-(t)}{\sqrt{6}}(\cos\theta_1\mathcal{M}_1(m_1)\mathcal{M}_0(m_2) + \cos\theta_2\mathcal{M}_0(m_1)\mathcal{M}_1(m_2)) \\
&\qquad - \frac{A_{ss}}{3}\mathcal{M}_0(m_1)\mathcal{M}_0(m_2) \;\Bigg|^2 \\
&= N\sum_{n=1}^{21} K_n(t, m_1, m_2)F_n(\Omega). \qquad (4.7)
\end{aligned}$$

In the last equality, a more compact formulation of this decay rate has been introduced. The functions K_n contain the dependence with the different amplitudes entering the decay and F_n give the angular distribution associated with each amplitude combination. These functions are shown in Tables 4.1 and 4.2.

In order to write down the rate corresponding to the CP-conjugated decay, $\overline{B}_s^0 \to (K^-\pi^+)_{J_1}(K^+\pi^-)_{J_2}$, the amplitudes A_k need to be substituted by the corresponding $\bar{A}_k$ in (4.7). Also, the decay angles for the conjugated process $\bar{\Omega} : \{\bar{\theta}_1, \bar{\theta}_2, \bar{\varphi}\}$ can be related to $\Omega : \{\theta_1, \theta_2, \varphi\}$ by

$$\begin{aligned}
\bar{\theta}_1 &= \theta_2 \\
\bar{\theta}_2 &= \theta_1 \\
\bar{\varphi} &= -\varphi, \qquad (4.8)
\end{aligned}$$

and the two body invariant mass $\bar{m}_{1(2)}$ must satisfy

$$\bar{m}_{1(2)} = m_{2(1)}. \qquad (4.9)$$

This is easily understood by considering $B_s^0 \to K^{*0}\overline{K}^{*0}$. As noted in the previous section, in the decay $B \to V_1V_2$, the helicity angles are defined with respect to the momenta of V_1 and V_2. In $B_s^0 \to K^{*0}\overline{K}^{*0}$, $V_1 = K^{*0}$ and $V_2 = \overline{K}^{*0}$. On the other hand, in the CP-conjugated decay $\overline{B}_s^0 \to \overline{K}^{*0}K^{*0}$, $V_1 = \overline{K}^{*0}$ and $V_2 = K^{*0}$. That is, the indices 1 and 2 have been exchanged and the decay variables become those in (4.8) and (4.9). Note that this transformation is equivalent to the exchange $A_K(t) \to \eta_k\bar{A}_K(t)$, where η_k is the CP-eigenvalue associated to the amplitude A_k, and so the decay rate for $\overline{B}_s^0$ decays can be written as

$$\frac{\mathrm{d}^5\bar{\Gamma}}{\mathrm{d}\Omega \mathrm{d}m_1 \mathrm{d}m_2} = N\sum_{n=1}^{21} \bar{K}_n(t, m_1, m_2)F_n(\Omega) \qquad (4.10)$$

where $F_n(\Omega)$ are the same functions as in (4.7).

Table 4.1: Values of the K_n and F_n functions listed in (4.7). The time dependence is encoded in the amplitudes, i.e. $A_k = A_k(t)$.

n	$K_n(t, m_1, m_2)$	$F_n(\Omega)$
1	$\lvert A_0\rvert^2 \lvert\mathcal{M}_1(m_1)\rvert^2 \lvert\mathcal{M}_1(m_2)\rvert^2$	$\cos^2\theta_1 \cos^2\theta_2$
2	$\lvert A_\parallel\rvert^2 \lvert\mathcal{M}_1(m_1)\rvert^2 \lvert\mathcal{M}_1(m_2)\rvert^2$	$\frac{1}{2}\sin^2\theta_1 \sin^2\theta_2 \cos^2\varphi$
3	$\lvert A_\perp\rvert^2 \lvert\mathcal{M}_1(m_1)\rvert^2 \lvert\mathcal{M}_1(m_2)\rvert^2$	$\frac{1}{2}\sin^2\theta_1 \sin^2\theta_2 \sin^2\varphi$
4	$\Re(A_\parallel A_0^*) \lvert\mathcal{M}_1(m_1)\rvert^2 \lvert\mathcal{M}_1(m_2)\rvert^2$	$\frac{1}{2\sqrt{2}}\sin 2\theta_1 \sin 2\theta_2 \cos\varphi$
5	$\Im(A_\perp A_0^*) \lvert\mathcal{M}_1(m_1)\rvert^2 \lvert\mathcal{M}_1(m_2)\rvert^2$	$-\frac{1}{2\sqrt{2}}\sin 2\theta_1 \sin 2\theta_2 \sin\varphi$
6	$\Im(A_\perp A_\parallel^*) \lvert\mathcal{M}_1(m_1)\rvert^2 \lvert\mathcal{M}_1(m_2)\rvert^2$	$-\frac{1}{2}\sin^2\theta_1 \sin^2\theta_2 \sin 2\varphi$
7	$\frac{1}{2}\lvert A_s^+ + A_s^-\rvert^2 \lvert\mathcal{M}_1(m_1)\rvert^2 \lvert\mathcal{M}_0(m_2)\rvert^2$	$\frac{1}{3}\cos^2\theta_1$
8	$\frac{1}{\sqrt{2}}\Re\Big(A_s^+ A_0^* \mathcal{M}_1^*(m_2)\mathcal{M}_0(m_2) + A_s^- A_0^* \mathcal{M}_1^*(m_2)\mathcal{M}_0(m_2)\Big) \lvert\mathcal{M}_1(m_1)\rvert^2$	$-\frac{2}{\sqrt{3}}\cos^2\theta_1 \cos\theta_2$
9	$\frac{1}{\sqrt{2}}\Re\Big(A_s^+ A_\parallel^* \mathcal{M}_1^*(m_2)\mathcal{M}_0(m_2) + A_s^- A_\parallel^* \mathcal{M}_1^*(m_2)\mathcal{M}_0(m_2)\Big) \lvert\mathcal{M}_1(m_1)\rvert^2$	$-\frac{1}{\sqrt{6}}\sin 2\theta_1 \sin\theta_2 \cos\varphi$
10	$\frac{1}{\sqrt{2}}\Im\Big((A_s^+)^* A_\perp \mathcal{M}_0^*(m_2)\mathcal{M}_0(m_2) + (A_s^-)^* A_\perp \mathcal{M}_0^*(m_2)\mathcal{M}_0(m_2)\Big) \lvert\mathcal{M}_1(m_1)\rvert^2$	$\frac{1}{\sqrt{6}}\sin 2\theta_1 \sin\theta_2 \sin\varphi$
11	$\frac{1}{\sqrt{2}}\Re\Big(A_s^+ A_{SS}^* \mathcal{M}_0^*(m_1)\mathcal{M}_1(m_1) + A_s^- A_{SS}^* \mathcal{M}_0^*(m_1)\mathcal{M}_1(m_1)\Big) \lvert\mathcal{M}_0(m_2)\rvert^2$	$\frac{2}{3\sqrt{3}}\cos\theta_1$

Table 4.2: Values of the K_n and F_n functions listed in (4.7), (cont).The time dependence is encoded in the amplitudes, i.e. $A_k = A_k(t)$. The mass function in K_{17} is defined as $\zeta(m_1, m_2) \equiv \mathcal{M}_1^*(m_1)\mathcal{M}_0^*(m_2)\mathcal{M}_0(m_1)\mathcal{M}_1(m_2)$.

n	$K_n(t, m_1, m_2)$	$F_n(\Omega)$
12	$\frac{1}{2}\lvert A_s^+ - \lvert A_s^-\rvert^2 \lvert\mathcal{M}_0(m_1)\rvert^2 \lvert\mathcal{M}_1(m_2)\rvert^2$	$\frac{1}{3}\cos^2\theta_2$
13	$\frac{1}{\sqrt{2}}\Re\Big(A_s^+ A_0^* \mathcal{M}_1^*(m_2)\mathcal{M}_0(m_2)$ $-A_s^- A_0^* \mathcal{M}_1^*(m_2)\mathcal{M}_0(m_2)\Big)\lvert\mathcal{M}_1(m_2)\rvert^2$	$\frac{2}{\sqrt{3}}\cos\theta_1\cos^2\theta_2$
14	$\frac{1}{\sqrt{2}}\Re\Big(A_s^+ A_\parallel^* \mathcal{M}_1^*(m_2)\mathcal{M}_0(m_2)$ $-A_s^- A_\parallel^* \mathcal{M}_1^*(m_2)\mathcal{M}_0(m_2)\Big)\lvert\mathcal{M}_1(m_2)\rvert^2$	$\frac{1}{\sqrt{6}}\sin\theta_1\sin 2\theta_2\cos\varphi$
15	$\frac{1}{\sqrt{2}}\Im\Big(-(A_s^+)^* A_\perp \mathcal{M}_0^*(m_2)\mathcal{M}_0(m_2)$ $-(A_s^-)^* A_\perp \mathcal{M}_0^*(m_2)\mathcal{M}_0(m_2)\Big)\lvert\mathcal{M}_1(m_2)\rvert^2$	$-\frac{1}{\sqrt{6}}\sin\theta_1\sin 2\theta_2\sin\varphi$
16	$\frac{1}{\sqrt{2}}\Re\Big(A_s^+ A_{SS}^* \mathcal{M}_0^*(m_1)\mathcal{M}_1(m_1)$ $-A_s^- A_{SS}^* \mathcal{M}_0^*(m_1)\mathcal{M}_1(m_1)\Big)\lvert\mathcal{M}_0(m_1)\rvert^2$	$-\frac{2}{3\sqrt{3}}\cos\theta_2$
17	$\left(\lvert A_s^+\rvert^2 - \lvert A_s^-\rvert^2\right)\Re\Big(\zeta(m_1, m_2)\Big)$ $+2\Im\left((A_s^+)^* A_s^-\right)\Im\Big(\zeta(m_1, m_2)\Big)$	$-\frac{1}{3}\cos\theta_1\cos\theta_2$
18	$\lvert A_{ss}\rvert^2 \lvert\mathcal{M}_0(m_1)\rvert^2 \lvert\mathcal{M}_0(m_2)\rvert^2$	$\frac{1}{9}$
19	$\Re\Big(A_{ss}A_0^* \mathcal{M}_1^*(m_1)\mathcal{M}_1^*(m_2)\mathcal{M}_0(m_1)\mathcal{M}_0(m_2)\Big)$	$-\frac{2}{3}\cos\theta_1\cos\theta_2$
20	$\Re\Big(A_{ss}A_\parallel^* \mathcal{M}_1^*(m_1)\mathcal{M}_1^*(m_2)\mathcal{M}_0(m_1)\mathcal{M}_0(m_2)\Big)$	$-\frac{\sqrt{2}}{3}\sin\theta_1\sin\theta_2\cos\varphi$
21	$\Im\Big(A_{ss}A_\perp^* \mathcal{M}_1^*(m_1)\mathcal{M}_1^*(m_2)\mathcal{M}_0(m_1)\mathcal{M}_0(m_2))$	$\frac{\sqrt{2}}{3}\sin\theta_1\sin\theta_2\sin\varphi$

4.2.1 Time evolution

The time evolution of the states $|B_s^0(t)\rangle$ and $|\overline{B}_s^0(t)\rangle$ induced by B_s^0-$\overline{B}_s^0$ mixing was described in section Sect. 2.2.1.2. As a consequence of the oscillation, the helicity amplitudes in the angular distribution are also time-dependent and follow

$$\begin{aligned} A_k(t) &= \langle k|H_W|B_s^0(t)\rangle = \left[g_+(t)A_k + \eta_k \frac{q}{p} g_-(t)\bar{A}_k\right] \\ \bar{A}_k(t) &= \langle k|H_W|\overline{B}_s^0(t)\rangle = \left[\frac{p}{q} g_-(t)A_k + \eta_k g_+(t)\bar{A}_k\right] \end{aligned} \tag{4.11}$$

where $A_k \equiv \langle k|H_W|B_s^0\rangle$ and $\bar{A}_k \equiv \langle k|H_W|\overline{B}_s^0\rangle$ are the amplitudes at $t = 0$. As noted above, all the final states considered are CP-eigenstates, i.e. $|\bar{k}\rangle = CP|k\rangle = \eta_f|k\rangle$, with CP-eigenvalue $\eta_k = 1$ for $k = 0, \|, S^-, SS$ and $\eta_k = -1$ for $k = \perp, S^+$ [1]

If the time dependence of the different amplitudes is made explicit, every function $K_n(t, m_1, m_2)$ can be written as

$$K_n(t, m_1, m_2) = \frac{1}{2} e^{\Gamma_s t} \left[a_n(m_1, m_2) \cosh\left(\frac{\Delta\Gamma t}{2}\right) + b_n(m_1, m_2) \sinh\left(\frac{\Delta\Gamma t}{2}\right) \right. \\ \left. + c_n(m_1, m_2) \cos(\Delta m_s t) + d_n(m_1, m_2) \sin(\Delta m_s t) \right] \tag{4.12}$$

where the coefficients a_n, b_n, c_n and d_n contain combinations between the amplitudes at $t = 0$ and the mass-dependent propagators. The values of these coefficients are given in Tables A.3 to A.6 in Appendix A.

It is easy to identify CP-violating quantities when taking a closer look at the coefficients a_n, b_n, c_n and d_n. There are four kinds of such observables:

- direct CP asymmetries: $\Re[A_k A_{k'}^* - \bar{A}_k \bar{A}_{k'}^*]$ (for $k = k'$, they become the familiar $|A_k|^2 - |\bar{A}_k|^2$), present in the coefficients a_n ($n = 8-11$) and c_n ($n = 1-4, 7, 13-16, 18, 20, 21$);
- indirect or mixing-induced CP asymmetries: $\Im[(A_k^* \bar{A}_{k'} + \bar{A}_k A_{k'}{}^*) e^{-i\phi_M}]$, present in the coefficients b_n ($n = 8-11$) and d_n ($n = 1-4, 7, 13-16, 18, 20, 21$);
- triple product asymmetries: $\Im[A_\perp A_k^* - \bar{A}_\perp \bar{A}_k]$, present in a_n ($n = 5, 6, 17, 19$) and c_{12};
- mixing-induced triple product asymmetries: $\Im[(\bar{A}_\perp A_k^* + A_{perp}{}^* \bar{A}_k) e^{-i\phi_M}]$, present in b_n ($n = 5, 6, 17, 19$) and d_{12}.

An equivalent expression to (4.12) can be found for the $\bar{K}_n$ functions,

$$\bar{K}_n(t, m_1, m_2) = \frac{1}{2} e^{\Gamma_s t} \left[\bar{a}_n(m_1, m_2) \cosh\left(\frac{\Delta\Gamma t}{2}\right) + \bar{b}_n(m_1, m_2) \sinh\left(\frac{\Delta\Gamma t}{2}\right) \right. \\ \left. + \bar{c}_n(m_1, m_2) \cos(\Delta m_s t) + \bar{d}_n(m_1, m_2) \sin(\Delta m_s t) \right] \tag{4.13}$$

---

[1] The CP-eigenvalues can be understood in terms of the total angular momentum of the final state. States with $L = 0$, (SS, S^- and a comnination of 0 and $\|$) or $L = 2$ (a different combination of 0 and $\|$) are CP-even, while those with $L = 1$ ($\perp, S^+$) are CP-odd.

where the time-independent coefficients $\bar{a}_n$, $\bar{b}_n$, $\bar{c}_n$ and $\bar{d}_n$ can be obtained from a_n, b_n, c_n and d_n by exchaging $A_k \leftrightarrow \eta_k \bar{A}_k$ and inverting the sign of the mixing phase $\phi_M = \arg(p/q)$. At this point, it is straight forward to show that

$$\bar{a}_n = a_n\ , \quad \bar{b}_n = b_n\ , \quad \bar{c}_n = -c_n\ , \quad \bar{d}_n = -d_n. \tag{4.14}$$

This means that, in order to measure all the *CP*-violating observables listed above, it is necessary to distinguish between B_s^0 and $\bar{B}_s^0$ decays.

4.3 Untagged analysis

The term *flavour tagging* (*B-tagging*, or just *tagging*) usually refers to the different techniques used to determine the flavour of the B meson at production time. The efficiency of this tagging process is generally low, of the order of a few per cent [86], since it relies on the identification of a flavour specific decay of the accompaning $\bar{B}$ meson to infer the flavour of the signal B, and viceversa, (different algorithms use the decays of the mesons produced in the hadronisation of the b quark). Based on the limited statistics expected for the $B_s^0 \to K^{*0}\bar{K}^{*0}$ decay[1], only the untagged analysis has been attempted.

The coefficients c_n and d_n, and so most of the direct and undirect *CP* asymmetries, can not be measured if separation between B and $\bar{B}$ is not available, since they vanish in the untagged decay rate,

$$\begin{aligned}\left(\frac{\mathrm{d}^5\left(\Gamma+\bar{\Gamma}\right)}{\mathrm{d}\Omega \mathrm{d}m_1 \mathrm{d}m_2 \mathrm{d}t}\right) &= \frac{1}{2}\, N \sum_n \left(K_n(t,m_1,m_2)+\bar{K}_n(t,m_1,m_2)\right) F_n(\Omega) \\ &= N \sum_n \left(a_n \cosh\left(\frac{\Delta\Gamma t}{2}\right) + b_n \sinh\left(\frac{\Delta\Gamma t}{2}\right)\right) F_n(\Omega).\end{aligned} \tag{4.15}$$

Nevertheless, the *CP*-violating observables encoded in the coefficients a_n and b_n still survive. These quantities can be determined by performing asymmetric integrals over the three angular variables. This will be explained in more detail in Sect. 4.3.2.

Additionally, the *CP*-averaged branching fraction and polarisation fractions for $B_s^0 \to K^{*0}\bar{K}^{*0}$ can be determined with no information about the B meson flavour or decay time, and compared to their SM prediction given in Sect. 2.3.2. In the next section the time-integrated model in the context of the Standard Model is obtained.

---

[1] The analysis presented here is based on 1.0 fb^{-1} of pp collisions at $\sqrt{s} = 7\,\mathrm{TeV}$ collected by LHCb during 2011. At that energy, the $b\bar{b}$ production cross section in the forward direction ($2 < \eta < 6$) has been measured to be $\sigma_{b\bar{b}} = 75.3 \pm 14.0\ \mu\mathrm{b}$ [87]. Taking the B_s^0 hadronisation fraction, $f_s = 0.107 \pm 0.005$ from [31], the expected number of $B_s^0 \to K^{*0}\bar{K}^{*0}$ events can be calculated as

$$N = \mathcal{L}_{int} \times 2 \times \sigma_{b\bar{b}} \times f_{B_s^0} \times \mathcal{B}(B_s^0 \to K^{*0}\bar{K}^{*0}) \times \left(\frac{2}{3}\right)^2 \times \varepsilon \sim 700$$

A branching fraction of 10^{-5} has been assumed for the $B_s^0 \to K^{*0}\bar{K}^{*0}$ decay and the factor $\frac{2}{3}$ is the branching fraction for $K^{*0} \to K^+\pi^-$. The efficiency of triggering, reconstructing and selecting this particular channel at LHCb (ε) is of the order of 1% (see Sect. 6.6).

4.3.1 Time integration in the Standard Model

The porlarisation fractions of $B_s^0 \to K^{*0}\overline{K}^{*0}$ can be determined from a time-integrated analysis of the untagged sample. In the SM, every amplitude taking part in this process (and the corresponding decays into *S–wave* final states) can be approximated by the dominant penguin contribution. Therefore, they can be parameterised as

$$A_k = |A_k| e^{i\delta_k} e^{i\phi_D/2} \tag{4.16}$$

where δ_k is a strong phase and ϕ_D is the weak phase associated to that penguin contribution and is common to all the amplitudes. Under this approximation, no *CP* violation in the decay is possible and so $|A_k| = |\bar{A}_k| \; \forall k$. Also, the triple product asymmetries a_n ($n = 5, 6, 17, 19$) become zero[1]. Moreover, as discussed in Sect. 2.3.2.3, the global *CP*-violating weak phase, $\phi_s = \phi_D - \phi_M$, is zero for this decay, which implies that all the mixing-induced triple product asymmetries b_n $(5, 6, 17, 19)$ vanish as well. Consequently, the interference terms among $A_\perp$ and the *CP*-even amplitudes (A_0, $A_\parallel$, A_s^- and A_{ss}) disappear from the final decay rate. Likewise, A_s^+ will only interfere with the *CP*-odd amplitude $A_\perp$, since the direct and indirect *CP* asymmetries, a_n and b_n with $n = 8 - 11$ are also zero[2]. The decay rate obtained after these approximations is given in Appendix A.

The last step is to perform the time integration of the decay rate. Assuming no experimental bias in the B meson lifetime distribution[3]

$$\begin{aligned} \int_0^\infty e^{-\Gamma_s t} \cosh\left(\frac{\Delta\Gamma t}{2}\right) dt &= \frac{1}{2}\left(\frac{1}{\Gamma_H} + \frac{1}{\Gamma_L}\right), \\ \int_0^\infty e^{-\Gamma_s t} \sinh\left(\frac{\Delta\Gamma t}{2}\right) dt &= \frac{1}{2}\left(\frac{1}{\Gamma_H} - \frac{1}{\Gamma_L}\right) \end{aligned} \tag{4.17}$$

and the untagged time–integrated decay rate can be written as

$$PDF(\Omega, m_1, m_2) = \left(\frac{\mathrm{d}^5\left(\Gamma + \bar{\Gamma}\right)}{\mathrm{d}\Omega \mathrm{d}m_1 \mathrm{d}m_2}\right)_{SM} = N \sum_{n=1}^{21} \tilde{K}_n(m_1, m_2) F_n(\Omega) \tag{4.18}$$

with the F_n and K_n functions defined in Table 4.3. A redefinition of the global amplitude phase would not change the decay rate, therefore only differences between strong phases can be measured. Therefore, the convention $\delta_0 = 0$ is taken and the rest of the phases are measured relative to the phase of A_0. Note also that the phases $\delta_\perp$ and δ_s^+ only enter the decay rate through their difference, meaning that they can not be measured individually. The mass propagators $\mathcal{M}_{0,1}(m)$ are described in the next section. Unitarity is ensured by requiring

$$|A_0|^2 + |A_\parallel|^2 + |A_\perp|^2 + |A_s^+|^2 + |A_s^-|^2 + |A_{SS}|^2 = 1. \tag{4.19}$$

[1,2] These quantities are proportional to $\sin(\phi_k - \phi_{k'})$ with $k \neq k'$ and therefore they vanish if the weak phase is the same for all amplitudes.

[3] The lifetime of the B meson is actually biased by the requirements imposed in the signal selection, but its global effect in the decay rate integration is expected to be small, $\mathcal{O}(\Delta\Gamma t_0)$ (t_0 being the turn-on-value of the acceptance function).

Table 4.3: Untagged time–integrated PDF terms, assuming SM ($\phi_k = \phi_l \;\; \forall k, l$ and $2\phi_k + \phi_q = 0$). $A_k = A_k(t = 0)$.

n	K_n	F_n
1	$\frac{1}{\Gamma_L}\lvert A_0\rvert^2 \lvert\mathcal{M}_1(m_1)\rvert^2 \lvert\mathcal{M}_1(m_2)\rvert^2$	$\cos^2\theta_1 \cos^2\theta_2$
2	$\frac{1}{\Gamma_L}\lvert A_\parallel\rvert^2 \lvert\mathcal{M}_1(m_1)\rvert^2 \lvert\mathcal{M}_1(m_2)\rvert^2$	$\frac{1}{2}\sin^2\theta_1 \sin^2\theta_2 \cos^2\varphi$
3	$\frac{1}{\Gamma_H}\lvert A_\perp\rvert^2 \lvert\mathcal{M}_1(m_1)\rvert^2 \lvert\mathcal{M}_1(m_2)\rvert^2$	$\frac{1}{2}\sin^2\theta_1 \sin^2\theta_2 \sin^2\varphi$
4	$\frac{1}{\Gamma_L}\lvert A_\parallel\rvert \lvert A_0\rvert \cos\delta_\parallel \lvert\mathcal{M}_1(m_1)\rvert^2 \lvert\mathcal{M}_1(m_2)\rvert^2$	$\frac{1}{2\sqrt{2}}\sin 2\theta_1 \sin 2\theta_2 \cos\varphi$
5	0	$-\frac{1}{2\sqrt{2}}\sin 2\theta_1 \sin 2\theta_2 \sin\varphi$
6	0	$-\frac{1}{2}\sin^2\theta_1 \sin^2\theta_2 \sin 2\varphi$
7	$\frac{1}{2}(\frac{\lvert A_s^+\rvert^2}{\Gamma_H} + \frac{\lvert A_s^-\rvert^2}{\Gamma_L})\lvert\mathcal{M}_1(m_1)\rvert^2 \lvert\mathcal{M}_0(m_2)\rvert^2$	$\frac{1}{3}\cos^2\theta_1$
8	$\frac{1}{\sqrt{2}}\frac{1}{\Gamma_L}\lvert A_s^-\rvert \lvert A_0\rvert \Re(e^{i\delta_s^-}\mathcal{M}_1^*(m_2)\mathcal{M}_0(m_2))\lvert\mathcal{M}_1(m_1)\rvert^2$	$-\frac{2}{\sqrt{3}}\cos^2\theta_1 \cos\theta_2$
9	$\frac{1}{\sqrt{2}}\frac{1}{\Gamma_L}\lvert A_s^-\rvert \lvert A_\parallel\rvert \Re(e^{i(\delta_s^- - \delta_\parallel)}\mathcal{M}_1^*(m_2)\mathcal{M}_0(m_2))\lvert\mathcal{M}_1(m_1)\rvert^2$	$-\frac{1}{\sqrt{6}}\sin 2\theta_1 \sin\theta_2 \cos\varphi$
10	$\frac{1}{\sqrt{2}}\frac{1}{\Gamma_H}\lvert A_s^+\rvert \lvert A_\perp\rvert \Im(e^{i(\delta_\perp - \delta_s^+)}\mathcal{M}_0^*(m_2)\mathcal{M}_0(m_2))\lvert\mathcal{M}_1(m_1)\rvert^2$	$\frac{1}{\sqrt{6}}\sin 2\theta_1 \sin\theta_2 \sin\varphi$
11	$\frac{1}{\sqrt{2}}\frac{1}{\Gamma_L}\lvert A_s^-\rvert \lvert A_{SS}\rvert \Re(e^{i(\delta_s^- - \delta_{SS})}\mathcal{M}_0^*(m_1)\mathcal{M}_1(m_1))\lvert\mathcal{M}_0(m_2)\rvert^2$	$\frac{2}{3\sqrt{3}}\cos\theta_1$
12	$\frac{1}{2}(\frac{\lvert A_s^+\rvert^2}{\Gamma_H} + \frac{\lvert A_s^-\rvert^2}{\Gamma_L})\lvert\mathcal{M}_0(m_1)\rvert^2 \lvert\mathcal{M}_1(m_2)\rvert^2$	$\frac{1}{3}\cos^2\theta_2$
13	$-\frac{1}{\sqrt{2}}\frac{1}{\Gamma_L}\lvert A_s^-\rvert \lvert A_0\rvert \Re(e^{i\delta_s^-}\mathcal{M}_1^*(m_1)\mathcal{M}_0(m_1))\lvert\mathcal{M}_1(m_2)\rvert^2$	$\frac{2}{\sqrt{3}}\cos\theta_1 \cos^2\theta_2$
14	$-\frac{1}{\sqrt{2}}\frac{1}{\Gamma_L}\lvert A_s^-\rvert \lvert A_\parallel\rvert \Re(e^{i(\delta_s^- - \delta_\parallel)}\mathcal{M}_1^*(m_1)\mathcal{M}_0(m_1))\lvert\mathcal{M}_1(m_2)\rvert^2$	$\frac{1}{\sqrt{6}}\sin\theta_1 \sin 2\theta_2 \cos\varphi$
15	$\frac{1}{\sqrt{2}}\frac{1}{\Gamma_H}\lvert A_s^+\rvert \lvert A_\perp\rvert \Im(e^{i(\delta_\perp - \delta_s^+)}\mathcal{M}_0^*(m_1)\mathcal{M}_0(m_1))\lvert\mathcal{M}_1(m_2)\rvert^2$	$-\frac{1}{\sqrt{6}}\sin\theta_1 \sin 2\theta_2 \sin\varphi$
16	$-\frac{1}{\sqrt{2}}\frac{1}{\Gamma_L}\lvert A_s^-\rvert \lvert A_{SS}\rvert \Re(e^{i(\delta_s^- - \delta_{SS})}\mathcal{M}_0^*(m_2)\mathcal{M}_1(m_2))\lvert\mathcal{M}_0(m_1)\rvert^2$	$-\frac{2}{3\sqrt{3}}\cos\theta_2$
17	$(\frac{\lvert A_s^+\rvert^2}{\Gamma_H} - \frac{\lvert A_s^-\rvert^2}{\Gamma_L})\Re(\mathcal{M}_1^*(m_1)\mathcal{M}_0^*(m_2)\mathcal{M}_0(m_1)\mathcal{M}_1(m_2))$	$-\frac{1}{3}\cos\theta_1 \cos\theta_2$
18	$\frac{1}{\Gamma_L}\lvert A_{SS}\rvert^2 \lvert\mathcal{M}_0(m_1)\rvert^2 \lvert\mathcal{M}_0(m_2)\rvert^2$	$\frac{1}{9}$
19	$\frac{1}{\Gamma_L}\lvert A_{SS}\rvert \lvert A_0\rvert \Re(e^{i\delta_{SS}}\mathcal{M}_1^*(m_1)\mathcal{M}_1^*(m_2)\mathcal{M}_0(m_1)\mathcal{M}_0(m_2))$	$-\frac{2}{3}\cos\theta_1 \cos\theta_2$
20	$\frac{1}{\Gamma_L}\lvert A_{SS}\rvert \lvert A_\parallel\rvert \Re(e^{i(\delta_{SS} - \delta_\parallel)}\mathcal{M}_1^*(m_1)\mathcal{M}_1^*(m_2)\mathcal{M}_0(m_1)\mathcal{M}_0(m_2))$	$-\frac{\sqrt{2}}{3}\sin\theta_1 \sin\theta_2 \cos\varphi$
21	0	$\frac{\sqrt{2}}{3}\sin\theta_1 \sin\theta_2 \sin\varphi$

4.3.1.1 Invariant mass propagators

In the present analysis, there are five variables in the fit, namely three angles and two masses. In this section the mass propagators used in the analysis for the $K^+\pi^-$ and $K^-\pi^+$ pairs with angular momentum zero(*S–wave*) and one (*P–wave*) are described.

The $K\pi$ P-wave

Similarly to the analysis described in [37], for the $K\pi$ *P–wave* amplitude (K^{*0}, $\overline{K}^{*0}$) the resonant masses are parameterised with a relativistic spin-1 Breit-Wigner propagator [30],

$$\mathcal{R}_1(m) = \frac{m_R \Gamma_1(m)}{(m_R^2 - m^2) - i m_R \Gamma_1(m)}, \tag{4.20}$$

where the subscript 1 means that the angular momentum is equal to one. The mass-dependent width is given by

$$\Gamma_1(m) = \Gamma_R \frac{m_R}{m} \frac{1 + r^2 q_R^2}{1 + r^2 q^2} \left(\frac{q}{q_R} \right)^3 \tag{4.21}$$

where m_R and Γ_R are the $K^{*0}(892)$ resonance mass and width, r is the interaction radius and q is the momentum of a daughter particle in the resonance rest frame:

$$q(m, m_A, m_B) = \frac{\sqrt{(m^2 - (m_A + m_B)^2)(m^2 - (m_A - m_B)^2)}}{2m}. \tag{4.22}$$

where m_A and m_B are the daugther masses ($m_A = m_K, m_B = m_\pi$ in this case) and q_R is this momentum evaluated at the resonance nominal mass, $m = m_R$. The values of the *P–wave* propagator parameters are summarized in Table 4.4.

The propagator (4.20) can also be re-written as:

$$\mathcal{R}_1(m) = \frac{1}{\cot \delta_1(m) - i} = \sin \delta_1(m) e^{i\delta_1(m)} \tag{4.23}$$

where

$$\cot \delta_1(m) = \frac{m_R^2 - m^2}{m_R \Gamma_1(m)}, \tag{4.24}$$

and here, $\delta_1(m)$ is the phase shift.

The $K\pi$ S-wave

In a narrow mass window around the K^{*0} pole, the $K\pi$ system is close to the production threshold, and the presence of a low mass resonant structure in the $I = 0$ partial wave is described by means of a standard scattering length and effective range parameterisation. This parameterisation, which effectively describes the contribution of the $K_0^*(800)$ or $\kappa(800)$ spin-zero meson, is used in conjunction with a relativistic Breit-Wigner corresponding to the $K_0^*(1430)$ resonance, also spin-zero, which is wide enough to contribute with its left tail to the above region of interest. The relative phase of both scalar contributions is actually determined by S–matrix unitarity, and gives rise to a popular parameterisation of the *S–wave* propagator $\mathcal{R}_0(m)$, used for the first time by the LASS experiment [88],

Table 4.4: Values of the spin dependent resonances used in the analysis. The mass of the resonance is m_J, Γ_J is the width, r the interaction radius, a the scattering length and b is the effective range.

	$(K\pi)_0^{*0}$ $J = 0$	$K^*(892)^0$ $J = 1$	$K_2^*(1430)^0$ $J = 2$
m_R(MeV)	$1435 \pm 5 \pm 5$	895.81 ± 0.19	1432.4 ± 1.3
Γ_R(MeV)	$279 \pm 6 \pm 21$	47.4 ± 0.6	109 ± 5
r(GeV^{-1})	-	3.0 ± 0.5	2.7 ± 1.3
a(GeV^{-1})	$1.95 \pm 0.09 \pm 0.06$	-	-
b(GeV^{-1})	$1.76 \pm 0.36 \pm 0.67$	-	-

$$\mathcal{R}_0(m) \propto \frac{1}{\cot\delta_\beta - i} + e^{2i\delta_\beta}\frac{1}{\cot\delta_\alpha(m) - i} \tag{4.25}$$

where

$$\cot\delta_\beta = \frac{1}{aq} + \frac{1}{2}bq \tag{4.26}$$

and

$$\cot\delta_\alpha(m) = \frac{m_R^2 - m^2}{m_R\Gamma_0(m)} \tag{4.27}$$

with $e^{2i\delta_\beta}$ being the factor required by S–matrix unitarity, m_R the nominal mass of the $K_0^*(1430)$ resonance, a the scattering length and b the effective range. The mass-dependent width, $\Gamma_0(m)$, is defined as

$$\Gamma_0(m) = \Gamma_R\frac{m_R}{m}\left(\frac{q}{q_R}\right) \tag{4.28}$$

with the same meaning of q and q_R as above. The parameters of the *S–wave* propagator can be found in Table 4.4.

The LASS parameterisation is known to provide a good description of the data of many experiments, including those where the $K\pi$ system is produced from B–meson decays [37, 89]. The presence of the $K_0^*(800)$ or $\kappa(800)$ resonance has been shown to be compatible with the LASS data [90], and this meson is by now a well established resonance, where the pole position in the complex s–plane has been determined with a high degree of consistency [91].

As an alternative to the LASS parameterisation, a more explicit model can be chosen where a spin-0 Breit-Wigner propagator (BW) is used for the $K_0^*(800)$ meson in a linear superposition with the $K_0^*(1430)$, usually referred to as an *Isobar model*

$$\mathcal{R}_0(m) = \alpha\ BW(m_\kappa, \Gamma_\kappa) + BW(m_{K_0^{*0}(1430)}, \Gamma_{K_0^{*0}(1430)}) \tag{4.29}$$

where α is a complex constant, which can be determined from the data. In the analysis present in this thesis, the LASS parameterisation was taken as the baseline model, albeit a full discussion of the results obtained following the isobar model, and their comparison with the main fit results, can be found in section 6.5.4.6.

Phase space factor and Normalisation

The invariant amplitude in each case is proportional to $\mathcal{R}_J(m)$ [16, 37]:

$$\mathcal{M}_J = N_J \frac{m}{q} \mathcal{R}_J \tag{4.30}$$

where N_J is a complex constant with two purposes. Its magnitude fixes the normalisation of the mass propagators to guarantee the definition of the squared amplitudes as fractions of different partial waves in the mass range considered. The constant phase is chosen to redefine the overall propagator phase at the nominal mass of the K^{*0} resonance to be zero. This sets the definition of the *S–wave* amplitude phases (δ_s^+, δ_s^- and δ_{SS}) as the phase difference between the *S–wave* and the *P–wave* amplitudes (in particular A_0, since $\delta_0 = 0$ is assumed) at the K^{*0} nominal mass.

To account for the four-body kinematics, the total squared amplitude is multiplied by the phase space factor

$$\mathrm{d}\Phi_4(P; p_1, p_2, p_3, p_4) = \frac{2}{3(2\pi)^{10}\ m_B} q_{K^{*0}} q_{\overline{K}^{*0}} q_B \mathrm{d}m_1 \mathrm{d}m_2 \mathrm{d}\cos\theta_1 \mathrm{d}\cos\theta_2 \mathrm{d}\varphi \tag{4.31}$$

where q_B is the momentum of the K^{*0} or $\overline{K}^{*0}$ in the B_s^0 rest frame and $q_{K^{*0}}$ ($q_{\overline{K}^{*0}}$) is the momentum of the K^+ (K^-) or π^- (π^+) in the K^{*0} ($\overline{K}^{*0}$) rest frame. The mass of the B_s^0 meson is represented by m_B, m_1 is the invariant mass of the $K^+\pi^-$ pair and m_2 is the invariant mass of the $K^-\pi^+$ pair.

4.3.1.2 Forward-Backward asymmetry

The interference between the P and S–waves in the $B \to (h_1 H_1)(h_2 H_2)$ decay creates an asymmetry about $\pi/2$ in the distribution of the polarisation angles θ_1 and θ_2 [92]. This asymmetry is given by the terms linear in $\cos\theta_{1,2}$ (terms 8, 11, 13, 16 and 19 in Table 4.3). The forward-backward asymmetry originates from the different number of events with $\cos\theta_i$ positive and negative and can be calculated by integrating the angular distribution in $\cos\theta_i$ in the positive and negative ranges. For example, the number of events with $\cos\theta_1$ positive (negative) N_F (N_B) at a given value of the mass, m_1, is defined by

$$N_F(m_1) = \int_0^1 \left\{ \int\int\int PDF(\Omega, m_1, m_2) \mathrm{d}\cos\theta_2 \mathrm{d}\varphi \mathrm{d}m_2 \right\} \mathrm{d}\cos\theta_1 \tag{4.32}$$

$$N_B(m_1) = \int_{-1}^0 \left\{ \int\int\int PDF(\Omega, m_1, m_2) \mathrm{d}\cos\theta_2 \mathrm{d}\varphi \mathrm{d}m_2 \right\} \mathrm{d}\cos\theta_1 \tag{4.33}$$

where PDF is the full angular distribution given by 4.18. Equivalent expressions can be obtained for $\cos\theta_2$ by exchanging the subscripts 1 and 2 in 4.33. By computing the integrals above, the following expression for the forward-backward asymmetry is obtained ($i = 1, 2$)

$$\begin{aligned} \mathcal{A}_{FB}(m_i) &= \frac{N_F(m_i) - N_B(m_i)}{N_F(m_i) + N_B(m_i)} = \\ &= -\frac{\sqrt{3}\, \Re\Big((A_0 (A_s^-)^* - A_{SS}^* A_s^-) \mathcal{M}_1(m_i) \mathcal{M}_0^*(m_i) \Big)}{D(m_i)}, \end{aligned} \tag{4.34}$$

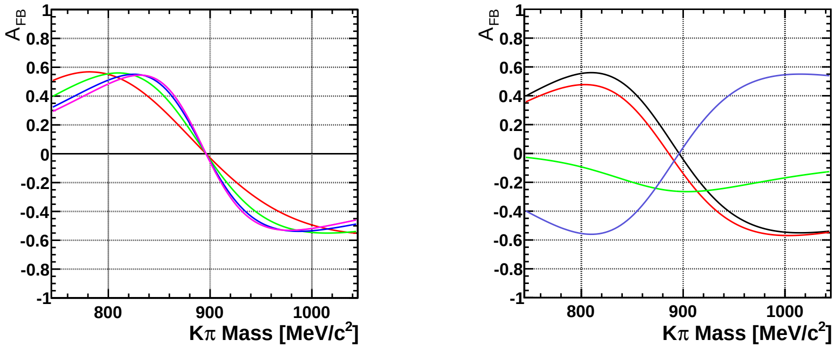

Figure 4.2: Asymmetry in $\cos\theta$ as a function of the $K\pi$ mass for different values of A_s^- (left, with a fixed value of $\delta_s = 0$) and δ_s (right, with a fixed value of $A_s^- = 0.20$)

where the denominator, $D(m_i)$, is given by

$$\begin{aligned} D(m_i) \quad = \quad & \left(|\hat{A}_P|^2 + \frac{\Gamma_L}{2}\left(\frac{|A_s^+|^2}{\Gamma_H} + \frac{|A_s^-|^2}{\Gamma_L}\right)\right)|\mathcal{M}_1(m_i)|^2 \\ & + \left(\frac{\Gamma_L}{2}\left(\frac{|A_s^+|^2}{\Gamma_H} + \frac{|A_s^-|^2}{\Gamma_L}\right) + |A_{SS}|^2\right)|\mathcal{M}_0(m_i)|^2. \end{aligned} \tag{4.35}$$

and $|\hat{A}_P|^2$ has been used to denote the sum $|A_0|^2 + |A_{||}|^2 + (\Gamma_L/\Gamma_H)\,|A_\perp|^2$.

The shape of $\mathcal{A}_{FB}$ is illustrated in Fig. 4.2 for different values of the amplitude A_s^- (left) and its phase difference with respect to the longitudinal polarisation A_0 (right). The magnitude of the later amplitudes are responsible of the strength of the asymmetry as function of $m_{K\pi}$. Also δ_s^- affects to the shape of $\mathcal{A}_{FB}$ by changing its $m_{K\pi}$ derivative.

4.3.2 Triple products and Direct *CP* asymmetries

As introduced in Sect. 2.3.2.5, two *CP*-violating TP asymmetries arise in $B \to VV$ decays that are proportional to the interference terms between the *CP*-odd amplitude $A_\perp$ and the two *CP*-even A_0 and $A_{||}$. In order to determine these *CP*-violating quantities a full angular analysis is not needed. Instead, it can be shown that they can be obtained from the following asymmetries in the azimuthal distribution, φ, [41]

$$\begin{aligned} A_T^{(1)} &= \frac{\Gamma(\mathrm{sign}(\cos\theta_1\cos\theta_2)\sin\varphi > 0) - \Gamma(\mathrm{sign}(\cos\theta_1\cos\theta_2)\sin\varphi < 0)}{\Gamma(\mathrm{sign}(\cos\theta_1\cos\theta_2)\sin\varphi > 0) + \Gamma(\mathrm{sign}(\cos\theta_1\cos\theta_2)\sin\varphi < 0)} \\ &= -\frac{2\sqrt{2}}{\pi}\frac{\Im(A_\perp A_0^* - \bar{A}_\perp \bar{A}_0^*)}{|A_0|^2 + |A_{||}|^2 + |A_\perp|^2 + |A_s^+|^2 + |A_s^-|^2 + |A_{SS}|^2} \end{aligned} \tag{4.36}$$

$$\begin{aligned} A_T^{(2)} &= \frac{\Gamma(\sin 2\varphi > 0) - \Gamma(\sin 2\varphi < 0)}{\Gamma(\sin 2\varphi > 0) + \Gamma(\sin 2\varphi < 0)} \\ &= -\frac{4}{\pi}\frac{\Im(A_\perp A_{||}^* - \bar{A}_\perp \bar{A}_{||}^*)}{|A_0|^2 + |A_{||}|^2 + |A_\perp|^2 + |A_s^+|^2 + |A_s^-|^2 + |A_{SS}|^2} \end{aligned} \tag{4.37}$$

When the *S–wave* contribution is taken into account, two more *CP*-even amplitudes, A_s^- and A_{ss}, are subject to interference with $A_\perp$. Asymmetric integration of the decay rate, analogous to 4.36 and 4.37, can be worked out to measure these two new quantities. Namely,

$$\begin{aligned} A_T^{(3)} &= \frac{\Gamma(\mathrm{sign}(\cos\theta_1+\cos\theta_2)\sin\varphi>0)-\Gamma(\mathrm{sign}(\cos\theta_1+\cos\theta_2)\sin\varphi<0)}{\Gamma(\mathrm{sign}(\cos\theta_1+\cos\theta_2)\sin\varphi>0)+\Gamma(\mathrm{sign}(\cos\theta_1+\cos\theta_2)\sin\varphi<0)} \\ &= \frac{32}{5\pi\sqrt{3}}\frac{\int\Im\left(\left(A_\perp A_s^{-*}-\bar{A}_\perp\bar{A}_s^{-*}\right)\mathcal{M}_1(m)\mathcal{M}_0^*(m)\right)\mathrm{d}m}{|A_0|^2+|A_\parallel|^2+|A_\perp|^2+|A_s^+|^2+|A_s^-|^2+|A_{SS}|^2} \end{aligned} \tag{4.38}$$

$$\begin{aligned} A_T^{(4)} &= \frac{\Gamma(\sin\varphi>0)-\Gamma(\sin\varphi<0)}{\Gamma(\sin\varphi>0)+\Gamma(\sin\varphi<0)} \\ &= \frac{3\pi}{4\sqrt{2}}\frac{\int\Im\left(\left(A_\perp A_{SS}^*-\bar{A}_\perp\bar{A}_{SS}^*\right)\mathcal{M}_1(m)\mathcal{M}_0^*(m)\right)\mathrm{d}m}{|A_0|^2+|A_\parallel|^2+|A_\perp|^2+|A_s^+|^2+|A_s^-|^2+|A_{SS}|^2} \end{aligned} \tag{4.39}$$

Since A_s^+ is also *CP*–odd, its interference terms with the *CP*–even amplitudes change sign when going from B_s^0 to $\bar{B}_s^0$ decay rate. In particular, these terms have the form $\Re(A_s^+A_k^*)$, with $k=0,\|,s^-,ss$. Consequently, new *CP*-violating quantities arise in the the untagged decay rate in the form $Re(A_s^+A_k^*-\bar{A}_s^+\bar{A}_k^*)$. These terms have the structure of a direct *CP* asymmetry. There are actually four of them, accessible from $B_s\to K^+\pi^-K^-\pi^+$ decays, which from now on will be designated as $A_D^{(i)}(i=1,4)$.

Parameterising each amplitude as $A_k=\sum_i a_k^i e^{i\delta_k^i}e^{i\phi_k^i}$, these terms can be written as follows

$$Re(A_s^+A_k^*-\bar{A}_s^+\bar{A}_k^*) = -2\sum_{ij} a_{s^+}^i a_k^j \sin(\delta_{s^+}^i-\delta_k^j)\sin(\phi_{s^+}^i-\phi_k^j). \tag{4.40}$$

and are only nonzero if the weak phase difference between two amplitudes is not zero. As in the case of the TP asymmetries, these quantities are very small in the Standard Model ($\mathcal{O}(\lambda^2)$) and the measurement of a large value for any $A_D^{(i)}$ would imply the presence of New Physics. These quantities can also be determined from the following asymmetries in the angular distribution

$$\begin{aligned} A_D^{(1)} &= \frac{\Gamma(\cos\theta_1\cos\theta_2(\cos\theta_1-\cos\theta_2)>0)-\Gamma(\cos\theta_1\cos\theta_2(\cos\theta_1-\cos\theta_2)<0)}{\Gamma(\cos\theta_1\cos\theta_2(\cos\theta_1-\cos\theta_2)>0)+\Gamma(\cos\theta_1\cos\theta_2(\cos\theta_1-\cos\theta_2)<0)} \\ &= \frac{\sqrt{2}}{5\sqrt{3}}\left[\frac{9\int\Re\left((A_s^+A_0^*-\bar{A}_s^+\bar{A}_0^*)\mathcal{M}_0(m)\mathcal{M}_1^*(m)\right)\mathrm{d}m}{|A_0|^2+|A_\parallel|^2+|A_\perp|^2+|A_s^+|^2+|A_s^-|^2+|A_{SS}|^2}\right. \\ &\qquad \left.+\frac{5\int\Re\left((A_s^+A_{SS}^*-\bar{A}_s^+\bar{A}_{SS}^*)\mathcal{M}_1(m)\mathcal{M}_0^*(m)\right)\mathrm{d}m}{|A_0|^2+|A_\parallel|^2+|A_\perp|^2+|A_s^+|^2+|A_s^-|^2+|A_{SS}|^2}\right] \end{aligned} \tag{4.41}$$

$$\begin{aligned} A_D^{(2)} &= \frac{\Gamma((\cos\theta_1-\cos\theta_2)\cos\varphi>0)-\Gamma((\cos\theta_1-\cos\theta_2)\cos\varphi<0)}{\Gamma((\cos\theta_1-\cos\theta_2)\cos\varphi>0)+\Gamma((\cos\theta_1-\cos\theta_2)\cos\varphi<0)} \\ &= -\frac{32}{5\pi\sqrt{3}}\frac{\int\Re\Big((A_s^+A_\parallel^*-\bar{A}_s^+\bar{A}_\parallel^*)\mathcal{M}_0(m)\mathcal{M}_1^*(m)\Big)\mathrm{d}m}{|A_0|^2+|A_\parallel|^2+|A_\perp|^2+|A_s^+|^2+|A_s^-|^2+|A_{SS}|^2} \end{aligned} \tag{4.42}$$

$$\begin{aligned} A_D^{(3)} &= \frac{\Gamma((\cos\theta_1 - \cos\theta_2) > 0) - \Gamma((\cos\theta_1 - \cos\theta_2) < 0)}{\Gamma((\cos\theta_1 - \cos\theta_2) > 0) + \Gamma((\cos\theta_1 - \cos\theta_2) < 0)} \\ &= \frac{2\sqrt{2}}{5\sqrt{3}} \left[\frac{3\int \Re\left((A_s^+ A_0^* - \bar{A}_s^+ \bar{A}_0^*)\mathcal{M}_0(m)\mathcal{M}_1^*(m)\right) \mathrm{d}m}{|A_0|^2 + |A_\parallel|^2 + |A_\perp|^2 + |A_s^+|^2 + |A_s^-|^2 + |A_{SS}|^2} \right. \\ &\qquad \left. + \frac{5\int \Re\left((A_s^+ A_{SS}^* - \bar{A}_s^+ \bar{A}_{SS}^*)\mathcal{M}_1(m)\mathcal{M}_0^*(m)\right) \mathrm{d}m}{|A_0|^2 + |A_\parallel|^2 + |A_\perp|^2 + |A_s^+|^2 + |A_s^-|^2 + |A_{SS}|^2} \right] \end{aligned} \tag{4.43}$$

$$\begin{aligned} A_D^{(4)} &= \frac{\Gamma((\cos^2\theta_1 - \cos^2\theta_2) > 0) - \Gamma((\cos^2\theta_1 - \cos^2\theta_2) < 0)}{\Gamma((\cos^2\theta_1 - \cos^2\theta_2) > 0) + \Gamma((\cos^2\theta_1 - \cos^2\theta_2) < 0)} \\ &= \frac{\Re\left(A_s^+ A_s^{-*} - \bar{A}_s^+ \bar{A}_s^{-*}\right)}{|A_0|^2 + |A_\parallel|^2 + |A_\perp|^2 + |A_s^+|^2 + |A_s^-|^2 + |A_{SS}|^2} \end{aligned} \tag{4.44}$$

4.3.3 Summary of the analysis strategy

The analyses presented in this thesis focus on the determination of the observables accesible to the untagged sample. In Chapter 5, the study of the first LHCb data (37 pb^{-1}) that lead to the discovery of the $B_s^0 \to K^{*0}\overline{K}^{*0}$ mode is described.

Chapter 6 summarizes the update of those results with a larger data sample (1.0 fb^{-1}). The *CP*-averaged branching fraction and polarisation fractions for $B_s^0 \to K^{*0}\overline{K}^{*0}$ were determined through the study of the angular distribution of the four body $(K^+\pi^-)(K^-\pi^+)$ final state, under the assumption of *CP*-conservation, following the Standard Model prediction. A model independent search for New Physics was also performed by measuring the four (*CP*-violating) TP asymmetries and four direct *CP* asymmetries associated with the interference between $B_s^0 \to K^{*0}\overline{K}^{*0}$ and the different *S–wave* contributions.

5

First observation of $B_s^0 \to K^{*0}\overline{K}^{*0}$

During 2010, LHCb collected the first pp collisions delivered by the LHC at a centre-of-mass energy of $\sqrt{s} = 7$ TeV. A data sample of corresponding to 37 pb^{-1} of integrated luminosity was recorded. In this chapter, the analysis of these first data, which led to the first observation of the $B_s^0 \to K^{*0}\overline{K}^{*0}$ decay, is presented.

5.1 Introduction

Before the start of the LHC, the decay channel $B_s^0 \to K^{*0}\overline{K}^{*0}$ had never been observed. Only an upper limit for the its branching fraction of 1.68×10^{-3} at 90% confidence level (CL) had been reported by the SLD experiment [93].

On the U-spin related channel, the $b \to d$ transition $B^0 \to K^{*0}\overline{K}^{*0}$, there is still some controversy. First, BaBar reported its discovery (with a 6σ statistical significance) and a measurement of its branching fraction of $(1.28^{+0.35}_{-0.30} \pm 0.11) \times 10^{-6}$ [94]. In the same paper, a measurement of its longitudinal polarisation fraction of $f_L = 0.80^{+0.10}_{-0.12} \pm 0.06$ was reported. A few years later, Belle set the upper limit $\mathcal{B}(B^0 \to K^{*0}\overline{K}^{*0}) < 0.8 \times 10^{-6}$ at 90% CL [95].

The strategy of the analysis detailed in this chapter can be summarized as follows. First, a set of selection requirements was defined to identify the signal candidates, i.e. $B_s^0 \to K^{*0}\overline{K}^{*0}$ decays where the K^{*0} ($\overline{K}^{*0}$) resonances decay subsequently into $K^+\pi^-$ ($K^-\pi^+$). This selection was optimised to reject most of the background while keeping the efficiency for the signal as high as possible.

Then, the four-body ($K^+\pi^-K^-\pi^+$) invariant mass spectrum of the signal candidates was analysed in order to extract the number of events corresponding to B_s^0 decays and determine the statistical significance of such a signal. The branching ratio of the signal can then be computed by comparing the observed number of signal candidates to the number of candidates for a reference decay channel with known branching fraction. In this case, the $B_d^0 \to J/\psi K^{*0}$ decay was chosen as the reference mode.

Additionally, a simplified version of the angular analysis presented in Chapter 4 was performed, using only candidates with a mass in a narrow window around the B_s^0 meson mass, with the objective of measuring the polarisation fractions of the $B_s^0 \to K^{*0}\overline{K}^{*0}$ decay.

5.2 Data sample and Event selection

5.2.1 Data and Monte Carlo samples

As explained, the present analysis is performed using the 2010 LHCb dataset, which includes ~ 37 pb^{-1} of integrated luminosity taken at $\sqrt{s} = 7$ TeV. The data belong to the `Reco08-Stripping12` campaign, and have been reconstructed with Brunel v37r8p6 [96] and analysed with DaVinci v26r3 [97].

Two Monte Carlo samples were used in this analysis, corresponding to the decays $B_s^0 \to K^{*0}\overline{K}^{*0}$ and $B_d^0 \to J/\psi K^{*0}$, that were modeled using EvtGen [98]. Both samples belong to the Monte Carlo production MC10, and were generated with the software corresponding to the Gauss release v39r0 [99], which uses GEANT4 v92r4 [100] for the full detector simulation. Then, they were reconstructed using Boole v21r9 [101] and Brunel v37r8p5.

The pp interactions have been simulated assuming a beam energy of 3.5 TeV and an average number of interactions per crossing $\nu = 2.5$, which corresponds to an average number of visible interactions per crossing of $\mu = 1.75$.

5.2.2 Event selection

In order to search for the decay process $B_s^0 \to K^{*0}(K^+\pi^-)\overline{K}^{*0}(K^-\pi^+)$ a number of offline selection criteria were applied. When a four-track secondary vertex is found, the reconstructed momentum of the B_s^0 candidate is used to calculate the smallest impact parameter with respect to all primary vertices in the event. Tracks are required to have $p_{\mathrm{T}} > 500$ MeV/c, and a large impact parameter (IP$\chi^2 > 9$) with respect to any PV. The difference in the natural logarithm of the likelihoods of the kaon and pion hypotheses must be greater than 2 for K^+ and K^- candidates, and less than 0 for π^+ and π^- candidates. In addition, the $K\pi$ combinations[1] must form an acceptable quality common vertex (χ^2/ndf < 9, where ndf is the number of degrees of freedom in the vertex fit) and must have an invariant mass within ± 150 MeV/c^2 of the nominal K^{*0} mass (this is around ± 3 times its decay width [16]). The K^{*0} and $\overline{K}^{*0}$ candidates must have $p_{\mathrm{T}} > 900$ MeV/c and the distance of closest approach (DOCA) between their trajectories must be less than 0.3 mm. The secondary vertex must be well fitted (χ^2/ndf< 5). Finally, the B_s^0 candidate momentum is required to point to the PV.

To improve the signal significance, a multivariate discriminant is defined that takes into account the properties of the $B_s^0 \to K^{*0}(K^+\pi^-)\overline{K}^{*0}(K^-\pi^+)$ signal, as well as those of the background. This discriminant, in particular a geometrical likelihood (GL) [11,102], takes the following set of variables as input:

- B_s^0 candidate impact parameter with respect to the closest primary vertex.
- Decay time of the B_s^0 candidate.
- Minimum IPχ^2 of the four tracks with respect to all primary vertices in the event.
- DOCA between the two K^{*0} trajectories reconstructed from the pion and kaon tracks.

---

[1] This expression refers hereafter to both charge combinations: $K^+\pi^-$ and $K^-\pi^+$.

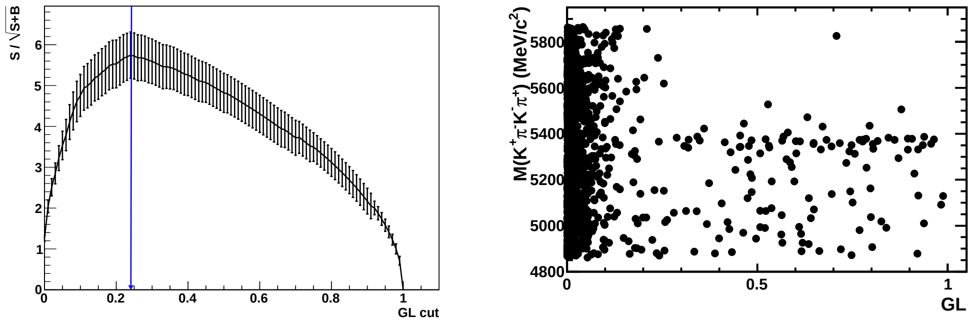

Figure 5.1: Left: $\frac{S}{\sqrt{S+B}}$ as a function of the GL cut. The optimal GL cut was found to be ~ 0.24. Right: Invariant mass versus GL scatter plot for $B_s^0 \to K^{*0}\overline{K}^{*0}$ candidates in data before any GL cut.

- p_{T} of the B_s^0 candidate.

For a given input sample, the above distributions are converted into a set of uncorrelated, Gaussian-distributed variables. Two vectors are defined for each event indicating its distance to the signal $\{S_i\}$ and to the background $\{B_i\}$ hypotheses by means of $\chi_S^2 = \sum S_i^2$ and $\chi_B^2 = \sum B_i^2$, where the index i runs over the five discriminating variables indicated above. The quantity $\Delta\chi^2 = \chi_S^2 - \chi_B^2$ is found to be a good discriminant between the two hypotheses and is used to construct the GL function in such a way that it is uniformly distributed in the range $[0, 1]$ for signal events and tends to have low values for the background. The GL was trained using a fully reconstructed $B_s^0 \to K^{*0}\overline{K}^{*0}$ simulation sample for the signal, and a selected background sample from the first 2 pb^{-1} of data (`Stripping09`), which is not used in the analysis.

The GL selection requirement was determined by maximising the figure of merit $\frac{S}{\sqrt{S+B}}$, where S and B are the number of events from the testing signal and background samples that survive each cut in the GL. The optimal cut was found to be GL>0.24 (see Fig. 5.1 left). The GL requirement together with the above selection criteria, resulted in the mass spectrum in Fig. 5.2 for the selected $K^+\pi^-K^-\pi^+$ candidates. Fig. 5.1 shows that the events with masses below the signal region have on average slightly higher GL values than those with masses above. This indicates the presence of a background from partially reconstructed B decays.

5.3 The $B_s^0 \to K^{*0}\overline{K}^{*0}$ signal

5.3.1 Four-body invariant mass fit

The invariant mass $M(K^+, \pi^-, K^-, \pi^+)$ of the selected canditates was then analysed. The model used to describe the data includes four different components. The signals from $B_{s(d)} \to K^+\pi^-K^-\pi^+$ decay modes are described by two Gaussian probability density functions (PDF) centred at the B^0 and B_s^0 masses respectively and sharing a common width. A decreasing exponential models the combinatorial background. Finally, the back-

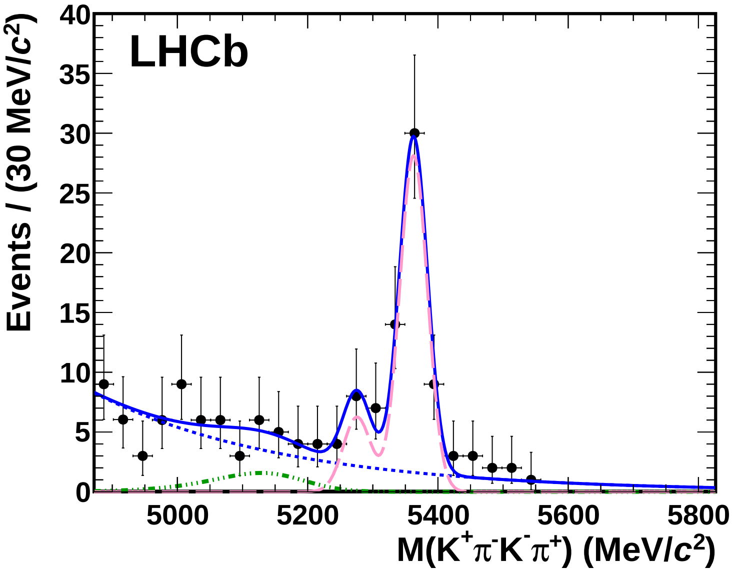

Figure 5.2: Fit to the $K^+\pi^-K^-\pi^+$ mass distribution of selected candidates. The fit model (dashed pink curve) includes a signal component that has two Gaussian components corresponding to the B_s^0 and B^0 decays. The background is described as an exponential component (dotted blue) plus the parametrisation described in (5.1) in the text (dash-dotted green).

ground coming from partially reconstructed B-decays is parameterised as follows:

$$PhysBkg(M) = M'\left(1 - \frac{M'^2}{M_p^2}\right)\Theta(M_p - M')e^{-k_p \cdot M'} \otimes G(M - M'; \sigma_p), \tag{5.1}$$

where Θ is the Heaviside-step function, $\otimes$ represents the convolution, M' is the variable over which the convolution integral is calculated, $G(M - M'; \sigma_p)$ is a Gaussian PDF with standard deviation σ_p and M_p and k_p are free parameters. With this model,

$$\begin{aligned} I(M) \quad &= \quad N_{B_s^0}\ G(M - m_{B_s^0}, \sigma) + N_{B^0}\ G(M - m_{B^0}, \sigma) \\ &\quad\quad +N_{Bkg}\left(f_p\ PhysBkg(M) + (1 - f_p)\ e^{-c_b M}\right) \end{aligned} \tag{5.2}$$

an extended maximum likelihood fit was performed to the four-body mass spectrum of the selected candidates. The fit results are given in Table 5.1. The measured B_s^0 signal yield in a window of ±50 MeV/c^2 around the B_s^0 mass is $N_{B_s^0} = 49.8 \pm 7.5(\text{stat.})$. The width of the B_s^0 peak is in good agreement with the LHCb resolution measured in decays with similar kinematics such as $B_s^0 \to J/\psi\phi$.

In order to calculate the significance of the B_s^0 signal, the fit was repeated excluding the B_s^0 signal component[1]. According to *Wilks' theorem* [103], the variation in the negative log-likelihood between both fits follows a $\chi^2(\Delta\text{ndf})$ distribution, where $\Delta\text{ndf} = 1$ is the difference in number of free parameters between the model with and without the B_s^0 signal.

---

[1] For this test, the mass and width of the $B_{s(d)}$ signals were fixed to those obtained from independent LHCb measurements in $B_s^0 \to J/\psi\phi$ and $B_d^0 \to J/\psi K^{*0}$ respectively: $m_{B_s^0} = (5362.88 \pm 0.84)$ MeV/c^2, $m_{B^0} = (5275.75 \pm 0.47)$ MeV/c^2 and $\sigma = (18.80 \pm 0.73)$ MeV/c^2.

Table 5.1: Fitted values of the model parameters for the mass spectrum, as described in the text. $N_{B_s^0}$ and N_{B^0} are the number of events for the B_s^0 and B^0 signals, $\mathrm{m}_{\mathrm{B}_s^0}$ is the fitted B_s^0 meson mass and σ is the Gaussian width. The mass difference between B_s^0 and B^0 was fixed to its nominal value [16]. N_{Bkg} is the number of background events in the full mass range (4900-5800 MeV/c^2), and c_b is the exponential parameter of the combinatorial background model. M_p, σ_p and k_p are the parameters of Eq. (5.1). Finally, f_p is the fraction of the background associated with Eq. (5.1).

Parameter	Value
$N_{B_s^0}$	50.1 ± 7.5
N_{B^0}	11.2 ± 4.3
N_{Bkg}	90 ± 10
$m_{B_s^0}$ (MeV/c^2)	5362.5 ± 4.8
σ (MeV/c^2)	21.2 ± 3.3
c_b (10^{-3}(MeV/$c^2)^{-1}$)	-3.37 ± 0.55
k_p (10^{-2}(MeV/$c^2)^{-1}$)	5.5 ± 5.3
f_p	$0.06^{+0.24}_{-0.05}$
M_p (MeV/c^2)	5170 ± 170
σ_p (MeV/c^2)	37 ± 23

Therefore, it is possible to turn this number into a probability according to χ^2-statistics, and from there to a Gaussian standard deviation. The obtained significance was 10.9 σ. The peak at the B^0 mass, though not significant, is compatible with the $B^0 \to K^{*0}\overline{K}^{*0}$ branching fraction measured by BaBar [94].

5.3.2 $B_s^0 \to K^{*0}\overline{K}^{*0}$ purity

As previously explained, among the $B_s^0 \to (K^+\pi^-)(K^-\pi^+)$ candidates identified in the previous section, not all of them correspond to $B_s^0 \to K^{*0}\overline{K}^{*0}$ events. In particular, scalar resonances (and non resonant production) in the $K\pi$ spectrum can not be distinguished from the vector-vector decay without further analysis.

The $K\pi$ mass combinations of the candidates with a four-body invariant mass within a ± 50 MeV/c^2 window around the B_s^0 signal were studied. A maximum likelihood fit in the $(m_{K^+\pi^-}, m_{K^-\pi^+})$ plane was perfomed. Three components were included in the signal model, namely a double Breit-Wigner distribution describing $B_s^0 \to K^{*0}\overline{K}^{*0}$ production, a symmetrized product of a Breit-Wigner and a nonresonant linear model adjusted for phase-space in the $K\pi$ mass, and a double nonresonant component.

The non-B_s^0 component under the peak, which is essentially combinatorial background, was included in the fit with a fixed yield determined from the results in Table 5.1. The shape of its mass distribution was extracted from a fit to the $K\pi$ mass spectrum observed in two 400 MeV/c^2 wide sidebands below and above the B_s^0 mass. The sizeable K^{*0} contribution present in this background was taken into account.

The fit result, as shown in Fig. 5.3, gives (62±18)% $K^{*0}\overline{K}^{*0}$ production. A model for $B_s^0 \to K^{*0}\overline{K}^{*0}(1430)$, representing a broad scalar state interfering with $B_s^0 \to K^{*0}\overline{K}^{*0}$ was also studied. The small number of events made it impossible to measure precisely

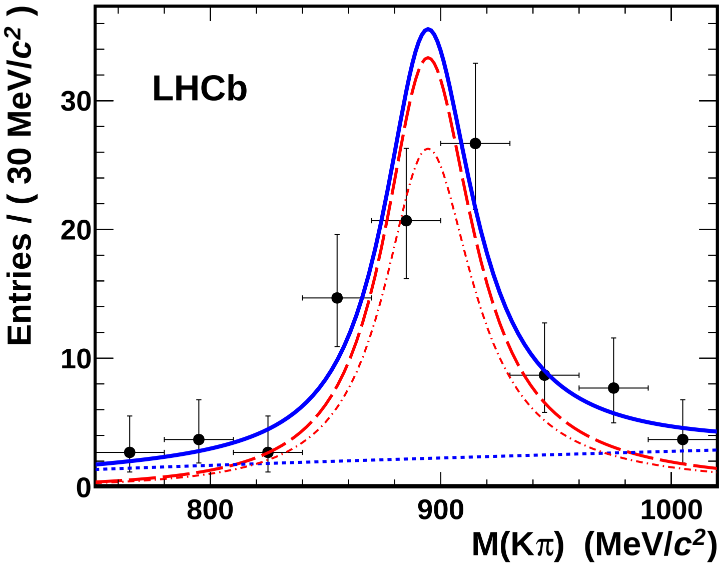

Figure 5.3: Background subtracted $K^+\pi^-$ and $K^-\pi^+$ combinations for selected candidates within a ± 50 MeV/c^2 window of the B_s^0 mass. The solid blue line shows the projection of the 2D fit model described in the text, indicating the K^{*0} $\overline{K}^{*0}$ yield (dashed-dotted red line) and a nonresonant component (blue dotted line), assumed to be a linear function times the two-body phase space. The dashed red line indicates the overall $B_s^0 \to K^{*0}X$ contribution.

the size of such a contribution for all values of the interfering phase. However, for values of the phase away from $\pi/2$ and $3\pi/2$ it was determined to be below 12%. Further study of this issue requires a larger data sample and was postponed until the 2011 data was available, see Chapter 6.

Additionally, other four-body B decays that could possibly fake a $B_s^0 \to K^{*0}\overline{K}^{*0}$ signal were also searched for; in particular, decays into charmed mesons like $B_s^0 \to D_s^-(\to K^+K^-\pi^-)\pi^+$. However, as the K^{*0} meson is light compared to the B_s^0 meson, the invariant masses of the three-body systems $K^+K^-\pi^\pm$ and $K^+\pi^-\pi^\pm$ are rather high, above those of the charmed hadrons. This kinematically excludes the possibility of contamination from $b \to c$ decays with very short charm flight distance.

5.4 Analysis of K^{*0} polarisation

Due to the small number of events available, a full mass-dependent angular analysis as the one propossed in Sect. 4.3.1 was not attempted. Instead, a mass integrated study of the angular distribution of the decay products, assuming no contamination from the *S–wave* amplitudes, was performed. Under these assumptions, the four-particle $K^+\pi^-K^-\pi^+$ distribution in the three helicity angles, θ_1, θ_2 and φ (defined in Fig. 4.1), is described by the three transversity amplitudes A_0, $A_\|$ and $A_\perp$. In a time-integrated and flavour-averaged analysis, and assuming no CP-violation arises in this decay as the Standard Model predicts, the angular distribution is given by

$$
\begin{aligned}
PDF(\theta_1, \theta_2, \varphi) \;=\; & \frac{1}{\Gamma_L}|A_0|^2 \cos^2\theta_1 \cos^2\theta_2 \\
& + \frac{1}{\Gamma_L}|A_\parallel|^2 \frac{1}{2}\sin^2\theta_1 \sin^2\theta_2 \cos^2\varphi \\
& + \frac{1}{\Gamma_H}|A_\perp|^2 \frac{1}{2}\sin^2\theta_1 \sin^2\theta_2 \sin^2\varphi \\
& + \frac{1}{\Gamma_L}\frac{1}{2\sqrt{2}}|A_L||A_\parallel| \cos\delta_\parallel \sin 2\theta_1 \sin 2\theta_2 \cos\varphi. \qquad (5.3)
\end{aligned}
$$

The measurable parameters of this PDF are the relative fraction of each of the amplitudes, usually referred to as *polarisation fractions*,

$$
f_{L,k} = \frac{|A_{0,k}|^2}{|A_L|^2 + |A_\parallel|^2 + |A_\perp|^2} \quad , \quad k = \parallel, \perp, \qquad (5.4)
$$

and $\delta_\parallel$, the phase difference between A_0 and $A_\parallel$. The definition (5.4) implies that $f_L + f_\parallel + f_\perp = 1$. The constants $\Gamma_{L,H}$ are the total widths of the light and heavy mass eigenstates of the B_s^0-system, respectively, and their values were fixed to those obtained from the total B_s^0 decay width, $\Gamma_s = (\Gamma_L + \Gamma_H)/2$, and the width difference, $\Delta\Gamma_s = \Gamma_L - \Gamma_H$, reported in [16].

The effects induced by the detector geometrical acceptance, and the reconstrucction and selection processes need to be taken into account before comparing (5.3) to data. These effects were determined using simulated $B_s^0 \to K^{*0}\overline{K}^{*0}$ events and were described in terms of the acceptance function ε, as a function fo the three decay angles. The acceptance function was found to be compatible with being constant in φ. In contrast, it has a significant dependence on the K^{*0} polarisation angle θ[1]. The two-dimensional angular acceptance function, $\varepsilon(\cos\theta_1,\cos\theta_2)$, drops asymmetrically as $\cos\theta_{1,2}$ becomes close to ±1, as a consequence of the minimum p and p_{T} of the tracks imposed by the reconstruction and selection . This effect is more important for the limit $\cos\theta \to +1$, i.e. when the π meson is emitted backwards with respect to the K^{*0} momentum. This acceptance function is shown in Fig. 5.4.

The Monte Carlo simulation of the K^{*0} acceptance was extensively cross-checked using the $B_d^0 \to J/\psi K^{*0}$ control channel, taking advantage of the fact that the K^{*0} polarisation in this channel was measured at the B-factory experiments [104, 105]. This acceptance shows no appreciable difference between K^{*0} and $\overline{K}^{*0}$, and a small average correlation, given the size of the simulated sample. Consequently, the one-dimensional acceptance $\epsilon_\theta(\cos\theta)$ has been used as the basis of the analysis, and it has been determined it in five bins of $\cos\theta$. Since the longitudinal polarisation fraction for the $B_d^0 \to J/\psi K^{*0}$ channel is well measured, a comparison between data and simulation is possible. Agreement was found including variations of the angular distribution with longitudinal and transverse K^{*0} momentum. In the region $\cos\theta > 0.6$ these variations were four times larger than for lower values of $\cos\theta$.

The background $\cos\theta$ distribution was studied in two 200 MeV/c^2 sidebands, defined below and above the B_s^0 signal region. Like the signal, it showed a dip close to $\cos\theta = +1$

---

[1] This notation refers to a generic θ angle, and will be followed from now on unless differences between θ_1 and θ_2 become relevant for the discussion.

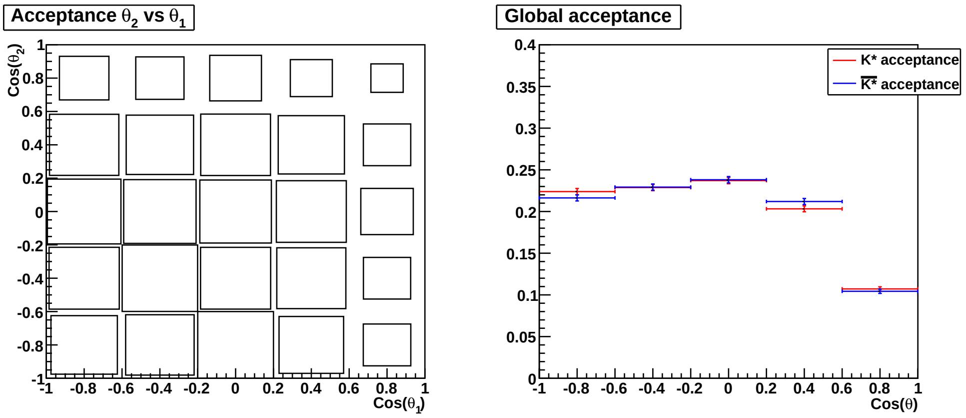

Figure 5.4: Left: Global 2D angular acceptance $\varepsilon(\theta_1, \theta_2)$ calculated using $B_s^0 \to K^{*0}\overline{K}^{*0}$ simulated events. Right: Projections of the previous acceptance function into $\cos\theta_1$ (red) and $\cos\theta_2$ (blue).

and it was parameterised as $\varepsilon_\theta \times (1 + \beta\cos\theta)$. A one parameter fit for β gave the result $\beta = -0.18 \pm 0.13$.

An unbinned maximum likelihood fit was then performed to the data in a ± 50 MeV/c^2 window around the B_s^0 mass, in the region $\cos\theta < 0.6$, according to the PDF

$$\begin{aligned} F(\theta_1, \theta_2, \varphi) &= (1-\alpha)\varepsilon_\theta(\theta_1)\varepsilon_\theta(\theta_2)I(\theta_1, \theta_2, \varphi) \\ &\quad + \alpha(1+\beta\cos\theta_1)(1+\beta\cos\theta_2)\varepsilon_\theta(\theta_1)\varepsilon_\theta(\theta_2). \end{aligned} \tag{5.5}$$

The background fraction α was determined from the fit to the B_s^0 mass spectrum described in Sect. 5.3.1. Only three parameters were allowed to vary in the fit, namely f_L, $f_{\|}$ and the phase difference $\delta_{\|}$.

One-dimensional projections of the fit results are shown in Fig. 5.5. The consistency of the measurement in various regions of the K^{*0} phase space, and of the impact parameter of the daughter particles, was checked. The experimental systematic error on f_L was estimated from the variation of the measurements amongst those regions to be 0.03.

The acceptance for $B_s^0 \to K^{*0}\overline{K}^{*0}$ is not uniform as a function of proper decay time due to the cuts made on the IP of the kaons and pions, and a small correction to the polarisation fractions, of order 3%, was applied in order to take into account this effect. It was calculated from the variation in the measured polarisation amplitudes induced by including a parametrisation of the time acceptance in Eq. 5.5. Note the different correction sign for each polarisation fraction, as a consequence of the fact that $\Delta\Gamma \neq 0$.

The sensitivity of the f_L measurement with respect to small variations of the $\cos\theta$ distribution has been tested. These variations could be attributed to experimental effects not accounted for in the simulation or to interference with other partial waves in the $K\pi$ system. A high statistics study using $B_d^0 \to J/\psi K^{*0}$ muon triggers revealed a small systematic difference between data and simulation in $\varepsilon_\theta(\cos\theta)$ as $\cos\theta$ approaches $+1$, which was taken into account as a correction in our analysis. When this correction in varied by $\pm 100\%$, f_L varies by ± 0.02 which was consider as an additional source of systematic error. The total systematic on f_L is thus ± 0.04.

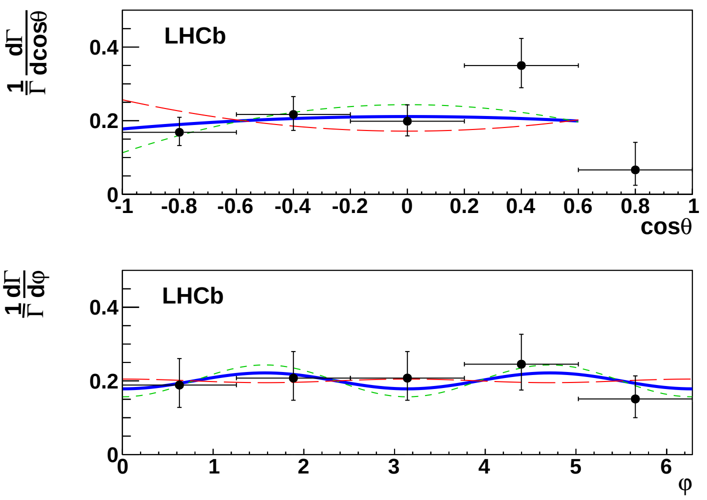

Figure 5.5: $\cos\theta$ (above) and φ (below) acceptance corrected distributions for events in the narrow window around the B_s^0 mass. The blue line is the projection of the fit model given by (5.3) for the measured values of the parameters f_L, $f_{\|}$ and $\delta_{\|}$. The dotted lines indicate $\pm 1\sigma$ variation of the f_L central value.

Finally, the K^{*0} longitudinal polarisation fraction $f_L = 0.31 \pm 0.12(\text{stat.}) \pm 0.04(\text{syst.})$ is measured, as well as the transverse components $f_{\|}$ and $f_{\perp}$. In the small sample available, the CP-odd component $f_{\perp}$ appears to be sizeable $f_{\perp} = 0.38 \pm 0.11(\text{stat.}) \pm 0.04(\text{syst.})$. A significant measurement of $\delta_{\|}$ could not be achieved ($\delta_{\|} = 1.47 \pm 1.85$).

As seen in (5.3), due to a nonzero $\Delta\Gamma$ time integration changes the relative proportion between the various terms of the angular distribution, with respect to their values at $t = 0$. Denoting the polarisation fractions that would have been measured under the assumption $\Delta\Gamma = 0$ as f_k^0 , it can be shown that the measured values are

$$f_k = f_k^0 \left(1 + \eta_k \frac{\Delta\Gamma}{2\Gamma}\right) \tag{5.6}$$

with CP eigenvalue $\eta_k = +1, +1, -1$ for $k = L, \|, \perp$. Given the current knowledge of $\Delta\Gamma/\Gamma$ [16], the magnitude of the correction to f_k amounts to 4.6%, and the associated systematic error related to the $\Delta\Gamma$ uncertainty is 2.6%, which has been neglected in comparison to other sources.

5.5 Determination of $\mathcal{B}(B_s^0 \to K^{*0}\overline{K}^{*0})$

The results of the previous sections can be brought together to provide a determination of the branching fraction of the $B_s^0 \to K^{*0}\overline{K}^{*0}$ decay based upon the use of a normalisation channel with a well measured branching fraction.

5.5.1 Selection of the control channel

The decay channel $B_d^0 \to J/\psi K^{*0}$, with $J/\psi \to \mu^+\mu^-$ and $K^{*0} \to K^+\pi^-$, was chosen as the normalisation channel. This decay has a similar topology to the signal, allowing the

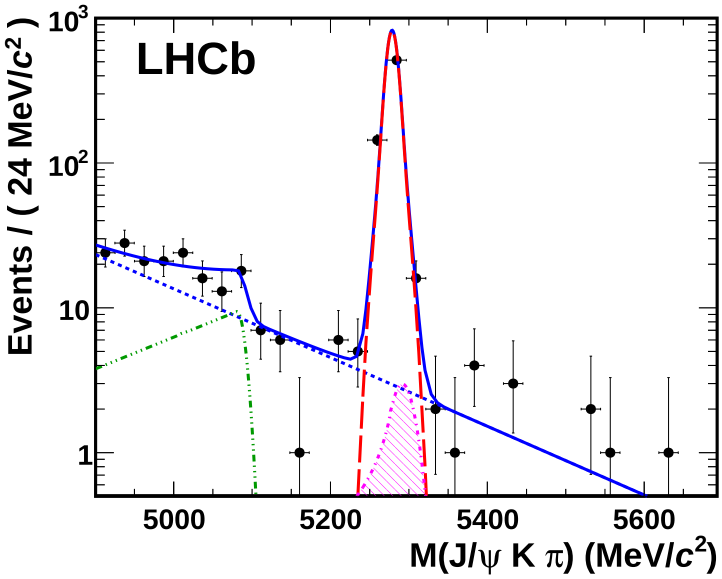

Figure 5.6: Fit to the mass distribution of selected $B_d^0 \to J/\psi K^{*0}$ events. The dashed red curve is the Gaussian component for the B signal. The green dashed-dotted line accounts for partially reconstructed $B \to J/\psi X$ (see Eq. 5.7). The pink hatched region accounts for a possible $B_s^0 \to J/\psi\phi$ contamination, parameterised as a sum of two Crystal-Ball functions [106]. The combinatorial background is parameterised as an exponential and indicated as a blue dotted line.

selection cuts to be harmonised, and it is copiously produced in the LHCb acceptance. The presence of two muons in the final state means that $B_d^0 \to J/\psi K^{*0}$ tends to be triggered by a muon rather than a hadron, leading to a higher efficiency than for $B_s^0 \to K^{*0}\overline{K}^{*0}$. The differences in the trigger can be mitigated by only considering $B_d^0 \to J/\psi K^{*0}$ candidates where the trigger decision was not allowed to be based on muon triggers that use tracks from the decay itself.

The offline selection criteria for $B_d^0 \to J/\psi K^{*0}$ were designed to mimic those of $B_s^0 \to K^{*0}\overline{K}^{*0}$. In particular, all cuts related to the B_s^0 vertex definition were kept the same. Also the same GL as for the signal was used.

The knowledge of the selection and trigger efficiencies for both the signal and normalisation channels is also needed . The overall detection efficiency was factorised as $\epsilon^{sel} \times \epsilon^{trig}$. The first factor ϵ^{sel} is the probability of the generated tracks being accepted in the LHCb angular coverage, reconstructed, and selected. The second factor ϵ^{trig} defines the efficiency of the trigger on the selected events. Both are indicated in Table 5.2, as calculated from Monte Carlo simulation, along with the number of selected events. Note that the branching fraction measurement depends only on the ratios of efficiencies between signal and control channels.

The event yield for the selected data was determined from a fit to the $J/\psi K^+\pi^-$ invariant mass spectrum as shown in Fig. 5.6. In this fit, a constrained J/ψ mass was used in order to improve the B^0 mass resolution and therefore background rejection. A component for the particular background source $B_s^0 \to J/\psi\phi$, with $\phi \to K^+K^-$, was

Table 5.2: Selection and trigger efficiencies obtained from simulation. The observed yield found for the signal and control channels in the full mass range are also indicated. The efficiency errors are statistical, derived from the size of the simulated samples.

	ϵ^{sel} (%)	ϵ^{trig} (%)	Yield
$B_s^0 \to K^{*0}\overline{K}^{*0}$	0.370 ± 0.005	37.12 ± 0.39	42.5 ± 6.7
$B_d^0 \to J/\psi K^{*0}$	0.547 ± 0.007	31.16 ± 0.63	657 ± 27
ratio	0.678 ± 0.013	1.191 ± 0.027	0.065 ± 0.011

included in the fit, with a parameterisation defined from simulation, yielding the result 8±8 events. The complete suppression of this background was confirmed using the Armenteros-Podolanski [107] plot for the K^{*0} kinematics. The fit model also includes a Gaussian signal for the B^0 meson, a combinatorial background component parameterised with an exponential function and an additional component to account for partially reconstructed $B \to J/\psi X$ [108]. This partially reconstructed component can be described as

$$\rho(M, \overline{M}, \mu, \kappa) \propto \begin{cases} e^{-\frac{1}{2}(\frac{M-\overline{M}}{\kappa})^2} & \text{if } M > \mu; \\ e^{-\frac{1}{2}(\frac{\mu-\overline{M}}{\kappa})^2 + \frac{(\overline{M}-\mu)(M-\mu)}{\kappa^2}} & \text{if } M \leq \mu. \end{cases} \tag{5.7}$$

where the parameters μ, κ and $\overline{M}$ are allowed to float. The fitted signal according to this model is indicated in the third column of Table 5.2.

A small fraction of the selected sample contains two alternative candidates for the reconstructed event, which share three of the particles but differ in the fourth one. Those events, which amount to 3.8 % (3.7%) in the signal (control) channels, were retained for the determination of the branching fraction.

5.5.2 Branching fraction determination

The branching fraction of $B_s^0 \to K^{*0}\overline{K}^{*0}$ was calculated through the expression

$$\begin{aligned} \mathcal{B}\left(B_s^0 \to K^{*0}\overline{K}^{*0}\right) = \lambda_{f_L} \times \frac{\epsilon^{sel}_{B_d^0 \to J/\psi K^{*0}}}{\epsilon^{sel}_{B_s^0 \to K^{*0}\overline{K}^{*0}}} \\ \times \frac{\epsilon^{trig}_{B_d^0 \to J/\psi K^{*0}}}{\epsilon^{trig}_{B_s^0 \to K^{*0}\overline{K}^{*0}}} \times \frac{N_{B_s^0 \to K^{*0}\overline{K}^{*0}}}{N_{B_d^0 \to J/\psi K^{*0}}} \\ \times \mathcal{B}_{vis}(B_d^0 \to J/\psi K^{*0}) \times \frac{f_d}{f_s} \times \frac{9}{4}, \end{aligned} \tag{5.8}$$

where $\mathcal{B}_{vis}(B_d^0 \to J/\psi K^{*0})$, the visible branching ratio, is the product $\mathcal{B}(B_d^0 \to J/\psi K^{*0}) \times \mathcal{B}(J/\psi \to \mu^+\mu^-) \times \mathcal{B}(K^{*0} \to K^+\pi^-)$. The numerical value of $\mathcal{B}(B_d^0 \to J/\psi K^{*0}) = (1.33 \pm 0.06) \times 10^{-3}$ is taken from the world average in [16], $\mathcal{B}(J/\psi \to \mu^+\mu^-) = 0.0593 \pm 0.0006$ [16] and $\mathcal{B}(K^{*0} \to K^+\pi^-) = 2/3$ [16]. The ratio of b-quark hadronisation factors that accounts for the different production rate of B^0 and B_s^0 mesons is $f_s/f_d = 0.253 \pm 0.031$ [109]. The factor 9/4 is the inverse square of the 2/3 branching fraction of $K^{*0} \to K^+\pi^-$. The number of candidate events in the signal and control channel data samples are designated by $N_{B_s^0 \to K^{*0}\overline{K}^{*0}}$ and $N_{B_d^0 \to J/\psi K^{*0}}$.

The correction factor λ_{f_L} is motivated by the fact that the overall efficiency of the LHCb detector is a linear function of the K^{*0} longitudinal polarisation f_L. Taking into account the measured value and errors reported in section 5.4, Monte Carlo simulation was used to estimate $\lambda_{f_L} = 0.812 \pm 0.059$.

Two sources of systematic uncertainty associated to the ratio of selection efficiencies have been considered. The first source results from discrepancies between data and simulation in the variables related to track and vertex quality, and the second is related to particle identification. A small difference observed in the average impact parameter of the particles was corrected for by introducing an additional smearing to the track parameters in the simulation [110]. While the absolute efficiencies vary significantly as a function of vertex resolution, the ratio of efficiencies remains stable. We have assigned a 2% uncertainty to the ratio, after comparison between simulation and the $B_d^0 \to J/\psi K^{*0}$ data. The K/π identification efficiency was determined using a sample of $B_d^0 \to J/\psi K^{*0}$ events selected without making use of the RICH detectors. As the signal channel contains one more kaon than the control channel, a correction factor of 1.098 ± 0.019 was applied to the branching fraction, and a 2% error was assigned to it. The efficiency of muon identification agrees with simulation within 1.1% [111]. All these factors are combined to produce an overall systematic uncertainty of 3.4% in the ratio of selection efficiencies. The uncertainty in the background model in the B_s^0 mass fit (±2 events) contributes an additional systematic error of 4.7%.

Trigger efficiencies can be determined, for particular trigger paths in LHCb, using the data driven algorithm described in [112]. This algorithm could be applied for the specific hadronic triggers used for $B_d^0 \to J/\psi K^{*0}$, but not for the small $B_s^0 \to K^{*0}\overline{K}^{*0}$ signal. The efficiency related to cuts on global event properties, applied during the 2010 data taking, is determined from J/ψ minimum bias triggers [111]. The result indicates a trigger efficiency of $(26.8 \pm 3.8)\%$, smaller than the simulation result of $(31.16 \pm 0.63)\%$ shown in Table 5.2. Although these are consistent within uncertainties, we nonetheless apply a -9% correction to the ratio of trigger efficiencies between $B_d^0 \to J/\psi K^{*0}$ and $B_s^0 \to K^{*0}\overline{K}^{*0}$ channels, taking into account correlations in the trigger probability. A systematic error of 11% was assigned for the uncertainty on the trigger efficiency, entirely limited by statistics, both in the signal and control channels. Detector occupancies, estimated by the average number of reconstructed tracks, are larger by 10% in the data than in the simulation. This implies an additional correction of $+4.5\%$ to the ratio of efficiencies, since the control channel is observed to be more sensitive to occupancy than the signal channel.

An $\sim 8\%$ S-wave contribution under the K^{*0} resonance in the $B_d^0 \to J/\psi K^{*0}$ channel has been observed by BaBar [105], and the data in a ± 70 MeV/c^2 mass interval around the K^{*0} mass [113] yields a $(9.0 \pm 3.6)\%$ extrapolation to the ± 150 MeV/c^2 mass window. The S-wave background doubles for the K^{*0} $\overline{K}^{*0}$ final state, and it may certainly have a different coupling for both channels. Our direct measurement reported in Sect. 5.3.2 of $(19 \pm 9)\%$ is still lacking precision to be used for this purpose. When evaluating the branching fraction, we have assumed a 9% S-wave contribution, and assigned a systematic error of 50% to this hypothesis. A summary of the various contributions to the systematic error can be seen in Table 5.3.

Table 5.3: Estimated systematic error sources in the $\mathcal{B}\left(B_s^0 \to K^{*0}\overline{K}^{*0}\right)$ measurement.

Systematic effect	Error (%)
Trigger efficiency	11.0
Global angular acceptance	7.2
S-wave fraction	5.0
Background subtraction	4.7
$B_d^0 \to J/\psi K^{*0}$ and $J/\psi \to \mu\mu$ BR uncertainty	4.6
Selection efficiency	3.4
Total	15.9

The final result is

$$\begin{aligned}\mathcal{B}(B_s^0 \to K^{*0}\overline{K}^{*0}) = (2.81 &\pm 0.46 \text{ (stat.)} \\ &\pm 0.45 \text{ (syst.)} \\ &\pm 0.34 \text{ } (f_s/f_d)) \times 10^{-5}.\end{aligned}$$

As it has been explained at the end of section 5.4, unequal normalisation factors arise upon time integration of individual polarisation amplitudes with well defined *CP*-eigenvalues. This has the interesting implication that the time-integrated flavour-averaged branching fraction (B_1) as determined above cannot be directly compared with theoretical predictions solely formulated in terms of the decay amplitudes ${\mathcal{A}_L}^2 + {\mathcal{A}_\parallel}^2 + {\mathcal{A}_\perp}^2$ (B_0). Meson oscillation needs to be taken into account, since two distinct particles with different lifetimes are involved. Owing to the fact that $\mathcal{A}_\perp$ is *CP*-odd, the relationship between these quantities reads as follows

$$B_0 = B_1\left(1 + \frac{\Delta\Gamma}{2\Gamma}(f_L + f_\parallel - f_\perp)\right). \tag{5.9}$$

According to the measurements presented in Sect. 5.4 the quantity $f_L + f_\parallel - f_\perp$ can be calculated. The correction to the branching fraction is small (3% if current values are taken for $\Delta\Gamma$), and thus it has not been applied to the present measurement.

5.6 Results discussion

The $b \to s$ penguin decay $B_s^0 \to K^{*0}\overline{K}^{*0}$ has been observed for the first time. Using 37 pb^{-1} of *pp* collisions at 7 TeV centre-of-mass energy, LHCb has found 49.8 ± 7.5 signal events in the mass interval $\pm 50\,\text{MeV}/c^2$ around the B_s^0 mass. Analysis of the $K\pi$ mass spectra shows that most of the signal comes from $B_s^0 \to K^{*0}\overline{K}^{*0}$, with some S-wave contribution which could not be determined directly from data. The branching fraction has been measured, with the result $\mathcal{B}\left(B_s^0 \to K^{*0}\overline{K}^{*0}\right) = (2.81 \pm 0.46(\text{stat.}) \pm 0.45(\text{syst.}) \pm 0.34\,(f_s/f_d)) \times 10^{-5}$. The *CP*-averaged longitudinal K^{*0} polarisation fraction has also been measured to be $f_L = 0.31 \pm 0.12(\text{stat.}) \pm 0.04(\text{syst.})$, as well as the *CP*-odd component $f_\perp = 0.38 \pm 0.11(\text{stat.}) \pm 0.04(\text{syst.})$.

When this measurement is considered in association with that of [94], it is remarkable that the longitudinal polarisation of the K^{*0} mesons seems to be quite different between $B_s^0 \to K^{*0}\overline{K}^{*0}$ ($f_L = 0.31 \pm 0.12(\text{stat.}) \pm 0.04(\text{syst.})$) and $B^0 \to K^{*0}\overline{K}^{*0}$ ($f_L = 0.80^{+0.10}_{-0.12}(\text{stat.}) \pm 0.06(\text{syst.})$), despite the fact that the two decays are related by a U-spin rotation. However, the ratio of the branching ratios of B_s^0 and B^0 decays is consistent with $1/\lambda^2$ where λ is the Wolfenstein parameter, as expected.

6

Time-integrated angular analysis of $B_s^0 \to K^{*0}\overline{K}^{*0}$

After the discovery of the $B_s^0 \to K^{*0}\overline{K}^{*0}$ decay channel was established with the analysis described in the previous chapter, a more detailed study of this process was performed with a higher integrated luminosity data sample taken by LHCb during 2011. With this larger dataset, the full angular analysis is feasible allowing an accurate determination of the *S–wave* contributions in the $B_s^0 \to (K^+\pi^-)(K^-\pi^+)$ final state. Also, a search for physics beyond the Standard Model can be performed through the measurement of the eight *CP*-violating quantities accessible to this decay.

6.1 Introduction

One of the principal motivation of this work has been the search for possible New Physics components to electroweak phases in the amplitudes describing the decay $B_s \to K^+\pi^-K^-\pi^+$ in a mass window of ±150 MeV/c^2 around the $K^{*0}(892)$ resonance for both $K^+\pi^-$ and $K^-\pi^+$ systems. As explained in Chapter 4, six amplitudes are needed to describe such a transition, which is dominated by the $B_s^0 \to K^{*0}(892)\overline{K}^{*0}(892)$ (vector-vector or VV) and the $B_s^0 \to K_0^*(800)\overline{K}^{*0}(892)$[1] (scalar-vector or SV) final states.

In an untagged and time integrated analysis, to which this study with only 1 fb^{-1} has been restricted, *CP*-violation and *T*-violation may be observable in 4 triple products and 4 direct-like *CP* asymmetries measurable from the interference terms [8]. These terms involve the two *CP*-odd amplitudes $A_\perp$ (VV) and A_s^+ (SV).

Additionally, the full angular and mass analysis of the 4-body final state is presented. The objective is to determine all magnitudes and measurable phases of the amplitudes $A_0, A_\parallel, A_\perp, A_s^+, A_s^-$, and A_{ss}, under the assumption, supported by the triple product analysis in Sect. 6.7, that the *CP*-violating terms are negligible. Taking into account these results, a determination of the branching fraction of the VV mode is also provided.

Particularly relevant to this analysis has been the measurement of the longitudinal fraction of the $K^{*0}(892)$ polarisation, and the magnitude of the overall S-wave contribution. Important theoretical activity has been generated in relation to $B_s \to K^{*0}\bar{K}^{*0}$

---

[1] This notation refers to both *CP*-conjugated final states: $B_s^0 \to K_0^*(800)\overline{K}^{*0}(892)$ and $B_s^0 \to K^{*0}(892)\overline{K_0^*}(800)$. Also, throughout this chapter the scalar contribution will be referred to as $K_0^*(800)$, which is nonetheless calculated as a superposition of a broad low mass structure and a $K_0^*(1430)$ relativistic amplitude.

decays and their potentiality for *CP*-violation analysis [4–6, 44], and additional studies have been issued more recently that include the scalar final states [114].

6.2 Data sample and Monte Carlo simulation

The analysis presented in this chapter is based on the data taken by LHCb during 2011. This data sample corresponds to 1 fb^{-1} of pp collisions at a centre-of-mass energy of $\sqrt{s} = 7$ TeV. Events have been reconstructed using Brunel v41r1 and analysed using DaVinci v29r2, as corresponds to the `Reco12-Stripping17` campaign.

The Monte Carlo samples used in this analysis belong to the MC11a generation. They correspond to the decay channels $B_s^0 \to K^{*0}\overline{K}^{*0}$ and $B^0 \to \phi K^{*0}$. For this simulation, the pp interactions per crossing $\nu = 2.0$, which corresponds to an average number of visible interactions per crossing $\mu = 1.4$. The samples were generated using the Gauss release v41r2 (which uses GEANT4 v94r2p1.p02 for the detector simulation), and reconstructed using Boole v23r1 and Brunel v41r1p1.

6.3 Event selection and Signal Yield

In this section, the selection requirements used to discriminate the $B_s^0 \to K^{*0}\overline{K}^{*0}$ signal from the background are presented, together with the study of specific B decays that could contaminate the selected sample due to its similarities with the signal. Finally, the study of the invariant mass of the four particles in the final state is described and the number of $B_s^0 \to (K^+\pi^-)(K^-\pi^+)$ candidates is measured.

6.3.1 Event selection

Events fulfilling the requirements in the `StrippingBs2Kst0Kst0Line` selection, coming from any physics trigger line[1], were considered. Then, an offline selection very similar to the one used in Sect. 5.2.2 was applied. Table 6.1 shows the relevant decisions in each step of the trigger. Stripping and offline selections requirements are summarized in Table 6.2.

Table 6.1: Trigger lines used for $B_s^0 \to K^{*0}\overline{K}^{*0}$ selection.

Trigger level	Trigger lines
L0	`L0Global_Decision`
Hlt1	`Hlt1Phys_Decision`
Hlt2	`Hlt2Phys_Decision`

To improve the signal significance a Geometrical Likelihood (GL) was introduced after the cuts indicated above. The GL was trained using truth-matched $B_s^0 \to K^{*0}\overline{K}^{*0}$ MC events as signal, from the MC11a generation. As background, a sample of ~ 2 pb^{-1} of 2010 data selected through the same stripping line was used. The signal region is excluded from the background sample by imposing $|M(K\pi K\pi) - m_{B_s^0}| > 30$ MeV/c^2. The variables combined into the GL are:

---

[1] This means that the candidates do not need to follow any specific trigger path.

Table 6.2: The signal selection requirements are indicated. The IPχ^2 is defined as the variation in the fit χ^2 for a given vertex (in this case it refers to the PV) reconstructed with and without the considered track. The B_s^0 meson candidate flight distance significance (FDS), is defined as FD/σ_{FD}, where FD is the distance between the PV and the B_s^0 decay vertex and σ_{FD} is the uncertainty in the determination of that distance. B_s^0 DOCA is the distance of closest approach between the K^{*0} and the $\overline{K}^{*0}$ trajectories. DLL$_{a-b}$ denotes the logarithm of the ratio between the probabilities of hypothesis a and b. The last two columns indicates the offline selection cuts, those on the right were applied after the GL definition.

	Stripping selection	Offline selection	
All tracks p_T	> 500 MeV		
All tracks IPχ^2	> 9		
All tracks χ^2		< 5	
$K^{\pm}$ DLL$_{K\pi}$	> -5	> 2	> 10
$K^{\pm}$ DLL$_{p-K}$			< 10
$\pi^{\pm}$ DLL$_{K-\pi}$	< 10	< 0	
K^{*0} mass window	± 150 MeV		
K^{*0} p_t	> 900 MeV		
K^{*0} vertex χ^2	< 9		
B$_s$ mass window	± 500 MeV		
B$_s$ DOCA	< 0.3 mm		
B$_s$ vertex χ^2/ndof	< 15	< 5	
B$_s$ FDS		> 15	
B$_s$ IPχ^2	< 25		
$B_s^0 \to K^{*0}\overline{K}^{*0}$ GL			> 0.14

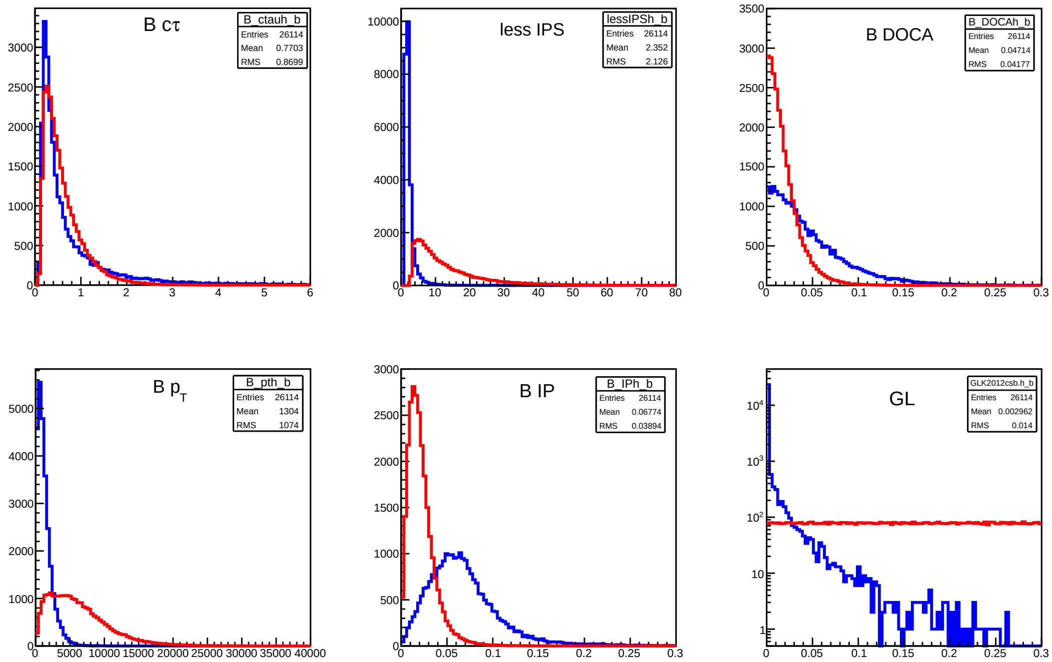

Figure 6.1: Signal (red) and background (blue) samples distribution in the different variables entering the definition of the Geometrical Likelihood discriminator and the GL itself.

- Lifetime of the B_s^0 candidate,
- Minimum $IP\chi^2$ of the four daughters track with respect to any the primary vertex,
- B_s^0 impact parameter,
- DOCA between the two K^{*0} candidates,
- p_T of the B.

Fig. 6.1 shows the signal and background distribution in these variables together with the response of the calculated GL for signal and background. As expected the GL distribution is flat for the signal and clusters near 0 for the background. The optimal GL cut was obtained by maximizing $\frac{S}{\sqrt{S+B}}$ for 500 $B_s^0 \to K^{*0}\overline{K}^{*0}$ expected events and 5000 background events, quantities chosen to approximate the S/B ratio expected after the rectangular-cut selection. The obtained result is ~ 0.14, see Fig. 6.2.

The selection requirements and the GL definition presented here are similar to those used in the analysis of 2011 data. The performace of the overall selection is therefore similar to what was dicussed in sec:ana$_2$010.

After the full selection, multiple candidates per event are very rare. Only one event in the final sample show two different candidates. For the subsequent analysis one of them was randomly discarded.

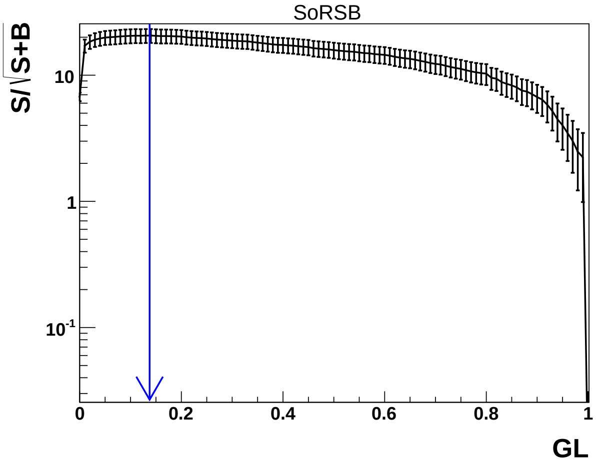

Figure 6.2: $S/\sqrt{S+B}$ as a function of the GL cut. The optimal GL cut was found to be ~ 0.14 and is idicated by the blue arrow in the plot.

6.3.2 Specific backgrounds

The need to keep a relatively wide mass window around the K^{*0} resonance, could allow peaking contribution from specific modes in the selected sample, mainly coming through the mis-identification of one of the four particles in the final state. Harder PID cuts have been applied in order to veto these crossfeeds, since in most cases there is no precise knowledge about their angular distribution.

$B^0 \to \rho K^{*0}$ decays are likely to be selected when a pion from the ρ decay is misidentified as a kaon. Fig. 6.3 shows the four body invariant mass (in the $K\pi K\pi$ hypothesis) of the events selected with different requirements in the $DLL_{k-\pi}$ of the kaon candidates. Events with smaller values of this discriminant tend to accumulate in the region between the B_s^0 and B^0 nominal masses, where the contribution from $B^0 \to \rho K^{*0}$ is expected. A sample of ~ 2 million Monte Carlo simulated $B^0 \to \rho K^{*0}$ events was analysed in order to estimate the expected size of this contribution in our dataset for different values of the $DLL_{k-\pi}$ cut. Requiring the $DLL_{k-\pi}$ of the kaons in the event to be greater than 10, only 10 events survive. By normalising to $B^0 \to \phi K^{*0}$ (following the same procedure that will be discussed in Sect. 6.6 for signal), the number of $B^0 \to \rho K^{*0}$ events expected in the signal region was estimated to be 3.5 ± 1.6 (8.9 ± 3.5 in the full mass range).

Another possible peaking contamination comes from $B^0 \to \phi K^{*0}$ decays when a kaon from the ϕ decay is identified as a pion. No specific PID cut is applied to reject this kind of events, since their contribution is expected in the low mass sideband, far from the B_s^0 signal region. Fig. 6.6(b) in the next section shows the invariant mass distribution under the $K\pi K\pi$ mass hypotheses, of $B^0 \to \phi K^{*0}$ Monte Carlo simulated events selected using the requirements in Table 6.2 (with the exception of the PID cuts in the mis-identified kaon).

Finally, a possible specific background coming from $\Lambda_b \to p\pi K\pi$ decays has also been identified. Although this mode has not yet been discovered, if a proton from such a decay were misidentified as a kaon, these events would accumulate between the mass of the B_s^0 and the mass of the Λ_b. Fig. 6.4 shows the scatter plot of the four body invariant mass evaluated under the proton (antiproton) mass hypothesis or the K^+ (K^-) mass

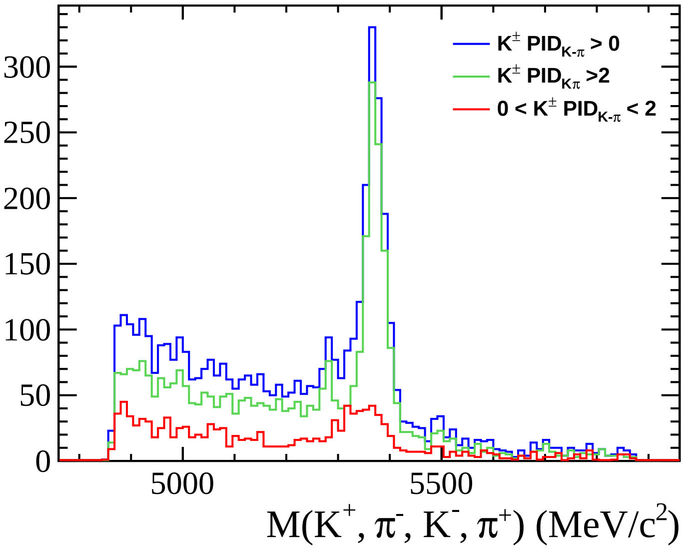

Figure 6.3: Invariant mass of the four particles in the final state for different cuts in the $PID_{K-\pi}$ of the kaon candidates.

hypothesis. The contaminating signal becomes evident when the RICH detector is used. In order to reject this source of background, the difference between the probabilities of proton and kaon hypothesis is required to be $DLL_{p-K} < 10$.

6.3.3 Four body mass fit

After the selection explained above an unbinned maximum likelihood fit was performed to the mass spectrum of the selected $K^+\pi^-K^-\pi^+$ candidates. The signal is modeled by a combination of two Crystal Ball distributions [106] that share a common mean and width. Their relative fraction and the parameters describing both tails (below and above a certain threshold) are extracted from a fit to $B_s^0 \to K^{*0}\overline{K}^{*0}$ simulated data, see Fig. 6.5, and fixed in the fit to the data. The low mass tail of the distribution accounts for events that undergo final state radiation while the high mass tail is present due to events reconstructed with lower resolution. We use this parametrisation to describe both B_s^0 and B^0 signals. The mass difference between B_s^0 and B^0 is fixed to the value calculated from [16]. The remaining two parameters (the mass of B_s^0 and a common width for B_s^0 and B^0 mesons) are determined from the fit.

Even though the contribution from the different crossfeed backgrounds considered in the previous section is suppressed by the PID cuts, a parameterisation for each of them has been included in the fit and the fraction of each mode with respect to the total number of background events, N_{bkg}, is allowed to float in the minimisation:

- $B^0 \to \rho K^{*0}$ events are parameterised using a Crystal Ball distribution. The parameters of the distribution are extracted from a fit to data. A very tight selection was applied to isolate $B^0 \to \rho K^{*0}$ signal (see Appendix B). Fig. 6.6(a) shows the invariant mass of the four particles in the final state under the $K\pi K\pi$ mass hypothesis for this sample.

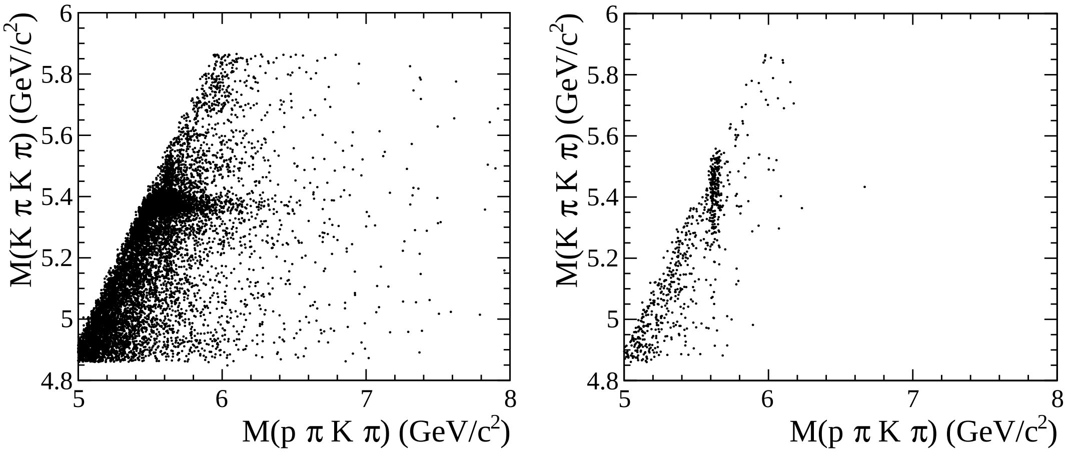

Figure 6.4: Left: Invariant mass of the four particles in the final state evaluated in the proton (antiproton) hypothesis versus the same mass in the K^+ (K^-) hypothesis when no p/K separation is attempted in the RICH detector. Right: The same scatter plot under the requirement $PID_{p-K} > 10$.

Table 6.3: Parameter values of the models describing the signal and the different peaking contributions taken into account in the invariant mass fit. The parameters α and n represent, respectively, the threshold and the order of the power law tail of the corresponding Crystal Ball distribution.

Parameter	$B_s^0 \to K^{*0}\overline{K}^{*0}$	$B^0 \to \rho K^{*0}$	$B^0 \to \phi K^{*0}$	$\Lambda_b^0 \to p\pi^-\overline{K}^{*0}$
μ (MeV/c^2)	5367.08 ± 0.11	5349.2 ± 1.6	5214.77 ± 0.69	5496.2 ± 1.6
σ (MeV/c^2)	14.418 ± 0.093	28.7 ± 1.3	19.70 ± 0.52	31.4 ± 1.0
α_1	1.71 ± 0.14	-0.86 ± 0.10	0.463 ± 0.025	0.306 ± 0.017
n_1	1.87 ± 0.12	8.8 ± 3.7	8.0 ± 1.1	3.82 ± 0.30
f_{CB1}	0.60 ± 0.14	1	0.987 ± 0.013	1
α_2	-2.00 ± 0.20	-	-0.49 ± 0.62	-
n_2	2.67 ± 0.61	-	4.0 ± 3.4	-

- $B^0 \to \phi K^{*0}$ contribution is modeled using a combination of two Crystal Ball distributions with parameters obtained from a fit to $B^0 \to \phi K^{*0}$ simulated events, see Fig. 6.6(b).

- Since no MC sample for $\Lambda_b^0 \to p\pi K\pi$ was available, a simplified four-momentum simulation for $\Lambda_b^0 \to (p\pi)\overline{K}^{*0}$ was used [115]. In it, the Λ_b momentum spectrum is taken from the one observed for B_s^0 in the full MC, and the 2-body phase-space is used to perform Λ_b decay into K^{*0} and a $p\pi$ system with the invariant mass observed in data. The resulting $M(K\pi K\pi)$ distribution, shown in figure Fig. 6.6(c), is modeled using a Crystal Ball distribution.

The parameters of these models are summarized in Table 6.3.

Additionaly, a modified ARGUS shape, i.e. a convolution of the ARGUS distribution [116] and a Gaussian, accounts for partially reconstructed B decays, and is described by:

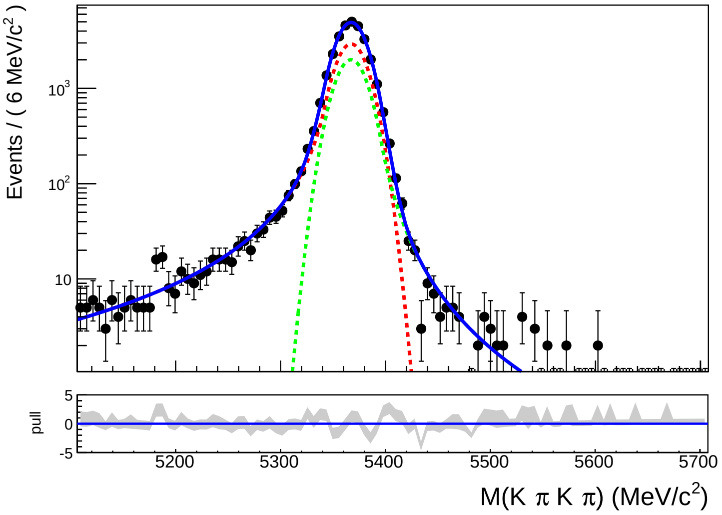

Figure 6.5: Fit to the four–body invariant mass spectrum of $B_s^0 \to K^{*0}\overline{K}^{*0}$ simulated data using the model described in the text, which contains a radiative component (red) and a high mass tail accounting for events reconstructed with low resolution (green).

$$f_P(m) \propto \cdot m' \left(1 - \frac{m'^2}{m_0^2}\right) \Theta(m_{PhysBkg} - m') e^{-k_{PhysBkg}\cdot m'} \otimes G(m - m'; \sigma) \tag{6.1}$$

where Θ is the Heaviside-step function, $\otimes$ stands for the convolution product, m' is the variable over which the convolution integral is calculated, $G(m - m'; \sigma_{PhysBkg})$ is a Gaussian p.d.f. with standard deviation $\sigma_{PhysBkg}$ representing the experimental resolution, which is forced to be the same as the signal one (σ). $m_{PhysBkg}$ and $k_{PhysBkg}$ determine the sape of the partially reconstructed background and are allowed to float during the minimisation. Finally, the combinatorial background is parameterised by a decreasing exponential with its slope (c_{comb}) floating in the fit.

By fitting this model to the mass spectrum of the $B_s^0 \to K^{*0}\overline{K}^{*0}$ selected candidates, the preferred value for the fraction of $B^0 \to \rho K^{*0}$ events hits the lower physical limit (by definition $f_{B^0\to\rho K^{*0}} \geq 0$). For the final result, the fraction of $B^0 \to \rho K^{*0}$ events is fixed to zero and the impact of a non-zero contribution from this decay is taken into account as a systematic uncertainty (see Sect. 6.6.5.1). The results of the fit to the four body mass spectrum are shown in Table 6.4. The fitted model is compared with data in Fig. 6.7.

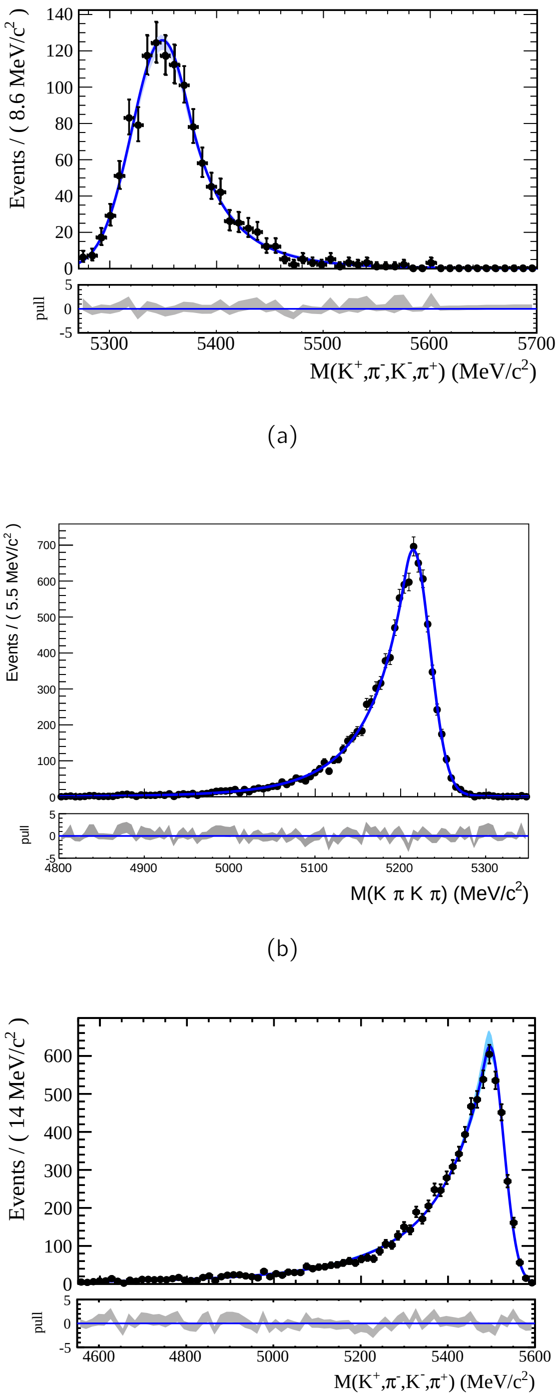

(a)

(b)

(c)

Figure 6.6: Parameterisation of the peaking backgrounds: (a) $B^0 \to \rho K^{*0}$ candidates selected from data when the mass hypothesis of one of the pions from the ρ decay is changed to the kaon hypothesis. (b) $B^0 \to \phi K^{*0}$ Monte Carlo simulated events when the mass hypothesis of one of the kaons from the ϕ decay is changed to the pion hypothesis. (c) ToyMC generated $\Lambda_b \to K^{*0} p \pi$ events when the mass hypothesis of the proton is changed into the kaon hypothesis.

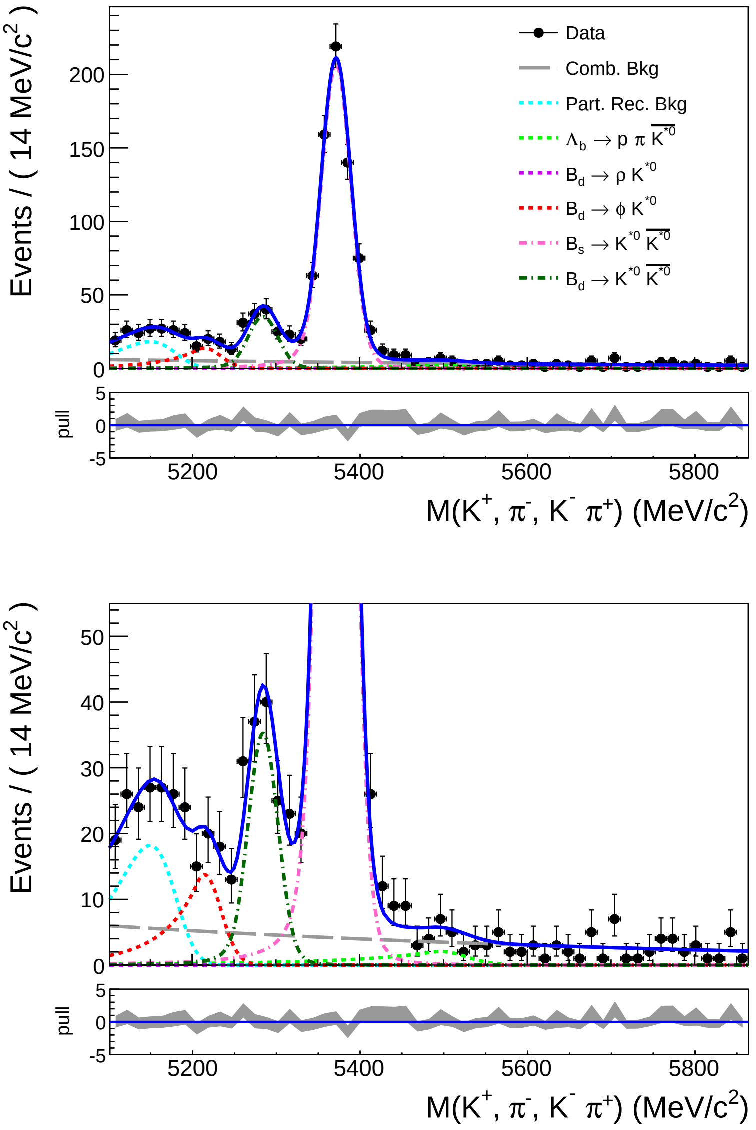

Figure 6.7: Results of the four-body invariant mass fit (top) and zoom around the low statistics region (bottom). The solid points represent the selected data and the blue solid line is the fitted model. The B_s^0 (B^0) signal peak is shown as a pink (dark green) dashed and dotted line. The different peaking background components are represented as dotted lines: $B^0 \to \phi K^{*0}$ (red), $\Lambda_b^0 \to p\pi^-\overline{K}^{*0}$ (green) and partially reconstructed decays (light blue). The grey dashed line is the combinatorial background component.

Table 6.4: Fitted values of the model parameters for the mass spectrum. N_s, N_d are the number of events for the B_s^0 and B^0 signals. $\mu_{B_s^0}$ and σ the mean and the resolution of the B_s^0 signal. $f_{PhysBkg}$, $f_{\Lambda_b \to p\pi K\pi}$ and $f_{B^0 \to \phi K^{*0}}$ are the fractions of each of the background sources refered to the total amount of background, N_{bkg}. The fraction of combinatorial background is $(1 - f_{PhysBkg} - f_{\Lambda_b \to p\pi K\pi} - f_{B^0 \to \phi K^{*0}})$.

Parameter	Fit Value
$\mu_{B_s^0}$ (MeV/c^2)	5371.81 ± 0.77
σ (MeV/c^2)	17.92 ± 0.77
N_s	697 ± 31
N_d	119 ± 20
N_{Bkg}	396 ± 36
$f_{\Lambda_b \to p\pi K\pi}$	0.061 ± 0.061
$f_{B^0 \to \phi K^{*0}}$	0.176 ± 0.075
$f_{PhysBkg}$	0.245 ± 0.087
c_{comb} (10^{-3}(MeV/c^2)$^{-1}$)	-1.4 ± 1.5
$k_{PhysBkg}$ (10^{-2}(MeV/c^2)$^{-1}$)	3.2 ± 2.1
$m_{PhysBkg}$ (MeV/c^2)	5189 ± 16

6.4 Acceptance effects

The detector geometry, the reconstruction and the selection of the signal candidates introduce characteristic effects that need to be taken into account whenever the modeling of the data is attempted. Thus the physical PDF presented in Sect. 4.1 must be corrected with a non-uniform efficiency function before it can be compared with data.

In the present analysis, this acceptance model was estimated using $B_s^0 \to K^{*0}\overline{K}^{*0}$ Monte Carlo simulated events. The most important feature in the acceptance is the drop at $\cos\theta_{(1,2)} \to +1$. In this limit, the π meson is produced in the direction opposite to the momentum of the K^{*0}, so its momentum is small and the efficiency of reconstructing the event decreases. In terms of the event selection, the requirement in the minimum transverse momentum (p_T) of the four final tracks is responsible for most of the effect, see Fig. 6.8.

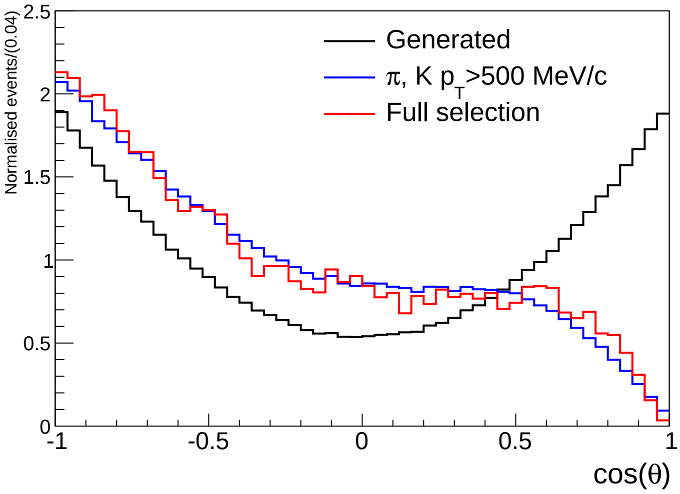

Figure 6.8: $\cos\theta_1$ distribution for MC simulated data applying different sets of cuts. The blue points represent events with K and π transverse momentum greater than 500 MeV/c. The red line corresponds to events passing the full selection described in Sect. 6.3.1.

The way the events have been triggered has an effect in the acceptance. Signal candidates are accepted at each stage of the trigger (L0, HLT1 or HLT2) if one of the final state particles fulfils the requirements of that particular stage. Additionally, events can also be retained when the particle responsible for the positive trigger decision is any other particle in the event. A different acceptance function is expected for events selected in each way. To take this into account, the MC sample was separated into two subsets: events that triggered on signal for every trigger level (TOS) and the rest of the sample (non-TOS), and a different acceptance function was calculated for each of these subsamples. In the following, two acceptance functions are always determined separately using TOS and non-TOS events.

The factorisation of the acceptance function was also studied. Due to the limited MC statistics available, attention was focused on possible correlations between the acceptance in $\cos\theta_{1(2)}$ and $m_{1(2)}$. The angular acceptance could be different in various regions of the $K\pi$ mass spectrum. In principle, the higher the mass, the broader the momentum of the pions and the smaller the drop of the acceptance at $\cos\theta \to 1$. However, looking at

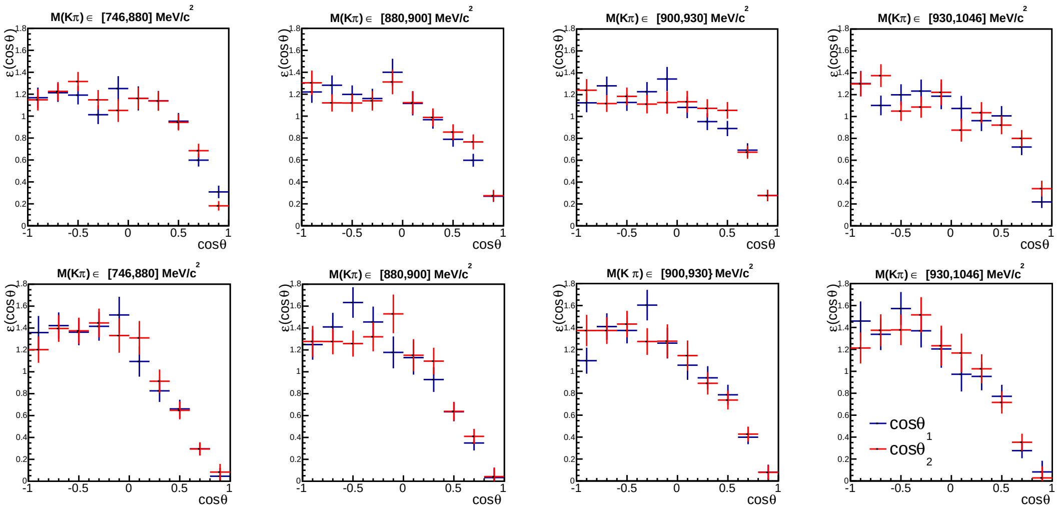

Figure 6.9: Acceptance as a function of $cos\theta_1$ ($cos\theta_2$) calculated in different $M(K^+\pi^-)$ ($M(K^-\pi^+)$) bins for TOS (top) and non-TOS (bottom) simulated events.

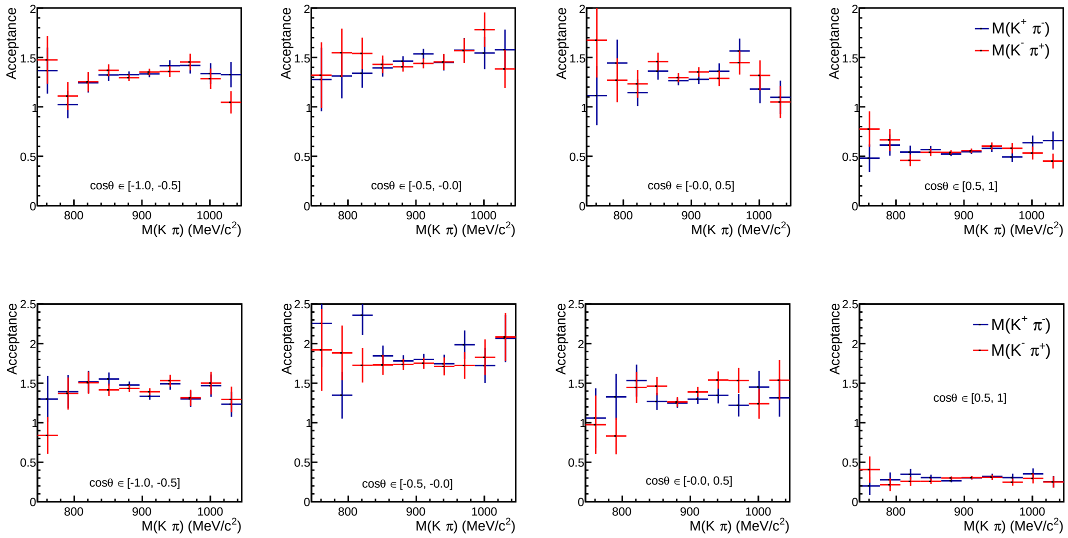

Figure 6.10: Acceptance as a function of the $K^+\pi^-$ ($K^-\pi^+$) invariant mass calculated in different bins of $\cos\theta_1$ ($\cos\theta_2$) for TOS (top) and non-TOS (bottom) simulated events.

Fig. 6.9, where the $\cos\theta$ projection of the acceptance for diferent bins in the $K\pi$ invariant mass is shown, no systematic evolution of the angular efficiency with the mass is visible. This effect is confirmed when the sample is separated according to the trigger configuration. Fig. 6.10, shows the mass acceptance in bins of $\cos\theta$ for TOS and non-TOS events. Again, no significant correlation between the acceptance in these two variables was found. The acceptance model is assumed then to be factorizable in the angular variables and the masses –acceptance function in φ will be shown to be compatible with a constant function in Sect. 6.4.1– for the mass window under study. Nevertheless, crosschecks with more general acceptance models were performed in order to assess the systematic uncertainties related with this assumption.

6.4.1 Angular Acceptance

The shape of the acceptance as a function of the three angular variables ($\cos\theta_1$, $\cos\theta_2$ and φ) has been calculated as a ratio between the angular distribution of the reconstructed MC-simulated data and the angular distribution expected from (4.18) for the parameter values

$$\begin{aligned} |A_0|^2 &= 0.64 \qquad \delta_{\|} = 3.14 \\ |A_{\|}|^2 &= 0.25 \qquad \delta_{\perp} = 3.14 \\ |A^+|^2 &= |A^-|^2 = |A_{ss}|^2 = 0 \end{aligned} \tag{6.2}$$

used at the generator level. The $\cos\theta_{1,2} - \varphi$ and φ projections of this 3D acceptance for TOS and non-TOS events are shown in Fig. 6.11. The acceptance as a function of the φ angles is found to be compatible with a flat function, the χ^2/ndf of the fit to a flat function is 7.872/9 (6.564/9) for TOS (non-TOS) samples.

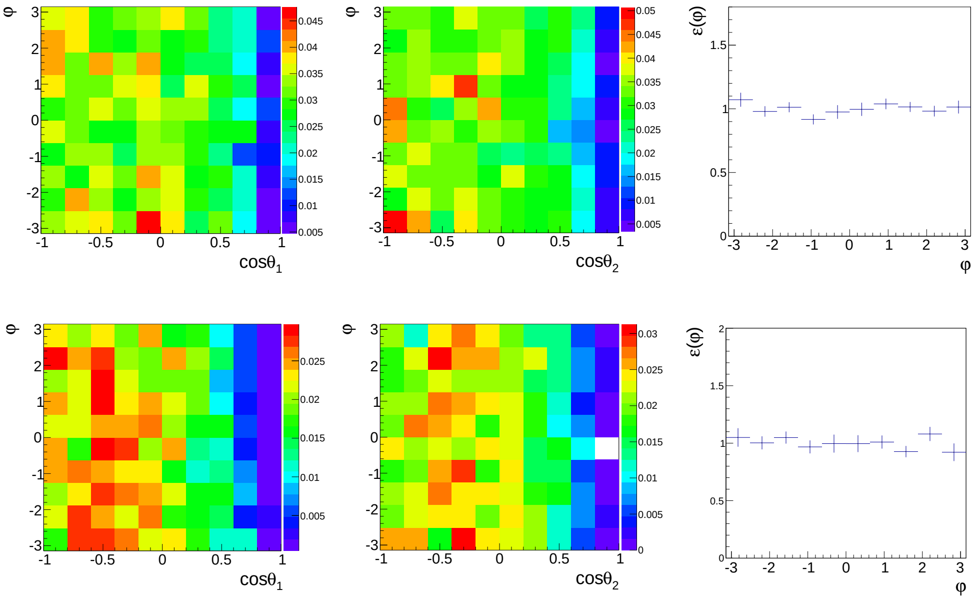

Figure 6.11: Projections of the 3D acceptance for TOS (top) and non-TOS (bottom).

Consequently the angular acceptance model used in the fit to the real data is a 2D histogram ($\cos\theta_1 \times \cos\theta_2$) obtained from the ratio between reconstructed and generated MC-simulated data distributions.

6.4.2 $M(K\pi)$ Acceptance

The average of the different $M(K\pi)$ acceptance functions shown in Fig. 6.10 was used to study the dependence of the acceptance with this variable. Fig. 6.12 shows this average for the TOS and non-TOS samples. A first order polynomial was fit to each of the histograms. As in both cases the slope of the fitted function is found to be compatible with zero, the acceptance function in the two body invariant mass is assumed to be flat.

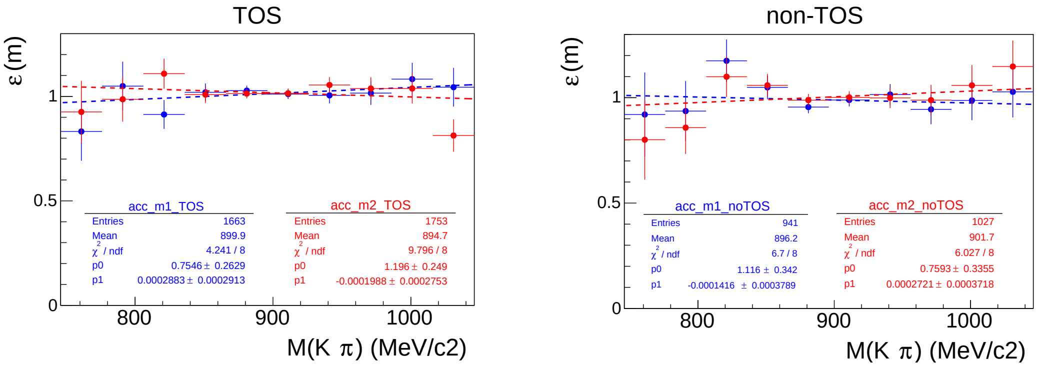

Figure 6.12: Acceptance as a function of $M(K\pi)$ for events in the TOS (left) and non-TOS (right) samples. The blue (red) points correspond to the invariant mass of the $K^+\pi^-$ ($K^-\pi^+$) combination or m_1(m_2). The result of a linear fit performed for each of the histograms is also presented as a dashed line.

6.4.3 MC-Data corrections

The angular acceptance has been corrected to take into account differences between data and MC simulation in the distribution of various observables. The efficiency of the PID requirements is obtained from data. High statistics samples of genuine $K^\pm$, $\pi^\pm$, p and $\bar{\text{p}}$ tracks are selected independently of the RICH information through purely kinematic selections. Some of these samples, of extremely high purity, are: $K^0_S \to \pi^+\pi^-$, $\Lambda \to p\pi^-$ and $D^{*+} \to D^0(K^-\pi^+)\pi^+$ [68]. Using such control samples the efficiency of each of the DLL cuts is then calculated in bins of the particle momentum and pseudorapidity. The results are shown in Fig. 6.13. The MC is reweighted using these efficiencies and the angular acceptance is recalculated. Fig. 6.14 shows the comparison between the $\cos\theta$ acceptance calculated before (relying on the MC description of the PID requirements effects) and after the correction. The reweighting causes a slight acceptance increase in the region $\cos\theta \sim -1$.

As it has been shown, the acceptance drop at $\cos\theta \sim 1$ is mainly caused by the cut in the p_{T} of kaons and pions. Differences in the p_{T} distributions of data and MC could therefore have a strong effect in the angular acceptance. The main discrepancy is observed in the p_{T} distributions of the positive and negative pions in the final state.

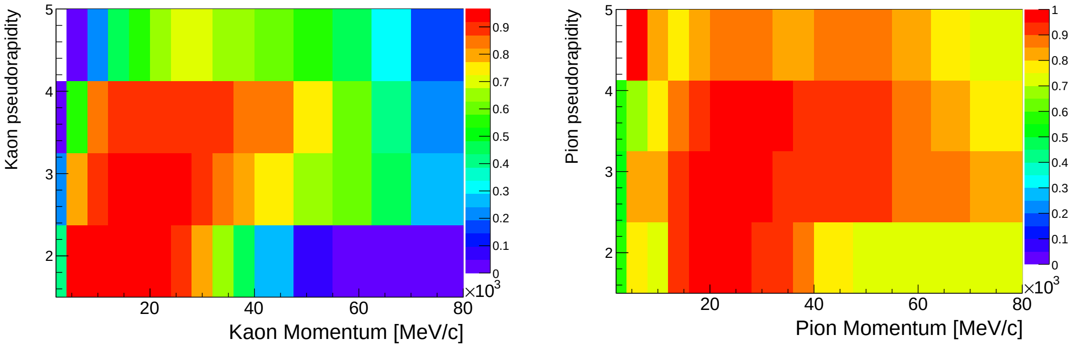

Figure 6.13: Efficiency of the PID selection of kaons and pions in $B_s^0 \to K^{*0}\overline{K}^{*0}$ candidates as a function of pseudorapidity.

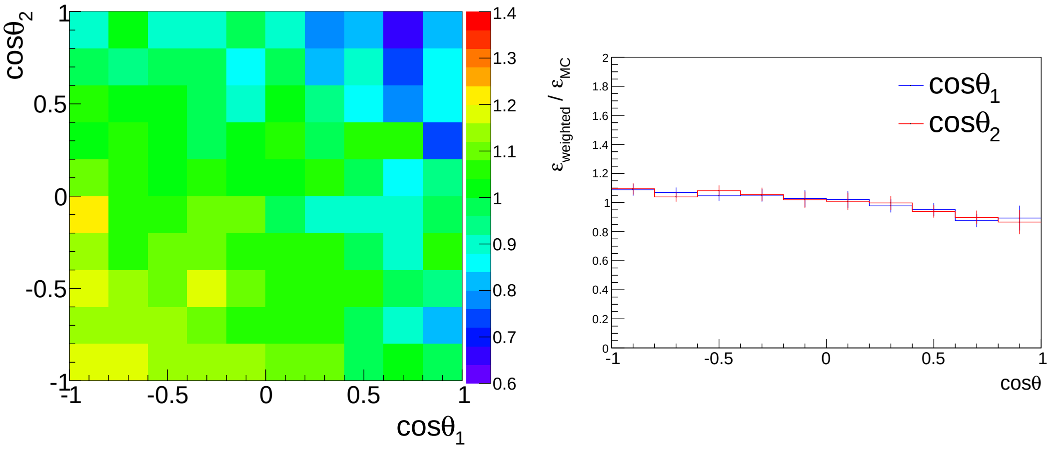

Figure 6.14: Effect of reweighting the MC sample according to the PID selection efficiencies calculated in data.

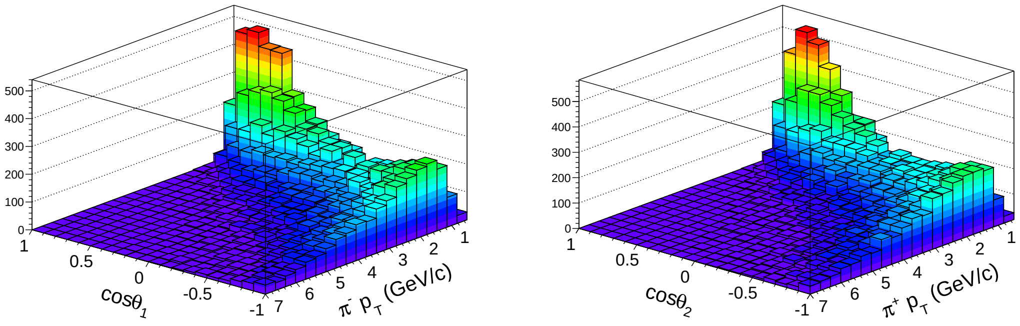

Figure 6.15: $\cos\theta$ distribution of the MC simulated data as a function of the transverse momentum of the pion.

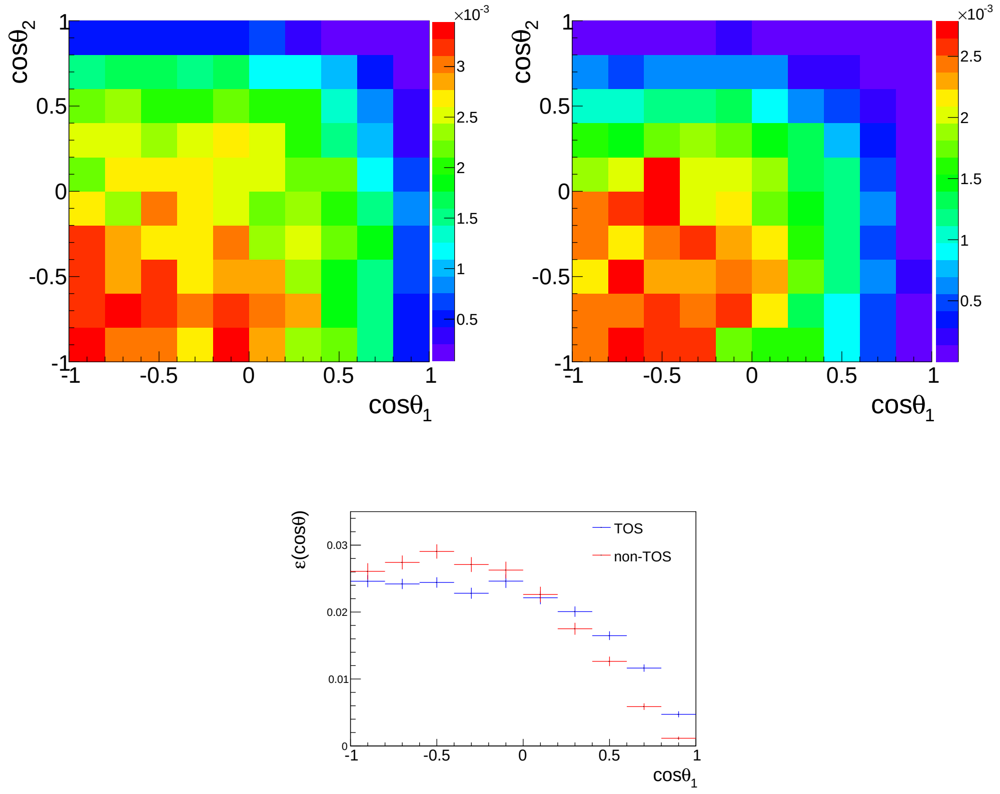

Figure 6.16: Top: Angular acceptance functions for TOS (left) and non-TOS (right) events calculated from $B_s^0 \to K^{*0}\overline{K}^{*0}$ Monte Carlo simulated data after reweighting with PID efficiencies observed in data. Bottom: $cos\theta_1$ projection of the TOS (blue) and non-TOS (red) acceptance functions.

However, this variable is strongly correlated with the angular distribution, as can be seen in Fig. 6.15 where the distribution of the MC simulated events in the plane cos(θ) - $p_{\mathrm{T,ß}}$ is shown. The Monte Carlo for $B_s^0 \to K^{*0}\overline{K}^{*0}$ was generated with a certain set of polarisation amplitudes and phases that may not agree with those observed in data. This has no effect on the calculated acceptance corrections but it could, however, induce differences between data and MC in some kinematic variables, for instance, the p_{T} of the daughter tracks. This could occur, for example, through the presence of S-wave in the data which is not present in the simulation. Still, genuine discrepancies between data and MC should be taken into account. In order not to overestimate these effects an iterative procedure is applied and a systematic uncertainty is assigned in Sect. 6.5.4.3.

To take into account the different proportion of TOS and non-TOS events in data and MC we will perform a simultaneous fit to TOS and non-TOS data aplying a different acceptance correction to each sample. Both acceptance functions are shown in Fig. 6.16.

6.5 Amplitude Analysis

The magnitude and phase of the different amplitudes contributing to the $B_s^0 \to K^{*0}\overline{K}^{*0}$ decay are determined using a 5D fit to the three helicity angles (Ω: $\cos\theta_1$, $\cos\theta_2$, φ) and the invariant mass of the two K-π pairs ($m_1 \equiv M(K^+\pi^-)$, $m_2 \equiv M(K^-\pi^+)$) of all the candidates with a four-body invariant mass $|M(K^+, \pi^-, K^-, \pi^+) - m_{B_s^0}| < 30\,\mathrm{MeV}/c^2$.

6.5.1 The 5-D model

The model used to describe the distribution of data in this five variables is given by

$$\mathcal{F}(\Omega, m1, m2) = (1 - f_{bkg})PDF(\Omega, m1, m2) \times \varepsilon(\Omega, m1, m2) + f_{bkg}PDF_{bkg}(\Omega, m1, m2) \tag{6.3}$$

where $PDF(\Omega, m1, m2)$ is the probability density function given by (4.18), $\varepsilon(\Omega, m1, m2)$ is the acceptance function describing the effects introduced by the data reconstruction, selection and triggering, and $PDF_{bkg}(\Omega, m1, m2)$ describes de distribution of the background, which is a fraction f_{bkg} of the full dataset.

In order to avoid non-physical values of the parameters during the minimisation, some of them have been rewritten as follows

$$\begin{aligned} f_\parallel &= x_\parallel \cdot (1 - f_L) \\ |A_s^+|^2 &= x_s^+ \cdot (1 - |A_s^-|^2) \\ |A_{ss}|^2 &= x_{ss} \cdot (1 - |A_s^-|^2 - |A_s^+|^2) \end{aligned} \tag{6.4}$$

where $x(f_\parallel)$, $x(|A_s^+|^2)$ and $x(|A_{ss}|^2)$ are free parameters allowed to float within (0,1), ensuring that the sum of all the squared amplitudes is never greater than 1. Consequently, the free parameters in the fit to the data are: f_L, $x_\parallel$, $|A_s^-|^2$, x_s^+, x_{ss}, $\delta_\parallel$, $(\delta_\perp - \delta_s^+)$, δ_s^-, δ_{ss}; where the usual definition of the polarisation fractions in $B_s^0 \to K^{*0}\overline{K}^{*0}$,

$$f_L = \frac{|A_0|^2}{|A_0|^2 + |A_\parallel|^2 + |A_\perp|^2} \qquad f_{\parallel,\perp} = \frac{|A_{\parallel,\perp}|^2}{|A_0|^2 + |A_\parallel|^2 + |A_\perp|^2} \tag{6.5}$$

has been assumed. Note that only the phase difference $(\delta_\perp - \delta_s^+)$ is accesible to the untagged analysis.

6.5.1.1 Background

The expected background fraction in the $\pm 30\,\mathrm{MeV}/c^2$ mass window around the B_s^0 mass is estimated from the mass fit to be $(2.64\pm0.27)\%$ for the TOS sample and $(4.53\pm0.52)\%$ in the non-TOS sample. The distribution of the background in the three angles and two masses is extracted from the events in the *right-hand* B_s^0 mass sideband ($[5550, 5700]$ MeV/c^2) with lower GL values (GL> 0.01), see Fig. 6.17. We parameterise the background component as the factorised product

$$p.d.f._{Bkg}(\Omega, m1, m2) = M_{Bkg}(m1) \times M_{Bkg}(m2) \times F_{Bkg}(\theta_1) \times F_{Bkg}(\theta_2) \tag{6.6}$$

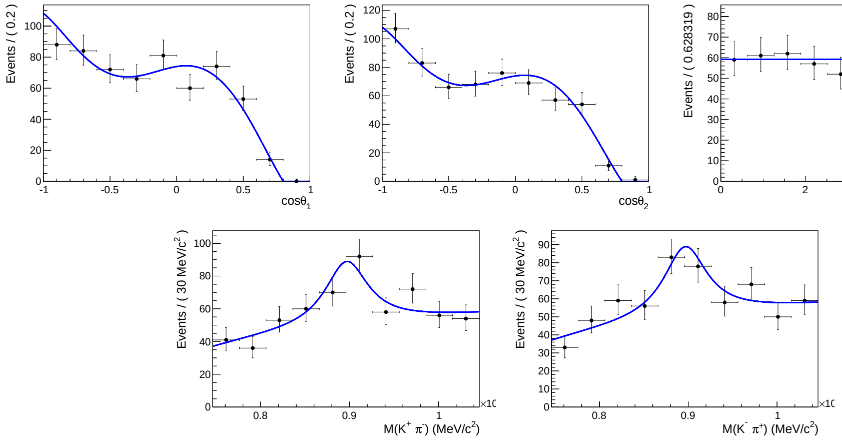

Figure 6.17: Angular and masses distributions of events in the sideband defined in the text. The blue line is the projection of the fitted background parameterisation.

with

$$
\begin{aligned}
M_{Bkg}(m) &= f_{\mathcal{B}}|\mathcal{M}_1(m)|^2 + (1-f_{\mathcal{B}})\log(\lambda^{bkg}m) \\
F_{Bkg}(\cos\theta) &= \begin{cases} 1+\sum_1^5 c_i^{bkg}(\cos\theta)^i & if \cos\theta < 0.8 \\ \quad 0 & if \cos\theta > 0.8 \end{cases}
\end{aligned} \qquad (6.7)
$$

where $\mathcal{M}(m1)$ is the spin-1 Breit-Wigner propagator defined in Sect. 4.3.1.1, and describe background candidates containing real K^{*0} mesons. The fraction of these events with respect to the total is represented by $f_{\mathcal{B}}$. The background distribution in φ is compatible with being flat. The result of this fit is shown in Table 6.5.

Table 6.5: Values of the parameters in the p.d.f. of the background component obtained from the fit to the events in the sideband.

Parameter	Value
$f_{\mathcal{B}}$	$0.182^{+0.032}_{-0.059}$
λ^{bkg}	$(-2.3 \pm 4.2) \times 10^{-4}(\text{MeV}/c^2)^{-1}$
c_1^{bkg}	0.18 ± 0.20
c_2^{bkg}	$-1.05^{+0.31}_{-0.27}$
c_3^{bkg}	-2.30 ± 0.89
c_4^{bkg}	0.68 ± 0.42
c_5^{bkg}	1.28 ± 0.76

Additionally, the $sFit$ formalism was also tried to describe the background. The results can be found in Appendix 6.5.3.4 and are compatible with those obtained using the $cFit$ approach.

6.5.2 Fit results

Using the model described above, an unbinned maximun likelihood fit has been performed simultaneously for TOS and non-TOS $B_s^0 \to K^{*0}\overline{K}^{*0}$ candidates with $|M(K^+,\pi^-,K^-,\pi^+) - m_{B_s^0}| < 30\,\mathrm{MeV}/c^2$. As already mentioned, the background fraction has been fixed to the one obtained from the fit to the $K\pi K\pi$ invariant mass spectrum.

The results of the fit are summarized in table 6.6. Fig. 6.18 shows the different projections of the fit. The evolution of the forward-backward asymmetry with the $K\pi$ invariant mass becomes more clear in Fig. 6.19, where the $\cos\theta_1$ ($\cos\theta_2$) distribution is shown for different bins of m_1 (m_2).

A low value of the longitudinal porlarisation fraction of the vector-vector component is measured. This results is compatible with that obtained in Sect. 5.4, and therefore still significantly smaller than the longitudinal polarisation fraction measured by BaBar for the U-spin rotated decay, $B^0 \to K^{*0}\overline{K}^{*0}$. Furthermore, the overall contribution of the *S–wave* amplitudes is found to be large, $|A_s^+|^2 + |A_s^-|^2 + |A_{ss}|^2 = 0.665 \pm 0.067$.

In Fig. 6.20, the profile likelihood[1] for the parameter f_L is given, showing parabolic behaviour around the minimum. Additionally, the (1-6 σ) contour between $|A_s^-|^2$ and f_L is shown in Fig. 6.21. No additional minimum with inverted values of $|A_s^-|^2$ and f_L, that would also describe the evolution of the forward backward asymmetry with the mass observed in data, is found.

Table 6.6: Results given by the simultaneous fit to $B_s^0 \to (K^+\pi^-)(K^-\pi^+)$ TOS and non-TOS candidates with $|M(K^+,\pi^-,K^-,\pi^+) - m_{B_s^0}| < 30\,\mathrm{MeV}/c^2$. The values of $f_\parallel$, $|A_s^+|^2$ and $|A_{ss}|^2$ are calculated, following (6.4), from the free parameters in the PDF, whose correlations have been taken into account in the error calculation.

Parameter	Value
f_L	0.201 ± 0.057
$x_\parallel$	0.269 ± 0.055
$\|A_s^-\|^2$	0.485 ± 0.051
x_s^+	0.222 ± 0.058
x_{ss}	0.164 ± 0.050
$\delta_\parallel$	5.31 ± 0.24
$\delta_\perp - \delta_s^+$	1.95 ± 0.21
δ_s^-	1.79 ± 0.19
δ_{ss}	1.06 ± 0.27
$f_\parallel$	0.215 ± 0.046
$\|A_s^+\|^2$	0.114 ± 0.037
$\|A_{ss}\|^2$	0.066 ± 0.022

---

[1] The profile likelihood for a particular parameter is obtained by minimising the likelihood with respect to the rest of the parameters, for each (fixed) value of the parameter of interest.

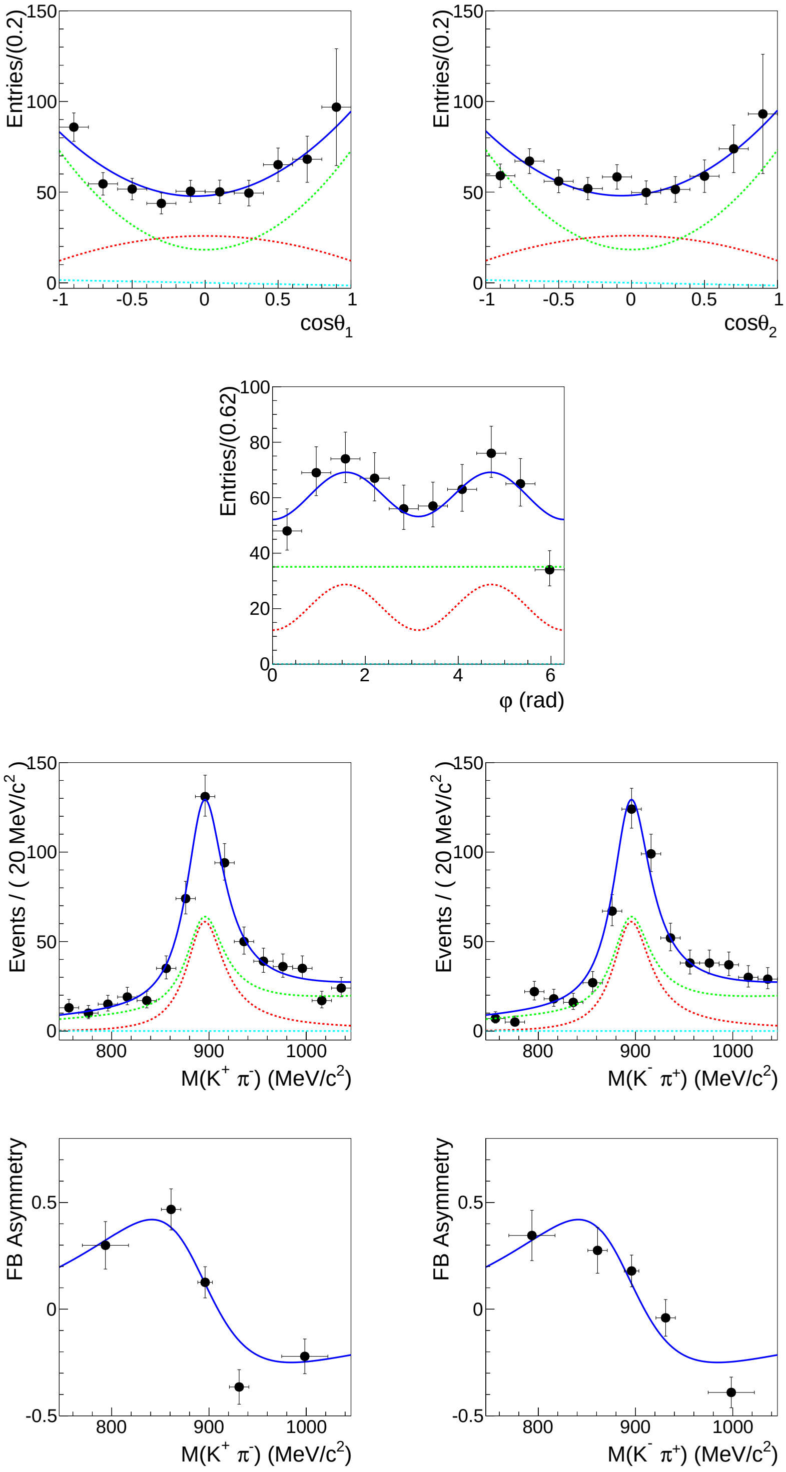

Figure 6.18: Projections of the model fitted to $B_s^0 \to (K^+\pi^-)(K^-\pi^+)$ data (blue solid line). The solid dots represent the selected data after the background component has been subtracted following (6.6) and the acceptance effect has been corrected. The red dashed line is the P-wave component, the green dashed line is the S-wave component and the light-blue dashed line represents the $\mathcal{A}_S^+\mathcal{A}_0$ interference term.

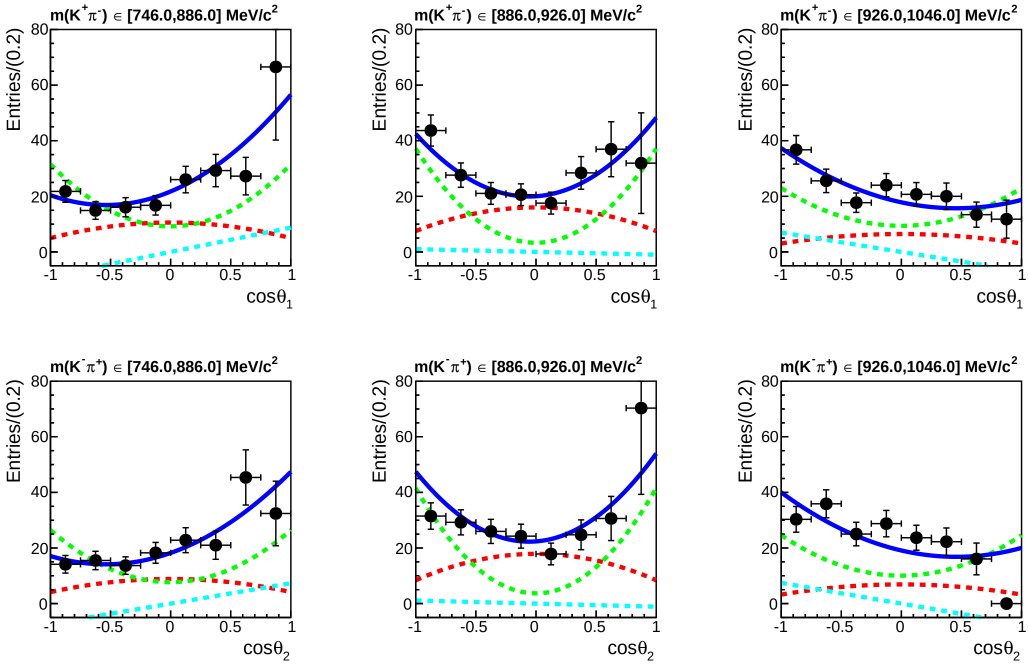

Figure 6.19: $\cos\theta_1$ (top) and $\cos\theta_2$ (bottom) distributions for different bins of m_1 and m_2 respectively. The solid dots represent the selected data after background subtraction and acceptance correction. The red dashed line is the *P–wave* component, the green dashed line is the *S–wave* component and the light-blue dashed line represents the $\mathcal{A}_S^{+}\mathcal{A}_0$ interference term.

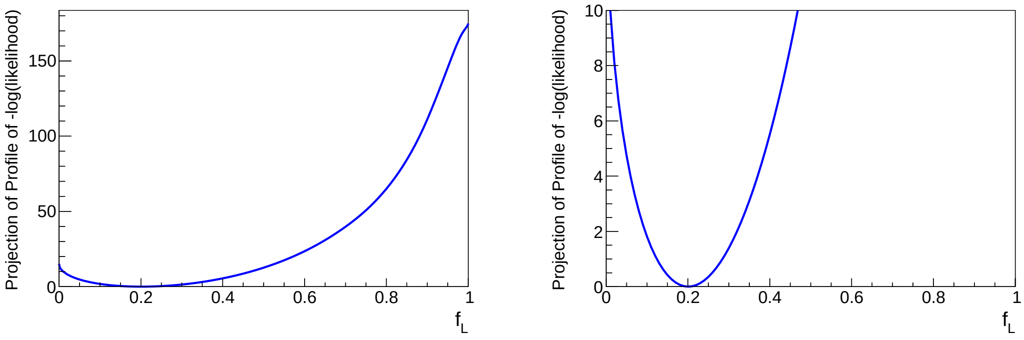

Figure 6.20: Negative $\Delta\log$ profile likelihood for the parameter f_L (left) and zoom around the minimum (right). Only the statistical uncertainty is included.

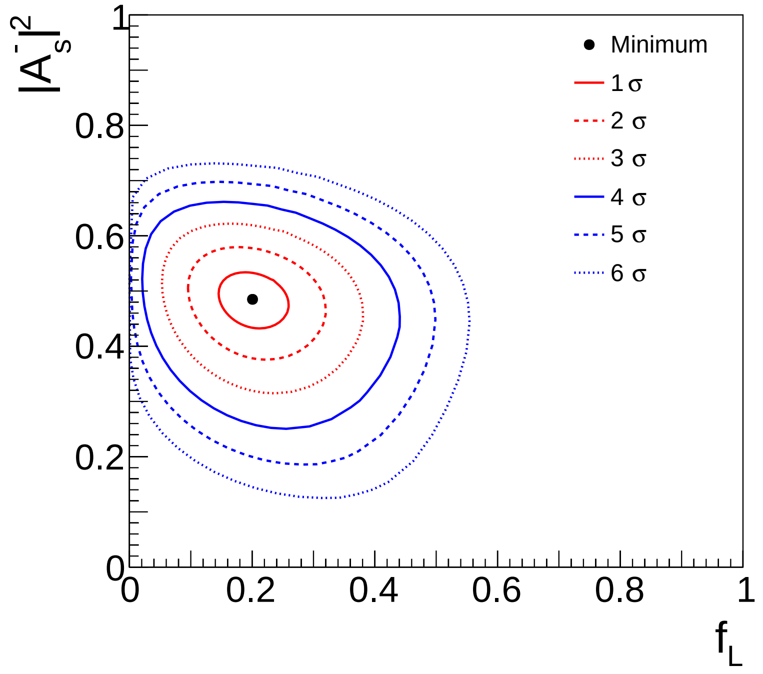

Figure 6.21: Likelihood confidence regions in the $|A_s^-|$ - f_L plane. The best fit result is represented by the black solid dot.

6.5.3 Additional cross-checks

The result obtained in the previous section confirms the low longitudinal polarisation fraction in the $B_s^0 \to K^{*0}\overline{K}^{*0}$ decay measured in Sect. 5.4 and reveals that the *S–wave* contribution is larger than those observed in similar decays, such as $B^0 \to \phi\phi$ [117] and $B_s^0 \to \phi\overline{K}^{*0}$ [118]. A series of crosschecks have been carried out in order to test the validity of this result.

6.5.3.1 $M(K^+\pi^-) \times M(K^-\pi^+)$ analysis in the wide mass window

Although the baseline analysis has focused on the ± 150 MeV/c^2 window around the nominal $K^{*0}(892)$ mass, an additional invariant mass analysis has been performed in an extended window, spanning the interval $[740, 1700]$ MeV/c^2, in order to assess the presence of higher partial waves.

In the neighbourhood of $M(K\pi) \sim 1430$ MeV/c^2 a resonance corresponding to the triplet states $K_J^*(1430)$ with $J = 0, 1, 2$, from $B_s^0 \to K_J^*(1430)\overline{K}^{*0}(892)$, is expected. A full mass-dependent angular analysis including all possible amplitudes with $J = 0, 1, 2$ and their corresponding interference terms, which would extend, with a similar level of precision, the one performed in the previous section, has not been attempted. Nonetheless a simplified version of such analysis is presented here, where only the invariant masses $m_1 \equiv M(K^+\pi^-)$ and $m_2 \equiv M(K^-\pi^+)$ are used, in the $m_1 \times m_2$ plane. This allows the relative contributions of the S, P, and D partial waves to be assessed and a rough estimate of their extrapolation into the region $|m_{1,2} - m_{K^{*0}(892)}| < 150$ MeV/c^2 to be made. It is particularly important to verify that the contribution of the D-wave is indeed negligible in the region allowed by our main analysis.

The data sample used in this section has been selected through the `StrippingBs2Kst_0Kst_0Line` stripping line from the same data sample described in Sect. 6.2. The requierements of this line, together with the offline cuts applied to the candidates are shown in Table 6.7. All physic trigger lines were considered in this study.

Fig. 6.22 shows the scatter plot of the $K^+\pi^-$ pair invariant mass versus the $K^-\pi^+$ pair invariant mass. The background has been subtracted in each 60×60 (MeV/c^2)^2 bin through a fit to the $K\pi K\pi$ invariant mass, like the one described in Sect. 6.3.1. A multichannel analysis has been performed on the background subtracted data, using only the information of the invariant masses, in order to determine the contributions from the various partial waves in the $K\pi$ system.

In this check the effect of the asymmetric acceptance in the angular integration is neglected, so the interference terms between *P–wave* and *S–wave* cancel out. The full model to describe the $K\pi$ invariant mass spectrum contains:

- *S–wave* component. The $K_0^*(1430)$ is combined with a non-resonant term using the LASS parameterisation described in Sect. 4.3.1.1. Alternatively, the *S–wave* component has been parameterised using the K–matrix formalism [119], see Appendix C.

- *P–wave*. The *P–wave* resonances are combined in a single propagator following the expressions given in Sect. 4.3.1.1

$$T_P = T_{\mathrm{K}^{*0}} + \gamma_1 T_{H,1} + \gamma_2 T_{H,2} \tag{6.8}$$

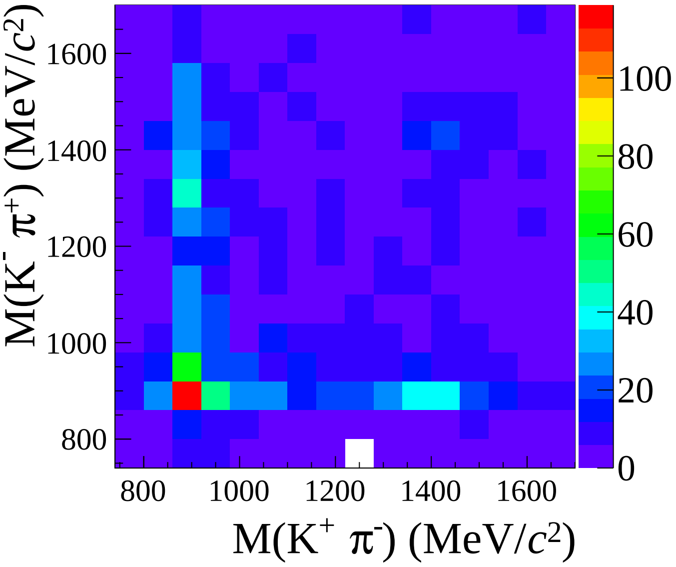

Figure 6.22: Background subtracted scatter plot of the $K^+\pi^-$ pair invariant mass versus the $K^-\pi^+$ pair invariant mass.

Table 6.7: Stripping and offline requierements used to select the wide mass window dataset. The GL discriminator is defined in Sect. 6.3.1

	Stripping selection	Offline selection
All tracks p_T	> 500 MeV	
All tracks IPχ^2	> 9	
All tracks `ProbNNghost`	< 0.8	
All tracks χ^2		< 5
$K^{\pm}$ DLL$_{K\pi}$	> 2	> 4
$K^{\pm}$ DLL$_{p-K}$		< 15
$\pi^{\pm}$ DLL$_{K-\pi}$	< 0	< -2
K^{*0} mass window	$[740, 2100]$ MeV/c^2	$[740, 1700]$ MeV/c^2
K^{*0} p_t	> 900 MeV	
K^{*0} vertex χ^2	< 9	
B$_s$ mass window	± 500 MeV	
B$_s$ daughters $\sum p_{\mathrm{T}\,i}$	> 5000 MeV/c	
B$_s$ DOCA	$< 0.3mm$	
B$_s$ DIRA	> 0.99	
B$_s$ vertex χ^2/ndof	< 15	< 5
B$_s$ FDS	> 9	> 15
B$_s$ IPχ^2	< 25	
Λ_b VETO (offline)	$\neg\left[\; \lvert M(p\pi K\pi) - m_{\Lambda_b}\rvert < 50 \;\;\&\;\; K\mathrm{DLL}_{\mathrm{p-K}} > 0 \;\right]$	
$B_s^0 \to K^{*0}\bar{K}^{*0}$ GL		> 0.14

where $T_{H,i}$ represents a higher *P–wave* resonance, $K^*(1410)$ and $K^*(1680)$. The mass and width of these resonances have been fixed to the values in [16]. In principle (see Ref. [120]) the high *P–wave* resonances should be negligible.

- *D–wave*. For the $K_2^*(1430)$ resonance the following relativistic Breit-Wigner parameterisation has been used:

$$\frac{m_R \Gamma_2(m)}{m_R^2 - m^2 - i m_R \Gamma_2(m)} \tag{6.9}$$

where the subscript 2 means the angular momentum $J = 2$, and the mass-dependent width $\Gamma_2(m)$ is given by

$$\Gamma_R \frac{m_R}{m} \left(\frac{1 + 3r^2 q_0^2 + r^4 q_0^4}{1 + 3r^2 q^2 + r^4 q^4} \right) \left(\frac{q}{q_0} \right)^5 \tag{6.10}$$

with m_R being the resonance mass, Γ_R the resonance width, q the momentum of the decay particles in the resonance rest frame, as given by equation 4.22, q_0 denotes this momentum evaluated at $m = m_R$, and r is the interaction radius. The $J = 2$ resonance parameter values are indicated in Table 4.4.

Note that the aim of this fit is to get an estimate of the amount of non K^{*0} events under the K^{*0} peak, rather than an accurate decomposition of the $K\pi$ spectrum. The results of the fit are shown in Table 6.8. The global *P–wave*, *S–wave* and *D–wave* fractions extrapolated to the ±150 MeV/c^2 mass window around the K^{*0} are also provided. As expected, a negligible contribution from the *D–wave* amplitude in the signal region is measured.

Concerning the $B_s^0 \to K^{*0}\overline{K}^{*0}$ contribution (f_{P-wave}), this result has to be compared with the result of the amplitude analysis once the effect of the angular acceptance has been taken into account. A detailed explanation on how to compute the *observed P–wave* fraction can be found in Sect. 6.6.3. The results are

$$\begin{aligned} f^{\text{angular}}_{B_s^0 \to K^{*0}\overline{K}^{*0}} &= 0.405 \pm 0.036 \\ f^{\text{wide-mass}}_{B_s^0 \to K^{*0}\overline{K}^{*0}} &= 0.618 \pm 0.088 \end{aligned}$$

The discrepancy between the two results can be explained by considering that the mass analysis in the larger window lacks some important ingredients such as the interference between different partial waves induced by the non-uniform angular acceptance. An equivalent analysis to the one performed in Sect. 6.5 extended to the wide mass window would require the introduction of the amplitudes describing the *D–wave* component as well as a careful description of the acceptance in a much larger region of phase space. Such an analysis lies outside the scope of the present work.

6.5.3.2 Fit in the narrow window

We have also performed the fit to the $B_s^0 \to K^{*0}\overline{K}^{*0}$ candidates with $|M(K,\pi) - m_{K^{*0}}| <$ 50 MeV/c^2, to crosscheck the low value of the longitudinal polarisation. The same normalisation of the mass propagators has been used, so the global *P–wave* contribution

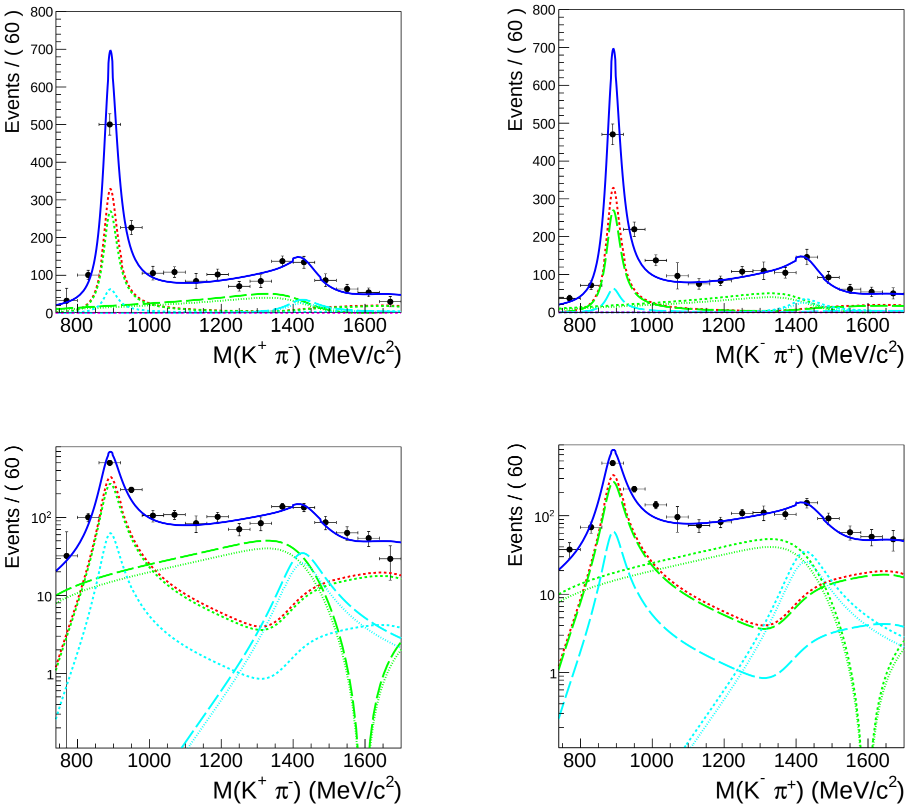

Figure 6.23: Result of the 2D fit to the background subtracted invariant mass distribution of $K^+\pi^-$ and $K^-\pi^+$ pairs in linear (top) and logarithmic scale (bottom). The different partial waves in the fit are represented: *P–wave* as a red line, *S–wave* as green lines and $D - wave$ as light blue lines.

Table 6.8: Result of the fit to the 2D invariant mass distribution of the two $K\pi$ pairs, with different models for the *S–wave*. The fraction of events corresponding to each partial wave in a narrow window around the K^{*0} mass, $|M(K\pi) - m_{K^{*0}}| < 150$ MeV/c^2, are also given.

Parameter	LASS parameterisation	K–matrix parameterisation
f_{PS} ($\times 2$)	0.219 ± 0.014	$0.181^{+0.023}_{-0.024}$
f_{PD} ($\times 2$)	0.051 ± 0.012	$0.065^{+0.017}_{-0.018}$
f_{SS}	$0.158^{+0.032}_{-0.028}$	$0.107^{+0.026}_{-0.025}$
f_{DD}	$0.0339^{+0.0090}_{-0.0085}$	$0.0222^{+0.0099}_{-0.0094}$
$\lvert\gamma_1\rvert$	$0.854^{+0.097}_{-0.045}$	$1.86^{+0.50}_{-0.49}$
$\arg(\gamma_1)$ (rad)	6.01 ± 0.75	$1.77^{+0.50}_{-0.63}$
$\lvert\gamma_2\rvert$	1.92 ± 0.21	1.12 ± 0.38
$\arg(\gamma_2)$ (rad)	$3.14^{+0.27}_{-0.44}$	$-1.92^{+0.65}_{-0.57}$
κ_S	-	$(3.4 \pm 1.4) \times 10^{-3}$
f_{P-wave} (± 150 MeV/c^2)	0.618 ± 0.088	0.64 ± 0.11
f_{S-wave} (± 150 MeV/c^2)	0.382 ± 0.087	0.35 ± 0.11
f_{D-wave} (± 150 MeV/c^2)	$(1.86 \pm 0.78) \times 10^{-4}$	$(5.9 \pm 2.8) \times 10^{-3}$

is still referred to the ±150 MeV/c^2 window around the K^{*0} nominal mass. Hence the fitted values for the parameters can be directly compared with those obtained in the previous section. The result of this fit is summarized in Table 6.9 and Fig. 6.24 shows the projection of the fit in the mass and angular variables.

Note that, altought the fitted values for the individual *S–wave* amplitudes ($|A_s^+|^2$, $|A_s^-|^2$ and $|A_{ss}|^2$) vary somewhat, the overall *S–wave* contribution ($|A_s^+|^2+|A_s^-|^2+|A_{ss}|^2$) remains constant: 0.665 ± 0.067 for the nominal fit and 0.697 ± 0.099 for the fit in the narrow mass window.

Table 6.9: Results given by the fit to $B_s^0 \to (K^+\pi^-)(K^-\pi^+)$ data with $|M(K,\pi) - m_{K^{*0}}| <$ 50 MeV/c^2. The values of $f_\parallel$, $|A_s^+|^2$ and $|A_{ss}|^2$ are calculated, following (6.4),from the free parameters in the PDF, whose correlations have been taken into account in the error calculation.

Parameter	Value
f_L	0.232 ± 0.079
$x_\parallel$	0.262 ± 0.063
$\|A_s^-\|^2$	0.598 ± 0.074
x_s^+	0.18 ± 0.12
x_{ss}	$0.084^{+0.127}_{-0.076}$
$\delta_\parallel$	5.66 ± 0.29
$\delta_\perp - \delta_s^+$	2.16 ± 0.42
δ_s^-	1.92 ± 0.21
δ_{ss}	1.62 ± 0.84
$f_\parallel$	0.201 ± 0.053
$\|A_s^+\|^2$	0.071 ± 0.057
$\|A_{ss}\|^2$	0.028 ± 0.033

6.5.3.3 One-dimensional fits to $\mathcal{A}_{FB}(m_{K\pi})$

The FB asymmetry in $\cos\theta_1$ ($\cos\theta_2$) as a function of m_1 (m_2) depends on the longitudinal amplitude A_0 and the *S–wave* amplitudes A_s^-,A_{ss} and A_s^+ following (4.34). Therefore, one can perform a unidimensional fit to the FB asymmetry obtained from data to determine the *S–wave* fraction, fixing the rest of the parameters to the values obtained from the full fit.

A simultaneous fit to the FB asymmetry in $\cos\theta_1$ and $\cos\theta_2$ was performed, by fixing all the parmeters in (4.34), except $|A_s^-|^2$ and δ_s^-, to the values obtained from the full mass-dependent angular fit. The obtained values for the floating parameters are

$$\begin{aligned} |A_s^-|^2 &= 0.55 \pm 0.13 \\ \delta_s^- &= 2.79 \pm 0.40 \end{aligned}$$

The result is shown Fig. 6.25. The value obtained for $|A_s^-|$ is again large and well compatible with the one obtained from the nominal fit.

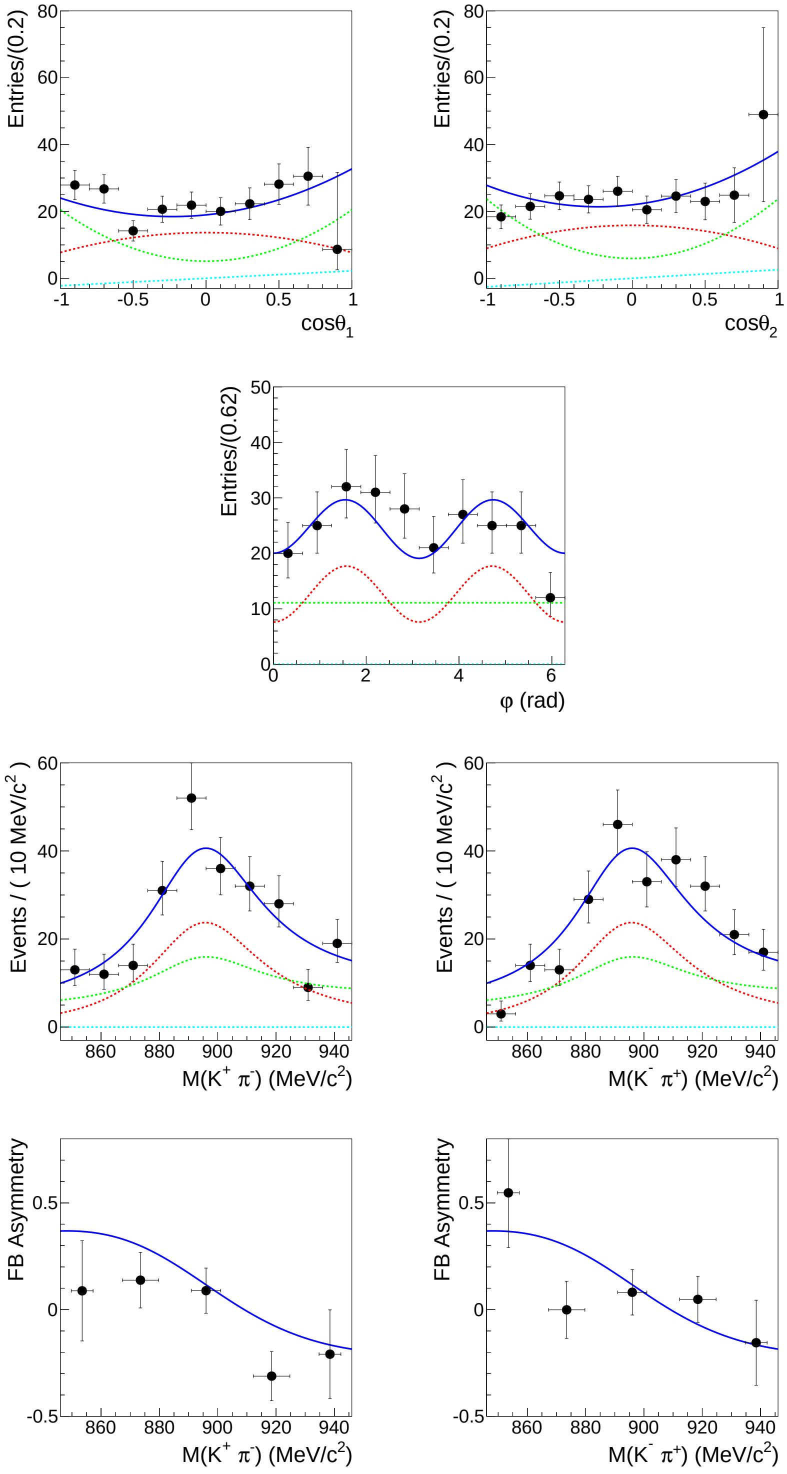

Figure 6.24: Projections of the model fitted to $B_s^0 \to (K^+\pi^-)(K^-\pi^+)$ data with $|M(K,\pi) - m_{K^{*0}}| < 50$ MeV/c^2 (blue solid line). The solid dots represent the selected data after the background component has been subtracted following (6.6) and the acceptance effect has been corrected. The red dashed line is the P-wave component, the green dashed line is the S-wave component and the light-blue dashed line represents the $\mathcal{A}_S^{+}\mathcal{A}_0$ interference term.

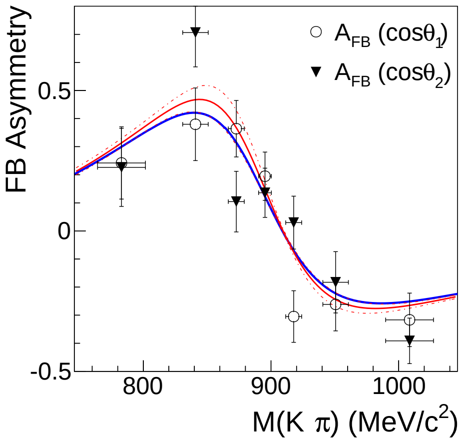

Figure 6.25: Result of the 1D-fit to the FB asymmetry in $\cos\theta_1$ (empty circles), $\cos\theta_2$ (full triangles). The red line is the projection of the 1D-model described by (4.34) (red dash lines represent the $\pm 1\sigma$ variation interval). The blue line is the corresponding projection of the nominal fit.

6.5.3.4 Background subtraction using *sFit* method

As a crosscheck to the model in Sect. 6.5.1.1, the *sFit* method [121] has been used to unfold the background from the $K\pi$ masses and angular distributions of the $B_s^0 \to (K^+\pi^-)(K^-\pi^+)$ candidates. This method relies on one or more control variables, in which the distribution of the signal and various background contributions are known, to define a per-event signal weight. In this case the four-body invariant mass is used as the control variable. Once the weights are calculated, they can be used to plot the distribution of the signal in the variables of interest or even to fit the data without the need of a parameterisation for the bakground component.

The model used for the $K^+\pi^-K^-\pi^+$ invariant mass fit is described in Sect. 6.3.3. Fig. 6.26 shows the result of the fit and the obtained weights for the B_s^0 and B^0 signals and the background component.

A weighted unbinned maximum likelihood fit is then performed using the B_s^0 signal weights [122]. The model describing the angular variables and the $K\pi$ pairs invariant mass is given by

$$\mathcal{F}_{sig}(\Omega, m1, m2) = PDF(\Omega, m1, m2) \times \varepsilon(\Omega) \tag{6.11}$$

where $PDF(\Omega, m1, m2)$ is the probability density function given by (4.18) and $\varepsilon(\Omega)$ is an simplified acceptance function calculated assuming equal proportion of TOS and non-TOS events in the sample.

The variation in the fitted parameters with respect to those obtained with the nominal fit is shown in Table 6.10. The projections of the fitted model in the three angular variables and the invariant mass of the two $K\pi$ pairs are shown in Fig. 6.27.

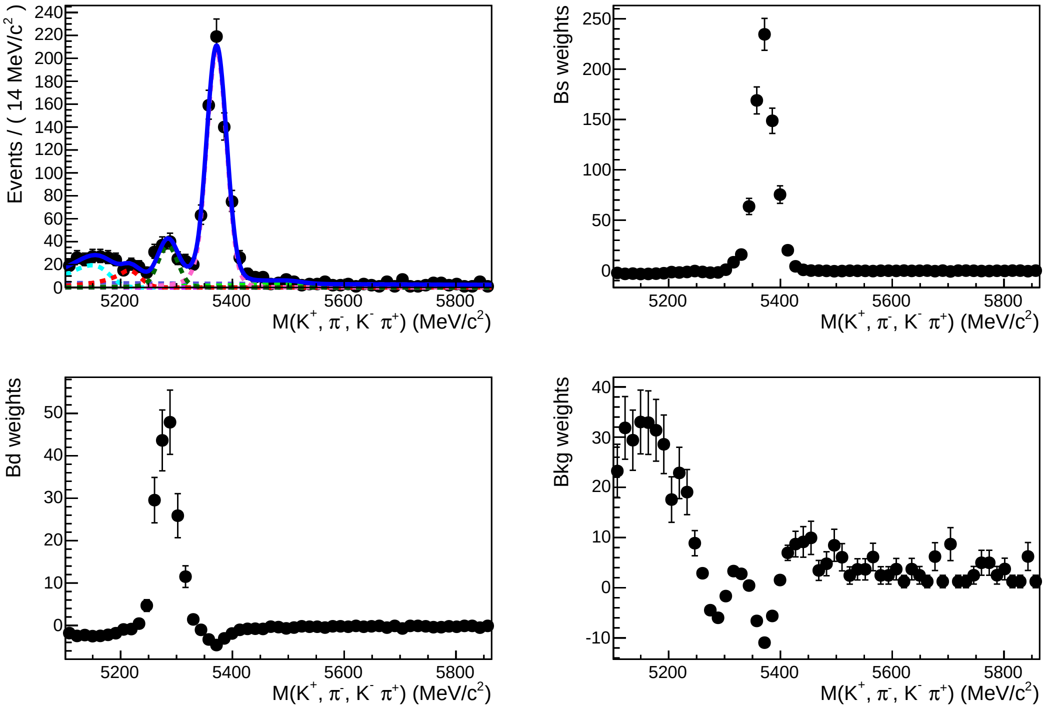

Figure 6.26: Result of the fit to the 4 body mass spectrum, from which we obtain the signal weights (top left). B_s^0 signal (top right), B^0 signal (bottom left) and background (bottom right) weights as a function of the invariant mass.

Table 6.10: Absolute variation in the fit results with respect to the $cFit$ method described in Sect. 6.5.1.1, Δ, obtained when the $sFit$ technique is used to separate the signal and combinatorial background distributions. The statistical uncertainty obtained with the $sFit$ method for each of the parameters is also provided.

Parameter	Δ	$sFit$ σ(stat)
f_L	0.008	0.050
$f_{\parallel}$	0.024	0.044
$\lvert A_s^-\rvert^2$	0.006	0.046
$\lvert A_s^+\rvert^2$	0.004	0.031
$\lvert A_{ss}\rvert^2$	0.007	0.016
$\delta_{\parallel}$	0.053	0.196
$\delta_{\perp} - \delta_s^+$	0.017	0.182
δ_s^-	0.060	0.173
δ_{ss}	0.169	0.210

Figure 6.27: Projections of the $sFit$ in the angular variables, the two $K\pi$ pairs masses and the FB asymmetries.

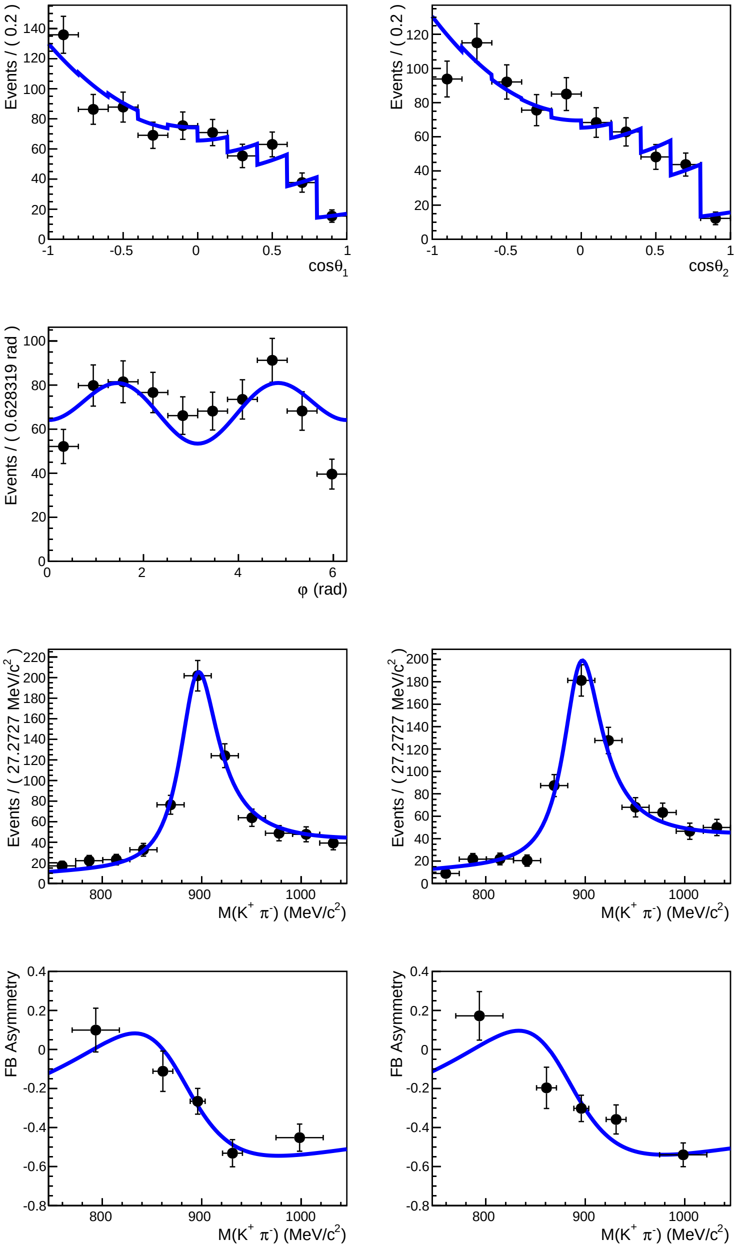

6.5.4 Systematic uncertainties

6.5.4.1 Fit bias

In order to study possible fit biases we have performed a simplified simulation study. Samples of the same size as the one found in data are generated from the PDF described in the previous sections, with values of the physics parameters similar to those obtained from the nominal fit to the data. These toy samples are then fitted using the same PDF, and the obtained parameters are compared with those used in generation to check that no bias is introduced in the analysis.

In total, 500 experiments are generated and fitted. The results of the gaussian fits to the pull distributions of the fitted parameters are shown in Fig. D.1 in Appendix D.1. In Table 6.11 the mean and width of these gaussian distributions are summarized. Fit biases are found to be very small and no significant under- or over-estimation of the uncertainties is found.

The maximum between the fit bias and its uncertainty is taken as a systematic uncertainty.

Table 6.11: Pull mean and width for the parameters obtained from the angular fit. The expected bias and systematic uncertainty are also quoted.

Parameter	Pull mean	Pull width	σ(stat)	Bias	Syst.
f_L	0.030 ± 0.033	1.000 ± 0.026	0.057	0.002 ± 0.002	0.002
$f_\parallel$	-0.094 ± 0.036	1.068 ± 0.031	0.046	-0.004 ± 0.002	0.004
$\lvert A_s^+\rvert^2$	-0.082 ± 0.038	1.070 ± 0.030	0.037	-0.003 ± 0.001	0.003
$\lvert A_s^-\rvert^2$	-0.064 ± 0.035	1.036 ± 0.029	0.051	-0.003 ± 0.002	0.003
$\lvert A_{ss}\rvert^2$	-0.064 ± 0.039	1.004 ± 0.032	0.022	-0.001 ± 0.001	0.001
$\delta_\parallel$	0.035 ± 0.032	0.958 ± 0.024	0.240	0.008 ± 0.008	0.008
$\delta_\perp - \delta_s^+$	-0.113 ± 0.032	0.967 ± 0.027	0.210	-0.024 ± 0.007	0.024
δ_s^-	0.112 ± 0.034	0.999 ± 0.029	0.190	0.021 ± 0.006	0.021
δ_{ss}	0.044 ± 0.031	0.941 ± 0.023	0.270	0.012 ± 0.008	0.012

6.5.4.2 MC statistics

In order to estimate the systematic error in the fit parameters induced by the limited statistics available in the MC, the data were fitted one thousand times after performing random variations of the acceptance function according to its statistical uncertainty. The results can be seen in Appendix D.2. The width of a gaussian fit to the pull obtained for each parameter was taken as the systematic uncertainty, see Table 6.12.

6.5.4.3 Data & Monte Carlo discrepancies

Appendix D.3 shows a comparison between the data and MC for the main variables entering the selection. From the point of view of the angular analysis, the discrepancies in the p_T spectrum of the B_s^0 meson and its daughters need to be taken into account, since the p_T selection cut is responsible for most of the acceptance effect.

Table 6.12: Systematic uncertainties of the parameters in the fit associated to the statistical uncertainty in the determintation of the detector angular acceptance.

Parameter	Pull width
f_L	0.0095
$f_{\parallel}$	0.0083
$\lvert A_s^-\rvert^2$	0.0072
$\lvert A_s^+\rvert^2$	0.0050
$\lvert A_{ss}\rvert^2$	0.0007
$\delta_{\parallel}$	0.0368
$\delta_{\perp} - \delta_s^+$	0.0192
δ_s^-	0.0357
δ_{ss}	0.0759

As it has been previously explained, part of these discrepancies can be related to the different set of polarisation amplitudes generated in the simulation and measured in data. The discrepancy coming from any different source needs to be taken into account when calculating the angular acceptance. In order to assess this effect an iterative procedure is applied. This procedure reweights the MC in helicity angles before comparing the B_s^0 and $\pi^{\pm}$ p_{T} spectra (the $K^{\pm}$ spectra are compatible between data and MC) with those in data to extract a correction. This correction is applied in the calculation of the new acceptance function and the full fit to the data is repeated. The procedure goes as follows:

1. Fit to data using the acceptance function calculated from the nominal MC simulation.
2. Reweight the Monte Carlo in the angular variables according to the result of the fit in step 1.
3. Compare the B_s^0 and $\pi^{\pm}$ p_{T} distributions between MC and data and extract a correction function for these variables.
4. Using the previous correction, recalculate the angular acceptance from Monte Carlo.
5. Use this new acceptance to fit to data.
6. Go back to step number 1, and repeat until the fit result converges.

This procedure is applied separately for TOS and non-TOS data sets. The variation of the parameter values in each iteration are shown in Table 6.13. The result of the fit converges after 4-5 iterations. The variations corresponding to the last iteration are applied as a correction to the analysis, and also taken as an estimate of the systematic error arising from incorrect description of the p_{T} spectra in the MC. The effect of the iterative procedure on the $\cos\theta$ acceptance function is illustrated in Fig. 6.28.

Additionally, it has been checked that the MC describes well the differences between TOS and non-TOS events. The ratio TOS/non-TOS found in data with the corresponding ratio predicted by simulation have been compared, see Fig. 6.29, and were found to be compatible with the available statistics. Thus, no additional systematic uncertainty is considered.

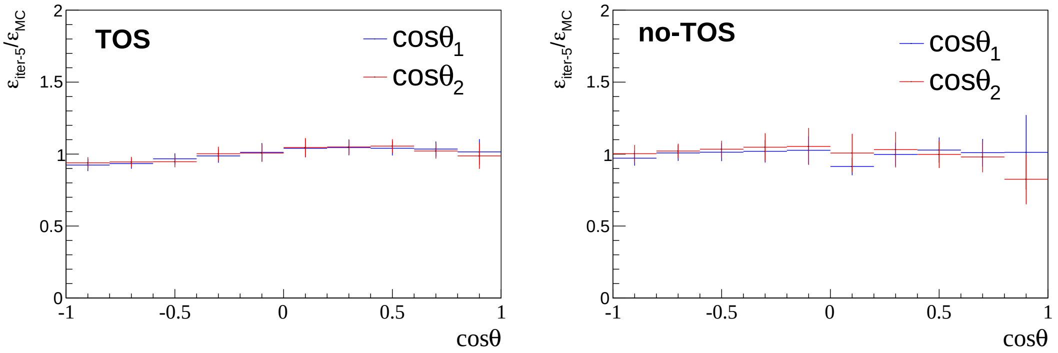

Figure 6.28: Ratio between the acceptance functions calculated from MC before and after the correction in the p_{T} spectra obtained with the iterative method described in the text. Left: TOS sample. Right: non-TOS sample.

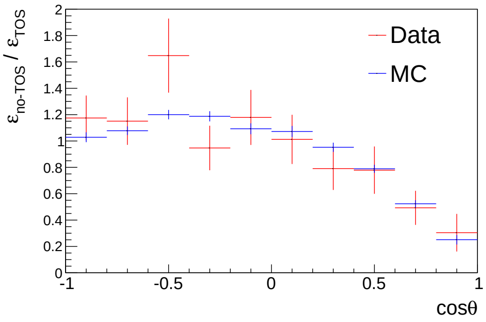

Figure 6.29: Comparison of the ratio between TOS and non-TOS angular acceptance functions for data and MC.

Table 6.13: Variation in the fit result for different acceptance functions calculated through the iterative procedure explained in the text. The variation in each iteration is given relative to the results of the nominal fit. The variation corresponding to the fifth iteration, after which the result is stable, is taken as a systematic uncertainty.

Δ	B_s^0 p_{T}	Iter 1	Iter 2	Iter 3	Iter 4	Iter 5	Syst.
f_L	0.0023	0.0094	0.0100	0.0101	0.0101	0.0101	0.0101
$f_\parallel$	-0.0006	-0.0034	-0.0037	-0.0038	-0.0038	-0.0038	-0.0038
$\lvert A_s^+\rvert^2$	-0.0005	-0.0009	-0.0018	-0.0020	-0.0021	-0.0021	-0.0021
$\lvert A_s^-\rvert^2$	0.0031	0.0085	0.0098	0.0101	0.0102	0.0102	0.0102
$\lvert A_{ss}\rvert^2$	0.0001	0.0002	0.0003	0.0003	0.0003	0.0003	0.0003
$\delta_\parallel$	-0.0058	-0.0269	-0.0379	-0.0408	-0.0415	-0.0417	-0.0417
$\delta_\perp - \delta_s^+$	-0.0024	0.0002	-0.0002	-0.0004	-0.0004	-0.0004	-0.0004
δ_s^-	-0.0185	-0.0580	-0.0709	-0.0742	-0.0750	-0.0753	-0.0753
δ_{ss}	-0.0260	-0.1269	-0.1718	-0.1838	-0.1869	-0.1877	-0.1877

6.5.4.4 Acceptance model

As explained in section Sect. 6.4.1, the acceptance function was assumed to be a factorizable function of the helicity angles and the invariant mass of the $K\pi$ pairs. To test the validity of this assumption, different models were tried for the acceptance function. The small statistics in the MC[1] and the strong acceptance effect in $\cos\theta_{1,2}$ makes a 5D treatment of the acceptance very difficult. As an alternative, a generic $\cos\theta$-$m_{K\pi}$ model was tried. The acceptance was described by

$$\varepsilon(m,\cos\theta) = \sum_{i,j} c^{ij} P_i(m') P_j(\cos\theta) \tag{6.12}$$

where P_i are Legendre polynomials of order i and $m' = 2(m - m_{\rm min})/(m_{\rm max} - m_{\rm min}) - 1$ is a renormalisation of the $K\pi$ invariant mass. The values of $m_{\rm min}$ and $m_{\rm max}$ are the boundaries of the considered $K\pi$ invariant mass range, $m_{\rm min} = m_{K^{*0}} - 150\ \ {\rm MeV}/c^2$ and $m_{\rm max} = m_{K^{*0}} + 150\ \ {\rm MeV}/c^2$. In order to calculate the c^{ij} coefficients from the Monte Carlo sample, one can take advantage of the general averaging procedure for a generic function $f(X)$ of the observables $X : \{m_1, m_2, \Omega\}$,

$$\begin{aligned}
\frac{1}{N_{gen}} \sum_{\text{accepted}} f(X) &= \frac{1}{N_{gen}} \sum_{\text{generated}} f(X)\epsilon(X) \\
&\approx \int PDF(X)\epsilon(X) f(X) dX
\end{aligned} \tag{6.13}$$

where $\epsilon(X)$ represents the efficiency of accepting an event and $PDF(X)$ is the probability density function used to generate the MC sample in ${\rm d}X \equiv {\rm d}m_1 {\rm d}m_2 {\rm d}(\cos\theta_1){\rm d}(\cos\theta_2){\rm d}\varphi$. In this particular case, the acceptance is assumed to factorise as $\epsilon(X) = \varepsilon(m_1, \cos\theta_1) \times \varepsilon(m_2, \cos\theta_2)$ (and be flat in ϕ). By choosing

$$f_{ij}(X) = \left(\frac{2i+1}{2} \, \frac{2j+1}{2} \, \frac{P_i(m'_1) P_j(\cos\theta_1)}{PDF(X)} \right), \tag{6.14}$$

the average provides the desired c^{ij} coefficients

$$\begin{aligned}
\frac{1}{N_{gen}} \sum_{\text{accepted}} f_{ij}(X_n) &\approx \left(\frac{2i+1}{2}\right)\left(\frac{2j+1}{2}\right) \int PDF(X)\epsilon(X) \frac{P_i(m'_1)P_j(\cos\theta_1)}{PDF(X)} {\rm d}X \\
&= C_{\rm norm} \left(\frac{2i+1}{2}\right)\left(\frac{2j+1}{2}\right) \times \\
&\quad \times \sum_{ab} c^{ab} \int P_a(m'_1) P_b(\cos\theta_1) P_i(m'_1) P_j(\cos\theta_1) {\rm d}m'_1 {\rm d}(\cos\theta_1) \\
&= C_{\rm norm} \;\; c^{ij},
\end{aligned} \tag{6.15}$$

where the orthogonality properties of the Legendre polynomials have been used in the last step. The factor

$$C_{\rm norm} = 2\pi \left(\frac{m_{\rm max} - m_{\rm min}}{2} \right)^2 \int \varepsilon(m', \cos\theta) {\rm d}m' {\rm d}(\cos\theta) \;, \tag{6.16}$$

---

[1] From $\sim 2\times10^6$ events generated, $\sim 20\times10^3$ are selected. The sample is then split in TOS (60%) and non-TOS (40%). However, these events are not evenly distributed in the decay variables. The MC sample was generated with high polarisation which means that regions where $\cos\theta_{1,2} \to 0$ are less populated. The same occurs in the tails of the $K\pi$ mass distribution.

Table 6.14: Acceptance coefficients calculated using the MC simulated TOS (left) and non-TOS (right) events as described in the text.

Coefficient TOS	Value
c^{00}	0.250
c^{01}	-0.091 ± 0.010
c^{02}	-0.091 ± 0.013
c^{03}	-0.049 ± 0.016
c^{04}	-0.027 ± 0.019
c^{10}	0.015 ± 0.014
c^{11}	-0.020 ± 0.020
c^{12}	0.054 ± 0.027
c^{13}	-0.027 ± 0.031
c^{14}	-0.043 ± 0.039
c^{20}	-0.065 ± 0.017
c^{21}	0.054 ± 0.022
c^{22}	-0.012 ± 0.036
c^{23}	0.056 ± 0.037
c^{24}	0.035 ± 0.045

Coefficient non-TOS	Value
c^{00}	0.250 ± 0.000
c^{01}	-0.182 ± 0.024
c^{02}	-0.132 ± 0.038
c^{03}	0.082 ± 0.046
c^{04}	-0.001 ± 0.046
c^{10}	-0.018 ± 0.049
c^{11}	0.025 ± 0.088
c^{12}	0.139 ± 0.089
c^{13}	-0.180 ± 0.104
c^{14}	0.039 ± 0.111
c^{20}	0.070 ± 0.056
c^{21}	-0.136 ± 0.118
c^{22}	0.107 ± 0.130
c^{23}	0.051 ± 0.126
c^{24}	-0.124 ± 0.122

is just a normalisation constant for the full acceptance and can be ignored.

Fig. 6.30 shows the acceptance for TOS events and Fig. 6.31 for non-TOS events. The data points correspond to $B_s^0 \to K^{*0}\overline{K}^{*0}$ MC simulated data which were divided by the generator PDF on an event by event basis. The curve is the projection of the acceptance calculated using the procedure described before. The values obtained for c^{ij} are shown in Table 6.14.

The fit to the data has been repeated using the acceptance calculated above. The difference in the fit parameters between the result obtained and the nominal one is shown in Table 6.15, and it is considered as an estimate of the systematic uncertainty.

Table 6.15: Variation in the fit result when the analytical parameterisation explained in the text is used as acceptance function.

Parameter	Δ
f_L	0.031
$f_{\parallel}$	-0.008
$\lvert A_s^-\rvert^2$	0.007
$\lvert A_s^+\rvert^2$	0.019
$\lvert A_{ss}\rvert^2$	-0.003
$\delta_{\parallel}$	-0.13
$\delta_{\perp} - \delta_s^+$	0.016
δ_s^-	-0.16
δ_{ss}	-0.096
total *S–wave*	0.022

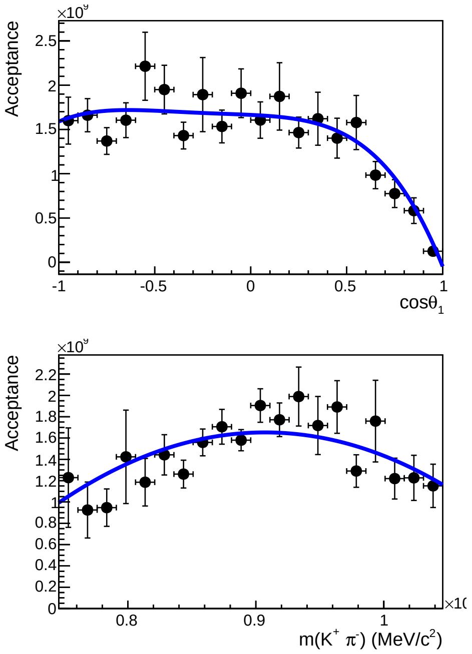

Figure 6.30: Acceptance of the TOS events as a function of the helicity angle and $m_{K\pi}$. The points correspond to MC simulated data and the blue curve is the projection of the acceptance calculated using the method described in the text.

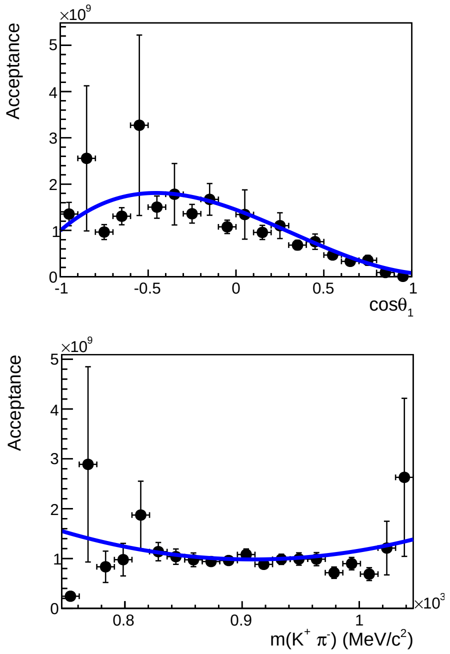

Figure 6.31: Acceptance of the non-TOS events as a function of the helicity angle and $m_{K\pi}$. The points correspond to MC simulated data and the blue curve is the projection of the acceptance calculated using the method described in the text.

6.5.4.5 Mass resolution

In order to estimate the effect of neglecting the mass resolution in the model of the $K\pi$ mass spectrum, a set of 1000 independent toy experiments was performed. The $K\pi$ mass was smeared according to a gaussian resolution of 5 MeV/c^2, similar to the one estimated from Monte Carlo simulation (see Appendix D.4), and the smeared data were fitted to the same model used at the generator level. The pull distributions of the fit parameters are shown in Fig. 6.32, while the mean and width from a gaussian fit to those distributions are summarized in Table 6.16. As expected, the overall contributions of the *S–wave* components, represented dominantly by the $|A_s^-|^2$ parameter, decreases as a consequence of the flatter K^{*0} line shape. But the effect is small in absolute terms of the *S–wave* fraction: -0.01 (22% of the statistical error). A small bias in the phases of the amplitudes was also found. These variations are taken as the systematic uncertainties associated to the invariant mass resolution.

Table 6.16: Pull mean and width for the parameters obtained from the angular fit. The expected bias and systematic uncertainty are also quoted.

Parameter	Pull mean	Pull width	σ(stat)	Bias	Syst.
f_L	-0.027 ± 0.035	0.998 ± 0.029	0.057	-0.002 ± 0.002	-
$f_\parallel$	-0.036 ± 0.034	1.019 ± 0.026	0.046	-0.002 ± 0.002	-
$\lvert A_s^+\rvert^2$	0.030 ± 0.037	1.014 ± 0.031	0.037	0.001 ± 0.001	-
$\lvert A_s^-\rvert^2$	-0.218 ± 0.033	0.987 ± 0.025	0.051	-0.011 ± 0.002	0.011
$\lvert A_{ss}\rvert^2$	-0.028 ± 0.041	0.965 ± 0.035	0.022	-0.001 ± 0.001	-
$\delta_\parallel$	-0.102 ± 0.031	0.944 ± 0.023	0.240	-0.024 ± 0.007	0.024
$\delta_\perp - \delta_s^+$	0.052 ± 0.034	1.032 ± 0.027	0.210	0.011 ± 0.007	0.011
δ_s^-	-0.117 ± 0.034	0.950 ± 0.026	0.190	-0.022 ± 0.006	0.022
δ_{ss}	0.161 ± 0.032	0.953 ± 0.026	0.270	0.043 ± 0.009	0.043

6.5.4.6 S-wave mass model

As described in Sect. 4.3.1.1, the *S–wave* component of the $K\pi$ spectrum is described by a combination of a relativistic Breit–Wigner amplitude and a non–resonant amplitude following [37]. Different models were tried to check the consistency of the result. The first variation consisted of parameterising the *S–wave* component only with a relativistic spin-0 Breit–Wigner propagator at the mass of $K_0^*(1430)$. A combination of two Breit–Wigner propagators (BW) at the poles of $\kappa(800)$ and $K_0^*(1430)$ following the Isobar model was also tried,

$$\mathcal{M}_0(m) = \alpha\ BW(m_\kappa, \Gamma_\kappa) + BW(m_{K_0^{*0}(1430)}, \Gamma_{K_0^{*0}(1430)}) \tag{6.17}$$

where the magnitude and phase of the constant α were both floating during the minimisation. Three different values of the mass and width of the κ state were tested:

$(A):\quad m_\kappa = 682 \pm 29\ \text{MeV}/c^2;\quad \Gamma_\kappa = 547 \pm 24\ \text{MeV}/c^2$

$(B):\quad m_\kappa = 658 \pm 13\ \text{MeV}/c^2;\quad \Gamma_\kappa = 557 \pm 24\ \text{MeV}/c^2$

$(C):\quad m_\kappa = 700 \pm 80\ \text{MeV}/c^2;\quad \Gamma_\kappa = 650 \pm 120\ \text{MeV}/c^2$

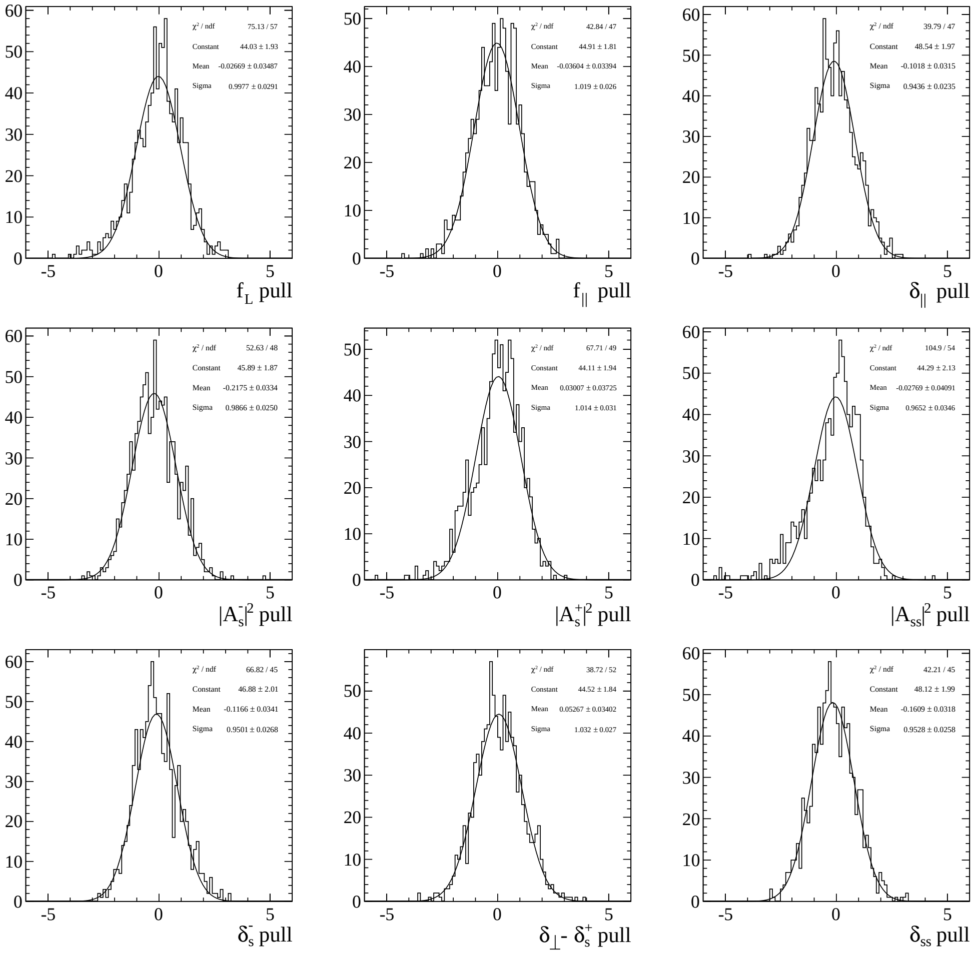

Figure 6.32: Pull distributions of the parameters in the fit obtained from toy experiments simulating data used for the final result including the effect of the mass resolution.

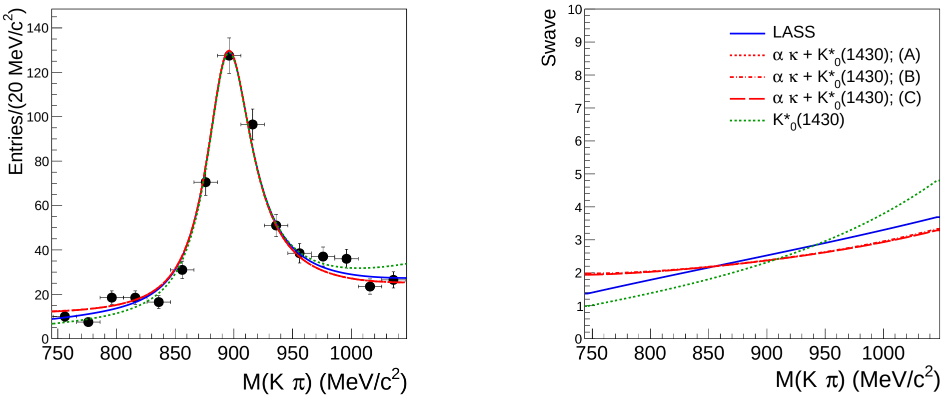

Figure 6.33: Different models for the *S–wave* mass propagator.

following [16], [91] and [90] respectively.

The results of the fit after these variations are summarized in Table 6.17. The information about the goodness-of-fit and significance with respect to the LASS parameterisation (defined in Sect. 4.3.1.1) are also provided, by means of the value of $\chi^2_L \equiv -2\log\mathcal{L}$ in the minimum. The difference $\Delta(\chi^2_L) = \chi^2_L - \chi^2_{L,LASS}$ can be used to compare the quality of the alternative fit with the nominal one. This quantity behaves as a $\chi^2(\Delta NDF)$, where $\Delta NDOF$ is the difference in the number of free parameters for each pair of models, thus it can be turned into a probability or into a number of Gaussian standard deviations. Since the quality of the fit when only the $K_0^*(1430)$ contributes to the *S–wave* mass propagator is significantly worse, only the maximum parameter variation between LASS and Isobar models is considered as a sytematic uncertainty.

Fig. 6.33 shows the projection of the three models together with the data distribution and the shape of the *S–wave* mass propagator.

Table 6.17: Variation in the results given by the fit to $B_s^0 \to K^{*0}\overline{K}^{*0}$ data, for different parameterisations of the *S–wave* invariant mass distribution.

Parameter	$K^*(1430)$	$\alpha\kappa + K^*(1430)$		
	(BW J=0)	[16] (A)	[91] (B)	[90] (C)
f_L	-0.0122	0.0207	0.0205	0.0204
$f_\parallel$	0.0122	-0.0047	-0.0042	-0.0045
$\|A_s^+\|^2$	0.0115	-0.0112	-0.0107	-0.0113
$\|A_s^-\|^2$	-0.0202	0.0008	-0.0007	0.0009
$\|A_{ss}\|^2$	-0.0015	-0.0025	-0.0020	-0.0025
$\delta_\parallel$	-0.0862	0.0023	-0.0035	0.0030
$\delta_\perp - \delta_s^+$	0.0260	-0.0010	0.0049	0.0044
δ_s^-	-0.1250	0.0334	0.0183	0.0307
δ_{ss}	-0.0838	-0.0022	-0.0176	-0.0104
$\|\alpha\|$	0	1.18 ± 0.47	1.23 ± 0.43	1.23 ± 0.49
$\arg(\alpha)$	0	3.6 ± 1.5	3.6 ± 1.6	3.6 ± 1.6
$f_{\kappa(800)}$ (%)	0	78	82	80
$\Delta(\chi^2_L)$	17.9	-2.5	-2.4	-2.5
Δ_{NDF}	0	2	2	2
$\sqrt{\|\Delta(\chi^2_L)\| - \Delta_{NDOF}}$	4.2σ	0.7σ	0.6σ	0.7σ

6.5.4.7 Model parameters

Mass propagator parameters The parameters entering the mass propagators definition for both *P–wave* and *S–wave* have been changed by $\pm 1\sigma$ (see Table 4.4) and the fit has been repeated. Table 6.18 summarizes the variation in the results induced by the error in those parameters. Most of these variations are much smaller than the systematic uncertainty established in Sect. 6.5.4.6, for those parameters no additional systematic

Table 6.18: Variation in the angular fit result induced by the uncertainty in the parameter of the mass propagators.

Parameter	*P–wave* propagator			*S–wave* propagator				Syst.
	m_1	Γ_1	r_1	m_0	Γ_0	a	b	
f_L	0.007	0.003	0.004	0.0022	0.0003	0.0011	0.0012	-
$f_{\|\|}$	0.001	0.000	0.000	0.0005	0.0002	0.0003	0.0003	-
$\|A_s^+\|^2$	0.002	0.001	0.002	0.0005	0.0004	0.0004	0.0009	-
$\|A_s^-\|^2$	0.003	0.003	0.004	0.0024	0.0005	0.0009	0.0015	0.0034
$\|A_{ss}\|^2$	0.002	0.005	0.008	0.0003	0.0002	0.0001	0.0004	0.0053
$\delta_{\|\|}$	0.003	0.003	0.004	0.0019	0.0022	0.0023	0.0050	0.0050
$\delta_\perp - \delta_s^+$	0.017	0.011	0.010	0.0101	0.0025	0.0027	0.0101	0.017
δ_s^-	0.010	0.008	0.012	0.0054	0.0060	0.0061	0.0052	-
δ_{ss}	0.003	0.015	0.013	0.0107	0.0065	0.0071	0.0085	-

uncertainty is considered. For the rest of them, the maximum variation is taken as the systematic uncertainty.

Background fraction Varying the fraction of background in $\pm1\sigma$ has a negligible effect in the result of the angular and mass fit, as shown in Table 6.19.

Table 6.19: Variation in the agular fit result induced by the uncertainty in the fraction of background events in TOS and not-TOS subsamples.

Parameter	f_{bkg}^{TOS}	$f_{bkg}^{non-TOS}$
f_L	0.0005	0.0013
$f_{\|\|}$	0.0003	0.0001
$\|A_s^-\|^2$	0.0009	0.0019
$\|A_s^+\|^2$	0.0005	0.0004
$\|A_{ss}\|^2$	0.0004	0.0031
$\delta_{\|\|}$	0.0012	0.0006
$\delta_\perp - \delta_s^+$	0.0006	0.0027
δ_s^-	0.0010	0.0009
δ_{ss}	0.0014	0.0045

6.5.4.8 Summary of systematic uncertainties

A summary of the different contributions to the final systematic uncertainty of the parameters obtained from the amplitude analysis is shown in table Table 6.20. The most important systematic effects come from the parameterisation of the angular acceptance and the modeling of the invariant mass propagators. The final systematic uncertainty for each of the parameters is obtained by adding in quadrature all the contributions.

Table 6.20: Systematic uncertainties of the parameters obtained from the amplitude analysis.

Source	f_L	$f_\parallel$	$\lvert A_s^-\rvert^2$	$\lvert A_s^+\rvert^2$	$\lvert A_{ss}\rvert^2$	$\delta_\parallel$	$\delta_\perp - \delta_s^+$	δ_s^+	δ_{ss}
Fit bias	0.0020	0.0040	0.0030	0.0030	0.0010	0.0080	0.024	0.0210	0.0120
MC stat	0.0095	0.0083	0.0050	0.0072	0.0007	0.0368	0.019	0.0357	0.0759
Data/MC	0.0101	0.0038	0.0021	0.0102	0.0003	0.0417	0.0004	0.0753	0.1877
Acceptance	0.0310	0.0080	0.0190	0.0070	0.0030	0.1300	0.0160	0.1600	0.0960
Mass resol	0.0000	0.0000	0.0000	0.0110	0.0000	0.0240	0.0110	0.0220	0.0430
Mass model	0.0207	0.0047	0.0113	0.0034	0.0053	0.0050	0.0171	0.0334	0.0177
Total	0.040	0.014	0.023	0.019	0.006	0.144	0.040	0.186	0.229

6.6 Branching ratio of $B_s^0 \to K^{*0}\overline{K}^{*0}$

Given the large value of the *S–wave* contribution found in the previous section, a fraction that could not be accurately determined in the analysis of 2010 data, an update of the $\mathcal{B}(B_s^0 \to K^{*0}\overline{K}^{*0})$ was performed. The strategy followed to measure this $\mathcal{B}$ is based upon the use of a normalisation channel with a known partial width. The decay $B^0 \to \phi K^{*0}$ was chosen for this purpose. The presence of four hadrons in the final state and the similar topology of both decays allows the harmonisation of their trigger and offline selections. The ratio of branching fractions of these two decays is given by

$$\begin{aligned}\frac{\mathcal{B}(B_s^0 \to K^{*0}\overline{K}^{*0})}{\mathcal{B}(B^0 \to \phi K^{*0})} &= \frac{\varepsilon_{B^0\to\phi K^{*0}}}{\varepsilon_{B_s^0\to K^{*0}\overline{K}^{*0}}} \times \frac{\lambda_{f_L}(B^0 \to \phi K^{*0})}{\lambda_{f_L}(B_s^0 \to K^{*0}\overline{K}^{*0})} \times \frac{N_{B_s^0} \times f_{B_s^0\to K^{*0}\overline{K}^{*0}}}{N_{B^0} \times f_{B^0\to\phi K^{*0}}} \\ &\times \frac{f_d}{f_s} \times \frac{\mathcal{B}(\phi \to K^+K^-)}{\mathcal{B}(K^{*0} \to K^+\pi^-)} \qquad (6.18)\end{aligned}$$

where $\frac{f_d}{f_s}$ is the ratio of b-quark hadronisation fractions that accounts for different yield of B^0 and B_s^0 mesons. $N_{B_s^0}$ and N_{B^0} represent the number of candidate events for $B_s^0 \to K^+\pi^-K^-\pi^+$ and $B^0 \to K^+K^-K^\pm\pi^\mp$ decays respectively. The amount of those corresponding to the resonant decays, $B_s^0 \to K^{*0}\overline{K}^{*0}$ and $B^0 \to \phi K^{*0}$, is given by the purity factors $f_{B_s^0\to K^{*0}\overline{K}^{*0}}$ and $f_{B^0\to\phi K^{*0}}$. $\varepsilon_{B^0\to\phi K^{*0}}/\varepsilon_{B_s^0\to K^{*0}\overline{K}^{*0}}$ is the ratio of reconstruction, selection and trigger efficiencies for signal and normalisation channel. The overall efficiency for each channel depends on the angular distribution of the particles in the final state, which motivates the factors λ_{f_L}. Both the purity and the λ_{f_L} factor for $B_s^0 \to K^{*0}\overline{K}^{*0}$ are calculated from the results of the angular analysis in Sect. 6.5, and combined in the factor

$$\kappa_{B_s^0\to K^{*0}\overline{K}^{*0}} = \lambda_{f_L}(B_s^0 \to K^{*0}\overline{K}^{*0}) \times \frac{1}{f_{B_s^0\to K^{*0}\overline{K}^{*0}}}. \qquad (6.19)$$

The factor corresponding to $B^0 \to \phi K^{*0}$ decay is calculated from the results in [118]. In the following sections, the determination of all the terms entering the branching fraction calculation is described in more detail, together with the estimation of the systematic uncertainties related to each of them.

6.6.1 Control channel: $B^0 \to \phi K^{*0}$

The selection cuts for the normalisation channel have been chosen to match those in [118], with the exception of the PID requirements that are tighter to harmonize with the signal selection. These cuts are shown in table Table 6.21. The definition of the multivariate discriminator $GL(B^0 \to \phi K^{*0})$ can be found in [118]. Regarding the trigger selection, similarly to the signal, all physics trigger lines are considered.

Fig. 6.34 shows the $K^+K^-K^\pm\pi^\mp$ invariant mass of the selected events. In order to extract the number of B^0 candidates an unbinned maximum likelihood fit was performed. The B^0 signal was modeled by a combination of a Crystal Ball and a Gaussian distributions that share a common mean. Their relative widht and fraction and the parameters describing the tail of the Crystal Ball are fixed to the values observed in $B^0 \to \phi K^{*0}$ simulated data. The signal from the recently discovered decay $B_s^0 \to \phi\overline{K}^{*0}$ is also described using this parameterisation. The mass difference between B^0 and B_s^0 is fixed to

Table 6.21: Offline selection cuts for $B^0 \to \phi K^{*0}$. $M(KK)$ is the invariant mass of the $K^+\pi^-$ pair forming the K^{*0} where the pion hypothesis is changed into a kaon hypothesis.

	Selection cuts
All tracks `ProbNNghost`	< 0.5
All tracks p_T	$> 500\ MeV/c$
All tracks IPχ^2	> 9
DLL$_{K\pi}(K^\pm)$	> 10
DLL$_{K\pi}(\pi^\pm)$	< 0
K^{*0} mass window	± 150 MeV/c^2
K^{*0} p_T	$> 900\ MeV/c$
K^{*0} vertex χ^2	< 9
K^{*0} DIRA	> 0
ϕ mass window	± 15 MeV/c^2
ϕ p_T	$> 900\ MeV/c$
ϕ vertex χ^2	< 9
B^0 mass window	$[5000, 5600]$ MeV/c^2
B^0 DOCA	< 0.3 mm
B^0 vertex χ^2/ndof	< 5
B_s^0 flight distance χ^2	> 15
B_s^0 IPχ^2	< 25
M(KK)	$< (m_\phi - 15)$ OR
	$> (m_\phi + 15)$ OR
GL($B^0 \to \phi K^{*0}$)	> 0.10

the value calculated from [16]. The partially reconstructed background is modeled using an ARGUS distribution, described by (6.1), with all its parameters floating in the fit. The combinatorial background is parameterised with a decreasing exponential. The results of the fit, as well as the values of the fixed parameters, are shown in Table 6.22.

6.6.2 Efficiency ratio

The ratio of efficiencies for $B_s^0 \to K^{*0}\overline{K}^{*0}$ and $B^0 \to \phi K^{*0}$ is calculated using MC simulated events. Four contributions are evaluated to get the global efficiency: generator efficiency (ε^{gen}), selection efficiency (ε^{sel}), PID efficiency (ε^{PID}) and trigger efficiency (ε^{trig}).

$$\varepsilon = \varepsilon^{gen} \times \varepsilon^{sel} \times \varepsilon^{PID} \times \varepsilon^{trig} \tag{6.20}$$

The generator efficiency accounts for the acceptance cuts applied to the event generator. The selection efficiency includes the effects of the offline reconstruction and the selection cuts. The efficiency of the PID cuts is computed separately since discrepancies in the PID variables between data and MC need to be taken into account. The trigger efficiency is the efficiency of the trigger for events that would be offline selected.

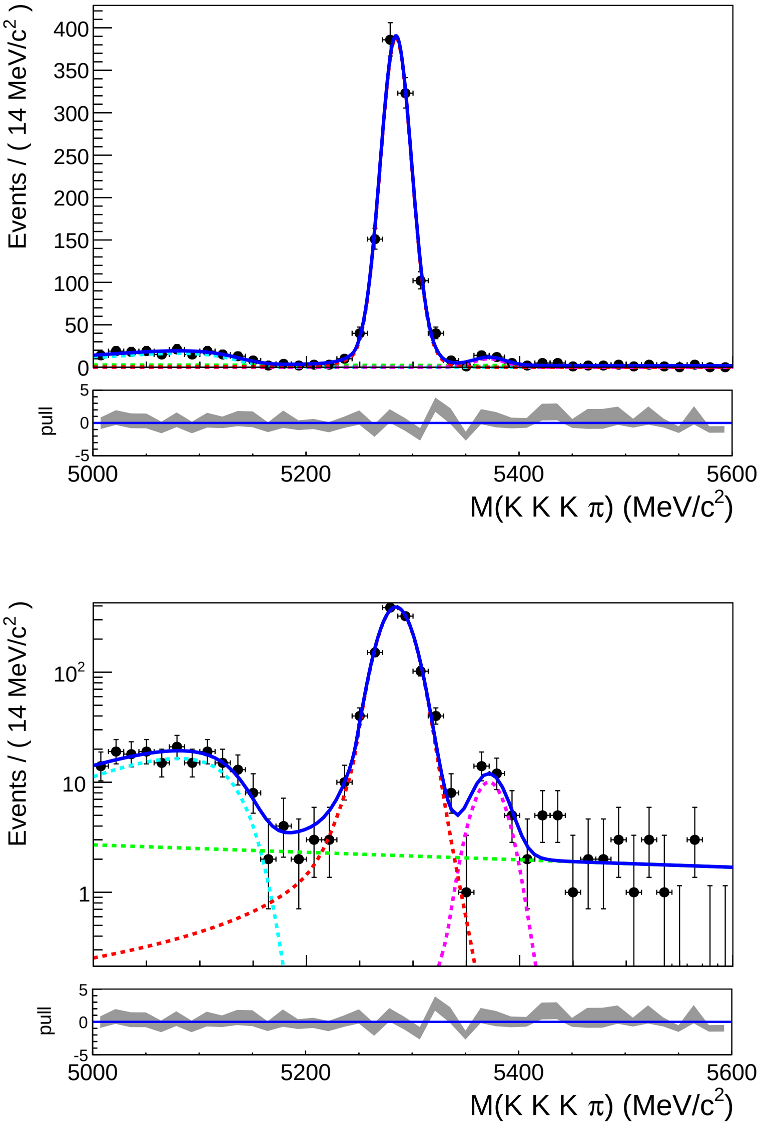

Figure 6.34: Result of the fit to the invariant mass of the selected $KKK\pi$ combinations in linear (top) and logarithmic (bottom) scales. The solid points represent the selected data and the blue solid line is the fitted model. The B^0 (B_s^0) signal peak is shown as a red (magenta) dashed line. The contribution from partially reconstructed decays is represented as a light-blue dashed line. The green dashed line is the combinatorial background component.

Table 6.22: Fitted values of the parameters in the invariant mass model for $B^0 \to K^+K^-K^\pm\pi^\mp$. The parameters quoted without error were fixed to the indicated value in the fit. μ_d is the mean of the B^0 peak, f_{CB} is the fraction of the Crystal Ball ($1 - f_{CB}$ is the fraction of the Gaussian), σ_{CB} is the width of the Crystal Ball, a_{CB} and n_{CB} are Crystal Ball parameters and σ_{Gauss} is the width of the signal Gaussian distribution. c_{bkg} is the slope of the exponential distribution describing the combinatorial background. $k_{PhysBkg}$ and $m_{PhysBkg}$ are the parameters of the ARGUS shape describing partially reconstructed events, that represent a fraction $f_{PhysBkg}$ of the total background.

Parameter	Value
N_{B^0}	1049 ± 33
$N_{B_s^0}$	27.1 ± 6.4
N_{Bkg}	234 ± 18
μ_d (MeV/c^2)	5283.98 ± 0.50
σ_{CB} (MeV/c^2)	14.65 ± 0.41
a_{CB}	2.56
n_{CB}	1.1
f_{CB}	0.915
σ_{Gauss} (MeV/c^2)	24.5
c_{bkg} ((MeV/c^2)$^{-1}$)	$(-0.8 \pm 1.3) \times 10^{-3}$
$f_{PhysBkg}$	0.613 ± 0.091
$k_{PhysBkg}$	$(1.40 \pm 0.41) \times 10^{-2}$
$m_{PhysBkg}$	5153.4 ± 9.3

6.6.2.1 Generator efficiency

Generator level efficiencies are found by generating simulated signal events using the MC11a release of Gauss (v41r4) and then counting how many events have all their final state particles falling within the LHCb geometric acceptance. The generator level efficiencies for signal and control channel are given in Table 6.23.

Additionally, EvtGen will not generate resonances with masses outside the range $m_0 \pm 15 \times \Gamma_0$, where m_0 and Γ_0 are the mass and the width of the resonance. This cutoff in the mass of the resonance applied at the generator level should also be taken into account in the global efficiency. We compute the global efficiency as

$$\varepsilon = \frac{N}{N^{gen}} \tag{6.21}$$

where N is the number of simulated events we have after reconstruction, trigger and selection processes, and N^{gen} is the number of generated events. To properly calculate the global efficiency we should replace N^{gen} by $N^{gen}/(1-\eta)$ (or ε by $\varepsilon \times (1-\eta)$), where η is the fraction of events with $|m - m0| > 15\Gamma_0$ according to the lineshape description used in generation [98]. In the case of $B_s^0 \to K^{*0}\overline{K}^{*0}$, this number is calculated by integrating the 2D distribution in $m(K^+\pi^-)$ and $m(K^-\pi^+)$,

$$\eta = \frac{\int\int_{m_{K^{*0}}+15\Gamma_{K^{*0}}}^{\infty} PDF(m_1, m_2)\mathrm{d}m_1\mathrm{d}m_2}{\int\int_{m_\pi+m_K}^{\infty} PDF(m_1, m_2)\mathrm{d}m_1\mathrm{d}m_2} \tag{6.22}$$

since $(m_\pi + m_K) > (m_{K^{*0}} - 15\Gamma_{K^{*0}})$. A equivalent expression can be written for $B^0 \to \phi K^{*0}$. The values obtained for η in both channels is shown in Table 6.23.

Table 6.23: Generator efficiencies for $B_s^0 \to K^{*0}\overline{K}^{*0}$ and $B^0 \to \phi K^{*0}$ decays and correction from the generator level mass cutoff.

Channel	ε^{gen} (%)	η
$B^0 \to \phi K^{*0}$	17.47 ± 0.04	0.09093 ± 0.00001
$B_s^0 \to K^{*0}\overline{K}^{*0}$	16.02 ± 0.04	0.02659 ± 0.00001

6.6.2.2 Selection efficiency

The reconstruction and selection efficiencies, contained in ε^{sel}, were calculated from $B_s^0 \to K^{*0}\overline{K}^{*0}$ and $B^0 \to \phi K^{*0}$ simulated data by applying the selection in table Table 6.2 and Table 6.21 respectively, with the exception of the PID cuts. Table 6.24 contains the selection efficiencies for both signal and normalisation channel. The uncertainties in the efficiencies are calculated using the binomial formula,

$$\sigma(\varepsilon) = \sqrt{\frac{\varepsilon(1-\varepsilon)}{N}} \tag{6.23}$$

where N is the total number of events before the selection is applied.

Table 6.24: Reconstruction and selection efficiencies for $B_s^0 \to K^{*0}\overline{K}^{*0}$ and $B^0 \to \phi K^{*0}$ decays.

Channel	ε^{sel} (%)
$B^0 \to \phi K^{*0}$	5.600 ± 0.023
$B_s^0 \to K^{*0}\overline{K}^{*0}$	4.605 ± 0.015
ratio	1.216 ± 0.006

6.6.2.3 PID efficiency

The efficiency associated with the particle identification cuts in the signal and normalisation channel selections is estimated in this section. As already mentioned, the discrepancies between data and MC in the PID variables, leading to discrepancies in the efficiencies, need to be taken into account. In order to do so, the same approach explained in Sect. 6.4.3 has been followed.Calibration samples have been used to determine the efficiency of selecting a known ID track by applying a certain PID cut as a function of the track properties. In this case, the momentum and pseudorapidity of the track were used. Fig. 6.13 shows the PID performance histograms for pions and kaons selected by imposing the DLL_{a-b} $(a, b = K, \pi, p)$ requirements in Table 6.2. This information is then used to reweight the $B_s^0 \to K^{*0}\overline{K}^{*0}$ MC sample and the average PID efficiency is computed. The same procedure is followed to reweight the $B^0 \to \phi K^{*0}$ MC according to the PID efficiencies corresponding to the requirements in Table 6.21.

The resulting PID efficiencies for signal and normalisation channel are summarized in Table 6.25.

Table 6.25: PID efficiencies for $B_s^0 \to K^{*0}\overline{K}^{*0}$ and $B^0 \to \phi K^{*0}$ decays. The efficiencies are calculated separately for different magnet polarities (Magnet Up and Magnet Down) and the average is computed.

Channel	ε^{sel} MU (%)	ε^{sel} MD(%)	ε^{sel} (%)
$B^0 \to \phi K^{*0}$	48.70 ± 0.14	48.44 ± 0.15	48.57 ± 0.10
$B_s^0 \to K^{*0}\overline{K}^{*0}$	45.00 ± 0.11	45.30 ± 0.11	45.15 ± 0.08
ratio	-	-	1.076 ± 0.003

6.6.2.4 Trigger efficiency

The trigger efficiencies for the signal and normalisation channels have been computed in two steps: the level-0 trigger (L0) efficiency and the High level trigger (HLT) efficiency,

$$\varepsilon^{trig} = \varepsilon^{L0} \times \varepsilon^{HLT}. \tag{6.24}$$

The L0 is responsible for the larger efficiency loss in triggering $B_s^0 \to K^{*0}\overline{K}^{*0}$ and $B^0 \to \phi K^{*0}$ decays, and its efficiency has been calculated directly from data as explained below. Simulated events have been used to determine the efficiency corresponding to the High level trigger.

The efficiency of any choice of trigger lines can be measured on real data using the

Table 6.26: L0 efficiencies for signal and normalisation channels calculated from data using the TISTOS technique.

Channel	ε^{L0} (%)
$B^0 \to \phi K^{*0}$	46.5 ± 3.9
$B_s^0 \to K^{*0}\overline{K}^{*0}$	47.8 ± 5.0
ratio	0.97 ± 0.13

TISTOS technique [112] as follows

$$\varepsilon^{trig} = \varepsilon^{TIS}\frac{N^{trig}}{N^{TIS}} \tag{6.25}$$

where TIS or “Triggered Independent of Signal” designates candidates triggered by tracks that do not belong to the final state of interest (for instance, tracks coming from decays of the accompanying b-quark) and N^{trig} is the total number of triggered events. The TIS efficiency, ε^{TIS}, can also be determined from data as

$$\varepsilon_i^{TIS} = \left(\frac{N^{TIS\&TOS}}{N^{TOS}}\right)_i \tag{6.26}$$

i being a small enough region of the signal B-meson phasespace (i.e. a B p_{T} bin) so the signal and underlying event properties are uncorrelated.

This procedure has been followed to calculate the level-0 trigger efficiency for $B_s^0 \to K^{*0}\overline{K}^{*0}$ and $B^0 \to \phi K^{*0}$. The bias induced in the calculation of ε^{TIS} when no binning in the B phasespace is considered is correlated with the topology of the decay under study. Given the similar topology of $B_s^0 \to K^{*0}\overline{K}^{*0}$ and $B^0 \to \phi K^{*0}$, the cancelation of this bias in the ratio of the trigger efficiencies is assumed to be a good approximation. This approximation was tested in simulated data as is explained in Sect. 6.6.5.3.

The number of $L0TIS$, $L0TOS$ and $L0TIS\&L0TOS$ events for signal and normalisation channels have been determined from a fit to the four body invariant mass spectrum of the events in each category, see Appendix E. The resulting L0 efficiencies are shown in Table 6.26.

The HLT efficiency, that includes the effect of HLT1 and HLT2 steps, has been determined using MC simulated $B_s^0 \to K^{*0}\overline{K}^{*0}$ and $B^0 \to \phi K^{*0}$ events. Table 6.27 shows the HLT trigger efficiencies estimated for both channels.

Table 6.27: HLT trigger efficiencies for $B_s^0 \to K^{*0}\overline{K}^{*0}$ and $B^0 \to \phi K^{*0}$ decays calculated from MC simulated data.

Channel	ε^{HLT} (%)
$B^0 \to \phi K^{*0}$	86.07 ± 0.29
$B_s^0 \to K^{*0}\overline{K}^{*0}$	85.97 ± 0.22
ratio	1.001 ± 0.004

6.6.3 Purity

The number of B_s^0 candidates in the invariant mass fit correspond rigorously to the number of $B_s^0 \to (K^+\pi^-)(K^-\pi^+)$ selected and triggered, with a $K\pi$ mass in a 150 MeV/c^2

window around the nominal K^{*0} mass. This includes K^{*0}, but also an *S–wave* component and the interference between the *S–wave* and *P–wave* components.

Here, everything that is not *S–wave* or *P–wave* and *S–wave* interference is considered as K^{*0} since the contamination from higher resonances is expected to be negligible, see Sect. 6.5.3.1. Therefore, the fraction of $B_s^0 \to K^{*0}\overline{K}^{*0}$ present in the sample is given by

$$f_{B_s^0\to K^{*0}\overline{K}^{*0}} = \frac{\displaystyle\int PDF(X; |A_s^+| = |A_s^-| = |A_{ss}| = 0)\ \varepsilon(X)\ \mathrm{d}X}{\displaystyle\int PDF(X)\ \varepsilon(X)\ \mathrm{d}X}, \tag{6.27}$$

where $X = \{\Omega, m_1, m_2\}$, $PDF(X)$ is the probability density function given by (4.18) and $\varepsilon(X)$ is the acceptance function (the efficiency as a function of X). Introducing the parameter values obtained from the amplitude analysis, see Table 6.6, this expression yields:

$$f_{B_s^0\to K^{*0}\overline{K}^{*0}} = 0.405 \pm 0.036. \tag{6.28}$$

where we have propagated the statistical uncertainties in the magnitude and phase of the different amplitudes.

A equivalent approach is needed to determine the fraction of $B^0 \to \phi K^{*0}$ within the $B_s^0 \to K^+\pi^-K^+K^-$ data. Using the results in [118], the value

$$f_{B^0\to\phi K^{*0}} = 0.760 \pm 0.018 \tag{6.29}$$

is obtained.

6.6.4 Overall angular acceptance

The last effect we need to take into account is the dependence of the overall (recontruction, selection and trigger) efficiency, ε, with the angular distribution of the particles in the final state of both signal and normalisation channels. This efficiency will be proportional to the integral of the observed angular distribution, divided by the integral of the physical distribution. For the $B_s^0 \to K^{*0}\overline{K}^{*0}$ signal (no *S–wave*) this means

$$\varepsilon \propto \frac{\int PDF(X; |A_s^+| = |A_s^-| = |A_{ss}| = 0)\ \varepsilon(X)\ \mathrm{d}X}{\int PDF(X; |A_s^+| = |A_s^-| = |A_{ss}| = 0)\ \mathrm{d}X} \tag{6.30}$$

The calculation of the efficiencies in the previous sections rely on MC simulated data which was generated with a certain choice of amplitudes that might differ from those measured in data. Thus the overall efficiency must be corrected by the factor

$$\lambda_{f_L} = \frac{\varepsilon_{data}}{\varepsilon_{MC}} = \frac{\int_X PDF(X; |A_s^+| = |A_s^-| = |A_{ss}| = 0)\ \varepsilon(X)\ \mathrm{d}X}{(1 - |A_s^+|^2 - |A_s^-|^2 - |A_{ss}|^2)\ \int PDF_{MC}(X)\ \varepsilon(X)\ \mathrm{d}X} \tag{6.31}$$

where $PDF_{MC}(X)$ represents the probability density function used in the generation of the MC sample. The numerator of (6.31) appears also in the expression used to compute the fraction of $B_s^0 \to K^{*0}\overline{K}^{*0}$, (6.27). Therefore, it is convenient to evaluate together

Table 6.28: Values of the κ factor calculated for $B_s^0 \to K^{*0}\overline{K}^{*0}$ and $B^0 \to \phi K^{*0}$ decays. This factor contains the purity and angular acceptance corrections to the efficiencies entering the $\mathcal{B}(B_s^0 \to K^{*0}\overline{K}^{*0})$ calculation.

Channel	κ
$B^0 \to \phi K^{*0}$	1.382 ± 0.035
$B_s^0 \to K^{*0}\overline{K}^{*0}$	3.123 ± 0.257
ratio	0.442 ± 0.038

$\lambda_{f_L}/f_{B_s^0 \to K^{*0}\overline{K}^{*0}}$ to take better into account the correlations when propagating the statistical uncertainties. The factor that enters the branching ratio expression, κ, is defined as

$$\begin{aligned} \kappa^{B_s^0 \to K^{*0}\overline{K}^{*0}} &\equiv \lambda_{f_L}(B_s^0 \to K^{*0}\overline{K}^{*0}) \times \frac{1}{f_{B_s^0 \to K^{*0}\overline{K}^{*0}}} \\ &= \frac{\int PDF(X)\, \varepsilon(X)\, \mathrm{d}X}{\int PDF_{MC}(X)\, \varepsilon(X)\, \mathrm{d}X} \times \frac{1}{1 - |A_s^+|^2 - |A_s^-|^2 - |A_{ss}|^2} \end{aligned} \tag{6.32}$$

This correction, associated to $B_s^0 \to K^{*0}\overline{K}^{*0}$, has been evaluated from the results in Table 6.6. The measurement in [118] allow an equivalent calculation for the $\kappa^{B^0 \to \phi K^{*0}}$. Both results are show in Table 6.28.

6.6.5 $\mathcal{B}(B_s^0 \to K^{*0}\overline{K}^{*0})$ systematic uncertainties

Three main systematic sources were considered in the calculation of the $\mathcal{B}(B_s^0 \to K^{*0}\overline{K}^{*0})$: the selection efficiency, the trigger efficiency and the mass fit bias and systematic uncertainties. The systematic uncertainties associated to the purity and angular correction are calculated by propagating the uncertainties on the results from the amplitude analysis assessed at Sect. 6.5.4.

6.6.5.1 Invariant mass fit

The systematic uncertainties induced by the model used in the mass fit are studied in this section. As explained before the B_s^0 signal (as well as the B^0 signal) is described using a double CB, where the different tails account for radiative processes and low resolution events respectively. An alternative model, consisting of a combination of a Crystal Ball and a Gaussian was tried and the variation in the number of B_s^0 signal events was taken as a systematic uncertainty.

Regarding the background description, the contribution coming from $B^0 \to \rho K^{*0}$ decays is the most likely to cause a bias in the B_s^0 yield, since this kind of events accumulate between the B^0 and B_s^0 peaks. However, the size of this contamination after the selection in Table 6.2 is expected to be small. As explained in Sect. 6.3.3, if the fraction of $B^0 \to \rho K^{*0}$ events is let free to float during the minimisation, the lower limit of the parameter allowed interval is hit. Thus, in the nominal fit the contribution from this decay is fixed to zero. In order to estimate the impact of this assumption, the nominal result is compared with the one obtained when the number of $B^0 \to \rho K^{*0}$ events is fixed to the one estimated from simulation ($N_{B^0 \to \rho K^{*0}} = 8.9 \pm 3.5$).

Table 6.29: Variation in the number of signal events, when the parameterisation of the different components of the fit is changed. The sum in quadrature of all the components is taken as systematic uncertainty.

	Signal	$B^0 \to \rho K^{*0}$ background					Total Systematic
		Data model		MC model		Syst	
		free	fixed	free	fixed		
$B_s^0 \to K^{*0}\overline{K}^{*0}$	8.2	0.12	6.54	0.04	4.15	6.54	10.5 (1.5%)
$B^0 \to \phi K^{*0}$	7.2					-	7.2 (0.7%)

Moreover, two different shapes were used to describe the shape of the $B^0 \to \rho K^{*0}$ contribution. The first one is described in Sect. 6.3.3, where a tightly selected sample of $B^0 \to \rho K^{*0}$ decays is used to fix the parameters of the model, a single Crystal Ball distribution. For the second one, a sample of $B^0 \to \rho K^{*0}$ MC events was selected using the $B_s^0 \to K^{*0}\overline{K}^{*0}$ stripping and offline selection (with the exception of the offline PID cuts) and fitted with the same shape to determine another set of parameters. Using these models for the $B^0 \to \rho K^{*0}$ background the mass fit was repeated and the largest variation in the number of B_s^0 candidates used as systematic uncertainty.

In the case of the normalisation channel, the fit was repeated with a different parameterisation of the signal shape, a combination of two Crystal Ball distributions. Table 6.29 summarizes the systematic uncertainties associated to the model used in the invariant mass fit for both channels.

Aditionally, biases in the invariant mass fit have been searched for, by generating and fitting 1000 toy MC experiments using the nominal invariant mass model and the parameter values extracted from data. The number of events generated for each toy experiment corresponds to the total number of events seen in data. The pull distribution for the signal yield is shown in Fig. 6.35. The central value and width of this distribution can be found in Table 6.30. Since the observed bias is compatible with zero, no correction to the number of B_s^0 candidates is applied. The uncertainty in the central value of the pull distribution is taken as a systematic uncertainty.

The same procedure was applied to the reference channel mass fit. Similarly, no

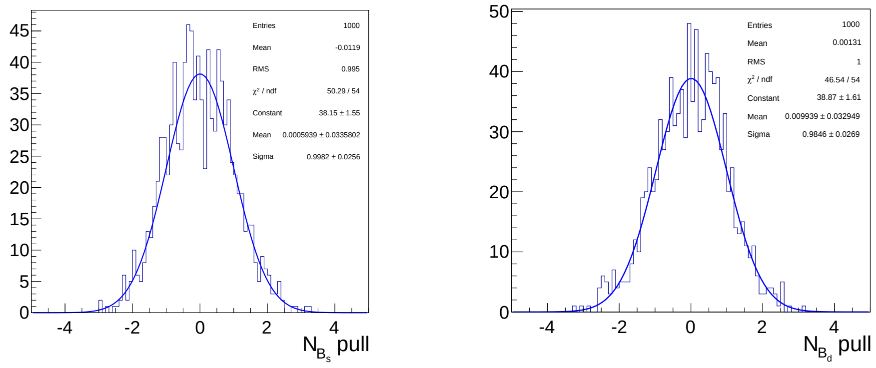

Figure 6.35: $B_s^0 \to (K^+\pi^-)(K^-\pi^+)$ (left) and $B^0 \to K^+K^-K^\pm\pi^\mp$ (right) yield pulls obtained from 1000 toy MC experiments generated and fitted with the corresponding mass model.

Table 6.30: Mean and width of the $B_s^0 \to (K^+\pi^-)(K^-\pi^+)$ and $B^0 \to K^+K^-K^\pm\pi^\mp$ yield pulls distribution obtained from 1000 toy MC experiments.

Yield	Pull mean	Pull width	Bias	Systematic
$N_{B_s^0}$	0.001 ± 0.034	0.998 ± 0.026	0.02	1.3
N_{B^0}	0.010 ± 0.033	0.985 ± 0.027	0.33	1.1

significant bias is observed, therefore no correction is applied and a systematic uncertainty is derived from the uncertainty in the pull mean.

6.6.5.2 Selection efficiencies

In order to assess the systematic uncertainty associated to the determination of the selection efficiency, the distribution of the main variables involved in the selection have been compared between $B_s^0 \to K^{*0}\overline{K}^{*0}$ data and MC simulation. In Appendix D.3 this comparison is shown. The most important differences appear for the B_s^0 meson p_{T} and IP significance, as well as for the secondary vertex χ^2. The effect of these discrepancies is expected to be small in the ratio of selection efficiencies $\varepsilon^{sel}_{B^0\to\phi K^{*0}}/\varepsilon^{sel}_{B_s^0\to K^{*0}\overline{K}^{*0}}$. Nevertheless, the size of the effect was estimated by correcting the MC distributions mentioned above to match those seen in data. The ratio of efficiencies was then recalculated, and the difference with respect to the nominal one was found to be 0.0089 (0.74%). This value is assigned as the systematic uncertainty.

6.6.5.3 Trigger efficiencies

In Sect. 6.6.2.4 the L0 trigger efficiency was determined directly from data using the TISTOS technique, considering no binning in the signal B-meson phase space. The bias induced in the ratio of efficiencies by that approximation can be determined using MC simulated data, where the L0 trigger efficiency can be computed directly as

$$\varepsilon^{L0}_{MC} = \frac{N^{L0}}{N_{sel}} \tag{6.33}$$

where N^{sel} is the number of MC events that survive the offline selection and N^{trig} is the number of those which also were selected by the L0 trigger decision. The L0 efficiency calculated above can be compared with the one obtained by applying the TISTOS technique to the MC sample. This comparison is shown in Table 6.31. The variation in the ratio of efficiencies estimated with the two different methods is considered as a systematic uncertainty in the branching ratio calculation.

Table 6.31: L0 trigger efficiencies for $B_s^0 \to K^{*0}\overline{K}^{*0}$ and $B^0 \to \phi K^{*0}$ calculated from MC simulated data with two different methods.

Channel	ε^{L0}_{MC} (%)	$\varepsilon^{L0}_{MC;TISTOS}$ (%)
$B^0 \to \phi K^{*0}$	37.54 ± 0.25	42.06 ± 0.20
$B_s^0 \to K^{*0}\overline{K}^{*0}$	50.38 ± 1.47	53.33 ± 1.14
ratio	0.893 ± 0.007	0.945 ± 0.034

Table 6.32: Summary of the relevant quantities in the $\mathcal{B}(B_s^0 \to K^{*0}\overline{K}^{*0})$ calculation. The first uncertainty is statistical, the second systematic (if just one is quoted, it represents the combination of statistical and systematic).

Parameter	Value
$N_{B_s^0}$	$697 \pm 31 \pm 11$
N_{B^0}	$1049 \pm 33 \pm 7$
$\kappa_{B^0\to\phi K^{*0}}/\kappa_{B_s^0\to K^{*0}\overline{K}^{*0}}$	$0.442 \pm 0.036 \pm 0.024$
$\varepsilon_{B^0\to\phi K^{*0}}/\varepsilon_{B_s^0\to K^{*0}\overline{K}^{*0}}$	$1.30 \pm 0.17 \pm 0.07$

6.6.6 $\mathcal{B}(B_s^0 \to K^{*0}\overline{K}^{*0})$ result

The results obtained in the previous sections were combined together in

$$\frac{\mathcal{B}(B_s^0 \to K^{*0}\overline{K}^{*0})}{\mathcal{B}(B^0 \to \phi K^{*0})} = \frac{f_d}{f_s} \times \frac{\varepsilon_{B^0\to\phi K^{*0}}}{\epsilon_{B_s^0\to K^{*0}\overline{K}^{*0}}} \times \frac{\kappa_{B^0\to\phi K^{*0}}}{\kappa_{B_s^0\to K^{*0}\overline{K}^{*0}}} \times \frac{N_{B_s^0}}{N_{B^0}} \times \frac{\mathcal{B}(\phi \to K^+K^-)}{\mathcal{B}(K^{*0} \to K^+\pi^-)} \qquad (6.34)$$

to determine $\mathcal{B}(B_s^0 \to K^{*0}\overline{K}^{*0})$ relative to $\mathcal{B}(B^0 \to \phi K^{*0})$. The values and uncertainties of the parameters in the previous expression are summarized in Table 6.32. The ratio between the hadronisation fractions has been taken from [123] and is $\frac{f_s}{f_d} = 0.259 \pm 0.015$. The value of $\mathcal{B}(\phi \to K^+K^-) = (0.489 \pm 0.005)$ is taken from [16] and $\mathcal{B}(K^{*0} \to K^+\pi^-) = 2/3$. Using these numbers, (6.34) leads to

$$\frac{\mathcal{B}(B_s^0 \to K^{*0}\overline{K}^{*0})}{\mathcal{B}(B^0 \to \phi K^{*0})} = 1.080 \pm 0.182(stat.) \pm 0.081(syst.) \pm 0.063(f_d/f_s)$$

Considering the value $\mathcal{B}(B^0 \to \phi K^{*0}) = (9.8 \pm 0.6) \times 10^{-6}$ from [16],

$$\mathcal{B}(B_s^0 \to K^{*0}\overline{K}^{*0}) = (10.6 \pm 1.8(stat.) \pm 1.0(syst) \pm 0.6(f_d/f_s)) \times 10^{-6}.$$

6.7 Triple products and direct *CP* asymmetries

The “true” TP asymmetries and direct *CP* asymmetries have been calculated for $B_s^0 \to K^{*0}\overline{K}^{*0}$ using Eqs. (4.36) - (4.39) and Eqs. (4.41) - (4.41), respectively. These quantities have been independently determined for TOS and non-TOS events. The angular distributions of the background have been parameterised using events from the high B_s^0 mass sideband, and subtracted according to the fraction present in each sample, see Sect. 6.5.1.1. After correcting for the angular acceptance, the data distribution in the relevant angular functions are shown in Fig. 6.36 (TOS) and Fig. 6.37 (non-TOS). Table 6.33 contains the TP and *CP* asymmetries measured for each sample. A weighted average between TOS and non-TOS is taken as the final result,

$$\begin{aligned}
A_T^1 &= 0.003 \pm 0.041(\text{stat.}) \pm 0.009(\text{syst.}),\\
A_T^2 &= 0.999 \pm 0.041(\text{stat.}) \pm 0.009(\text{syst.}),\\
A_T^3 &= 0.019 \pm 0.041(\text{stat.}) \pm 0.008(\text{syst.}),\\
A_T^4 &= -0.040 \pm 0.041(\text{stat.}) \pm 0.008(\text{syst.}),\\
A_D^1 &= -0.061 \pm 0.041(\text{stat.}) \pm 0.012(\text{syst.}),\\
A_D^2 &= 0.081 \pm 0.041(\text{stat.}) \pm 0.008(\text{syst.}),\\
A_D^3 &= -0.079 \pm 0.041(\text{stat.}) \pm 0.023(\text{syst.}),\\
A_D^4 &= -0.081 \pm 0.041(\text{stat.}) \pm 0.010(\text{syst.}).
\end{aligned}$$

One of the main sources of systematic error in these measurements is the effect of the angular acceptance. The angular acceptance correction is more relevant in the case of the four *CP* asymmetries with respect to the triple product asymmetries, as can be seen in Fig. 6.38. Two sources of systematics related to the angular acceptance have been considered, following the same approach as in the case of the amplitude analysis: the difference in the p_{T} spectra between data and MC (Sect. 6.5.4.3) and the statistical error in the acceptance description (Sect. 6.5.4.2).

The lifetime dependence of the different amplitudes are modified by the lifetime biasing cuts in the selection. This could induce a bias in the measured TPA and *CP* asymmetries. To determine the size of this effect, a set of toy MC samples was generated using a

Table 6.33: TP asymmetries and *CP* asymmetries measured with $B_s^0 \to K^{*0}\overline{K}^{*0}$ TOS and non-TOS events. Only statistical uncertainties are shown.

Asymmetry	TOS	non-TOS	Average
A_T^1	0.028 ± 0.058	-0.023 ± 0.059	0.003 ± 0.041
A_T^2	-0.034 ± 0.058	0.052 ± 0.059	0.009 ± 0.041
A_T^3	-0.014 ± 0.058	0.051 ± 0.059	0.019 ± 0.041
A_T^4	-0.011 ± 0.058	-0.069 ± 0.059	-0.040 ± 0.041
A_D^1	-0.004 ± 0.058	-0.117 ± 0.059	-0.061 ± 0.041
A_D^2	0.087 ± 0.058	0.075 ± 0.059	0.081 ± 0.041
A_D^3	-0.140 ± 0.057	-0.018 ± 0.059	-0.079 ± 0.041
A_D^4	-0.118 ± 0.057	-0.044 ± 0.059	-0.081 ± 0.041

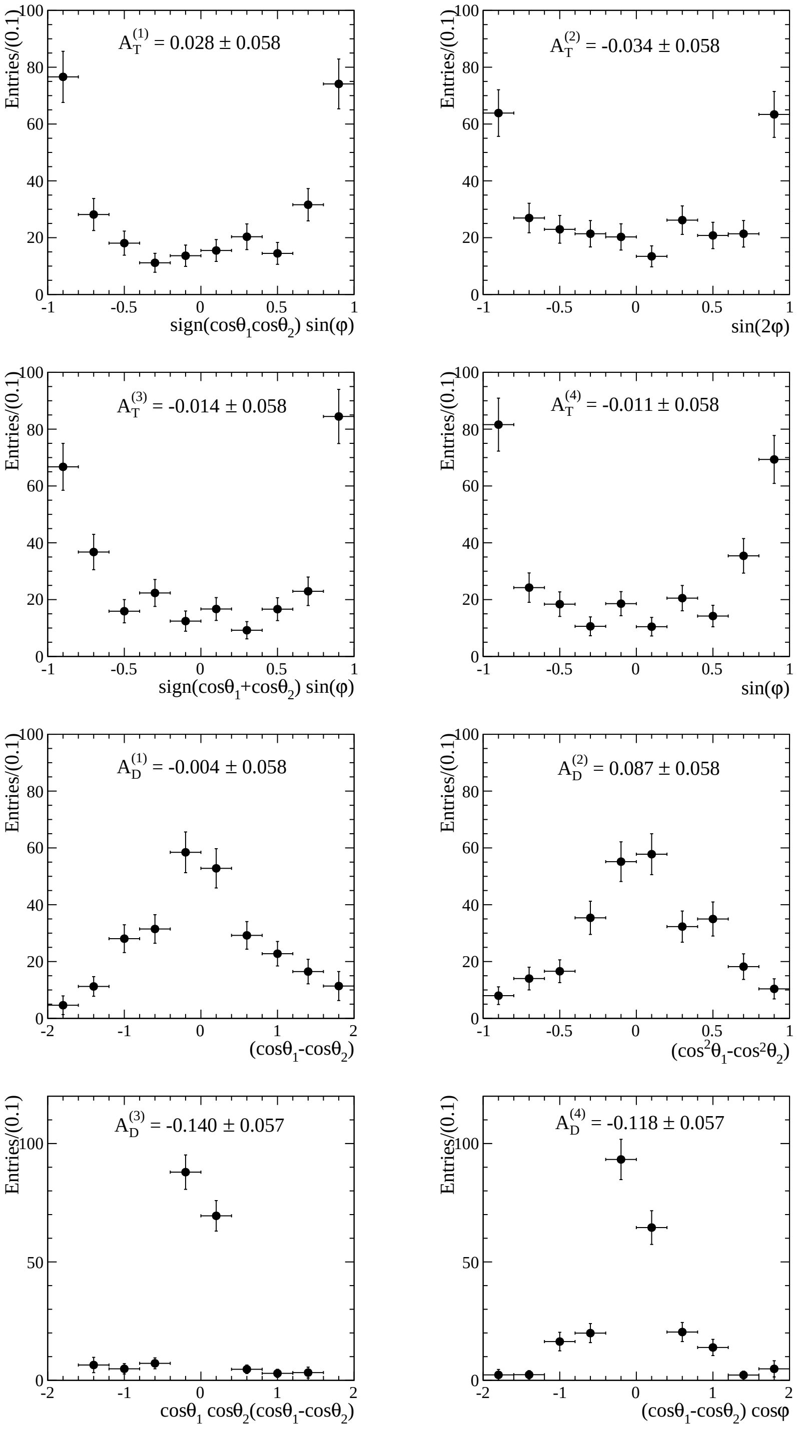

Figure 6.36: Background subtracted and acceptance corrected angular distributions of TOS events used in the determination of the true TP asymmetries (top) and *CP* asymmetries (bottom).

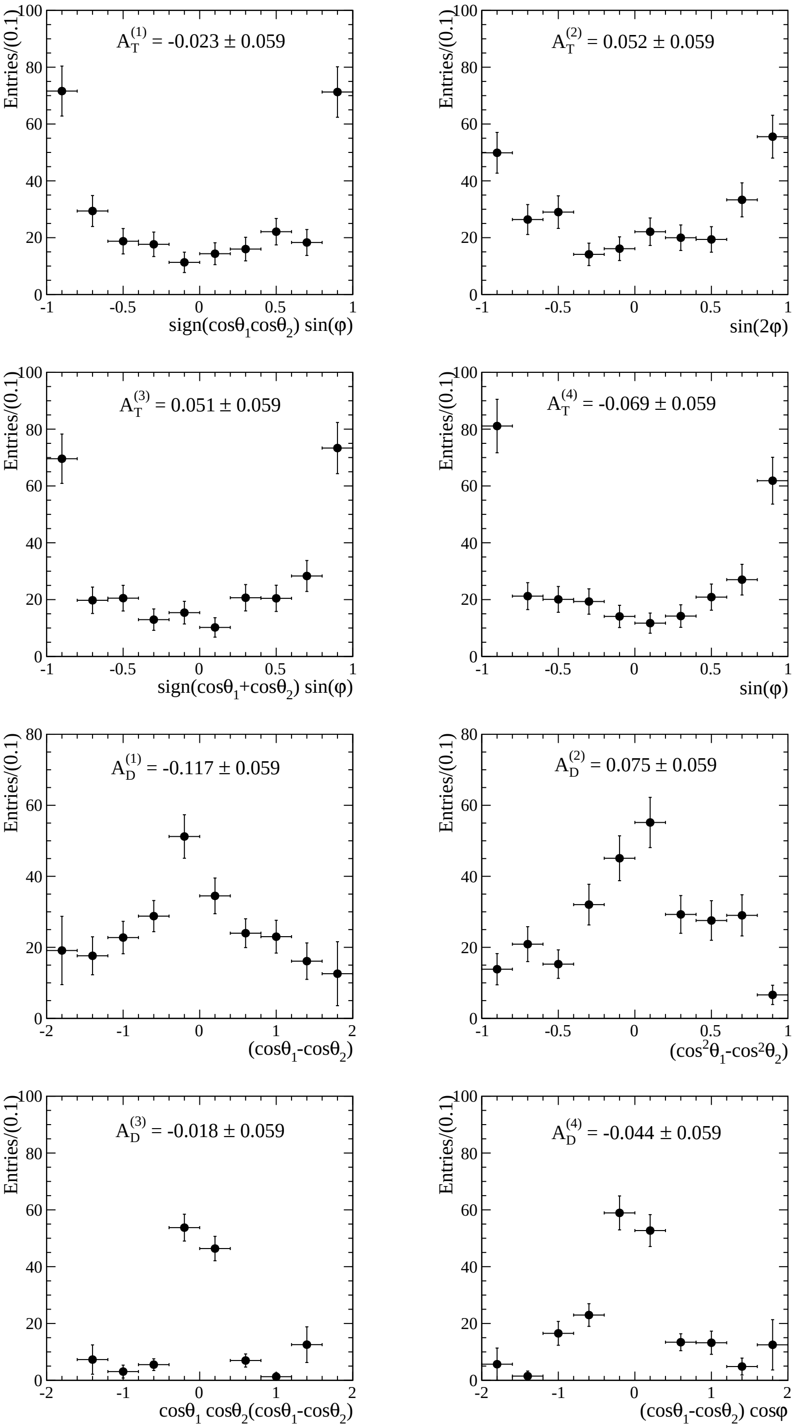

Figure 6.37: Background subtracted and acceptance corrected angular distributions of NO-TOS events used in the determination of the true TP asymmetries (top) and *CP* asymmetries (bottom).

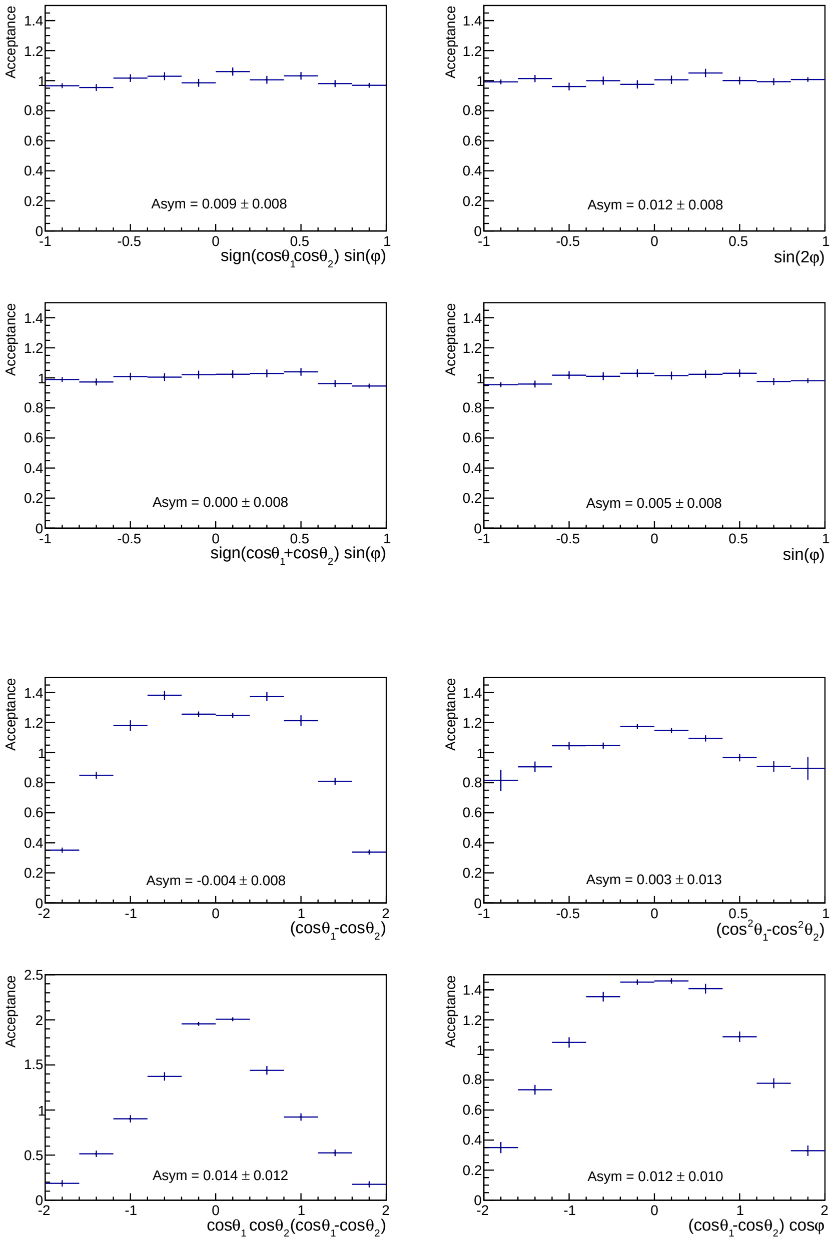

Figure 6.38: Angular acceptance function projected in the four triple products (top) and the four angular functions generating *CP* asymmetries (bottom).

Table 6.34: Summary of the systematic uncertainties on the Triple Products asymmetries for the $B_s^0 \to K^{*0}\overline{K}^{*0}$ decay mode. The total systematic uncertainty is the quadratic sum of the individual components.

Source	Angular Acceptance	Lifetime Acceptance	Background Fraction	MC Statistics	Total
A_T^1	0.0033	0.0030	0.0002	0.0074	0.0086
A_T^2	0.0044	0.0026	0.0003	0.0071	0.0087
A_T^3	0.0031	0.0014	0.0002	0.0072	0.0080
A_T^4	0.0028	0.0010	0.0003	0.0075	0.0081
A_D^1	0.0085	0.0011	0.0005	0.0078	0.0116
A_D^2	0.0014	0.0010	0.0004	0.0080	0.0081
A_D^3	0.0197	0.0087	0.0002	0.0073	0.0227
A_D^4	0.0047	0.0028	0.0003	0.0078	0.0095

time-dependent PDF that includes the change in efficiency as a function of the lifetime of the B_s^0. The lifetime acceptance was parameterised using full generated $B_s^0 \to K^{*0}\overline{K}^{*0}$ MC, see Appendix D.5. From the comparison of the values measured for the different asymmetries with the ones that had been generated, the systematic uncertainty coming from the lifetime acceptance was estimated.

Finally, the background fraction has been changed by $\pm 1\sigma$ in order to estimate the systematic effect in the measured asymmetries. The results of the systematic studies are summarised in Table 6.34.

6.8 Result discussion

The decay channel $B_s^0 \to (K^+\pi^-)(K^-\pi^+)$ has been studied using 1.0 fb^{-1} of data taken by LHCb during 2011, which corresponds to pp collisions at $\sqrt{s} = 7$ TeV centre-of-mass energy.

Two different analyses have been performed. First, using the Standard Model description of this process, the angular distribution of the decay products was analysed as a function of the $K\pi$ pairs invariant mass, in order to measure the polarisation fractions of the decay $B_s^0 \to K^{*0}\overline{K}^{*0}$ as well as the magnitude and phase of the various *S–wave* amplitudes. The low polarisation of the vector-vector decay is confirmed by the measurement $f_L = 0.201 \pm 0.057(\text{stat.}) \pm 0.040\text{syst.}$, and a large *S–wave* contribution is found $(0.665 \pm 0.067(\text{stat.}) \pm 0.030(\text{syst.}))$.

In addition, a new determination of the branching fraction of $B_s^0 \to K^{*0}\overline{K}^{*0}$ was performed, using $B_s^0 \to \phi\overline{K}^{*0}$ as normalisation channel. The measurement yielded $\mathcal{B}(B_s^0 \to K^{*0}\overline{K}^{*0}) = (10.6 \pm 1.8(\text{stat.}) \pm 1.0(\text{syst.}) \pm 0.6(f_d/f_s)) \times 10^{-6}$, compatible with the theoretical prediction [2]. It is important to note that the previous measurement given in Sect. 5.5.2, used an extrapolation from $B_d^0 \to J/\psi K^{*0}$ to estimate the *S–wave* contribution. This significantly augmented the value of the $\mathcal{B}$ to $(2.81\pm0.73)\times10^{-5}$. The measurement given in this section takes into account the *S–wave* component measured through the angular analysis of $B_s^0 \to (K^+\pi^-)(K^-\pi^+)$, which is found to be much larger than that assumed in Sect. 5.5.2. The 2010 measurement can be rescaled to include the *S–wave* fraction determined in Sect. 6.5, which reduces it to 1.1×10^{-5}, compatible with the subsequent measurement with 2011 data.

The second analysis is a search for New Physics effects. The SM predicts *CP*-violation in this decay to be negligible, therefore a measurement of a large value of any *CP*-asymmetry would be a sign of physics beyond the SM. Eight *CP*-violating quantities accessible to the untagged sample were measured from their corresponding angular asymmetries. However, within the statistical precision all of them were found to be compatible with *CP*-conservation.

7
Conclusions

In this thesis, the study of the decay channel $B_s^0 \to K^{*0}\overline{K}^{*0}$ with the first data collected by LHCb during 2010 and 2011 is presented. The datasets correspond, respectively, to 37 pb^{-1} and 1.0 fb^{-1} of proton-proton collisions at a centre-of-mass energy of $\sqrt{s} = 7$ TeV.

$B_s^0 \to K^{*0}\overline{K}^{*0}$ is an example of a Flavour-Chaging Neutral Current process, which is mediated by penguin diagrams in the Standard Model. This feature makes it very sensitive to new heavy particles circulating in the loop. Predictions for the branching ratio and polarisation fractions of this decay have been given in the context of QCD factorisation. Additionally, no *CP*-violation is expected in this decay within the Standar Model, as long as subdominant penguins are neglected. *CP* observables in this process, such as triple product asymmetries, therefore provide a good handle to test theories beyond the Standard Model.

The first observation of this decay channel has been reported. Using the dataset recorded by LHCb during 2010, a clear $B_s^0 \to (K^+\pi^-)(K^-\pi^+)$ signal was found with a statistical significance of more than 10σ. Normalising to the $B_d^0 \to J/\psi K^{*0}$ decay channel, the branching ratio of $B_s^0 \to K^{*0}\overline{K}^{*0}$ was measured, assuming the contribution from scalar $K\pi$ production in the final state is equivalent to what was measured in the normalisation channel [105]. The result is the following,

$$\mathcal{B}\left(B_s^0 \to K^{*0}\overline{K}^{*0}\right) = (2.81 \pm 0.46(\text{stat.}) \pm 0.45(\text{syst.}) \pm 0.34\,(f_s/f_d)) \times 10^{-5}$$

Additionally, a simplified analysis of the angular distribution of the decay products was also carried out to measure the longitudinal polarisation fraction,

$$f_L = 0.31 \pm 0.12(\text{stat.}) \pm 0.04(\text{syst.})$$

With the larger sample recorded by LHCb during 2011, a more precise time integrated and untagged analysis was carried out of the decay $B_s^0 \to (K^+\pi^-)(K^-\pi^+)$. The analysed observables were the three decay angles in the helicity basis and the masses of the $K^+\pi^-$ and $K^-\pi^+$ systems, in a ± 150 MeV/c^2 window of the $K^{*0}(892)$. In this window, the final state is dominated by the resonant components $B_s \to K^{*0}(892)\bar{K}^{*0}(892)$, $B_s \to K^{*0}(892)(K^-\pi^+)_0$ and $B_s \to (K^+\pi^-)_0(K^-\pi^+)_0$, which we designate generically as *P–wave* and *S–wave*. Among the 6 amplitudes contributing, two of them are *CP*-odd, the transversity $A_\perp$ in the *P–wave* and A_s^+ in the *S–wave*, and the rest are *CP*-even.

Two approaches have been followed in this analysis. In one of them a determination is performed, in a model independent way, of the 8 angular asymmetries that are sensitive to

CP-violation, accessible, even in the case of untagged analysis, through the interference terms between either of the *CP*-odd amplitudes and the rest of *CP*-even amplitudes. Four of them are true triple products asymmetries ($A_T^{(i)}$), and the other four are direct *CP*-asymmetries ($A_D^{(i)}$). The measured asymmetries are the following,

$$\begin{aligned}
A_T^1 &= 0.003 \pm 0.041(\text{stat.}) \pm 0.009(\text{syst.}),\\
A_T^2 &= 0.999 \pm 0.041(\text{stat.}) \pm 0.009(\text{syst.}),\\
A_T^3 &= 0.019 \pm 0.041(\text{stat.}) \pm 0.008(\text{syst.}),\\
A_T^4 &= -0.040 \pm 0.041(\text{stat.}) \pm 0.008(\text{syst.}),\\
\\
A_D^1 &= -0.061 \pm 0.041(\text{stat.}) \pm 0.012(\text{syst.}),\\
A_D^2 &= 0.081 \pm 0.041(\text{stat.}) \pm 0.008(\text{syst.}),\\
A_D^3 &= -0.079 \pm 0.041(\text{stat.}) \pm 0.023(\text{syst.}),\\
A_D^4 &= -0.081 \pm 0.041(\text{stat.}) \pm 0.010(\text{syst.}).
\end{aligned}$$

Within the statistical precision, none of them show significant *CP*-violation. This is expected in the Standard Model, even in the presence of a non-zero weak phase ϕ_s, since the above observables depend to lowest order on differences between weak phases of interfering amplitudes.

In the second approach, a combined angular and mass analysis was performed that included the 6 helicity amplitudes in the ±150 MeV/c^2 $K^{*0}(892)$ mass window, where the *CP*-violating interference terms were neglected. As a result of this analysis, all magnitudes and measurable phases of the helicity amplitudes were determined. A strong *S–wave* component was found ($0.665\pm0.067\pm0.030$), mostly *CP*-even. The longitudinal component of the $K^{*0}(892)$ polarisation is measured to be low

$$f_L = 0.201 \pm 0.057(\text{stat.}) \pm 0.040(\text{syst.}),$$

and compatible with the previous measurement. As a further consequence of the angular and mass analyses, the branching fraction of the vector-vector mode $B_s \to K^{*0}(892)\bar{K}^{*0}(892)$ has been determined to yield

$$\mathcal{B}(B_s^0 \to K^{*0}\overline{K}^{*0}) = (10.6 \pm 1.8(\text{stat.}) \pm 1.0(\text{syst.}) \pm 0.6(f_d/f_s)) \times 10^{-6}.$$

This result is in good agreement with the central values of existing theoretical predictions [2] which show larger systematic errors. It is also compatible with the previous measurement, when the large *S–wave* contribution observed in $B_s^0 \to (K^+\pi^-)(K^-\pi^+)$ is properly taken into account.

This work opens the way for a high statistics flavour tagged and time dependent analysis of the B_s^0 oscillation, in order to probe the electroweak phase ϕ_s common to all *CP*-even and *CP*-odd states, predicted to be very small in the Standard Model.

Summary

The Standard Model (SM) of Particle Physics is currently the most reliable description of fundamental particles and their interactions. Despite its success in explaining a large variety of phenomena, the SM fails to incorporate elements such as gravity, Dark Matter or neutrino's oscillation. Several New Physics (NP) models have been proposed to solve these issues. It is the objective of experiments such as the Large Hadron Collider (LHC) at CERN to test NP models predictions and to look for departures from the SM expectations.

B-physics constitutes an excellent benchmark for measuring SM parameters such as the CKM matrix elements or CP-violation. Furthermore, $b \to q$ flavour-changing neutral current (FCNC) processes, are very sensitive to deviations from the SM induced by NP particles circulating in the loops. One example of such a process is the decay $B_s^0 \to K^{*0}\overline{K}^{*0}$.

The LHCb experiment at the LHC was designed to study rare decays and CP violation in b-hadron decays, with the hope of revealing physics beyond the SM. The work presented in this thesis corresponds to the analysis of the decay mode $B_s^0 \to K^{*0}\overline{K}^{*0}$ with the data taken by LHCb during 2010 and 2011.

S.1 $B_s^0 \to K^{*0}\overline{K}^{*0}$ in the Standard Model

Within the SM, the FCNC $b \to sd\bar{d}$ transition responsible for the $B_s^0 \to K^{*0}\overline{K}^{*0}$ decay proceeds through one-loop gluonic penguin transitions, dominated by a virtual intermediate top quark coupling to a W boson. Extensions of the SM predict additional one-loop contributions that could introduce sizeable effects on the dynamics of the transition.

Predicting the observables accesible to exclusive hadronic decays, such as $B_s^0 \to K^{*0}\overline{K}^{*0}$, is complicated, since the hadronisation process introduces intrinsically non-perturbative effects. Theoretical predictions can be made within QCD factorisation (QCDf) framework, by decomposing the hadronic matrix element into from factors and decay constants. In this context, the available prediction for the branching fraction of this decay mode is $\mathcal{B}(B_s^0 \to K^{*0}\overline{K}^{*0}) = (9.1^{+11.3}_{-6.8}) \times 10^{-6}$, which improves to $(7.9^{+4.3}_{-3.9}) \times 10^{-6}$ when experimental input from $B^0 \to \phi K^{*0}$ is used.

Since the K^{*0} resonances have spin 1, $B_s^0 \to K^{*0}\overline{K}^{*0}$ is, in fact, three different decays with K^{*0} helicities $h = 0, \pm 1$. Therefore, it is described by three different amplitudes that can be disentangled through an angular analysis of the decay products of the two K^{*0} mesons. The relative fraction corresponding to the longitudinal amplitude ($h = 0$) has also been calculated in QCDf yielding $f_L = 0.63^{+0.42}_{-0.29}$ ($0.72^{+0.16}_{-0.21}$ when input from $B^0 \to \phi K^{*0}$ is used).

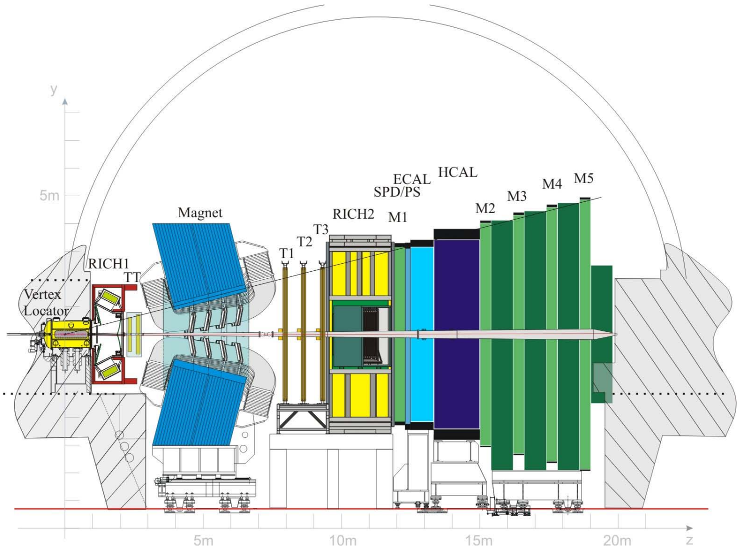

Figure S.1: View of the LHCb detector.

Regarding *CP* violation, the SM predicts it to be negligible for this decay due to the strong suppression of the subdominant penguin contributions. Therefore, if any *CP*-violating quantity is measured to be large for this decay, this would be a signal of physics beyond the SM.

S.2 LHCb experiment at the LHC

LHCb is one of the four big detectors placed along the LHC accelerator at CERN. It is dedicated to the study of *CP* violation and rare decays in hadrons containing *b*-quarks.

The correct identification of the primary vertex (PV), where the *b*-hadron is produced, and secondary vertex (SV), where the *b*-hadron decays, is essential for all the LHCb analyses. This task becomes more difficult as the instantaneous luminosity increases, due to the larger number of *pp* interactions. In order to limit the effect of overlapping events, LHCb works at an instantaneous luminosity smaller than that of other LHC experiments.

S.2.1 The LHCb detector

The LHCb detector is a single-arm spectrometer with a forward angular coverage from approximately 10 mrad to 300 (250) mrad in the bending (non-bending) plane of the magnet. The main elements of LHCb, shown in Fig. S.1, are:

- Magnet: A warm dipole that provides an integrated field of 4 $\mathrm{T} \cdot \mathrm{m}$.
- Vertex Locator (VELO): Silicon detector that provides precise information of the production and decay vertices of *b*-hadrons (PV and SV).
- Tracking System: Composed of the *Tracker Turiciensis* (TT) before the magnet and three *Tracking Stations* (T1, T2, T3) after the magnet. This system allows the reconstruction of the trajectory of charged particles. In the TStations, the inner part (IT) uses silicon microstrip sensors, and the outer one uses drift tubes.

- Two Ring Imaging Cherenkov Detectors (RICH): These two detectors (RICH-1 before the magnet and RICH-2 after the magnet) have the task of identifying charged particles over the momentum range 2-100 GeV/c.

- Calorimeter System: SPD (*Scintillator Pad Detector*), PS (*PreShower*), ECAL (*Electromagnetic CALorimeter*) and HCAL (*Hadronic CALorimeter*) compose the calorimeter system. The purpose of this subdetector is to provide identification of electrons and hadrons with measurements of position and energy.

- Muon System: A combination of MWPC (*Multi Wire Proportional Cambers* and GEM (*Gas Electron Multiplier*) are used to identify muons that have passed through the calorimeters.

The rate of events taken by LHCb from proton-proton LHC collisions is in the order of several million per second, too high to be managed. The LHCb trigger system uses the information collected by the different subdetectors to reduce this huge amount of events, while retaining as many interesting b decays as possible, before they are transferred to long-term data storage. In particular, during 2011 the LHCb trigger reduced the rate from ~ 15 MHz to ~ 3 kHz, by exploting the main signatures of particles coming from b-hadron decays (high p_{T}, impact parameter,etc).

The analysis of this thesis is based on the data taken by LHCb from the LHC pp collision at a centre-of-mass energy of $\sqrt{s} = 7$ TeV during 2010 and 2011. The integrated luminosity corresponds to 37 pb^{-1} and 1.0 fb^{-1} respectively.

S.3 The $B_s^0 \to (K^+\pi^-)(K^-\pi^+)$ decay rate

The $B_s^0 \to K^{*0}\overline{K}^{*0}$ decay was searched for in the charged final state $B_s^0 \to (K^+\pi^-)(K^-\pi^+)$, where the $K\pi$ pairs are required to have an invariant mass within ± 150 MeV/c^2 of the $K^{*0}(892)$ nominal mass. In this mass window, an scalar component (S) is found in addition to the vector resonance (V). The decay is therefore described by six different amplitudes. Three of them are the amplitudes describing the $B \to V_1V_2$ decay (*P–wave*), which, in the transversity basis, are: A_0, $A_\parallel$ and $A_\perp$. The other three (*S–wave*) correspond to the decays[1]: $B \to V_1S_2$ (A_{VS}), $B \to S_1V_2$ (A_{SV}) and $B \to S_1S_2$ (A_{ss}).

It is convenient to define the linear combinations $A_s^+ = (A_{VS}+A_{SV})/\sqrt{2}$, $A_s^- = (A_{VS}-A_{SV})/\sqrt{2}$, so the decay rate can be entirely written in terms of amplitudes associated to CP-even (0, $\parallel$, s^-,ss) and CP-odd ($\perp$, s^+) eigenstates.

S.3.1 Amplitude analysis in the SM

In order to disentangle all of these contributions, the angular distribution of the decay products has to be compared with the differential decay rate corresponding to the interfering combination of the amplitudes. Furthermore, the mixing in the neutral B_s^0 meson system introduces a time dependence in these amplitudes, which is different for A_f and $\bar{A}_f$, the amplitudes describing $B \to f$ and $\overline{B} \to \bar{f}$ respectively. However, due to the small size of the data sample available, *flavour tagging* algorithms, used to determine the

---

[1] The underscript 1 (2) corresponds the $K^+\pi^-$ ($K^-\pi^+$) pair.

flavour of the B_s^0 meson at the production time, could not be applied. Consequently, an untagged and time-integrated analysis was carried out.

The decay rate can thus be written as a function of the three angles in the helicity basis ($\Omega : \{\cos\theta_1, \cos\theta_2, \varphi\}$) and the invariant mass of the $K^+\pi^-$ (m_1) and the $K^-\pi^+$ (m_2) pairs as follows

$$\frac{\mathrm{d}\Gamma}{\mathrm{d}\Omega \mathrm{d}m_1 \mathrm{d}m_2} = \sum_{n=1}^{21} K_n(m_1, m_2) F_n(\Omega), \tag{S.1}$$

where the functions K_n contain the dependence with the different amplitudes and F_n give the angular distribution associated with each amplitude combination. Assuming no CP-violation, following the prediction of the Standard Model, simplifies the functions K_n. In particular, every term proportional to the interference between a CP-odd and a CP-even amplitude vanish. The reason is that those terms are proportional to Triple Product aysmmetries and direct CP asymmetries, which are CP-violating quantities.

S.3.2 Triple Product and Direct asymmetries

Although no distinction between B and $\overline{B}$ decays is made in the analysis presented here, a CP-violation study is still possible. In $B \to VV$ decays two CP-violating triple products asymmetries (TPA) arise in the untagged sample. In particular, these TPA are proportional to the interference terms between the CP-odd amplitude $A_\perp$ and the two CP-even amplitudes A_0 and $A_\parallel$. When the *S–wave* contribution is taken into account, two more CP-even amplitudes are subject to interference with $A_\perp$. Additionally, interferences between the CP-odd amplitude A_s^+ and the CP-even amplitudes give rise to four CP-violating quantities that have been verified to have the structure of direct CP asymmetries.

Therefore, eight CP-violating observables, four TPA $A_T^{(i)}$ and four direct CP asymmetries $A_D^{(i)}$ ($i = 1, ..., 4$), are measurable with the available sample. It can be shown that these observables can be determined from an asymmetric angular integration of the decay rate following

$$A_{T,D}^{(i)} = \frac{N(U_{T,D}^i(\Omega) > 0) - N(U_{T,D}^i(\Omega) < 0)}{N(U_{T,D}^i(\Omega) > 0) + N(U_{T,D}^i(\Omega) < 0)} \tag{S.2}$$

where $U_{T,D}^{(i)}$ is the angular function associated with the term in the decay rate proportional to $A_{T,D}^{(i)}$. Table S.1 contain the definition of each of the CP-violating observables in terms of the amplitudes and their corresponding angular function $U_{T,D}^{(i)}$. Since no CP-violation is expected within the SM for this process, the measurement of a large value for any of these quantities would be a signal of New Physics.

S.4 First observation of $B_s^0 \to K^{*0}\overline{K}^{*0}$

No evidence for the $B_s^0 \to K^{*0}\overline{K}^{*0}$ decay had been found before the start of the LHC, and only an upper limit for its branching fraction, $\mathcal{B}(B_s^0 \to K^{*0}\overline{K}^{*0}) < 1.68 \times 10^{-3}$ at a 90% CL, had been reported by the SLD collaboration.

Both BaBar and Belle collaborations reported searches for the U-spin rotated channel, $B^0 \to K^{*0}\overline{K}^{*0}$. However, whilst BaBar claimed the discovery and presented a branching

Table S.1: Summary of the *CP*-violating observables which can be measured in the untagged analysis of $B_s^0 \to (K^+\pi^-)(K^-\pi^+)$ and the angular functions associated to each of them. The middle column gives the TPA or direct *CP* asymmetry which give rise to each of the observables.

Observable	TPA / Direct *CP* asymmetry	$U^i_{T,D}(\Omega)$
$A_T^{(1)}$	$\Im(A_\perp A_0^* - \bar{A}_\perp \bar{A}_0^*)$	$\text{sign}(\cos\theta_1\cos\theta_2)\sin\varphi$
$A_T^{(2)}$	$\Im(A_\perp A_\parallel^* - \bar{A}_\perp \bar{A}_\parallel^*)$	$\sin 2\varphi$
$A_T^{(3)}$	$\Im(A_\perp (A_s^-)^* - \bar{A}_\perp (\bar{A}_s^-)^*)$	$\text{sign}(\cos\theta_1 + \cos\theta_2)\sin\varphi$
$A_T^{(4)}$	$\Im(A_\perp A_{ss}^* - \bar{A}_\perp \bar{A}_{ss}^*)$	$\sin\varphi$
$A_D^{(1)}$	$\Re(A_s^+ A_0^* - \bar{A}_s^+ \bar{A}_0^*)$, $\Re(A_s^+ A_{ss} - \bar{A}_s^* \bar{A}_{ss}^*)$	$\cos\theta_1\cos\theta_2(\cos\theta_1 - \cos\theta_2)$
$A_D^{(2)}$	$\Re(A_s^+ A_\parallel^* - \bar{A}_s^+ \bar{A}_\parallel^*)$	$(\cos\theta_1 - \cos\theta_2)\cos\varphi$
$A_D^{(3)}$	$\Re(A_s^+ A_0^* - \bar{A}_s^+ \bar{A}_0^*)$, $\Re(A_s^+ A_{ss} - \bar{A}_s^* \bar{A}_{ss}^*)$	$(\cos\theta_1 - \cos\theta_2)$
$A_D^{(4)}$	$\Re(A_s^+ (A_s^-)^* - \bar{A}_s^+ (\bar{A}_s^-)^*)$	$(\cos^2\theta_1 - \cos^2\theta_2)$

ratio measurement of $(1.28^{+0.35}_{-0.30} \pm 0.11) \times 10^{-6}$, Belle set an upper limit of $\mathcal{B}(B^0 \to K^{*0}\overline{K}^{*0}) < 0.8 \times 10^{-6}$ at 90% CL a few years later. In the same paper, BaBar also reported a measurement of the longitudinal polarisation fraction for $B^0 \to K^{*0}\overline{K}^{*0}$ of $f_L = 0.80^{+0.10}_{-0.12} \pm 0.06$.

The search for $B_s^0 \to K^{*0}\overline{K}^{*0}$ at LHCb is presented here, based in the data collected from LHC pp collisions at $\sqrt{s} = 7$ TeV during 2010, which corresponds to 37 pb^{-1} of integrated luminosity.

S.4.1 Event selection

In the search for $B_s^0 \to K^{*0}\overline{K}^{*0}$, a first set of selection criteria was applied to reduce most of the background. Essentially, candidates are required to have four high-p_T charged tracks forming a well-defined vertex separated from the primary pp interaction. Based on the particle identification system, these four tracks need to be to be compatible with the hypothesis of two $K\pi$ pairs, which are also required to have an invariant mass within ± 150 MeV/c^2 of the $K^{*0}(892)$ nominal mass.

Further background reduction was achieved by defining a multivariate discriminant from information regarding the event topology, the Geometrical Likelihood (GL). The GL was trained using Monte Carlo $B_s^0 \to K^{*0}\overline{K}^{*0}$ events to simulate the signal and a small data sample of early 2010 data (excluded from the rest of the analysis) as background.

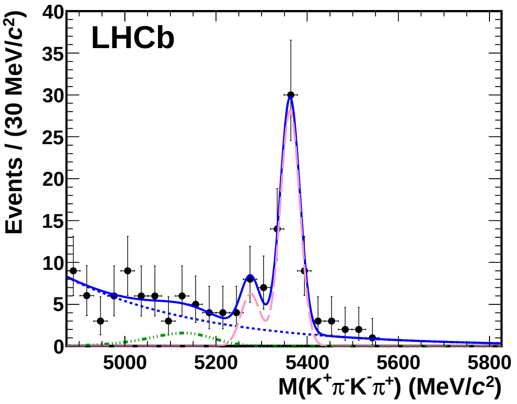

Figure S.2: Fit to the $K^+\pi^-K^-\pi^+$ mass distribution of selected candidates. The fit model (dashed pink curve) includes two signal components corresponding to the B_s^0 and B^0 decays. The background is described as a combinatorial component (dotted blue) plus a contribution from partially reconstructed decays (dash-dotted green).

S.4.2 Invariant mass spectrum

The invariant mass of the four reconstructed particles for the candidates selected with the previously described criteria is shown in Fig. S.2. From a maximum likelihood fit to this spectrum the number of $B_s^0 \to (K^+\pi^-)(K^-\pi^+)$ candidates was determined. The model used to describe the data includes the signals from $B_{s(d)} \to K^+\pi^-K^-\pi^+$ decay modes, described by two Gaussian probability density functions (PDF), a decreasing exponential to model the combinatorial background and a modified ARGUS distribution to parameterise the background coming from partially reconstructed B-decays.

The measured B_s^0 signal yield in a window of $\pm 50\,\text{MeV}/c^2$ around the B_s^0 mass is $N_{B_s^0} = 49.8 \pm 7.5(\text{stat.})$, with a significance of $10.9\,\sigma$. The peak at the B^0 mass, though not significant, is compatible with the $B^0 \to K^{*0}\overline{K}^{*0}$ branching fraction measured by BaBar.

S.4.3 Angular analysis

Due to the small size of the signal, a simplified version of the angular analysis presented in Sect. S.3.1 was performed: a mass integrated fit to the angular distribution, assuming no contamination from the *S–wave* amplitudes. The measurable parameters were the relative fraction of each of the transversity amplitudes, usually referred to as *polarisation fractions*,

$$f_{L,k} = \frac{|A_{0,k}|^2}{|A_L|^2 + |A_\parallel|^2 + |A_\perp|^2} \quad , \quad k = \parallel, \perp, \tag{S.3}$$

and $\delta_\parallel$, the phase difference between A_0 and $A_\parallel$.

The effects induced by the detector geometrical acceptance, and the reconstrucction and selection processes were determined using simulated $B_s^0 \to K^{*0}\overline{K}^{*0}$ events, and were described in terms of an acceptance function of the decay angles. The acceptance function was found compatible with being constant in φ. In contrast, it has a strong dependence

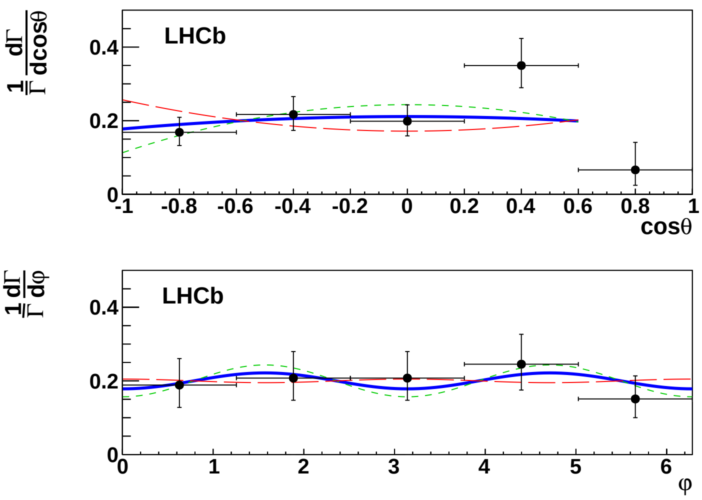

Figure S.3: $\cos\theta$ (above) and φ (below) acceptance corrected distributions for $B_s^0 \to K^{*0}\overline{K}^{*0}$ candidates. The blue line is the projection of the fit model for the measured values of the parameters f_L, $f_\parallel$ and $\delta_\parallel$. The dotted lines indicate $\pm1\sigma$ variation of the f_L central value.

on the K^{*0} polarisation angle θ, dropping asymmetrically as $\cos\theta_{1,2}$ becomes close to ±1, as a consequence of the minimum p and $p_{\rm T}$ of the tracks imposed by the reconstruction and selection. This effect is more important for the limit $\cos\theta \to +1$, i.e. when the π meson is emitted backwards with respect to the K^{*0} momentum.

After modifying the decay rate to take into account the acceptance, an unbinned maximum likelihood was performed to the angular distribution of the candidates with a four-body invariant mass in a ±50 MeV/c^2 window around the B_s^0 mass. The remaining background was parameterised using data from the B_s^0 sidebands and fixed to the fraction determined from the the invariant mass fit. The result is shown in Fig. S.3. The K^{*0} polarisation fractions were measured to be $f_L = 0.31 \pm 0.12(\text{stat.}) \pm 0.04(\text{syst.})$ and $f_\perp = 0.38 \pm 0.11(\text{stat.}) \pm 0.04(\text{syst.})$. A significant measurement of $\delta_\parallel$ could not be achieved ($\delta_\parallel = 1.47 \pm 1.85$). The main contribution to the systematic uncertainties previously quoted come from the determination of the angular acceptance, where data from the decay $B_d^0 \to J/\psi K^{*0}$ weres used to correct the acceptance description obtained from simulation.

It is remarkable that the longitudinal polarisation of the K^{*0} mesons seems to be quite different between $B_s^0 \to K^{*0}\overline{K}^{*0}$ and $B^0 \to K^{*0}\overline{K}^{*0}$, despite the fact that the two decays are related by a U-spin rotation.

S.4.4 Branching ratio determination

In order to determine the branching ratio for the $B_s^0 \to K^{*0}\overline{K}^{*0}$ decay, the number of events observed has been normalised to the number of candidates found for a reference channel with known $\mathcal{B}$. The decay $B_d^0 \to J/\psi K^{*0}$ was chosen for this purpose because it has a similar topology to the signal.

The following expression was used

$$\mathcal{B}\left(B_s^0 \to K^{*0}\overline{K}^{*0}\right) = \lambda_{f_L} \times \frac{\epsilon^{sel}_{B_d^0 \to J/\psi K^{*0}}}{\epsilon^{sel}_{B_s^0 \to K^{*0}\overline{K}^{*0}}} \times \frac{\epsilon^{trig}_{B_d^0 \to J/\psi K^{*0}}}{\epsilon^{trig}_{B_s^0 \to K^{*0}\overline{K}^{*0}}} \times \frac{N_{B_s^0 \to K^{*0}\overline{K}^{*0}}}{N_{B_d^0 \to J/\psi K^{*0}}}$$
$$\times \mathcal{B}_{vis}(B_d^0 \to J/\psi K^{*0}) \times \frac{f_d}{f_s} \times \frac{9}{4}, \tag{S.4}$$

The ratio of reconstruction and selection efficiencies (ϵ^{sel}) was calculated using simulation, and validated in data. The correction factor λ_L, takes into account the effect of the different polarisation between data and Monte Carlo in the determination of these efficiencies. Trigger efficiencies for normalisation and signal channels were directly obtained from data. Trigger differences induced by the two muons from the J/ψ decay were mitigated by only considering candidates selected by the hadronic trigger.

The number of candidates for the normalisation channel was obtained by fitting the invariant mass spectrum, $M(J/\psi, K, \pi)$. The ratio with the number of signal candidates was then corrected to take into account the non-resonant contribution in the $K\pi$ system, which was extrapolated from a previous BaBar measurement in $B_d^0 \to J/\psi K^{*0}$ decays.

Finally, the wold average of the visible branching ratio, $\mathcal{B}_{vis}(B_d^0 \to J/\psi K^{*0})$, which is the product $\mathcal{B}(B_d^0 \to J/\psi K^{*0}) \times \mathcal{B}(J/\psi \to \mu^+\mu^-) \times \mathcal{B}(K^{*0} \to K^+\pi^-)$, and the ratio of B_s^0 and B^0 production fractions measured by LHCb were used. The result obtained is

$$\mathcal{B}(B_s^0 \to K^{*0}\overline{K}^{*0}) = (2.81 \pm 0.46\ (\text{stat.}) \pm 0.45\ (\text{syst.}) \pm 0.34\ (f_s/f_d)) \times 10^{-5},$$

compatible with theoretical estimations within the Standard Model.

S.5 Time integrated untagged analysis of $B_s^0 \to K^{*0}\overline{K}^{*0}$

A more detailed analysis of the decay channel $B_s^0 \to K^{*0}\overline{K}^{*0}$ was performed with a higher luminosity data sample collected by LHCb during 2011, from LHC *pp* collisions at $\sqrt{s} = 7$ TeV. The full amplitude analysis described in Sect. S.3.1 was performed and provided a more accurate measurement of the polarisation fractions along with the first determination of the *S–wave* contributions in the $B_s^0 \to (K^+\pi^-)(K^-\pi^+)$. This also allowed a more precise measurement of $\mathcal{B}(B_s^0 \to K^{*0}\overline{K}^{*0})$. A search for physics beyond the SM was performed through the measurement of the eight *CP*-violating observables accessible to the untagged analysis of this sample.

S.5.1 Event selection and signal yield

$B_s^0 \to K^{*0}\overline{K}^{*0}$ candidates were selected from data using a set of requirements similar to those applied in the analysis of 2010 data. The GL was redefined using a new sample of $B_s^0 \to K^{*0}\overline{K}^{*0}$ simulated data and the same background sample.

Peaking background contributions from three specific *b*-hadron decays were identified: $B^0 \to \rho K^{*0}$, $B^0 \to \phi K^{*0}$ and $\Lambda_b^0 \to p\pi K\pi$. $B^0 \to \rho K^{*0}$ decays are likely to be selected when a pion from the ρ decay is misidentified as a kaon, and they accumulate in the region between the B^0 and B_s^0 nominal masses in the four-body mass spectrum. Strong particle identification requirements were applied in order to suppress this contamination. A similar

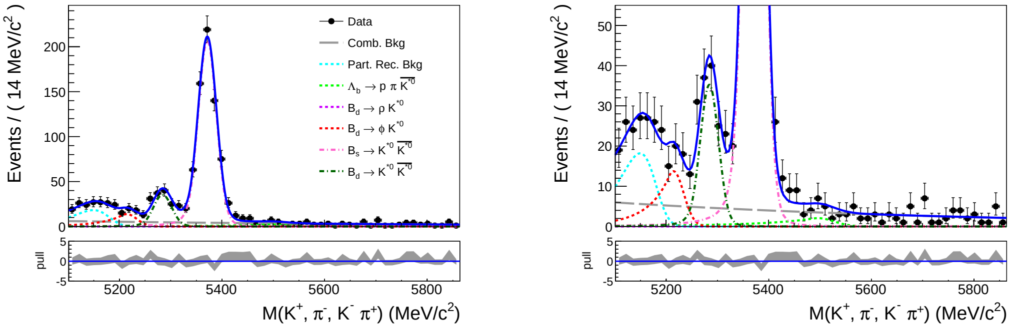

Figure S.4: Results of the four-body invariant mass fit (left) and zoom around the low statistics region (right). The solid points represent the selected data and the blue solid line is the fitted model. The B_s^0 (B^0) signal peak is shown as a pink (dark green) dashed and dotted line. The different peaking background components are represented as dotted lines: $B^0 \to \phi K^{*0}$ (red), $\Lambda_b^0 \to p\pi K\pi$ (green) and partially reconstructed decays (light blue). The grey dashed line is the combinatorial background component.

case is the decay $B^0 \to \phi K^{*0}$ when a kaon from the ϕ decay is identified as a pion. This contribution is expected to appear in the low mass sideband. The last contaminating decay, $\Lambda_b^0 \to p\pi K\pi$, had not been reported before, but it enters this spectrum in the high mass sideband when the proton is misidentified as a kaon.

Taking into account all of these contributions, an unbinned maximum likelihood fit was performed to the mass spectrum of the selected $B_s^0 \to (K^+\pi^-)(K^-\pi^+)$ candidates.The fit result is shown in Fig. S.4. A total of 697 ± 31 $B_s^0 \to (K^+\pi^-)(K^-\pi^+)$ candidates were found.

S.5.2 Amplitude analysis of $B_s^0 \to (K^+\pi^-)(K^-\pi^+)$

The magnitude and phase of each of the different amplitudes contributing to the $B_s^0 \to (K^+\pi^-)(K^-\pi^+)$ in a ± 150 MeV$/c^2$ mass window around the K^{*0} mass were determined using a 5-dimensional fit to the candidates' distribution in the three helicity angles and the invariant mass of the two $K\pi$ pairs. Candidates with a four-body invariant mass within a ± 30 MeV$/c^2$ of the B_s^0 meson nominal mass were considered. The background was parameterised using events from the high-mass sideband and fixed to the fraction calculated from the result of the fit to the four-body invariant mass spectrum.

The acceptance function in each of the 5 variables entering the fit was extensively studied using both $B_s^0 \to K^{*0}\overline{K}^{*0}$ simulated events and data. As a conclusion, the angular and mass dependence of the acceptance were assumed to be factorisable. Furthermore, the efficiency as a function of m_1, m_2 and φ was found compatible with being constant. The final model is based in a 2-dimensional acceptance function, $\varepsilon(\cos\theta_1, \cos\theta_2)$, which drops rapidly as $\cos\theta_{1,2} \to 1$, due, as explained, to the low momentum of the π meson in such a configuration.

The candidates were split in two categories according to their trigger path. A different acceptance correction was applied to each of the subsamples and and a simultaneous fit was performed. The fit result is shown in Fig. S.5. The low polarisation of the $B_s^0 \to K^{*0}\overline{K}^{*0}$ decay is confirmed by the result $f_L = 0.201 \pm 0.057(\text{stat.}) \pm 0.040(\text{syst.})$.

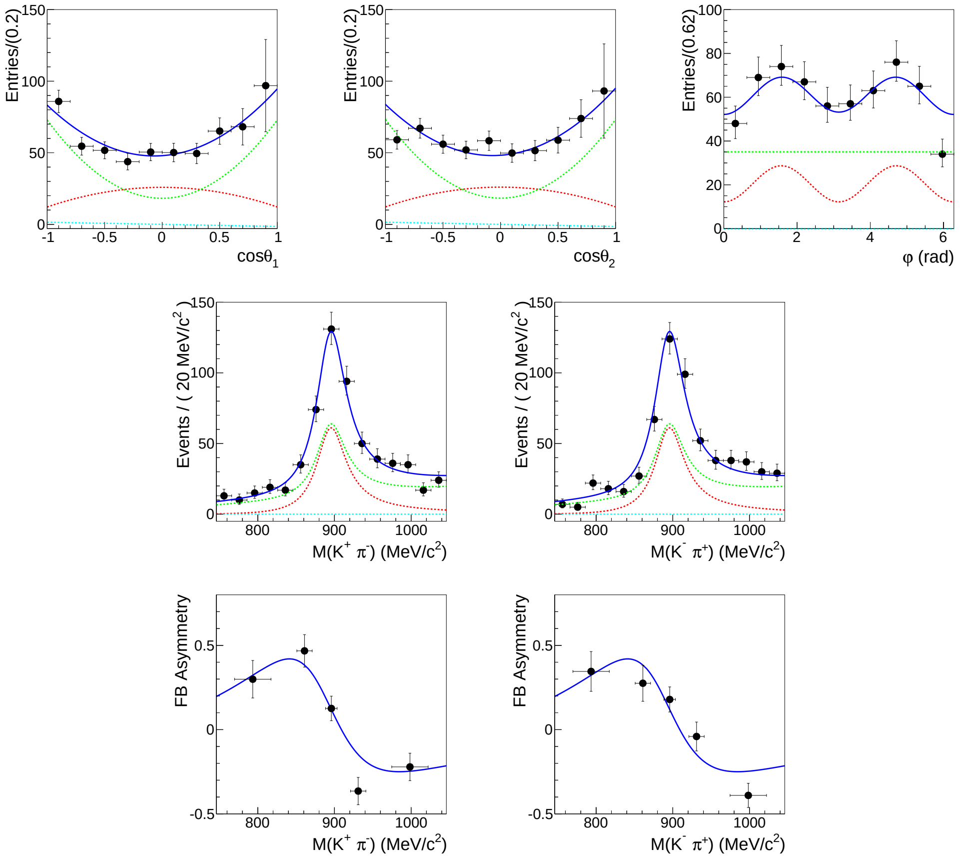

Figure S.5: Projections of the 5D model fitted to $B_s^0 \to (K^+\pi^-)(K^-\pi^+)$ data (blue solid line). The solid dots represent the selected data after background subtraction and acceptance correction. The red dashed line is the P-wave component, the green dashed line is the S-wave component and the light-blue dashed line represents the $A_S^+ A_0$ interference term. The two bottom plots show the forward-backward asymmetry in $\cos\theta$ as a function of the corresponding $K\pi$ pair invariant mass for data and the fitted model.

Additionally, a large *S–wave* contribution is found $(0.665 \pm 0.067(\text{stat.}) \pm 0.030(\text{syst.}))$. The main source of the final systematic uncertainty quoted above come from the parameterisation of the angular acceptance and the modeling of the invariant mass propagators.

S.5.3 Determination of $\mathcal{B}(B_s^0 \to K^{*0}\overline{K}^{*0})$

Given the large value of the *S–wave* contribution found in the amplitude analysis, which could not be accurately determined in the analysis of 2010 data, an update on the measurement of the $\mathcal{B}(B_s^0 \to K^{*0}\overline{K}^{*0})$ was performed. The strategy followed to measure this branching fraction is based upon the use of the normalisation channel $B^0 \to \phi K^{*0}$, due to the presence of four hadrons in the final state of both decays and their similar topology.

The ratio of branching fractions for these two processes is given by

$$\begin{aligned}\frac{\mathcal{B}(B_s^0 \to K^{*0}\overline{K}^{*0})}{\mathcal{B}(B^0 \to \phi K^{*0})} &= \frac{\varepsilon^{sel}_{B^0\to\phi K^{*0}}}{\varepsilon^{sel}_{B_s^0\to K^{*0}\overline{K}^{*0}}} \times \frac{\varepsilon^{trig}_{B^0\to\phi K^{*0}}}{\varepsilon^{trig}_{B_s^0\to K^{*0}\overline{K}^{*0}}} \times \frac{\lambda_{f_L}(B^0 \to \phi K^{*0})}{\lambda_{f_L}(B_s^0 \to K^{*0}\overline{K}^{*0})} \\ &\times \frac{N_{B_s^0} \times f_{B_s^0\to K^{*0}\overline{K}^{*0}}}{N_{B^0} \times f_{B^0\to\phi K^{*0}}} \times \frac{f_d}{f_s} \times \frac{\mathcal{B}(\phi \to K^+K^-)}{\mathcal{B}(K^{*0} \to K^+\pi^-)} \qquad \text{(S.5)}\end{aligned}$$

where f_d/f_s is the ratio of the b-quark hadronisation fractions and accounts for the different yields of B^0 and B_s^0 mesons.

The quantities $N_{B_s^0}$ and N_{B^0} represent the number of candidate events for $B_s^0 \to K^+\pi^-K^-\pi^+$ and $B^0 \to K^+K^-K^\pm\pi^\mp$ decays respectively. They were determined from the corresponding fit to the four-body invariant mass spectrum. The ammount of those corresponding to the resonant decays, $B_s^0 \to K^{*0}\overline{K}^{*0}$ and $B^0 \to \phi K^{*0}$, is given by the purity factors $f_{B_s^0\to K^{*0}\overline{K}^{*0}}$ and $f_{B^0\to\phi K^{*0}}$.

The ratio of reconstruction and selection efficiencies, ε^{sel}, was calculated using $B_s^0 \to K^{*0}\overline{K}^{*0}$ and $B^0 \to \phi K^{*0}$ simulated events and validated using data. The inefficiency induced by the particle identification requirements was determined separately using high-statistics control channels. The ratio of trigger efficiencies, ε^{trig}, was computed through a data driven method.

The overall efficiency for each channel depends on the angular distribution of the particles in the final state, which motivates the factors λ_{f_L}. Both the purity and the λ_{f_L} factor for $B_s^0 \to K^{*0}\overline{K}^{*0}$ are calculated from the results of the angular analysis. The factor corresponding to $B^0 \to \phi K^{*0}$ decay is calculated using the results obtained in the dedicated $B^0 \to \phi K^{*0}$ LHCb analysis.

Using the world average branching fraction for the reference channel, the result obtained is

$$\mathcal{B}(B_s^0 \to K^{*0}\overline{K}^{*0}) = (10.6 \pm 1.8(stat.) \pm 1.0(syst) \pm 0.6(f_d/f_s)) \times 10^{-6},$$

compatible with the SM prediction. It is important to note that the previous measurement used an extrapolation from $B_d^0 \to J/\psi K^{*0}$ to estimate the *S–wave* contribution. The 2010 measurement can be rescaled to include the *S–wave* fraction determined in Sect. S.5.2, which yields 1.1×10^{-6}, compatible with the subsequent measurement with 2011 data.

S.5.4 Triple product and direct *CP* asymmetries

Finally, all of the eight *CP*-violating observables accesible to the untagged analysis of the decay $B_s^0 \to (K^+\pi^-)(K^-\pi^+)$ were measured, by computing the asymmetries in (S.2). Candidates with a four-body invariant mass within ± 30 MeV/c^2 of the B_s^0 meson nominal mass were considered.

For each of the angular distributions, the background was parameterised using events from the high-mass sideband, normalised to the number of events calculated from the result of the fit to the four-body invariant mass spectrum and subtracted. Those distributions were also corrected by the angular acceptance earlier determined from $B_s^0 \to K^{*0}\overline{K}^{*0}$ simulated events. The lifetime biasing selection can introduce small variations in the measurement of these asymmetries. This effect, together with the angular acceptance correction are the two main sources of systematic uncertainty.

The measured asymmetries are the following,

$$\begin{aligned}
A_T^1 &= 0.003 \pm 0.041(\text{stat.}) \pm 0.009(\text{syst.}),\\
A_T^2 &= 0.999 \pm 0.041(\text{stat.}) \pm 0.009(\text{syst.}),\\
A_T^3 &= 0.019 \pm 0.041(\text{stat.}) \pm 0.008(\text{syst.}),\\
A_T^4 &= -0.040 \pm 0.041(\text{stat.}) \pm 0.008(\text{syst.}),\\
\\
A_D^1 &= -0.061 \pm 0.041(\text{stat.}) \pm 0.012(\text{syst.}),\\
A_D^2 &= 0.081 \pm 0.041(\text{stat.}) \pm 0.008(\text{syst.}),\\
A_D^3 &= -0.079 \pm 0.041(\text{stat.}) \pm 0.023(\text{syst.}),\\
A_D^4 &= -0.081 \pm 0.041(\text{stat.}) \pm 0.010(\text{syst.}).
\end{aligned}$$

Within the statistical precision, none of them show significant *CP* violation. This result is, therefore, compatible with the Standard Model prediction.

Resumo e Conclusións

O Modelo Estándar (SM) de Física de Partículas é, na actualidade, a descrición máis fiable das partículas elementais e as súas interaccións. A pesar do seu éxito explicando unha gran variedade de fenómenos, o SM non incorpora elementos como a Gravidade, a Materia Escura ou a oscilación de neutrinos. Distintos modelos de Nova Física (NP) foron propostos para resolver estes problemas. O obxectivo de experimentos como o Gran Colisor de Hadróns (LHC) no CERN é o de poñer a proba as predicións destes novos modelos e procurar desviacións do SM.

A física dos hadróns B, hadróns que conteñen un quark b, constitúe un excelente contexto para a medida dos parámetros do SM tales como os elementos da matriz CKM ou a violación de CP. Ademais, as correntes neutras con cambio de sabor (FCNC) $b \to q$ son moi sensibles a posibles desviacións do SM inducidas por partículas de NP circulando nos *loops*. Un exemplo deste tipo de proceso é a desintegración $B_s^0 \to K^{*0}\overline{K}^{*0}$.

O experimento LHCb no LHC foi deseñado para o estudo de desintegracións raras e da violación de CP no contexto dos hadróns B, coa intención de revelar a natureza da física alén o SM. O traballo presentado nesta tese corresponde coa análise do modo de desintegración $B_s^0 \to K^{*0}\overline{K}^{*0}$ cos datos recollidos polo LHCb durante 2010 e 2011.

R.1 $B_s^0 \to K^{*0}\overline{K}^{*0}$ no Modelo Estándar

No SM a FCNC $b \to sd\bar{d}$, responsable do decaemento $B_s^0 \to K^{*0}\overline{K}^{*0}$, sucede a través dunha transición de tipo *penguin* gluónico, dominado por un quark top virtual que se acopla a un bosón W. Algunhas extensións do SM predín contribución adicionais que poderían introducir efectos apreciables na dinámica da transición.

Predicir os observables accesibles a desintegracións hadrónicas exclusivas, como $B_s^0 \to K^{*0}\overline{K}^{*0}$, é complicado debido a que o proceso de hadronización introduce efectos intrínsecamente non perturbativos. Poden facerse predicións teóricas no ámbito da QCDf (factorización de QCD), no que os elementos de matriz hadrónicos pódense descompoñer en factores de forma e constantes de desintegración. Neste contexto, a predición dispoñible para a fracción de desintegración é $\mathcal{B}(B_s^0 \to K^{*0}\overline{K}^{*0}) = (9.1^{+11.3}_{-6.8}) \times 10^{-6}$, que mellora ata $(7.9^{+4.3}_{-3.9}) \times 10^{-6}$ cando se usa información experimental do proceso $B^0 \to \phi K^{*0}$.

Dado que a resonancia K^{*0} ten spin 1, $B_s^0 \to K^{*0}\overline{K}^{*0}$ é en realidade tres decaementos distintos, cada un cunha helicidade distinta para os K^{*0}'s, $h = 0, \pm 1$. Polo tanto, este proceso ven descrito por tres amplitudes diferentes que poden ser desentrelazadas a través dunha análise angular dos produtos da desintegración dos K^{*0}'s. A fracción relativa

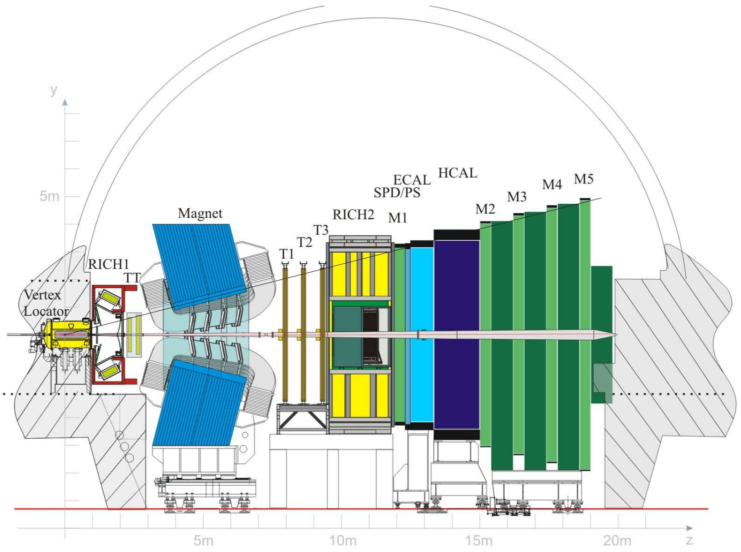

Figura R.6: View of the LHCb detector.

correspondente á amplitude lonxitudinal ($h = 0$) foi calculada tamén en QCDf para obter $f_L = 0.63^{+0.42}_{-0.29}$ ($0.72^{+0.16}_{-0.21}$ cando se usa información do proceso $B^0 \to \phi K^{*0}$).

En relación á violación de *CP*, o SM predí que debe ser desprezable para este decaemento debido a que a contribución penguin subdominante está moi suprimida. Polo tanto, se neste proceso se medis un valor elevado para algún observable que viole *CP*, esa medida constituiría un sinal de física alén o SM.

R.2 O experimento LHCb no LHC

LHCb é un dos catro grandes experimentos que analizan os datos do LHC no CERN. Está dedicado ao estudo da violación de *CP* e de decaementos raros en hadróns que conteñen quarks *b*.

A identificación precisa do vértice primario (PV), onde se produce o hadrón *B*, e o vértice secundario (SV), onde o hadrón *B* se desintegra, é esencial para tódolas análises de LHCb. Esta tarefa vólvese máis difícil a medida que a luminosidade instantánea aumenta, debido ao crecente número de interaccións *pp*. Para limitar o número de interaccións simultáneas, LHCb traballa a unha luminosidade menor que a dos outros experimentos do LHC.

R.2.1 O detector LHCb

LHCb é un espectrómetro de brazo único que cubre a zona dianteira cunha cobertura angular desde aproximadamente 10 mrad a 300 (250) mrad no plano perpendicular ao campo magnético (paralelo ao campo magnético). Os principais elementos de LHCb, mostrado na Fig. R.6, son:

- Imán: Un dipolo a temperatura ambiente que proporciona un campo integrado de $4\ \mathrm{T \cdot m}$.

- Localizador de vértices (VELO): Detector de silicio que proporciona información precisa sobre o PV e o SV.
- Sistema de trazado: Composto polo *Tracker Turiciensis* (TT) antes do imán e tres estacións de trazado (T1,T2,T3) despois do imán. Este sistema permite a reconstrucción das traxectorias de partículas cargadas. Nas estacións de trazado, a parte interna (IT) usa sensores de micortiras de silicio e a parte externa (OT) está formada por tubos de deriva.
- Dous detectores de aneis Cherenkov (RICH): Estes dous detectores (RICH-1 antes do imán e RICH-2 despois) encárganse da identificación de partículas cargadas no rango de momento de 2 a 100 GeV/c.
- Sistema de calorímetros: SPD/PS (capa cintiladora previa), ECAL (Calorímetro electromagnético) e HCAL (Calorímetro Hadrónico) compoñen este sistema. O propósito de este subdetector é o de identificar electróns e hadróns mediante medidas de posición e enerxía.
- Sistema de detección de muóns: Composto por unha combinación de MWPC (*Multi Wire Proportional Cambers*) e GEM (*Gas Electron Multiplier*), emprégase na identificación de muóns.

O fluxo de sucesos tomados por LHCb a partires das colisión protón-protón do LHC é da orde de varios millóns por segundo, demasiado elevado para ser directamente almacenado. O sistema de *trigger* de LHCb fai uso da información recollida por differentes subdetectores para facer unha selección rápida e reducir esta enorme cantidade de sucesos, tentando reter tantos procesos interesantes como sexa posible, antes da almacenaxe final cara á análise. En particular, durante 2011 o trigger de LHCb reduciu a frecuencia de datos de $\sim$ 15 MHz a $\sim$ 3 kHz, explotando as características propias das partículas creadas en desintegracións de hadróns B (elevado p_{T}, parámetro de impacto,etc).

A análise desta tese baséase nos datos recollidos polo LHCb durante 2010 e 2011 a partir das colisión pp a unha enerxía no centro de masas de $\sqrt{s} = 7$ TeV proporcionadas polo LHC. Estas mostras corresponden a unha luminosidade integrada de 37 pb^{-1} e 1.0 fb^{-1}, respectivamente.

R.3 A desintegración $B_s^0 \to (K^+\pi^-)(K^-\pi^+)$

A procura do proceso $B_s^0 \to K^{*0}\overline{K}^{*0}$ en LHCb centrouse no estado final cargado $B_s^0 \to (K^+\pi^-)(K^-\pi^+)$ requerindo que o os pares $K\pi$ tiveran unha masa invariante contida dentro dun intervalo de ± 150 MeV/c^2 ao redor da masa nominal do $K^{*0}(892)$. Atopouse que, ademais da resonancia vectorial (V), unha compoñente escalar aparece neste intervalo. Deste xeito, o decaemento ven descrito por seis amplitudes distintas. Tres delas son as amplitudes que describen a desintegración $B \to V_1 V_2$ (*onda–P*), que, na base de transversidade, son: A_0, $A_{||}$ e $A_{\perp}$. As outras tres (*onda–S*) corresponden ós decaementos[1] $B \to V_1 S_2$ (A_{VS}), $B \to S_1 V_2$ (A_{SV}) e $B \to S_1 S_2$ (A_{ss}).

É conveniente definir as combinacións lineais $A_s^+ = (A_{VS} + A_{SV})/\sqrt{2}$ e $A_s^- = (A_{VS} - A_{SV})/\sqrt{2}$, de modo que a fracción de desintegración poida ser expresada exclusivamente

---

[1] O subíndice 1 (2) corresponde á parella $K^+\pi^-$ ($K^-\pi^+$).

en base a amplitudes asociadas a autoestados de *CP* pares (0, $\|$, s^-,ss) e impares ($\perp$, s^+).

R.3.1 Análise de amplitudes no SM

Co obxectivo de desentrelazar todas estas contribucións, a distribución angular dos produtos da desintegración ten que ser comparada coa fracción de desintegración diferencial correspondente á combinacion coherente das amplitudes. Ademais, a mestura no sistema de mesóns B_s^0 neutros introduce unha dependencia temporal nestas amplitudes, que é distinta para A_f e $\bar{A}_f$, amplitudes relativas a $B \to f$ e $\overline{B} \to \bar{f}$ respectivamente. Non obstante, debido ao pequeno tamaño da mostra de datos dispoñible, algoritmos de *flavour tagging*, utilizados para determinar o sabor do mesón B_s^0 no tempo de produción, non puideron ser aplicados. Por conseguinte, levouse a cabo unha análise da mostra $B + \overline{B}$, denominada comunmente como análise *sen marcado de sabor* , integrada no tempo.

Consideramos, polo tanto, a fracción de desintegración diferencial nos tres ángulos da base de helicidade (Ω : $\{\cos\theta_1, \cos\theta_2, \varphi\}$) e nas masas invariantes das parellas $K^+\pi^-$ (m_1) e $K^-\pi^+$ (m_2), que pode expresarse como segue,

$$\frac{\mathrm{d}\Gamma}{\mathrm{d}\Omega \mathrm{d}m_1 \mathrm{d}m_2} = \sum_{n=1}^{21} K_n(m_1, m_2) F_n(\Omega), \tag{R.6}$$

onde as funcións K_n conteñen a dependencia nas distintas amplitudes e F_n son as distribucións angulares asociadas con cada combinación de amplitudes. Supoñendo que non se viola *CP*, tal e como predí o SM, as funcións K_n se simplifican. En particular, tódolos termos proporcionais á interferencia entre unha amplitude impar e outra par desaparecen. A razón é que eses termos son proporcionais a asimetrías de Productos Triples e asimetrías de *CP* directas, que por definición violan *CP*.

R.3.2 Productos Triples e asimetrías de *CP* directas

A pesar de que na análise presentada aquí non se fixo distinción entre B e $\overline{B}$, un estudo da violación de *CP* é aínda posible. Na análise sen marcado de sabor dunha desintegración $B \to VV$ poden definirse dúas asimetrías asociadas con Productos Triples (TPA) que violan *CP*. En particular, estas TPA son proporcionais ós termos de interferencia entre a amplitude *CP*-impar $A_\perp$ e as dúas amplitudes *CP*-pares A_0 e $A_\|$. Cando se considera tamén a contribución da *onda–S* dúas amplitudes pares adicionais están suxeitas a interferir con $A_\perp$. Ademais, os termos de interferencia entre a amplitude impar A_s^+ e todas as amplitudes pares orixinan outros catro observables de violación de *CP* con estructura similar á das asimetrías de *CP* directas.

Deste xeito, oito observables, catro TPA $A_T^{(i)}$ e catro asimetrías *CP* directas $A_D^{(i)}$ ($i = 1, ..., 4$), poden ser determinadas a partir dos datos dispoñibles. Demostrouse tamén que estes observables poden ser medidos a través dunha integración asimétrica de certas distribucións angulares seguindo

$$A_{T,D}^{(i)} = \frac{N(U_{T,D}^i(\Omega) > 0) - N(U_{T,D}^i(\Omega) < 0)}{N(U_{T,D}^i(\Omega) > 0) + N(U_{T,D}^i(\Omega) < 0)} \tag{R.7}$$

Cuadro R.2: Resumo dos observables de violación de *CP* medibles na análise sen marcado de sabor do decaemento $B_s^0 \to (K^+\pi^-)(K^-\pi^+)$ e das funcións angulares asociadas ós mesmos. A columna intermedia mostra a TPA ou asimetría de *CP* directa que orixina cada observable.

Observable	TPA / asimetría *CP* directa	$U^{i}_{T,D}(\Omega)$
$A_T^{(1)}$	$\Im(A_\perp A_0^* - \bar{A}_\perp \bar{A}_0^*)$	$\mathrm{sign}(\cos\theta_1\cos\theta_2)\sin\varphi$
$A_T^{(2)}$	$\Im(A_\perp A_\parallel^* - \bar{A}_\perp \bar{A}_\parallel^*)$	$\sin 2\varphi$
$A_T^{(3)}$	$\Im(A_\perp (A_s^-)^* - \bar{A}_\perp (\bar{A}_s^-)^*)$	$\mathrm{sign}(\cos\theta_1 + \cos\theta_2)\sin\varphi$
$A_T^{(4)}$	$\Im(A_\perp A_{ss}^* - \bar{A}_\perp \bar{A}_{ss}^*)$	$\sin\varphi$
$A_D^{(1)}$	$\Re(A_s^+ A_0^* - \bar{A}_s^+ \bar{A}_0^*)$, $\Re(A_s^+ A_{ss} - \bar{A}_s^* \bar{A}_{ss}^*)$	$\cos\theta_1\cos\theta_2(\cos\theta_1 - \cos\theta_2)$
$A_D^{(2)}$	$\Re(A_s^+ A_\parallel^* - \bar{A}_s^+ \bar{A}_\parallel^*)$	$(\cos\theta_1 - \cos\theta_2)\cos\varphi$
$A_D^{(3)}$	$\Re(A_s^+ A_0^* - \bar{A}_s^+ \bar{A}_0^*)$, $\Re(A_s^+ A_{ss} - \bar{A}_s^* \bar{A}_{ss}^*)$	$(\cos\theta_1 - \cos\theta_2)$
$A_D^{(4)}$	$\Re(A_s^+ (A_s^-)^* - \bar{A}_s^+ (\bar{A}_s^-)^*)$	$(\cos^2\theta_1 - \cos^2\theta_2)$

onde $U^{(i)}_{T,D}$ é a función angular asociada co termo, na fracción de desintegración diferencial, que é proporcional a $A^{(i)}_{T,D}$. Table R.2 contén a definición de cada un dos observables de violación de *CP* en base ás distintas amplitudes e a súa correspondente función angular $U^{(i)}_{T,D}$. Dado que o SM predí que non existe violación de *CP* neste proceso, un valor elevado de calquera destas cantidades sería un sinal de Nova Física.

R.4 Descubrimento do decaemento $B_s^0 \to K^{*0}\overline{K}^{*0}$

Previamente ao acendido do LHC, non se tiña atopado evidencia do decaemento $B_s^0 \to K^{*0}\overline{K}^{*0}$ e tan só un límite superior para a súa fracción de desintegración, $\mathcal{B}(B_s^0 \to K^{*0}\overline{K}^{*0}) < 1.68 \times 10^{-3}$ ao 90 % de nivel de confianza (CL), fora publicado pola colaboración SLD.

Tanto BaBar como Belle presentaran as súas procuras polo modo rotado por U-spin, $B^0 \to K^{*0}\overline{K}^{*0}$. Porén, mentres BaBar anunciou o descubrimento da canle e mediu unha fracción de desintegración de $(1.28^{+0.35}_{-0.30} \pm 0.11) \times 10^{-6}$, a colaboración Belle, uns anos despois, publicou únicamente o límite superior $\mathcal{B}(B^0 \to K^{*0}\overline{K}^{*0}) < 0.8 \times 10^{-6}$ ao 90 % de CL. No mesmo artigo, BaBar tamén presentou a súa medida da fracción de polarización lonxitudinal para o $B^0 \to K^{*0}\overline{K}^{*0}$, $f_L = 0.80^{+0.10}_{-0.12} \pm 0.06$.

Preséntase aquí a procura do $B_s^0 \to K^{*0}\overline{K}^{*0}$ no LHCb, baseada nos datos tomados a partir das colisións pp a $\sqrt{s} = 7$ TeV producidas no LHC durante 2010, que corresponden a 37 pb^{-1} de luminosidade integrada.

R.4.1 Selección do sinal

Na procura do $B_s^0 \to K^{*0}\overline{K}^{*0}$, aplicáronse primeiro un conxunto de criterios de selección para reducir a maior parte do fondo. Esencialmente, esíxese que os candidatos teñan catro trazas cargadas de alto p_T que formen un vértice secundario ben definido e separado da interacción pp primaria. En base ao sistema de identificación de partículas, estas catro trazas deben ser compatibles coa hipótese de dúas parellas $K\pi$, que ademais deberán ter unha masa invariante dentro dunha ventá de $\pm 150\ \mathrm{MeV}/c^2$ ao redor da masa nominal do $K^{*0}(892)$.

O fondo reduciuse aínda máis usando un discriminante multivariable baseado na información topolóxica do evento, a *Geometrical Likelihood* (GL). A GL foi adestrada usando sucesos Monte Carlo de $B_s^0 \to K^{*0}\overline{K}^{*0}$ para simular o sinal e unha pequena mostra de datos tomados a comezos de 2010 (excluídos da subsequinte análise) como fondo.

R.4.2 Espectro de masa invariante

A masa invariante das catro partículas reconstruídas para os candidatos seleccionados cos criterios descritos previamente móstrase na Fig. R.7. Usando un axuste de máxima verosimilitud a este espectro, extraeuse o número de candidatos de $B_s^0 \to (K^+\pi^-)(K^-\pi^+)$. O modelo usado para describir os datos inclue dúas funcións de densidade de probabilidade (PDF) gaussianas correspondentes aos sinais de $B_{s(d)} \to K^+\pi^-K^-\pi^+$, unha exponencial decrecente para modelar o fondo combinatorio e unha distribución ARGUS modificada para parametrizar o fondo orixinado por decaementos de hadróns B parcialmente reconstruídos.

Como resultado, nunha ventá de masa de $\pm 50\,\mathrm{MeV}/c^2$ ao redor da masa do B_s^0, atopáronse $N_{B_s^0} = 49.8 \pm 7.5(\mathrm{stat.})$ candidatos do sinal $B_s^0 \to (K^+\pi^-)(K^-\pi^+)$, cunha significancia estatística de 10.9 σ. O sinal atopado en torno a masa do B^0, aínda que non é significativo, é compatible coa fracción de desintegración medida por BaBar para o $B^0 \to K^{*0}\overline{K}^{*0}$.

R.4.3 Análise angular

Debido ao pequeno tamaño do sinal, levouse a cabo unha versión simplificada da análise angular presentada na Sect. R.3.1: un axuste á distribución angular integrado na masa e supoñendo que a contribución das amplitudes de *onda–S* é nula. Os parámetros medibles son as fraccións relativas de cada amplitude de transversidade, normalmente denominadas *fraccións de polarización*,

$$f_{L,k} = \frac{|A_{0,k}|^2}{|A_L|^2 + |A_\parallel|^2 + |A_\perp|^2} \quad , \quad k = \parallel, \perp, \tag{R.8}$$

e $\delta_\parallel$, a diferencia de fase entre A_0 e $A_\parallel$.

Os efectos introducidos pola aceptancia xeométrica do detector, e os procesos de reconstrucción e selección determináronse usando una simulación de sucesos de $B_s^0 \to K^{*0}\overline{K}^{*0}$, e modelouse en base a unha función de aceptancia dependente dos tres angulos do decaemento. Atopouse que a aceptancia en función de φ é compatible cunha función constante. Polo contrario, a aceptancia varía fortemente co ángulo de polarización do K^{*0}

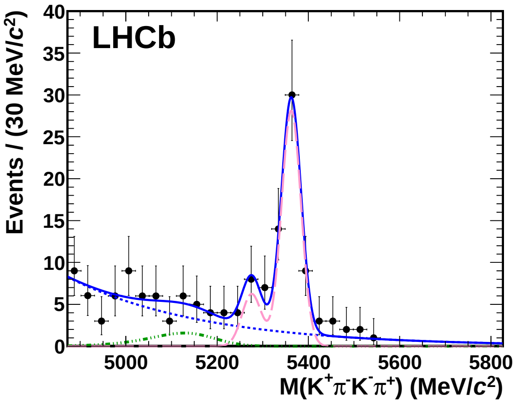

Figura R.7: Axuste á distribución da masa invariante de $K^+\pi^-K^-\pi^+$ para os candidatos seleccionados. O modelo (liña rosa discontinua) inclúe dúas compoñentes de sinal correspondentes a os decaementos de B_s^0 e B^0. O fondo descríbese como unha compoñente combinatoria (liña azul de puntos) máis unha contribución orixinada por desintegracións parcialmente reconstruídas (liña verde discontinua).

θ, caendo asimetricamente a medida que $\cos\theta_{1,2}$ se achega a ± 1 como consecuencia dos requerimentos de mínimo p e mínimo p_{T} das trazas esixidos durante a reconstrucción e a selección. Este efecto é máis importante para o límite $\cos\theta \to +1$, é dicir, cando o meson π se emite en dirección oposta á do momento do K^{*0}.

Tras modificar a fracción de desintegración diferencial para ter en conta a aceptancia, levouse a cabo un axuste de máxima verosimilitude á distribución angular daqueles candidatos cunha masa invariate dos catro corpos contida nun intervalo de ± 50 MeV/c^2 ao redor da masa do B_s^0. O fondo restante, foi parametrizado usando os datos correspondentes á rexión de alta masa do espectro e a súa normalización fixouse ao número de eventos medidos no axuste a ese mesmo espectro. O resultado do axuste angular móstrase na Fig. R.8. As fraccións de polarización medidas son $f_L = 0.31 \pm 0.12(\text{stat.}) \pm 0.04(\text{syst.})$ e $f_\perp = 0.38 \pm 0.11(\text{stat.}) \pm 0.04(\text{syst.})$. Non se acadou unha medida significativa da fase $\delta_\parallel$ ($\delta_\parallel = 1.47 \pm 1.85$). A principal contribución ao erro sistemático que se indica nos resultados anteriores ven da determinación da aceptancia angular, na que se usou o decaemento $B_d^0 \to J/\psi K^{*0}$ para correxir a descripción obtida coa simulación.

Cabe destacar que a polarización dos mesóns K^{*0} parece ser moi distinta nos procesos $B_s^0 \to K^{*0}\overline{K}^{*0}$ e $B^0 \to K^{*0}\overline{K}^{*0}$, a persar de que ambos modos están relacionados pola simetría de U-spin.

R.4.4 Determinación da fracción de desintegración

Co fin de determinar a fracción de desintegración para o decaemento $B_s^0 \to K^{*0}\overline{K}^{*0}$, o número de candidatos observado normalizouse ao número de candidatos atopados para un modo de referencia con $\mathcal{B}$ coñecida. Elixiuse para este propósito o decaemento $B_d^0 \to J/\psi K^{*0}$ por ter unha topoloxía similar á do sinal.

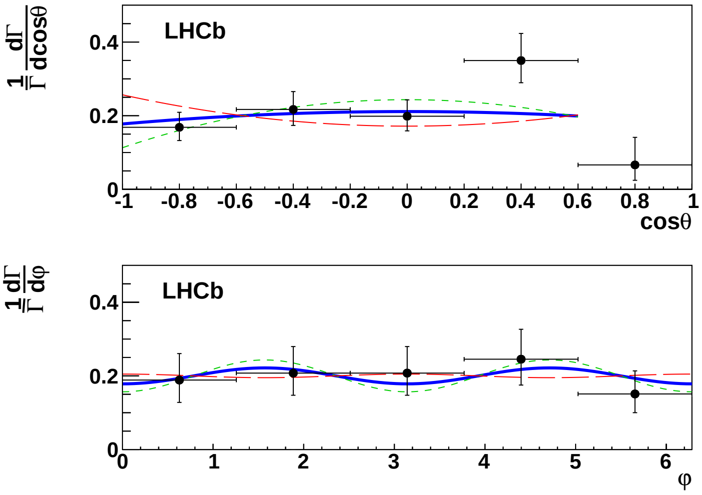

Figura R.8: Distribucións en $\cos\theta$ (arriba) e φ (abaixo) dos candidatos de $B_s^0 \to K^{*0}\overline{K}^{*0}$ trala corrección por acceptancia. A liña azul é a proxección do modelo para os valores medidos dos parámetros f_L, $f_\parallel$ e $\delta_\parallel$. As liñas discontinuas indican unha variación de $\pm1\sigma$ do valor central de f_L.

Empregouse, para o cálculo, a seguinte expresión

$$\begin{aligned}\mathcal{B}\left(B_s^0 \to K^{*0}\overline{K}^{*0}\right) &= \lambda_{f_L} \times \frac{\epsilon^{sel}_{B_d^0\to J/\psi K^{*0}}}{\epsilon^{sel}_{B_s^0\to K^{*0}\overline{K}^{*0}}} \times \frac{\epsilon^{trig}_{B_d^0\to J/\psi K^{*0}}}{\epsilon^{trig}_{B_s^0\to K^{*0}\overline{K}^{*0}}} \times \frac{N_{B_s^0\to K^{*0}\overline{K}^{*0}}}{N_{B_d^0\to J/\psi K^{*0}}} \\ &\quad \times \mathcal{B}_{vis}(B_d^0 \to J/\psi K^{*0}) \times \frac{f_d}{f_s} \times \frac{9}{4}, \qquad \text{(R.9)}\end{aligned}$$

O cociente de eficiencias de reconstrucción e selección (ϵ^{sel}) calculouse usando simulación e validouse nos datos. O factor de corrección λ_{f_L}, encárgase de correxir o efecto da distinta polarización nos datos e no Monte Carlo cando se calculan esas eficiencias. As eficiencias de trigger para o modo de referencia e o sinal obtivéronse directamente dos datos. Para mitigar as diferencias no trigger entre os dous canles de desintegración, inducidas principalmente polos dous muóns orixinados no decaemento do J/ψ, consideráronse unicamente aqueles candidatos seleccionados polo trigger hadrónico.

O número de candidatos para o modo de normalizacion obtívose dun axuste ao espectro de masa invariante $M(J/\psi, K, \pi)$. O cociente co número de candidatos do sinal corrixiuse despois para ter en conta a contribución non resonante no sistema $K\pi$. Esta contribución calculouse extrapolando unha medida existente no proceso $B_d^0 \to J/\psi K^{*0}$ publicada por BaBar.

Finalmente, empregáronse o promedio mundial para a fracción de desintegración visible, $\mathcal{B}_{vis}(B_d^0 \to J/\psi K^{*0})$, que non é máis que o produto $\mathcal{B}(B_d^0 \to J/\psi K^{*0}) \times \mathcal{B}(J/\psi \to \mu^+\mu^-) \times \mathcal{B}(K^{*0} \to K^+\pi^-)$, e o cociente de fraccións de produción de B^0 e B_s^0 medido por LHCb. O resultado obtido é

$$\mathcal{B}(B_s^0 \to K^{*0}\overline{K}^{*0}) = (2.81 \pm 0.46\ (\text{stat.}) \pm 0.45\ (\text{syst.}) \pm 0.34\ (f_s/f_d)) \times 10^{-5},$$

compatible coas estimacións teóricas para o Modelo Estándar.

R.5 Análise sen marcado de sabor e integrada no tempo de $B_s^0 \to K^{*0}\overline{K}^{*0}$

Unha análise máis detallada da canle de desintegración $B_s^0 \to K^{*0}\overline{K}^{*0}$ levouse a cabo cunha mostra de datos de maior luminosidade recollida polo LHCb durante 2011, a partir das colisións *pp* a $\sqrt{s} = 7$ TeV no LHC. Unha medida máis precisa das fraccións de polarización e a primeira determinación das contribucións de *onda–S* en $B_s^0 \to (K^+\pi^-)(K^-\pi^+)$ acadáronse a través da análise de amplitudes descrita na Sect. R.3.1. Este resultado permitiu á súa vez unha medida máis precisa da $\mathcal{B}(B_s^0 \to K^{*0}\overline{K}^{*0})$. Tamén se levou a cabo unha procura de física alén o SM a través da medida dos oito observables de violación de *CP* accesibles á análise sen marcado de sabor desta mostra.

R.5.1 Selección e determinación do sinal

Os candidatos de $B_s^0 \to K^{*0}\overline{K}^{*0}$ seleccionáronse nos datos usando un conxunto de criterios parecidos aos empregados na análise dos datos de 2010. A GL foi redefinida cunha nova simulación de sucesos de $B_s^0 \to K^{*0}\overline{K}^{*0}$ e a mesma mostra de fondo.

Identificáronse tres contribucións resonantes orixinadas por decaementos específicos de hadróns *B* distintos do sinal: $B^0 \to \rho K^{*0}$, $B^0 \to \phi K^{*0}$ e $\Lambda_b^0 \to p\pi K\pi$. O modo $B^0 \to \rho K^{*0}$ pode confundirse fácilmente co sinal cando un dos pións da desintegración do ρ é identificado como kaón. Estes sucesos acumúlanse na rexión intermedia entre as massas nominais do B^0 e do B_s^0 no espectro de masa invariante dos catro corpos. Co fin de suprimir esta contaminación, aplicáronse requerimentos moi estritos na identificacion dos kaons. Un caso similar é o modo $B^0 \to \phi K^{*0}$ cando un dos kaóns da desintegración do ϕ identifícase erróneamente como pion, de modo que estes eventos aparecen la rexión de baixa masa. Finalmente, o decaemento $\Lambda_b^0 \to p\pi K\pi$, que non se tiña observado ata o de agora, aparece na rexión de alta masa cando o protón é identificado como kaón.

Tendo en conta todas estas contribucións, levouse a cabo un axuste de máxima verosimilitude ao espectro de masa dos candidatos seleccionados. O resultado deste axuste móstrase na Fig. R.9. Atopouse un total de 697 ± 31 candidatos de $B_s^0 \to (K^+\pi^-)(K^-\pi^+)$.

R.5.2 Análise de amplitudes en $B_s^0 \to (K^+\pi^-)(K^-\pi^+)$

O módulo e fase das amplitudes que contribúen ao proceso $B_s^0 \to (K^+\pi^-)(K^-\pi^+)$ nun intervalo de ± 150 MeV/c^2 ao redor da masa do K^{*0} foron determinadas a través dun axuste 5-dimensional á distribución dos datos nos tres ángulos de helicidade e na masa invariante das dúas parellas $K\pi$. Consideráronse neste estudo os candidatos cunha masa dos catro corpos contida nunha ventá de ± 30 MeV/c^2 ao redor da masa do mesón B_s^0. O fondo parametrizouse usando datos da rexión de alta masa e a fixouse á fracción obtida do axuste ao espectro de masa dos catro corpos.

Estudouse en profundidade a aceptancia en función de cada unha das 5 variables do axuste, empregando tanto datos como simulación de $B_s^0 \to K^{*0}\overline{K}^{*0}$. Como conclusión deste estudo, supúxose que as aceptancias nos ángulos e na masa factorizan. Ademais, atopouse que a aceptancia en m_1, m_2 e φ é compatible cunha función constante. O modelo final de aceptancia baséase na función bidimensional $\varepsilon(\cos\theta_1, \cos\theta_2)$, que cae

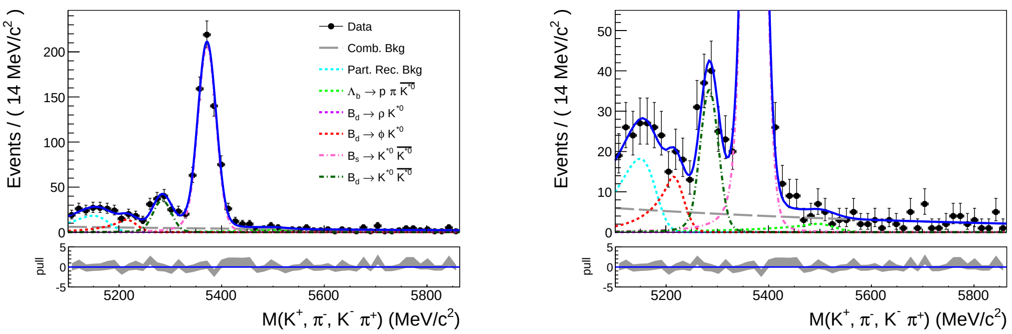

Figura R.9: Resultado do axuste á masa invariante dos catro corpos (esquerda) e zoom na rexión de baixa estatística (dereita). Os puntos representan os datos seleccionados e a liña azul continua o modelo axustado. O sinal de B_s^0 (B^0) móstrase como unha liña rosa (verde escura) discontinua. As diferentes contribucións resonantes están representadas por liñas de puntos: $B^0 \to \phi K^{*0}$ (vermella), $\Lambda_b^0 \to p\pi K\pi$ (verde) e decaementos de mesóns B parcialmente reconstruídos (azul claro). A liña gris discontinua é a compoñente de fondo combinatorio.

rápidamente a medida que $\cos\theta_{1,2} \to 1$, debido ao baixo momento dos mesóns π nesa configuración.

Os candidatos separáronse en dúas categorías atendendo ao xeito do que foron seleccionados no trigger. Unha corrección de aceptancia distinta aplicouse a cada categoría e un axuste simultáneo ás dúas mostras levouse a cabo. O resultado do axuste móstrase na Fig. R.10. Confírmase nesta análise a baixa polarización no decaemento $B_s^0 \to K^{*0}\overline{K}^{*0}$, $f_L = 0.201 \pm 0.057(\text{stat.}) \pm 0.040(\text{syst.})$. Ademais, mídese unha contribución elevada da *onda–S* ($0.665 \pm 0.067(\text{stat.}) \pm 0.030(\text{syst.})$). As principais fontes de erro sistemático son a parametrización da aceptancia angular e o modelado dos propagadores de masa no sistema $K\pi$.

R.5.3 Determinación da $\mathcal{B}(B_s^0 \to K^{*0}\overline{K}^{*0})$

Dado o elevado valor da contribución de *onda–S* atopado na análise de amplitudes, que non se puidera determinar na análise dos datos de 2010, decidiuse repetir a medida da $\mathcal{B}(B_s^0 \to K^{*0}\overline{K}^{*0})$. A estratexia seguida para a medida desta fracción de desintegración baséase na utilización do modo de referencia $B^0 \to \phi K^{*0}$, debido á presencia de catro hadróns no estado final de ambos decaementos e á súa similar topoloxía.

O cociente de fraccións de desintegración para estes dous procesos ven dado por

$$\begin{aligned}\frac{\mathcal{B}(B_s^0 \to K^{*0}\overline{K}^{*0})}{\mathcal{B}(B^0 \to \phi K^{*0})} &= \frac{\varepsilon^{sel}_{B^0\to\phi K^{*0}}}{\varepsilon^{sel}_{B_s^0\to K^{*0}\overline{K}^{*0}}} \times \frac{\varepsilon^{trig}_{B^0\to\phi K^{*0}}}{\varepsilon^{trig}_{B_s^0\to K^{*0}\overline{K}^{*0}}} \times \frac{\lambda_{f_L}(B^0 \to \phi K^{*0})}{\lambda_{f_L}(B_s^0 \to K^{*0}\overline{K}^{*0})} \\ &\times \frac{N_{B_s^0} \times f_{B_s^0\to K^{*0}\overline{K}^{*0}}}{N_{B^0} \times f_{B^0\to\phi K^{*0}}} \times \frac{f_d}{f_s} \times \frac{\mathcal{B}(\phi \to K^+K^-)}{\mathcal{B}(K^{*0} \to K^+\pi^-)} \qquad \text{(R.10)}\end{aligned}$$

onde f_d/f_s é o cociente de fraccións de hadronización do quark b, que ten en conta a producción desigual de mesóns B^0 e B_s^0.

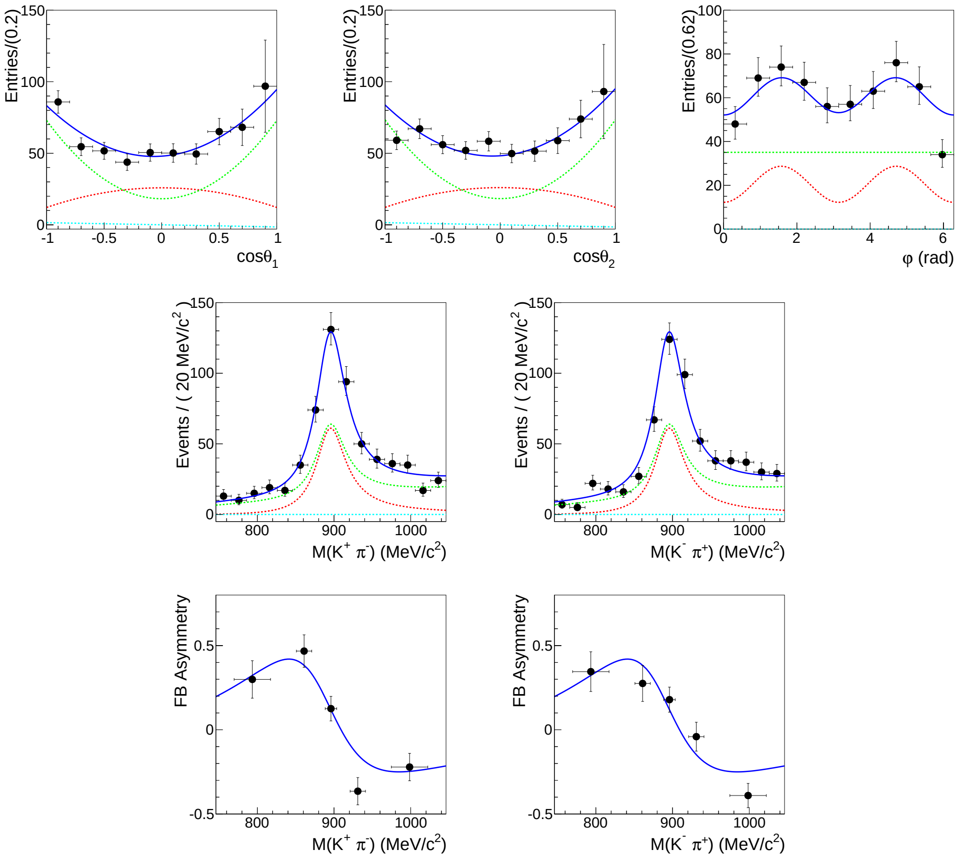

Figura R.10: Proxeccións do modelo 5D axustado aos datos de $B_s^0 \to (K^+\pi^-)(K^-\pi^+)$ (liña azul continua). Os puntos representas os candidatos seleccionados trala subtracción do fondo e a corrección por aceptancia. A liña vermella discontinua é a compoñente de *onda–P*, a verde discontinua a compoñente de *onda–S* e a azul claro discontinua representa o termo de interferencia $A_S^+ A_0$. As dúas últimas figuras mostran a evolución da asimetría en $\cos\theta$ como función da masa do correspondente par $K\pi$, tanto para os datos como para o modelo axustado.

As cantidades $N_{B_s^0}$ e N_{B^0} representan o número de candidatos observados para os procesos $B_s^0 \to K^+\pi^-K^-\pi^+$ e $B^0 \to K^+K^-K^\pm\pi^\mp$, respectivamente. Estes números foron determinados a partir do correspondente axuste ao espectro da masa invariante dos catro corpos. A fracción deles que corresponde á producción resonante, $B_s^0 \to K^{*0}\overline{K}^{*0}$ ou $B^0 \to \phi K^{*0}$, ven dada polos factores de pureza $f_{B_s^0\to K^{*0}\overline{K}^{*0}}$ e $f_{B^0\to\phi K^{*0}}$.

O cociente de eficiencias de reconstrucción e selección, ε^{sel}, calculouse a partir da simulación de sucesos $B_s^0 \to K^{*0}\overline{K}^{*0}$ e $B^0 \to \phi K^{*0}$, e validouse usando os datos. A ineficiencia inducida polos requerimentos impostos na identificación das partículas determinouse por separado a partir de modos de control de alta estatística. O cociente de efficiencias de trigger, ε^{trig}, extraeuse dos propios datos.

A eficiencia global para cada decaemento depende da distribución angular das partículas no estado final, o que motiva a presencia dos factores λ_{f_L}. Tanto a pureza como o factor λ_{f_L} para o $B_s^0 \to K^{*0}\overline{K}^{*0}$ foron calculados a partir do resultado da análise de amplitudes. Os factores correspondente ao decaemento $B^0 \to \phi K^{*0}$ determinouse en base aos resultados obtidos nunha análise dedicada ao $B^0 \to \phi K^{*0}$ en LHCb.

Usando o promedio mundial para a fracción de desintegración do modo de referencia, o resultado obtido é

$$\mathcal{B}(B_s^0 \to K^{*0}\overline{K}^{*0}) = (10.6 \pm 1.8(stat.) \pm 1.0(syst) \pm 0.6(f_d/f_s)) \times 10^{-6},$$

compatible coa predición do SM. É importante notar que a medida previa deste observable baseábase nunha extrapolación da contribución de *onda–S* medida en $B_d^0 \to J/\psi K^{*0}$. A medida de 2010 pode reescalarse para incluír a fracción de *onda–S* determinada na Sect. R.5.2, resultando en 1.1×10^{-6}, compatible coa subsecuente medida nos datos de 2011.

R.5.4 Medida das ATP e asimetrías de *CP* directas

Finalmetne, os oito observables de violación de *CP* accesibles á análise sen marcado de sabor do decaemento $B_s^0 \to (K^+\pi^-)(K^-\pi^+)$ foron determinadas a través da medida das asimetrías definidas en (R.7). Consideráronse aqueles candidatos cunha masa invariante dos catro corpos dentro dunha ventá de ±30 MeV/c^2 ao redor da masa do B_s^0.

Para cada unha das distribucións angulares, o fondo foi parametrizado usando sucesos da rexión de alta masa, normalizado ao número de sucesos calculados a partir do resultado do axuste á masa dos catro corpos e subtraído. As distribucións resultantes foron despois correxidas pola aceptancia angular determinada anteriormente a partir da simulación de $B_s^0 \to K^{*0}\overline{K}^{*0}$. Os criterios de selección nesgan a distribución en tempo propio do B_s^0, o cal pode inducir pequenas variacións na medida das asimetrías. Este efecto, xunto coa corrección por aceptancia angular, son as dúas fontes principais de erro sistemático.

As asimetrías determinadas son as seguintes,

$$\begin{aligned}
A_T^1 &= 0.003 \pm 0.041(\text{stat.}) \pm 0.009(\text{syst.}),\\
A_T^2 &= 0.999 \pm 0.041(\text{stat.}) \pm 0.009(\text{syst.}),\\
A_T^3 &= 0.019 \pm 0.041(\text{stat.}) \pm 0.008(\text{syst.}),\\
A_T^4 &= -0.040 \pm 0.041(\text{stat.}) \pm 0.008(\text{syst.}),
\end{aligned}$$

$$\begin{aligned} A_D^1 &= -0.061 \pm 0.041(\text{stat.}) \pm 0.012(\text{syst.}), \\ A_D^2 &= 0.081 \pm 0.041(\text{stat.}) \pm 0.008(\text{syst.}), \\ A_D^3 &= -0.079 \pm 0.041(\text{stat.}) \pm 0.023(\text{syst.}), \\ A_D^4 &= -0.081 \pm 0.041(\text{stat.}) \pm 0.010(\text{syst.}). \end{aligned}$$

Dentro da precisión estatística, ningunha delas mostra un sinal significativo de violación de *CP*. Este resultado é, polo tanto, compatible coa predición do Modelo Estándar.

R.6 Conclusións

Nesta tese preséntase o estudo do canal de desintegración $B_s^0 \to K^{*0}\overline{K}^{*0}$ cos primeiros datos tomados polo experimento LHCb durante 2010 e 2011. As dúas mostras corresponden con 37 pb^{-1} e 1.0 fb^{-1} de colisións protón-protón a unha enerxía no centro de masas de $\sqrt{s} = 7$ TeV.

$B_s^0 \to K^{*0}\overline{K}^{*0}$ é un exemplo de corrente neutra con cambio de sabor, mediado por diagrams tipo penguin no Modelo Estándar. Esta característica faino moi sensible a novas partículas circulando no loop. Predicións para a fracción de desintegración e as fraccións de polarización téñense calculado no contexto da factorización QCD. Ademais, o Modelo Estandar non predí violación de *CP* para este proceso mentres as contribucións de penguins subdominantes se desprece. Observables de violación de *CP* neste proceso, como por exemplo as asimetrías asociadas a produtos triples, son unha excelente ferramenta para poñer a proba modelos de física alén o Modelo Estándar.

Reportouse aquí a primeira observación deste canal de desintegración. Usando os datos recollidos por LHCb durante 2010, atopouse un sinal claro de $B_s^0 \to (K^+\pi^-)(K^-\pi^+)$ cunha significancia estatística maior de 10 σ. Normalizando ao canal de decaemento $B_d^0 \to J/\psi K^{*0}$, mediuse a fracción de desintegración do $B_s^0 \to K^{*0}\overline{K}^{*0}$, supoñendo que a contribución escalar no sistema $K\pi$ é equivalente á medida no canal de normalización [105]. O resultado obtido é o seguinte,

$$\mathcal{B}\left(B_s^0 \to K^{*0}\overline{K}^{*0}\right) = (2.81 \pm 0.46(\text{stat.}) \pm 0.45(\text{syst.}) \pm 0.34\,(f_s/f_d)) \times 10^{-5}$$

Ademais, levouse a cabo unha análise simplificada da distribución angular dos produtos da desintegración para medir a fracción de polarización lonxitudinal,

$$f_L = 0.31 \pm 0.12(\text{stat.}) \pm 0.04(\text{syst.})$$

Coa maior mostra de datos tomada por LHCb durante 2011, levouse a cabo unha análise máis precisa do proceso $B_s^0 \to (K^+\pi^-)(K^-\pi^+)$, aínda que sin información do sabor do meson B_s^0 e integrada no tempo. As variables deste análise son os tres ángulos da desintegración na base de helicidade e as masas invariantes dos sistemas $K^+\pi^-$ e $K^-\pi^+$, nun intervalo de ± 150 MeV/c^2 ao redor da masa do K^{*0}. Nesta ventá, o estado final está dominado polas contribucións resonantes $B_s \to K^{*0}(892)\overline{K}^{*0}(892)$, $B_s \to K^{*0}(892)(K^-\pi^+)_0$ e $B_s \to (K^+\pi^-)_0(K^-\pi^+)_0$, que designamos de xeito xenérico como *onda–P* e *onda–S*. Entre as 6 amplitudes que contribúen a este proceso, dúas son *CP*-impares, $A_\perp$ na *onda–P* e A_s^+ na *onda–S*, e o resto son *CP*-pares.

Este estudo componse de dúas partes diferenciadas. Na primeira, determináronse, dun xeito independente de ningún modelo, 8 asimetrías sensibles a violación de *CP*, accesibles, incluso no caso da mostra sen marcado de sabor, a través dos termos de interferencia entre cada unha das amplitudes CP-impares e as amplitudes CP-pares. Catro delas son asimetrías asociadas a produtos triples ($A_T^{(i)}$), e as outras catro son asimetrías de CP diretas ($A_D^{(i)}$). Os valores medidos son os seguintes,

$$\begin{aligned}
A_T^1 &= 0.003 \pm 0.041(\text{stat.}) \pm 0.009(\text{syst.}),\\
A_T^2 &= 0.999 \pm 0.041(\text{stat.}) \pm 0.009(\text{syst.}),\\
A_T^3 &= 0.019 \pm 0.041(\text{stat.}) \pm 0.008(\text{syst.}),\\
A_T^4 &= -0.040 \pm 0.041(\text{stat.}) \pm 0.008(\text{syst.}),
\end{aligned}$$

$$\begin{aligned}
A_D^1 &= -0.061 \pm 0.041(\text{stat.}) \pm 0.012(\text{syst.}),\\
A_D^2 &= 0.081 \pm 0.041(\text{stat.}) \pm 0.008(\text{syst.}),\\
A_D^3 &= -0.079 \pm 0.041(\text{stat.}) \pm 0.023(\text{syst.}),\\
A_D^4 &= -0.081 \pm 0.041(\text{stat.}) \pm 0.010(\text{syst.}).
\end{aligned}$$

Dentro da precisión estatística, ningunha destas asimetrías mostra signos de violación de CP. Esto é compatible coa predición do Modelo Estándar, incluso na presenza de unha fase débil ϕ_s distinta de cero, dado que os observables anteriores son proporcionais, á primeira orde, a diferencias de fases débiles entre as amplitudes que interfiren.

Na segunda parte deste estudo, levouse a cabo unha análise combinada da distribución angular e da masa na ventá de ± 150 MeV/c^2 ao redor do K^{*0}, na que se incluíron as 6 amplitudes. Os termos de interferencia proporcionais aos observables de violación de CP medidos na primeira parte do estudo foron desprezados. Como resultado desta análise, determináronse os módulos e fases das distintas amplitudes. Atopouse una forte contribución da *onda–S*, maioritariamente CP-par. A compoñente lonxitudinal do $K^{*0}(892)$ medida é considerablemente baixa,

$$f_L = 0.201 \pm 0.057(\text{stat.}) \pm 0.040(\text{syst.}),$$

e compatible coa medida previa nos datos de 2010. Como consecuencia da análise angular e na masa, a fracción de desintegracion do modo $B_s \to K^{*0}(892)\bar{K}^{*0}(892)$ foi determinado de novo obténdose,

$$\mathcal{B}(B_s^0 \to K^{*0}\overline{K}^{*0}) = (10.6 \pm 1.8(\text{stat.}) \pm 1.0(\text{syst.}) \pm 0.6(f_d/f_s)) \times 10^{-6}.$$

Este resultado está en bo acordo co valor central das predicións teóricas existentes [2], que mostran ademais un erro sistemático maior. Está tamén de acordo co valor medido previamente, cando a elevada contribución da *onda–S* en $B_s^0 \to (K^+\pi^-)(K^-\pi^+)$ se ten en conta dun xeito apropiado.

Este traballo abre o camiño para a futura análise dependente do tempo e con marcado do sabor do mesón B_s^0 cunha mostra de maior estatística, co obxectivo de determinar a fase electrodébil ϕ_s común para todas as amplitudes (CP-pares e CP-impares), que o Modelo Estándar predí moi pequena.

APPENDIX A

The $B_s^0 \to (K^+\pi^-)(K^-\pi^+)$ decay rate

In the present work the decay channels $B_s^0 \to (K^+\pi^-)_{J_1}(K^-\pi^+)_{J_2}$ in the mass region $|M(K\pi) - m_{K^{*0}(892)}| < 150$ MeV/c^2 are studied. In such region, the final states with $J_{1,2} = 0, 1$ are expected to be the dominant contributions. The decay rate for such process can be written as

$$\begin{aligned}
\frac{d^5\Gamma}{d\Omega dm_1 dm_2} \propto \Bigg| \quad & \Big(\quad A_0 \cos\theta_1 \cos\theta_2 + \frac{A_\parallel}{\sqrt{2}} \sin\theta_1 \sin\theta_2 \cos\varphi \\
& \quad + i\frac{A_\perp}{\sqrt{2}} \sin\theta_1 \sin\theta_2 \sin\varphi \quad \Big) \mathcal{M}_1(m_1)\mathcal{M}_1(m_2) \\
& - \quad \frac{A_{VS}}{\sqrt{3}} \cos\theta_1 \mathcal{M}_1(m_1)\mathcal{M}_0(m_2) \\
& + \quad \frac{A_{SV}}{\sqrt{3}} \cos\theta_2 \mathcal{M}_0(m_1)\mathcal{M}_1(m_2) \\
& - \quad \frac{A_{ss}}{3} \mathcal{M}_0(m_1)\mathcal{M}_0(m_2) \quad \Bigg|^2
\end{aligned} \tag{A.1}$$

where A_0, $A_\parallel$ and $A_\perp$ represent the three different polarisation amplitudes contributing to the $B \to V_1V_2$ decay (V_i is a vector meson), which in the considered mass region corresponds to the decay $B_s^0 \to K^{*0}\overline{K}^{*0}$. A_{VS} represents the amplitude corresponding to $J_1 = 1$ and $J_2 = 0$, or $B_s^0 \to K^{*0}(K^-\pi^+)_0$, where the scalar combination $(K^-\pi^+)_0$ is usually identified with an interference between the resonances κ (or $K_0^*(800)$) and $K_0^*(1430)$ [1]. A_{SV} corresponds to the equivalent amplitude with $J_1 = 0$ and $J_2 = 1$. A_{SS} represents the amplitude of the B_s^0 decay into two scalars, $J_1 = J_2 = 0$. $\mathcal{M}_J(m_i)$ are the invariant mass propagators corresponding to each amplitude. Finally, m_1 denotes the invariant mass of the $K^+\pi^-$ pair whilst m_2 reffers to $K^-\pi^+$, and the angular variables, $\Omega : \{\cos\theta_1, \cos\theta_2, \varphi\}$ are defined in Fig. A.1.

---

[1] Sometimes an additional nonresonant component is included.

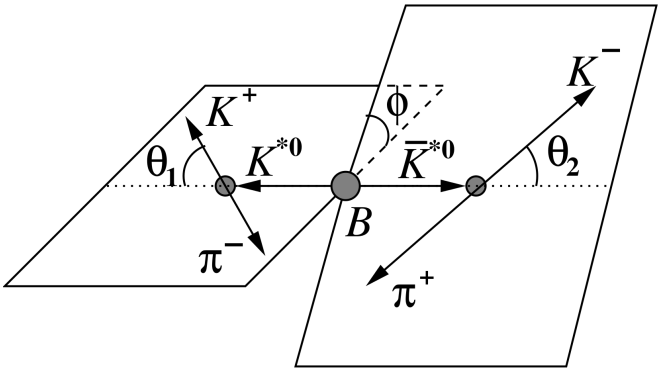

Figure A.1: Definition of the angles involved in the analysis for the $B_s^0 \to K^{*0}\overline{K}^{*0}$.

For the *CP*-conjugated process, $\overline{B}_s^0 \to (K^-\pi^+)_{J_1}(K^+\pi^-)_{J_2}$, the decay rate is

$$
\begin{aligned}
\frac{d^5\Gamma}{\Gamma d\Omega dm_1 dm_2} \propto \Bigg| \quad \Bigg(\quad & \bar{A}_0 \cos\theta_1 \cos\theta_2 + \frac{\bar{A}_\parallel}{\sqrt{2}} \sin\theta_1 \sin\theta_2 \cos\varphi \\
& -i\frac{\bar{A}_\perp}{\sqrt{2}} \sin\theta_1 \sin\theta_2 \sin\varphi \quad \Bigg) \mathcal{M}_1(m_1)\mathcal{M}_1(m_2) \\
- \quad & \frac{\bar{A}_{VS}}{\sqrt{3}} \cos\theta_2 \mathcal{M}_0(m_1)\mathcal{M}_1(m_2) \\
+ \quad & \frac{\bar{A}_{SV}}{\sqrt{3}} \cos\theta_1 \mathcal{M}_1(m_1)\mathcal{M}_0(m_2) \\
- \quad & \frac{\bar{A}_{ss}}{3} \mathcal{M}_0(m_1)\mathcal{M}_0(m_2) \quad \Bigg|^2
\end{aligned}
\tag{A.2}
$$

The exchange of the indices 1 and 2, and the sign shift of the term proportional to $A_\perp$ come from the reparameterisation

$$
\begin{aligned}
\bar{\theta}_1 &= \theta_2 \\
\bar{\theta}_2 &= \theta_1 \\
\bar{\varphi} &= -\varphi,
\end{aligned}
\tag{A.3}
$$

which relates the characteristic decay variables of B_s^0 (θ_1, θ_2 and φ) and $\overline{B}_s^0$ ($\bar{\theta}_1$, $\bar{\theta}_2$ and $\bar{\varphi}$) decays.

At this point, it is convenient to introduce the amplitudes

$$
\begin{aligned}
A_s^+ &= \frac{1}{\sqrt{2}}(A_{VS} + A_{SV}) \\
A_s^- &= \frac{1}{\sqrt{2}}(A_{VS} - A_{SV}).
\end{aligned}
\tag{A.4}
$$

which correspond to decays into the *CP*-odd and *CP*-even states $|s^+\rangle$ and $|s^-\rangle$ defined as

$$
\begin{aligned}
|s^+\rangle &= \frac{1}{\sqrt{2}}\left(|K^{*0}(K^-\pi^+)_0\rangle + |(K^+\pi^-)_0\overline{K}^{*0}\rangle\right) \\
|s^-\rangle &= \frac{1}{\sqrt{2}}\left(|K^{*0}(K^-\pi^+)_0\rangle - |(K^+\pi^-)_0\overline{K}^{*0}\rangle\right).
\end{aligned}
\tag{A.5}
$$

In this basis, the decay rates for B_s^0 and $\bar{B}_s^0$ take the form

$$\begin{aligned}\frac{d^5\Gamma}{d\Omega dm_1 dm_2} \propto \Bigg| & \Bigg(A_0 \cos\theta_1 \cos\theta_2 + \frac{A_\parallel}{\sqrt{2}} \sin\theta_1 \sin\theta_2 \cos\varphi \\ & + i\frac{A_\perp}{\sqrt{2}} \sin\theta_1 \sin\theta_2 \sin\varphi \Bigg) \mathcal{M}_1(m_1)\mathcal{M}_1(m_2) \\ & - \frac{A_s^+}{\sqrt{6}}(\cos\theta_1 \mathcal{M}_1(m_1)\mathcal{M}_0(m_2) - \cos\theta_2 \mathcal{M}_0(m_1)\mathcal{M}_1(m_2)) \\ & - \frac{A_s^-}{\sqrt{6}}(\cos\theta_1 \mathcal{M}_1(m_1)\mathcal{M}_0(m_2) + \cos\theta_2 \mathcal{M}_0(m_1)\mathcal{M}_1(m_2)) \\ & - \frac{A_{ss}}{3}\mathcal{M}_0(m_1)\mathcal{M}_0(m_2) \Bigg|^2 \end{aligned} \tag{A.6}$$

$$\begin{aligned}\frac{d^5\bar{\Gamma}}{d\Omega dm_1 dm_2} \propto \Bigg| & \Bigg(\bar{A}_0 \cos\theta_1 \cos\theta_2 + \frac{\bar{A}_\parallel}{\sqrt{2}} \sin\theta_1 \sin\theta_2 \cos\varphi \\ & - i\frac{\bar{A}_\perp}{\sqrt{2}} \sin\theta_1 \sin\theta_2 \sin\varphi \Bigg) \mathcal{M}_1(m_1)\mathcal{M}_1(m_2) \\ & + \frac{\bar{A}_s^+}{\sqrt{6}}(\cos\theta_1 \mathcal{M}_1(m_1)\mathcal{M}_0(m_2) - \cos\theta_2 \mathcal{M}_0(m_1)\mathcal{M}_1(m_2)) \\ & - \frac{\bar{A}_s^-}{\sqrt{6}}(\cos\theta_1 \mathcal{M}_1(m_1)\mathcal{M}_0(m_2) + \cos\theta_2 \mathcal{M}_0(m_1)\mathcal{M}_1(m_2)) \\ & - \frac{\bar{A}_{ss}}{3}\mathcal{M}_0(m_1)\mathcal{M}_0(m_2) \Bigg|^2 . \end{aligned} \tag{A.7}$$

Expanding the expressions above, the decay rates can be rewritten as follows

$$\frac{d^5\Gamma}{d\Omega dm_1 dm_2} \propto \sum_{n=1}^{21} K_n(t, m_1, m_2) F_n(\Omega) \tag{A.8}$$

where each term is a product of an angular function, F_n, times a coefficient containing the dependence with the amplitudes and the $K\pi$ invariant mass, $K_n(t, m_1, m_2)$. Note that the dependence of the K_n functions with the B_s^0 meson lifetime, t, is encoded in the decay amplitudes. A equivalent expression can be derived for $\bar{B}_s^0$ decays, in terms of the corresponding functions $\bar{K}_n(t, m_1, m_2)$. The definition of the functions F_n are shown in Table A.1. K_n and $\bar{K}_n$ are defined in Table A.2[1].

---

[1] The mass dependence of the functions K_{17} and $\bar{K}_{17}$ has been summarized in $\zeta(m_1, m_2) \equiv \mathcal{M}_1^*(m_1)\mathcal{M}_0^*(m_2)\mathcal{M}_0(m_1)\mathcal{M}_1(m_2)$

Table A.1: Definition of the angular functions, $F_n(\Omega)$, in the decay rate of the $B_s^0 \to (K^+\pi^-)(K^-\pi^+)$ decay, see (A.8), and its *CP* conjugated process.

n	$F_n(\Omega)$
1	$\cos^2(\theta_1)\cos^2(\theta_2)$
2	$\frac{1}{2}\sin^2(\theta_1)\sin^2(\theta_2)\cos^2(\varphi)$
3	$\frac{1}{2}\sin^2(\varphi)\sin^2(\theta_1)\sin^2(\theta_2)$
4	$\sqrt{2}\cos(\varphi)\cos(\theta_1)\cos(\theta_2)\lvert\sin(\theta_1)\rvert\lvert\sin(\theta_2)\rvert$
5	$-\sqrt{2}\sin(\varphi)\cos(\theta_1)\cos(\theta_2)\lvert\sin(\theta_1)\rvert\lvert\sin(\theta_2)\rvert$
6	$-\sin(\varphi)\sin^2(\theta_1)\sin^2(\theta_2)\cos(\varphi)$
7	$\frac{1}{3}\cos^2(\theta_1)$
8	$-\frac{2\sqrt{3}}{3}\cos^2(\theta_1)\cos(\theta_2)$
9	$-\frac{\sqrt{6}}{3}\cos(\varphi)\cos(\theta_1)\lvert\sin(\theta_1)\rvert\lvert\sin(\theta_2)\rvert$
10	$\frac{\sqrt{6}}{3}\sin(\varphi)\cos(\theta_1)\lvert\sin(\theta_1)\rvert\lvert\sin(\theta_2)\rvert$
11	$\frac{2\sqrt{3}}{9}\cos(\theta_1)$
12	$\frac{1}{3}\cos^2(\theta_2)$
13	$\frac{2\sqrt{3}}{3}\cos(\theta_1)\cos^2(\theta_2)$
14	$\frac{\sqrt{6}}{3}\cos(\varphi)\cos(\theta_2)\lvert\sin(\theta_1)\rvert\lvert\sin(\theta_2)\rvert$
15	$-\frac{\sqrt{6}}{3}\sin(\varphi)\cos(\theta_2)\lvert\sin(\theta_1)\rvert\lvert\sin(\theta_2)\rvert$
16	$-\frac{2\sqrt{3}}{9}\cos(\theta_2)$
17	$\frac{1}{3}\cos(\theta_1)\cos(\theta_2)$
18	$\frac{1}{9}$
19	$-\frac{2}{3}\cos(\theta_1)\cos(\theta_2)$
20	$-\frac{\sqrt{2}}{3}\cos(\varphi)\lvert\sin(\theta_1)\rvert\lvert\sin(\theta_2)\rvert$
21	$\frac{\sqrt{2}}{3}\sin(\varphi)\lvert\sin(\theta_1)\rvert\lvert\sin(\theta_2)\rvert$

Table A.2: Definition of the mass dependent coefficients $K_n(t, m_1, m_2)$ and $\bar{K}_n(t, m_1, m_2)$ entering the decay rate that describes the $B_s^0 \to (K^+\pi^-)(K^-\pi^+)$ decay and its *CP* conjugated process.

n	$K_n(t, m_1, m_2)$	$Kbar_n(t, m_1, m_2)$
1	$\lvert A_0\rvert^2 \lvert\mathcal{M}_1(m_1)\rvert^2 \lvert\mathcal{M}_1(m_2)\rvert^2$	$\lvert\bar{A}_0\rvert^2 \lvert\mathcal{M}_1(m_1)\rvert^2 \lvert\mathcal{M}_1(m_2)\rvert^2$
2	$\lvert A_\parallel\rvert^2 \lvert\mathcal{M}_1(m_1)\rvert^2 \lvert\mathcal{M}_1(m_2)\rvert^2$	$\lvert\bar{A}_\parallel\rvert^2 \lvert\mathcal{M}_1(m_1)\rvert^2 \lvert\mathcal{M}_1(m_2)\rvert^2$
3	$\lvert A_\perp\rvert^2 \lvert\mathcal{M}_1(m_1)\rvert^2 \lvert\mathcal{M}_1(m_2)\rvert^2$	$\lvert\bar{A}_\perp\rvert^2 \lvert\mathcal{M}_1(m_1)\rvert^2 \lvert\mathcal{M}_1(m_2)\rvert^2$
4	$\Re\left(A_0 {A_\parallel}^*\right) \lvert\mathcal{M}_1(m_1)\rvert^2 \lvert\mathcal{M}_1(m_2)\rvert^2$	$\Re\left(\bar{A}_0 \bar{A}_\parallel^*\right) \lvert\mathcal{M}_1(m_1)\rvert^2 \lvert\mathcal{M}_1(m_2)\rvert^2$
5	$\Im\left(A_0 {A_\perp}^*\right) \lvert\mathcal{M}_1(m_1)\rvert^2 \lvert\mathcal{M}_1(m_2)\rvert^2$	$-\Im\left(\bar{A}_0 \bar{A}_\perp^*\right) \lvert\mathcal{M}_1(m_1)\rvert^2 \lvert\mathcal{M}_1(m_2)\rvert^2$
6	$\Im\left(A_\parallel {A_\perp}^*\right) \lvert\mathcal{M}_1(m_1)\rvert^2 \lvert\mathcal{M}_1(m_2)\rvert^2$	$-\Im\left(\bar{A}_\parallel \bar{A}_\perp^*\right) \lvert\mathcal{M}_1(m_1)\rvert^2 \lvert\mathcal{M}_1(m_2)\rvert^2$
7	$\frac{1}{2}\left(\lvert A_S^+\rvert^2 + \lvert A_S^-\rvert^2 + 2\Re\left(A_S^-(A_S^+)^*\right)\right) \lvert\mathcal{M}_1(m_1)\rvert^2 \lvert\mathcal{M}_0(m_2)\rvert^2$	$\frac{1}{2}\left(\lvert\bar{A}_s^+\rvert^2 + \lvert\bar{A}_s^-\rvert^2 - 2\Re\left(\bar{A}_S^-(\bar{A}_S^+)^*\right)\right) \lvert\mathcal{M}_0(m_2)\rvert^2 \lvert\mathcal{M}_1(m_1)\rvert^2$
8	$\frac{\sqrt{2}}{2}\Re\left(\left(A_S^+ + A_S^-\right) {A_0}^*\mathcal{M}_0(m_2)\mathcal{M}_1(m_2)^*\right) \lvert\mathcal{M}_1(m_1)\rvert^2$	$\frac{\sqrt{2}}{2}\Re\left(\left(-\bar{A}_s^+ + \bar{A}_s^-\right) \bar{A}_0^*\mathcal{M}_0(m_2)\mathcal{M}_1(m_2)^*\right) \lvert\mathcal{M}_1(m_1)\rvert^2$
9	$\frac{\sqrt{2}}{2}\Re\left(\left(A_S^+ + A_S^-\right) {A_\parallel}^*\mathcal{M}_0(m_2)\mathcal{M}_1(m_2)^*\right) \lvert\mathcal{M}_1(m_1)\rvert^2$	$\frac{\sqrt{2}}{2}\Re\left(\left(-\bar{A}_s^+ + \bar{A}_s^-\right) \bar{A}_\parallel^*\mathcal{M}_0(m_2)\mathcal{M}_1(m_2)^*\right) \lvert\mathcal{M}_1(m_1)\rvert^2$
10	$\frac{\sqrt{2}}{2}\Im\left(\left(A_S^+ + A_S^-\right) {A_\perp}^*\mathcal{M}_0(m_2)\mathcal{M}_1(m_2)^*\right) \lvert\mathcal{M}_1(m_1)\rvert^2$	$\frac{\sqrt{2}}{2}\Im\left(\left(\bar{A}_s^+ - \bar{A}_s^-\right) \bar{A}_\perp^*\mathcal{M}_0(m_2)\mathcal{M}_1(m_2)^*\right) \lvert\mathcal{M}_1(m_1)\rvert^2$
11	$\frac{\sqrt{2}}{2}\Re\left(\left(A_S^+ + A_S^-\right) A_{ss}^*\mathcal{M}_1(m_1)\mathcal{M}_0(m_1)^*\right) \lvert\mathcal{M}_0(m_2)\rvert^2$	$\frac{\sqrt{2}}{2}\Re\left(\left(-\bar{A}_s^+ + \bar{A}_s^-\right) \bar{A}_{SS}^*\mathcal{M}_1(m_1)\mathcal{M}_0(m_1)^*\right) \lvert\mathcal{M}_0(m_2)\rvert^2$
12	$\frac{1}{2}\left(\lvert A_S^+\rvert^2 + \lvert A_S^-\rvert^2 - 2\Re\left(A_S^- {A_S^+}^*\right)\right) \lvert\mathcal{M}_0(m_1)\rvert^2 \lvert\mathcal{M}_1(m_2)\rvert^2$	$\frac{1}{2}\left(\lvert\bar{A}_S^+\rvert^2 + \lvert\bar{A}_S^-\rvert^2 + 2\Re\left(\bar{A}_S^-(\bar{A}_S^+)^*\right)\right) \lvert\mathcal{M}_0(m_1)\rvert^2 \lvert\mathcal{M}_1(m_2)\rvert^2$
13	$\frac{\sqrt{2}}{2}\Re\left(\left(A_S^+ - A_S^-\right) {A_0}^*\mathcal{M}_0(m_1)\mathcal{M}_1(m_1)^*\right) \lvert\mathcal{M}_1(m_2)\rvert^2$	$-\frac{\sqrt{2}}{2}\Re\left(\left(\bar{A}_s^+ + \bar{A}_s^-\right) \bar{A}_0^*\mathcal{M}_1(m_1)\mathcal{M}_0(m_1)^*\right) \lvert\mathcal{M}_1(m_2)\rvert^2$
14	$\frac{\sqrt{2}}{2}\Re\left(\left(A_S^+ - A_S^-\right) {A_\parallel}^*\mathcal{M}_0(m_1)\mathcal{M}_1(m_1)^*\right) \lvert\mathcal{M}_1(m_2)\rvert^2$	$-\frac{\sqrt{2}}{2}\Re\left(\left(\bar{A}_s^+ + \bar{A}_s^-\right) \bar{A}_\parallel^*\mathcal{M}_0(m_1)\mathcal{M}_1(m_1)^*\right) \lvert\mathcal{M}_1(m_2)\rvert^2$
15	$\frac{\sqrt{2}}{2}\Im\left(\left(A_S^+ - A_S^-\right) {A_\perp}^*\mathcal{M}_0(m_1)\mathcal{M}_1(m_1)^*\right) \lvert\mathcal{M}_1(m_2)\rvert^2$	$\frac{\sqrt{2}}{2}\Im\left(\left(\bar{A}_s^+ + \bar{A}_s^-\right) \bar{A}_\perp^*\mathcal{M}_0(m_1)\mathcal{M}_1(m_1)^*\right) \lvert\mathcal{M}_1(m_2)\rvert^2$
16	$\frac{\sqrt{2}}{2}\Re\left(\left(A_S^+ - A_S^-\right) A_{ss}^*\mathcal{M}_1(m_2)\mathcal{M}_0(m_2)^*\right) \lvert\mathcal{M}_0(m_1)\rvert^2$	$-\frac{\sqrt{2}}{2}\Re\left(\left(\bar{A}_s^+ + \bar{A}_s^-\right) \bar{A}_{SS}^*\mathcal{M}_1(m_2)\mathcal{M}_0(m_2)^*\right) \lvert\mathcal{M}_0(m_1)\rvert^2$
17	$\left(\lvert A_S^+\rvert^2 - \lvert A_S^-\rvert^2\right) \Re\left(\zeta(m_1, m_2)\right) + \Im\left(A_s^+(A_s^-)^*\right) \Im\left(\zeta(m_1, m_2)\right)$	$\left(\lvert A_S^+\rvert^2 - \lvert A_S^-\rvert^2\right) \Re\left(\zeta(m_1, m_2)\right) - \Im\left(A_s^+(A_s^-)^*\right) \Im\left(\zeta(m_1, m_2)\right)$
18	$\lvert A_{ss}\rvert^2 \lvert\mathcal{M}_0(m_1)\rvert^2 \lvert\mathcal{M}_0(m_2)\rvert^2$	$\lvert\bar{A}_{ss}\rvert^2 \lvert\mathcal{M}_0(m_1)\rvert^2 \lvert\mathcal{M}_0(m_2)\rvert^2$
19	$\Re\left(A_{ss}{A_0}^*\mathcal{M}_0(m_1)\mathcal{M}_0(m_2)\mathcal{M}_1(m_1)^*\mathcal{M}_1(m_2)^*\right)$	$\Re\left(\bar{A}_{ss}\bar{A}_0^*\mathcal{M}_0(m_1)\mathcal{M}_0(m_2)\mathcal{M}_1(m_1)^*\mathcal{M}_1(m_2)^*\right)$
20	$\Re\left(A_{ss}{A_\parallel}^*\mathcal{M}_0(m_1)\mathcal{M}_0(m_2)\mathcal{M}_1(m_1)^*\mathcal{M}_1(m_2)^*\right)$	$\Re\left(\bar{A}_{ss}\bar{A}_\parallel^*\mathcal{M}_0(m_1)\mathcal{M}_0(m_2)\mathcal{M}_1(m_1)^*\mathcal{M}_1(m_2)^*\right)$
21	$\Im\left(A_{ss}{A_\perp}^*\mathcal{M}_0(m_1)\mathcal{M}_0(m_2)\mathcal{M}_1(m_1)^*\mathcal{M}_1(m_2)^*\right)$	$-\Im\left(\bar{A}_{ss}\bar{A}_\perp^*\mathcal{M}_0(m_1)\mathcal{M}_0(m_2)\mathcal{M}_1(m_1)^*\mathcal{M}_1(m_2)^*\right)$

When the time evolution is included in the decay rate, it can be shown that each function $K_n(t, m_1, m_2)$ takes the form

$$K_n(t, m_1, m_2) = \frac{1}{2} e^{\Gamma_s t} \quad \Big[\quad a_n(m_1, m_2) \cosh\left(\frac{\Delta\Gamma t}{2}\right) + b_n(m_1, m_2) \sinh\left(\frac{\Delta\Gamma t}{2}\right) \\ c_n(m_1, m_2) \cos(\Delta m_s t) + d_n(m_1, m_2) \sin(\Delta m_s t) \Big] \quad (A.9)$$

where the coefficients a_n, b_n, c_n and d_n contain combinations of the amplitudes at $t = 0$ and the mass-dependent propagators. The values of these coefficients are given in Tables A.3 to A.6[1]

The coefficients $\bar{a}_n$, $\bar{b}_n$, $\bar{c}_n$ and $\bar{d}_n$ describing the *CP* conjugated decay can be calculated from a_n, b_n, c_n and d_n by exchanging $A_f \leftrightarrow \eta_f \bar{A}_f$, where η_f is the *CP*-eigenvalue of the $|f\rangle$ final state, and changing the sign of the mixing phase, ϕ_M. This transformation leads to the relations

$$\bar{a}_n = a_n\ , \quad \bar{b}_n = b_n\ , \quad \bar{c}_n = -c_n\ , \quad \bar{d}_n = -d_n. \quad (A.10)$$

In the Standard Model, the decay amplitudes for this process are dominated by just one contribution, $A_f \simeq A_f e^{i\delta_f} e^{i\phi_D}$, with one strong phase δ_f (in priciple different for each amplitude) and one weak phase ϕ_D (common for all the amplitudes)[2]. Moreover, the measurable weak phase arising in the interference between this decay and the B_s^0-mixing, $\phi_s^{B_s^0 \to K^{*0}\bar{K}^{*0}} = 2\phi_D + \phi_M$, is expected to be very small. Therefore, within the Standard Model, no *CP*-violation is expected to arise in this process,

$$\lambda_f \equiv \frac{\bar{A}_f}{A_f} e^{-i\phi_M} \simeq e^{-i\phi_s^{B_s^0 \to K^{*0}\bar{K}^{*0}}} \simeq 1 \ \ \forall f \quad (A.11)$$

Under this assumption, the oscillation terms in the decay rate, those proportional to $\cos(\Delta m_s t)$ and $\sin(\Delta m_s t)$, vanish and the time-dependent functions in the *untagged* decay rate, $\tilde{K}_n(t, m_1, m_2)$, can be written as

$$\tilde{K}_n(t, m_1, m_2) = \tilde{a}_n(m_1, m_2) \cosh\left(\frac{\Delta\Gamma t}{2}\right) + \tilde{b}_n(m_1, m_2) \sinh\left(\frac{\Delta\Gamma t}{2}\right) \quad (A.12)$$

with the coefficients $\tilde{a}_n$ and $\tilde{b}_n$ shown in Table A.7.

When the functions (A.12) are integrated over the B_s^0 lifetime, the decay rate takes the form

$$\left(\frac{d^5\left(\Gamma + \bar{\Gamma}\right)}{d\Omega dm_1 dm_2}\right) \propto \sum_{n=1}^{21} \tilde{K}_n(m_1, m_2) F_n(\Omega) \quad (A.13)$$

whith the functions $\tilde{K}_n(m_1, m_2)$ defined in Table 4.3.

---

[1] In these definitions, ϕ_M represents the weak phase mediating the B_s^0-$\bar{B}_s^0$ mixing (see Sect. 2.2.4.1).

[2] The corresponding *CP*-conjugated amplitude is then $\bar{A}_f \simeq |A_f| e^{i\delta_f} e^{-i\phi_D}$.

Table A.3: a_n coefficients in (A.9). The mass function in a_{17} is defined as $\zeta(m_1, m_2) \equiv \mathcal{M}_1^*(m_1)\mathcal{M}_0^*(m_2)\mathcal{M}_0(m_1)\mathcal{M}_1(m_2)$

n	a_n
1	$\left(\lvert A_0\rvert^2 + \lvert\bar{A}_0\rvert^2\right) \lvert\mathcal{M}_1(m_1)\rvert^2 \lvert\mathcal{M}_1(m_2)\rvert^2$
2	$\left(\lvert A_\parallel\rvert^2 + \lvert\bar{A}_\parallel\rvert^2\right) \lvert\mathcal{M}_1(m_1)\rvert^2 \lvert\mathcal{M}_1(m_2)\rvert^2$
3	$\left(\lvert A_\perp\rvert^2 + \lvert\bar{A}_\perp\rvert^2\right) \lvert\mathcal{M}_1(m_1)\rvert^2 \lvert\mathcal{M}_1(m_2)\rvert^2$
4	$\Re\left(A_0 A_\parallel{}^* + \bar{A}_0\bar{A}_\parallel^*\right) \lvert\mathcal{M}_1(m_1)\rvert^2 \lvert\mathcal{M}_1(m_2)\rvert^2$
5	$\Im\left(A_0 A_\perp{}^* - \bar{A}_0\bar{A}_\perp^*\right) \lvert\mathcal{M}_1(m_1)\rvert^2 \lvert\mathcal{M}_1(m_2)\rvert^2$
6	$\Im\left(A_\parallel A_\perp{}^* - \bar{A}_\parallel\bar{A}_\perp^*\right) \lvert\mathcal{M}_1(m_1)\rvert^2 \lvert\mathcal{M}_1(m_2)\rvert^2$
7	$\frac{1}{2}\left\{\left(\lvert A_s^-\rvert^2 + \lvert A_s^+\rvert^2\right) + \left(\lvert\bar{A}_s^-\rvert^2 + \lvert\bar{A}_s^+\rvert^2\right)\right.$ $\left. + 2\Re\left(A_s^- A_s^{+*} - \bar{A}_s^-(\bar{A}_s^+)^*\right)\right\} \lvert\mathcal{M}_0(m_2)\rvert^2 \lvert\mathcal{M}_1(m_1)\rvert^2$
8	$\frac{\sqrt{2}}{2}\Re\left\{\left(A_s^- A_0{}^* + \bar{A}_s^-\bar{A}_0^* + A_s^+ A_0^* - \bar{A}_s^+\bar{A}_0^*\right)\mathcal{M}_0(m_2)\mathcal{M}_1(m_2)^*\right\} \lvert\mathcal{M}_1(m_1)\rvert^2$
9	$\frac{\sqrt{2}}{2}\Re\left\{\left(A_s^- A_\parallel{}^* + \bar{A}_s^-\bar{A}_\parallel^* + A_s^+ A_\parallel{}^* - \bar{A}_s^+\bar{A}_\parallel^*\right)\mathcal{M}_0(m_2)\mathcal{M}_1(m_2)^*\right\} \lvert\mathcal{M}_1(m_1)\rvert^2$
10	$\frac{\sqrt{2}}{2}\Im\left\{\left(A_s^- A_\perp{}^* - \bar{A}_s^-\bar{A}_\perp^* + A_s^+ A_\perp{}^* + \bar{A}_s^+\bar{A}_\perp^*\right)\mathcal{M}_0(m_2)\mathcal{M}_1(m_2)^*\right\} \lvert\mathcal{M}_1(m_1)\rvert^2$
11	$\frac{\sqrt{2}}{2}\Re\left\{\left(A_s^- A_{ss}^* + \bar{A}_s^-\bar{A}_{ss}^* + A_s^+ A_{ss}^* - \bar{A}_s^+\bar{A}_{ss}^*\right)\mathcal{M}_1(m_1)\mathcal{M}_0(m_1)^*\right) \lvert\mathcal{M}_0(m_2)\rvert^2$
12	$\frac{1}{2}\left\{\left(\lvert A_s^-\rvert^2 + \lvert A_s^+\rvert^2\right) + \left(\lvert\bar{A}_s^-\rvert^2 + \lvert\bar{A}_s^+\rvert^2\right)\right.$ $\left. - 2\Re\left(A_s^- A_s^{+*} - \bar{A}_s^-(\bar{A}_s^+)^*\right)\right\} \lvert\mathcal{M}_0(m_1)\rvert^2 \lvert\mathcal{M}_1(m_2)\rvert^2$
13	$-\frac{\sqrt{2}}{2}\Re\left\{\left(A_s^- A_0^* + \bar{A}_s^-\bar{A}_0^* - A_s^+ A_0{}^* + \bar{A}_s^+\bar{A}_0^*\right)\mathcal{M}_0(m_1)\mathcal{M}_1(m_1)^*\right\} \lvert\mathcal{M}_1(m_2)\rvert^2$
14	$-\frac{\sqrt{2}}{2}\Re\left\{\left(A_s^- A_\parallel^* + \bar{A}_s^-\bar{A}_\parallel^* - A_s^+ A_\parallel{}^* + \bar{A}_s^+\bar{A}_\parallel^*\right)\mathcal{M}_0(m_1)\mathcal{M}_1(m_1)^*\right\} \lvert\mathcal{M}_1(m_2)\rvert^2$
15	$-\frac{\sqrt{2}}{2}\Im\left\{\left(A_s^- A_\perp{}^* - \bar{A}_s^-\bar{A}_\perp^* - A_s^+ A_\perp{}^* - \bar{A}_s^+\bar{A}_\perp^*\right)\mathcal{M}_0(m_1)\mathcal{M}_1(m_1)^*\right\} \lvert\mathcal{M}_1(m_2)\rvert^2$
16	$-\frac{\sqrt{2}}{2}\Re\left\{\left(A_s^- A_{ss}^* + \bar{A}_s^-\bar{A}_{ss}^* - A_s^+ A_{ss}^* + \bar{A}_s^+\bar{A}_{ss}^*\right)\mathcal{M}_1(m_2)\mathcal{M}_0(m_2)^*\right\} \lvert\mathcal{M}_0(m_1)\rvert^2$
17	$\left\{\left(\lvert A_s^+\rvert^2 - \lvert A_s^-\rvert^2\right) + \left(\lvert\bar{A}_s^+\rvert^2 - \lvert\bar{A}_s^-\rvert^2\right)\right\}\Re(\zeta(m_1, m_2))$ $+2\Im\left(A_s^- A_s^{+*} - \bar{A}_s^-(\bar{A}_s^+)^*\right)\Im(\zeta(m_1, m_2))$
18	$\left(\lvert A_{ss}\rvert^2 + \lvert\bar{A}_{ss}\rvert^2\right) \lvert\mathcal{M}_0(m_1)\rvert^2 \lvert\mathcal{M}_0(m_2)\rvert^2$
19	$\Re\left\{\left(A_{ss}A_0{}^* + \bar{A}_{ss}\bar{A}_0^*\right)\mathcal{M}_0(m_1)\mathcal{M}_0(m_2)\mathcal{M}_1(m_1)^*\mathcal{M}_1(m_2)^*\right\}$
20	$\Re\left\{\left(A_{ss}A_\parallel{}^* + \bar{A}_{ss}\bar{A}_\parallel^*\right)\mathcal{M}_0(m_1)\mathcal{M}_0(m_2)\mathcal{M}_1(m_1)^*\mathcal{M}_1(m_2)^*\right\}$
21	$\Im\left\{\left(A_{ss}A_\perp{}^* - \bar{A}_{ss}\bar{A}_\perp^*\right)\mathcal{M}_0(m_1)\mathcal{M}_0(m_2)\mathcal{M}_1(m_1)^*\mathcal{M}_1(m_2)^*\right\}$

Table A.4: b_n coefficients in (A.9). The mass function in a_{17} is defined as $\zeta(m_1, m_2) \equiv \mathcal{M}_1^*(m_1)\mathcal{M}_0^*(m_2)\mathcal{M}_0(m_1)\mathcal{M}_1(m_2)$

n	b_n
1	$-2\Re\big(A_0\bar{A}_0^* e^{i\phi_M}\big)\,\lvert\mathcal{M}_1(m_1)\rvert^2\,\lvert\mathcal{M}_1(m_2)\rvert^2$
2	$-2\Re\big(A_\parallel\bar{A}_\parallel^* e^{i\phi_M}\big)\,\lvert\mathcal{M}_1(m_1)\rvert^2\,\lvert\mathcal{M}_1(m_2)\rvert^2$
3	$2\Re\big(A_\perp\bar{A}_\perp^* e^{i\phi_M}\big)\,\lvert\mathcal{M}_1(m_1)\rvert^2\,\lvert\mathcal{M}_1(m_2)\rvert^2$
4	$-\Re\big\{\big(A_0\bar{A}_\parallel^* + A_\parallel\bar{A}_0^*\big)\,e^{i\phi_M}\big\}\,\lvert\mathcal{M}_1(m_1)\rvert^2\,\lvert\mathcal{M}_1(m_2)\rvert^2$
5	$\Im\big\{\big(A_0\bar{A}_\perp^* + A_\perp\bar{A}_0^*\big)\,e^{i\phi_M}\big\}\,\lvert\mathcal{M}_1(m_1)\rvert^2\,\lvert\mathcal{M}_1(m_2)\rvert^2$
6	$\Im\big\{\big(A_\parallel\bar{A}_\perp^* + A_\perp\bar{A}_\parallel^*\big)\,e^{i\phi_M}\big\}\,\lvert\mathcal{M}_1(m_1)\rvert^2\,\lvert\mathcal{M}_1(m_2)\rvert^2$
7	$\Re\big\{\big(A_s^+ + A_s^-\big)\,\big(\bar{A}_s^+ - \bar{A}_s^-\big)^*\,e^{i\phi_M}\big\}\,\lvert\mathcal{M}_0(m_2)\rvert^2\,\lvert\mathcal{M}_1(m_1)\rvert^2$
8	$-\frac{\sqrt{2}}{2}\Re\big\{\bigl((A_s^-\bar{A}_0^* + \bar{A}_0^* A_s^+)e^{i\phi_M}$ $-(A_0^*(\bar{A}_s^+) - \bar{A}_s^- A_0{}^*)e^{-i\phi_M}\bigr)\,\mathcal{M}_0(m_2)\mathcal{M}_1(m_2)^*\big\}\,\lvert\mathcal{M}_1(m_1)\rvert^2$
9	$-\frac{\sqrt{2}}{2}\Re\big\{\bigl((A_s^-\bar{A}_\parallel^* + A_s^+\bar{A}_\parallel^*)e^{i\phi_M}$ $+(\bar{A}_s^- A_\parallel{}^* - \bar{A}_s^+ A_\parallel{}^*)e^{-i\phi_M}\bigr)\,\mathcal{M}_0(m_2)\mathcal{M}_1(m_2)^*\big\}\,\lvert\mathcal{M}_1(m_1)\rvert^2$
10	$\frac{\sqrt{2}}{2}\Im\big\{\bigl((A_s^-\bar{A}_\perp^* + A_s^+\bar{A}_\perp^*)e^{i\phi_M}$ $-(\bar{A}_s^- A_\perp{}^* - \bar{A}_s^+ A_\perp{}^*)e^{-i\phi_M}\bigr)\,\mathcal{M}_0(m_2)\mathcal{M}_1(m_2)^*\big\}\,\lvert\mathcal{M}_1(m_1)\rvert^2$
11	$-\frac{\sqrt{2}}{2}\Re\big\{\bigl((\bar{A}_{ss}^* A_s^- + \bar{A}_{ss}^* A_s^+)e^{i\phi_M}$ $+(A_{ss}^*\bar{A}_s^- - A_{ss}^*\bar{A}_s^+)e^{-i\phi_M}\bigr)\,\mathcal{M}_1(m_1)\mathcal{M}_0(m_1)^*\big\}\,\lvert\mathcal{M}_0(m_2)\rvert^2$
12	$\Re\big\{\big(A_s^+ - A_s^-\big)\,\big(\bar{A}_s^+ + \bar{A}_s^-\big)^*\,e^{i\phi_M}\big\}\,\lvert\mathcal{M}_0(m_1)\rvert^2\,\lvert\mathcal{M}_1(m_2)\rvert^2$
13	$\frac{\sqrt{2}}{2}\Re\big\{\bigl((A_s^-\bar{A}_0^* - A_s^+\bar{A}_0^*)e^{i\phi_M}$ $+(A_0^*\bar{A}_s^- + \bar{A}_s^+ A_0{}^*)e^{-i\phi_M}\bigr)\,\mathcal{M}_0(m_1)\mathcal{M}_1(m_1)^*\big\}\,\lvert\mathcal{M}_1(m_2)\rvert^2$
14	$\frac{\sqrt{2}}{2}\Re\big\{\bigl(A_s^-\bar{A}_\parallel^* - A_s^+\bar{A}_\parallel^*)e^{i\phi_M}$ $+(A_\parallel^*\bar{A}_s^- + \bar{A}_s^+ A_\parallel{}^*)e^{-i\phi_M}\bigr)\,\mathcal{M}_0(m_1)\mathcal{M}_1(m_1)^*\big\}\,\lvert\mathcal{M}_1(m_2)\rvert^2$
15	$-\frac{\sqrt{2}}{2}\Im\big\{\bigl(A_s^-\bar{A}_\perp^* - A_s^+\bar{A}_\perp^*)e^{i\phi_M}$ $-(\bar{A}_s^- A_\perp{}^* + \bar{A}_s^+ A_\perp{}^*)e^{-i\phi_M}\bigr)\,\mathcal{M}_0(m_1)\mathcal{M}_1(m_1)^*\big\}\,\lvert\mathcal{M}_1(m_2)\rvert^2$
16	$\frac{\sqrt{2}}{2}\Re\big\{\bigl((A_s^-\bar{A}_{ss}^* - A_s^+\bar{A}_{ss}^*)e^{i\phi_M}$ $+(A_{ss}^*\bar{A}_s^+ + A_{ss}^*\bar{A}_s^-)e^{-i\phi_M}\bigr)\,\mathcal{M}_1(m_2)\mathcal{M}_0(m_2)^*\big\}\,\lvert\mathcal{M}_0(m_1)\rvert^2$
17	$-\Re\big\{\big(A_s^-(\bar{A}_s^-)^* + A_s^+(\bar{A}_s^+)^*\big)\,e^{i\phi_M}\big\}\,\Re(\zeta(m_1, m_2))$ $-\Im\big\{\big(A_s^+(\bar{A}_s^-)^* + (A_s^-(\bar{A}_s^+)^*\big)\,e^{i\phi_M}\big\}\,\Im(\zeta(m_1, m_2))$
18	$-2\Re\big(A_{ss}\bar{A}_{ss}^* e^{i\phi_M}\big)\,\lvert\mathcal{M}_0(m_1)\rvert^2\,\lvert\mathcal{M}_0(m_2)\rvert^2$
19	$-\Re\big\{\big(A_{ss}\bar{A}_0^* e^{i\phi_M} + \bar{A}_{ss}A_0{}^* e^{-i\phi_M}\big)\,\mathcal{M}_0(m_1)\mathcal{M}_0(m_2)\mathcal{M}_1(m_1)^*\mathcal{M}_1(m_2)^*\big\}$
20	$-\Re\big\{\big(A_{ss}\bar{A}_\parallel^* e^{i\phi_M} + \bar{A}_{ss}A_\parallel{}^* e^{-i\phi_M}\big)\,\mathcal{M}_0(m_1)\mathcal{M}_0(m_2)\mathcal{M}_1(m_1)^*\mathcal{M}_1(m_2)^*\big\}$
21	$\Im\big\{\big(A_{ss}\bar{A}_\perp^* e^{i\phi_M} - \bar{A}_{ss}A_\perp{}^* e^{-i\phi_M}\big)\,\mathcal{M}_0(m_1)\mathcal{M}_0(m_2)\mathcal{M}_1(m_1)^*\mathcal{M}_1(m_2)^*\big\}$

Table A.5: c_n coefficients in (A.9). The mass function in c_{17} is defined as $\zeta(m_1, m_2) \equiv \mathcal{M}_1^*(m_1)\mathcal{M}_0^*(m_2)\mathcal{M}_0(m_1)\mathcal{M}_1(m_2)$

N	c_k
1	$\left(\lvert A_0\rvert^2 - \lvert\bar{A}_0\rvert^2\right) \lvert\mathcal{M}_1(m_1)\rvert^2 \lvert\mathcal{M}_1(m_2)\rvert^2$
2	$\left(\lvert A_\parallel\rvert^2 - \lvert\bar{A}_\parallel\rvert^2\right) \lvert\mathcal{M}_1(m_1)\rvert^2 \lvert\mathcal{M}_1(m_2)\rvert^2$
3	$\left(\lvert A_\perp\rvert^2 - \lvert\bar{A}_\perp\rvert^2\right) \lvert\mathcal{M}_1(m_1)\rvert^2 \lvert\mathcal{M}_1(m_2)\rvert^2$
4	$\Re\left(A_0 {A_\parallel}^* - \bar{A}_0 \bar{A}_\parallel^*\right) \lvert\mathcal{M}_1(m_1)\rvert^2 \lvert\mathcal{M}_1(m_2)\rvert^2$
5	$\Im\left(A_0 {A_\perp}^* + \bar{A}_0 \bar{A}_\perp^*\right) \lvert\mathcal{M}_1(m_1)\rvert^2 \lvert\mathcal{M}_1(m_2)\rvert^2$
6	$\Im\left(A_\parallel {A_\perp}^* + \bar{A}_\parallel \bar{A}_\perp^*\right) \lvert\mathcal{M}_1(m_1)\rvert^2 \lvert\mathcal{M}_1(m_2)\rvert^2$
7	$\frac{1}{2}\left\{\left(\lvert A_s^-\rvert^2 + \lvert A_s^+\rvert^2\right) - \left(\lvert\bar{A}_s^-\rvert^2 + \lvert\bar{A}_s^+\rvert^2\right)\right.$ $\left. +2\Re\left(A_s^- {A_s^+}^* + \bar{A}_s^- (\bar{A}_s^+)^*\right)\right\} \lvert\mathcal{M}_1(m_1)\rvert^2 \lvert\mathcal{M}_0(m_2)\rvert^2$
8	$\frac{\sqrt{2}}{2}\Re\left\{\left(A_s^- {A_0}^* - \bar{A}_s^- \bar{A}_0^* + A_s^+ A_0^* + \bar{A}_s^+ \bar{A}_0^*\right) \mathcal{M}_0(m_2)\mathcal{M}_1(m_2)^*\right\} \lvert\mathcal{M}_1(m_1)\rvert^2$
9	$\frac{\sqrt{2}}{2}\Re\left\{\left(A_s^- {A_\parallel}^* - \bar{A}_s^- \bar{A}_\parallel^* + A_s^+ A_\parallel^* + \bar{A}_s^+ \bar{A}_\parallel^*\right) \mathcal{M}_0(m_2)\mathcal{M}_1(m_2)^*\right\} \lvert\mathcal{M}_1(m_1)\rvert^2$
10	$\frac{\sqrt{2}}{2}\Im\left\{\left(A_s^- {A_\perp}^* + \bar{A}_s^- \bar{A}_\perp^* + A_s^+ A_\perp^* - \bar{A}_s^+ \bar{A}_\perp^*\right) \mathcal{M}_0(m_2)\mathcal{M}_1(m_2)^*\right\} \lvert\mathcal{M}_1(m_1)\rvert^2$
11	$\frac{\sqrt{2}}{2}\Re\left\{\left(A_s^- {A_{ss}}^* + \bar{A}_s^- \bar{A}_{ss}^* + A_s^+ A_{ss}^* - \bar{A}_s^+ \bar{A}_{ss}^*\right) \mathcal{M}_1(m_1)\mathcal{M}_0(m_1)^*\right\} \lvert\mathcal{M}_0(m_2)\rvert^2$
7	$\frac{1}{2}\left\{\left(\lvert A_s^-\rvert^2 + \lvert A_s^+\rvert^2\right) - \left(\lvert\bar{A}_s^-\rvert^2 + \lvert\bar{A}_s^+\rvert^2\right)\right.$ $\left. -2\Re\left(A_s^- {A_s^+}^* + \bar{A}_s^- (\bar{A}_s^+)^*\right)\right\} \lvert\mathcal{M}_1(m_1)\rvert^2 \lvert\mathcal{M}_0(m_2)\rvert^2$
13	$-\frac{\sqrt{2}}{2}\Re\left\{\left(A_s^- {A_0}^* - \bar{A}_s^- \bar{A}_0^* - A_s^+ A_0^* - \bar{A}_s^+ \bar{A}_0^*\right) \mathcal{M}_0(m_1)\mathcal{M}_1(m_1)^*\right\} \lvert\mathcal{M}_1(m_2)\rvert^2$
14	$-\frac{\sqrt{2}}{2}\Re\left\{\left(A_s^- {A_\parallel}^* - \bar{A}_s^- \bar{A}_\parallel^* - A_s^+ A_\parallel^* - \bar{A}_s^+ \bar{A}_\parallel^*\right) \mathcal{M}_0(m_1)\mathcal{M}_1(m_1)^*\right\} \lvert\mathcal{M}_1(m_2)\rvert^2$
15	$-\frac{\sqrt{2}}{2}\Im\left\{\left(A_s^- {A_\perp}^* + \bar{A}_s^- \bar{A}_\perp^* - A_s^+ {A_\perp}^* + \bar{A}_s^+ \bar{A}_\perp^*\right) \mathcal{M}_1(m_1)^*\mathcal{M}_0(m_1)\right\} \lvert\mathcal{M}_1(m_2)\rvert^2$
16	$-\frac{\sqrt{2}}{2}\Re\left\{\left(A_s^- {A_{ss}}^* - \bar{A}_s^- \bar{A}_{ss}^* - A_s^+ A_{ss}^* - \bar{A}_s^+ \bar{A}_{ss}^*\right) \mathcal{M}_1(m_2)\mathcal{M}_0(m_2)^*\right\} \lvert\mathcal{M}_0(m_1)\rvert^2$
17	$\left\{\left(\lvert A_s^+\rvert^2 - \lvert\bar{A}_s^+\rvert^2\right) - \left(\lvert A_s^-\rvert^2 - \lvert\bar{A}_s^-\rvert^2\right)\right\} \Re(\zeta(m_1, m_2))$ $-2\Im\left(A_s^+ {A_s^-}^* + \bar{A}_s^+ (\bar{A}_s^-)^*\right)\Im(\zeta(m_1, m_2))$
18	$\left(\lvert A_{ss}\rvert^2 - \lvert\bar{A}_{ss}\rvert^2\right) \lvert\mathcal{M}_0(m_1)\rvert^2 \lvert\mathcal{M}_0(m_2)\rvert^2$
19	$\Re\left\{\left(A_{ss} {A_0}^* - \bar{A}_{ss} \bar{A}_0^*\right) \mathcal{M}_0(m_1)\mathcal{M}_0(m_2)\mathcal{M}_1(m_1)^*\mathcal{M}_1(m_2)^*\right\}$
20	$\Re\left\{\left(A_{ss} {A_\parallel}^* - \bar{A}_{ss} \bar{A}_\parallel^*\right) \mathcal{M}_0(m_1)\mathcal{M}_0(m_2)\mathcal{M}_1(m_1)^*\mathcal{M}_1(m_2)^*\right\}$
21	$\Im\left\{\left(A_{ss} {A_\perp}^* + \bar{A}_{ss} \bar{A}_\perp^*\right) \mathcal{M}_0(m_1)\mathcal{M}_0(m_2)\mathcal{M}_1(m_1)^*\mathcal{M}_1(m_2)^*\right\}$

Table A.6: d_n coefficients in (A.9). The mass function in d_{17} is defined as $\zeta(m_1, m_2) \equiv \mathcal{M}_1^*(m_1)\mathcal{M}_0^*(m_2)\mathcal{M}_0(m_1)\mathcal{M}_1(m_2)$

n	d_n
1	$-2\Im\big(A_0\bar{A}_0^* e^{i\phi_M}\big) \lvert\mathcal{M}_1(m_1)\rvert^2 \lvert\mathcal{M}_1(m_2)\rvert^2$
2	$-2\Im\big(A_\parallel\bar{A}_\parallel^* e^{i\phi_M}\big) \lvert\mathcal{M}_1(m_1)\rvert^2 \lvert\mathcal{M}_1(m_2)\rvert^2$
3	$2\Im\big(A_\perp\bar{A}_\perp^* e^{i\phi_M}\big) \lvert\mathcal{M}_1(m_1)\rvert^2 \lvert\mathcal{M}_1(m_2)\rvert^2$
4	$\Im\left\{\big(A_0\bar{A}_\parallel^* + \bar{A}_0^* A_\parallel\big)\, e^{i\phi_M}\right\} \lvert\mathcal{M}_1(m_1)\rvert^2 \lvert\mathcal{M}_1(m_2)\rvert^2$
5	$\Re\left\{\big(A_0\bar{A}_\perp^* + \bar{A}_0^* A_\perp\big)\, e^{i\phi_M}\right\} \lvert\mathcal{M}_1(m_1)\rvert^2 \lvert\mathcal{M}_1(m_2)\rvert^2$
6	$\Re\left\{\big(A_\parallel\bar{A}_\perp^* + \bar{A}_\parallel^* A_\perp\big)\, e^{i\phi_M}\right\} \lvert\mathcal{M}_1(m_1)\rvert^2 \lvert\mathcal{M}_1(m_2)\rvert^2$
7	$\Im\left\{(A_s^+ - A_s^-)(\bar{A}_s^+ + \bar{A}_s^-)^* e^{i\phi_M}\right\} \lvert\mathcal{M}_0(m_2)\rvert^2 \lvert\mathcal{M}_1(m_1)\rvert^2$
8	$\frac{\sqrt{2}}{2}\Im\big\{\big((A_s^-\bar{A}_0^* + A_s^+\bar{A}_0^*)e^{i\phi_M}$ $+(\bar{A}_s^+ A_0^* - \bar{A}_s^- {A_0}^*)e^{-i\phi_M}\big)\, \mathcal{M}_0(m_2)\mathcal{M}_1(m_2)^*\big\} \lvert\mathcal{M}_1(m_1)\rvert^2$
9	$\frac{\sqrt{2}}{2}\Im\big\{\big((A_s^-\bar{A}_\parallel^* + A_s^+\bar{A}_\parallel^*)e^{i\phi_M}$ $+(\bar{A}_s^+ {A_\parallel}^* - \bar{A}_s^- {A_\parallel}^*)e^{-i\phi_M}\big)\, \mathcal{M}_0(m_2)\mathcal{M}_1(m_2)^*\big\} \lvert\mathcal{M}_1(m_1)\rvert^2$
10	$\frac{\sqrt{2}}{2}\Re\big\{\big((A_s^-\bar{A}_\perp^* + A_s^+\bar{A}_\perp^*)e^{i\phi_M}$ $-(\bar{A}_s^+ {A_\perp}^* - \bar{A}_s^- {A_\perp}^*)e^{-i\phi_M}\big)\, \mathcal{M}_0(m_2)\mathcal{M}_1(m_2)^*\big\} \lvert\mathcal{M}_1(m_1)\rvert^2$
11	$\frac{\sqrt{2}}{2}\Im\big\{\big((A_s^-\bar{A}_{ss}^* + A_s^+\bar{A}_{ss}^*)e^{i\phi_M}$ $+(\bar{A}_s^+ A_{ss}^* - \bar{A}_s^- A_{ss}^*)e^{-i\phi_M}\big)\, \mathcal{M}_0(m_1)^*\mathcal{M}_1(m_1)\big\} \lvert\mathcal{M}_0(m_2)\rvert^2$
12	$\Im\left\{\big(A_s^+ + A_s^-\big)\big(\bar{A}_s^+ - \bar{A}_s^-\big)\, e^{i\phi_M}\right\} \lvert\mathcal{M}_0(m_1)\rvert^2 \lvert\mathcal{M}_1(m_2)\rvert^2$
13	$-\frac{\sqrt{2}}{2}\Im\big\{\big((A_s^-\bar{A}_0^* - A_s^+\bar{A}_0^*)e^{i\phi_M}$ $-(\bar{A}_s^+ {A_0}^* + \bar{A}_s^- A_0^*)e^{-i\phi_M}\big)\, \mathcal{M}_1(m_1)^*\mathcal{M}_0(m_1)\big\} \lvert\mathcal{M}_1(m_2)\rvert^2$
14	$-\frac{\sqrt{2}}{2}\Im\big\{\big((A_s^-\bar{A}_\parallel^* - A_s^+\bar{A}_\parallel^*)e^{i\phi_M}$ $-(\bar{A}_s^+ {A_\parallel}^* + \bar{A}_s^- A_\parallel^*)e^{-i\phi_M}\big)\, \mathcal{M}_0(m_1)\mathcal{M}_1(m_1)^*\big\} \lvert\mathcal{M}_1(m_2)\rvert^2$
15	$-\frac{\sqrt{2}}{2}\Re\big\{\big((A_s^-\bar{A}_\perp^* - A_s^+\bar{A}_\perp^*)e^{i\phi_M}$ $+(\bar{A}_s^- {A_\perp}^* + \bar{A}_s^+ {A_\perp}^*)e^{-i\phi_M}\big)\, \mathcal{M}_0(m_1)\mathcal{M}_1(m_1)^*\big\} \lvert\mathcal{M}_1(m_2)\rvert^2$
16	$-\frac{\sqrt{2}}{2}\Im\big\{\big((A_s^-\bar{A}_{ss}^* - A_s^+\bar{A}_{ss}^*)e^{i\phi_M}$ $-(\bar{A}_s^- A_{ss}^* + \bar{A}_s^+ A_{ss}^*)e^{-i\phi_M}\big)\, \mathcal{M}_0(m_2)^*\mathcal{M}_1(m_2)\big\} \lvert\mathcal{M}_0(m_1)\rvert^2$
17	$-\Im\big\{(A_s^+(\bar{A}_s^+)^* + A_s^-(\bar{A}_s^-)^*)e^{i\phi_M}\big\}\Re(\zeta(m_1, m_2))$ $-\Re\big\{(A_s^+(\bar{A}_s^-)^* + A_s^-(\bar{A}_s^+)^*)e^{i\phi_M}\big\}\Im(\zeta(m_1, m_2))$
18	$-2\Im\big(A_{ss}\bar{A}_{ss}^* e^{i\phi_M}\big) \lvert\mathcal{M}_0(m_1)\rvert^2 \lvert\mathcal{M}_0(m_2)\rvert^2$
19	$\Im\left\{\big(A_{ss}\bar{A}_0^* e^{i\phi_M} - \bar{A}_{ss}{A_0}^* e^{-i\phi_M}\big)\, \mathcal{M}_0(m_1)\mathcal{M}_0(m_2)\mathcal{M}_1(m_1)^*\mathcal{M}_1(m_2)^*\right\}$
20	$\Im\left\{\big(A_{ss}\bar{A}_\parallel^* e^{i\phi_M} - \bar{A}_{ss}{A_\parallel}^* e^{-i\phi_M}\big)\, \mathcal{M}_0(m_1)\mathcal{M}_0(m_2)\mathcal{M}_1(m_1)^*\mathcal{M}_1(m_2)^*\right\}$
21	$\Re\left\{\big(A_{ss}\bar{A}_\perp^* e^{i\phi_M} + \bar{A}_{ss}{A_\perp}^* e^{-i\phi_M}\big)\, \mathcal{M}_0(m_1)\mathcal{M}_0(m_2)\mathcal{M}_1(m_1)^*\mathcal{M}_1(m_2)^*\right\}$

Table A.7: Coefficients $\tilde{a}_n$ and $\tilde{b}_n$ as defined in (A.12). Since only phase difference between amplitudes are measurable, the convention $\delta_0 = 0$ has been taken.

n	$\tilde{a}_n$	$\tilde{b}_n$
1	$\lvert A_0\rvert^2\lvert\mathcal{M}_1(m_1)\rvert^2\lvert\mathcal{M}_1(m_2)\rvert^2$	$-\lvert A_0\rvert^2\lvert\mathcal{M}_1(m_1)\rvert^2\lvert\mathcal{M}_1(m_2)\rvert^2$
2	$\lvert A_\parallel\rvert^2\lvert\mathcal{M}_1(m_1)\rvert^2\lvert\mathcal{M}_1(m_2)\rvert^2$	$-\lvert A_\parallel\rvert^2\lvert\mathcal{M}_1(m_1)\rvert^2\lvert\mathcal{M}_1(m_2)\rvert^2$
3	$\lvert A_\perp\rvert^2\lvert\mathcal{M}_1(m_1)\rvert^2\lvert\mathcal{M}_1(m_2)\rvert^2$	$\lvert A_\perp\rvert^2\lvert\mathcal{M}_1(m_1)\rvert^2\lvert\mathcal{M}_1(m_2)\rvert^2$
4	$\lvert A_\parallel\rvert\lvert A_0\rvert\cos\delta_\parallel\lvert\mathcal{M}_1(m_1)\rvert^2\lvert\mathcal{M}_1(m_2)\rvert^2$	$-\lvert A_\parallel\rvert\lvert A_0\rvert\cos\delta_\parallel\lvert\mathcal{M}_1(m_1)\rvert^2\lvert\mathcal{M}_1(m_2)\rvert^2$
5	0	0
6	0	0
7	$\frac{1}{2}\left(\lvert A_s^+\rvert^2+\lvert A_s^-\rvert^2\right)\lvert\mathcal{M}_1(m_1)\rvert^2\lvert\mathcal{M}_0(m_2)\rvert^2$	$\frac{1}{2}\left(\lvert A_s^+\rvert^2-\lvert A_s^-\rvert^2\right)\lvert\mathcal{M}_1(m_1)\rvert^2\lvert\mathcal{M}_0(m_2)\rvert^2$
8	$\frac{1}{\sqrt{2}}\lvert A_s^-\rvert\lvert A_0\rvert\Re\left(e^{i\delta_s^-}\mathcal{M}_1^*(m_2)\mathcal{M}_0(m_2)\right)\lvert\mathcal{M}_1(m_1)\rvert^2$	$-\frac{1}{\sqrt{2}}\lvert A_s^-\rvert\lvert A_0\rvert\Re\left(e^{i\delta_s^-}\mathcal{M}_1^*(m_2)\mathcal{M}_0(m_2)\right)\lvert\mathcal{M}_1(m_1)\rvert^2$
9	$\frac{1}{\sqrt{2}}\lvert A_s^-\rvert\lvert A_\parallel\rvert\Re\left(e^{i(\delta_s^--\delta_\parallel)}\mathcal{M}_1^*(m_2)\mathcal{M}_0(m_2)\right)\lvert\mathcal{M}_1(m_1)\rvert^2$	$-\frac{1}{\sqrt{2}}\lvert A_s^-\rvert\lvert A_\parallel\rvert\Re\left(e^{i(\delta_s^--\delta_\parallel)}\mathcal{M}_1^*(m_2)\mathcal{M}_0(m_2)\right)\lvert\mathcal{M}_1(m_1)\rvert^2$
10	$\frac{1}{\sqrt{2}}\lvert A_s^+\rvert\lvert A_\perp\rvert\Im\left(e^{i(\delta_\perp-\delta_s^+)}\mathcal{M}_0^*(m_2)\mathcal{M}_0(m_2)\right)\lvert\mathcal{M}_1(m_1)\rvert^2$	$\frac{1}{\sqrt{2}}\lvert A_s^+\rvert\lvert A_\perp\rvert\Im\left(e^{i(\delta_\perp-\delta_s^+)}\mathcal{M}_0^*(m_2)\mathcal{M}_1(m_2)\right)\lvert\mathcal{M}_1(m_1)\rvert^2$
11	$\frac{1}{\sqrt{2}}\lvert A_s^-\rvert\lvert A_{ss}\rvert\Re\left(e^{i(\delta_s^--\delta_{ss})}\mathcal{M}_0^*(m_1)\mathcal{M}_1(m_1)\right)\lvert\mathcal{M}_0(m_2)\rvert^2$	$-\frac{1}{\sqrt{2}}\lvert A_s^-\rvert\lvert A_{ss}\rvert\Re\left(e^{i(\delta_s^--\delta_{ss})}\mathcal{M}_0^*(m_1)\mathcal{M}_1(m_1)\right)\lvert\mathcal{M}_0(m_2)\rvert^2$
12	$\frac{1}{2}\left(\lvert A_s^+\rvert^2+\lvert A_s^-\rvert^2\right)\lvert\mathcal{M}_0(m_1)\rvert^2\lvert\mathcal{M}_1(m_2)\rvert^2$	$\frac{1}{2}\left(\lvert A_s^+\rvert^2-\lvert A_s^-\rvert^2\right)\lvert\mathcal{M}_1(m_1)\rvert^2\lvert\mathcal{M}_0(m_2)\rvert^2$
13	$-\frac{1}{\sqrt{2}}\lvert A_s^-\rvert\lvert A_0\rvert\Re\left(e^{i\delta_s^-}\mathcal{M}_1^*(m_1)\mathcal{M}_0(m_1)\right)\lvert\mathcal{M}_1(m_2)\rvert^2$	$\frac{1}{\sqrt{2}}\lvert A_s^-\rvert\lvert A_0\rvert\Re\left(e^{i\delta_s^-}\mathcal{M}_1^*(m_2)\mathcal{M}_0(m_2)\right)\lvert\mathcal{M}_1(m_1)\rvert^2$
14	$-\frac{1}{\sqrt{2}}\lvert A_s^-\rvert\lvert A_\parallel\rvert\Re\left(e^{i(\delta_s^--\delta_\parallel)}\mathcal{M}_1^*(m_1)\mathcal{M}_0(m_1)\right)\lvert\mathcal{M}_1(m_2)\rvert^2$	$\frac{1}{\sqrt{2}}\lvert A_s^-\rvert\lvert A_\parallel\rvert\Re\left(e^{i(\delta_s^--\delta_\parallel)}\mathcal{M}_1^*(m_2)\mathcal{M}_0(m_2)\right)\lvert\mathcal{M}_1(m_1)\rvert^2$
15	$\frac{1}{\sqrt{2}}\lvert A_s^+\rvert\lvert A_\perp\rvert\Im\left(e^{i(\delta_\perp-\delta_s^+)}\mathcal{M}_0^*(m_1)\mathcal{M}_0(m_1)\right)\lvert\mathcal{M}_1(m_2)\rvert^2$	$\frac{1}{\sqrt{2}}\lvert A_s^+\rvert\lvert A_\perp\rvert\Im\left(e^{i(\delta_\perp-\delta_s^+)}\mathcal{M}_0^*(m_2)\mathcal{M}_1(m_2)\right)\lvert\mathcal{M}_1(m_1)\rvert^2$
16	$-\frac{1}{\sqrt{2}}\lvert A_s^-\rvert\lvert A_{ss}\rvert\Re\left(e^{i(\delta_s^--\delta_{ss})}\mathcal{M}_0^*(m_2)\mathcal{M}_1(m_2)\right)\lvert\mathcal{M}_0(m_1)\rvert^2$	$\frac{1}{\sqrt{2}}\lvert A_s^-\rvert\lvert A_{ss}\rvert\Re\left(e^{i(\delta_s^--\delta_{ss})}\mathcal{M}_0^*(m_1)\mathcal{M}_1(m_1)\right)\lvert\mathcal{M}_0(m_2)\rvert^2$
17	$\left(\lvert A_s^+\rvert^2-\lvert A_s^-\rvert^2\right)\Re\left(\zeta(m_1,m_2)\right)$	$\left(\lvert A_s^+\rvert^2+\lvert A_s^-\rvert^2\right)\Re\left(\zeta(m_1,m_2)\right)$
18	$\lvert A_{ss}\rvert^2\lvert\mathcal{M}_0(m_1)\rvert^2\lvert\mathcal{M}_0(m_2)\rvert^2$	$-\lvert A_{ss}\rvert^2\cos(2\phi_{ss}+\phi_q)\lvert\mathcal{M}_0(m_1)\rvert^2\lvert\mathcal{M}_0(m_2)\rvert^2$
19	$\lvert A_{ss}\rvert\lvert A_0\rvert\Re\left(e^{i\delta_{ss}}\mathcal{M}_1^*(m_1)\mathcal{M}_1^*(m_2)\mathcal{M}_0(m_1)\mathcal{M}_0(m_2)\right)$	$-\lvert A_{ss}\rvert\lvert A_0\rvert\Re\left(e^{i\delta_{ss}}\mathcal{M}_1^*(m_1)\mathcal{M}_1^*(m_2)\mathcal{M}_0(m_1)\mathcal{M}_0(m_2)\right))$
20	$\lvert A_{ss}\rvert\lvert A_\parallel\rvert\Re\left(e^{i(\delta_{ss}-\delta_\parallel)}\mathcal{M}_1^*(m_1)\mathcal{M}_1^*(m_2)\mathcal{M}_0(m_1)\mathcal{M}_0(m_2)\right)$	$-\lvert A_{ss}\rvert\lvert A_\parallel\rvert\Re\left(e^{-i(\delta_{ss}-\delta_\parallel)}\mathcal{M}_1^*(m_1)\mathcal{M}_1^*(m_2)\mathcal{M}_0(m_1)\mathcal{M}_0(m_2)\right)$
21	0	0

APPENDIX B

Selection of $B^0 \to \rho K^{*0}$

For the selection of the $B^0 \to \rho K^{*0}$ sample, 2011 and 2012 data from the stripping line `StrippingBetaSQ2B4piSelection`, in the Stripping20 campaign, were used. This stripping selection is optimised to identify B decays into quasi two-body final states. The offline selection requirements applied to these initial candidates are summarized in Table B.1.

For further background reduction a BDT discriminant was defined by combining the following variables:

- Isolation of the B vertex.
- B vertex χ^2.
- Track χ^2.
- Minimum IP χ^2 of the tracks.
- Minimum transverse momentum of the tracks.
- Minimum transverse momentum of K^{*0} and ρ.
- Maximum IP χ^2 of K^{*0} and ρ.
- B flight distance.
- B DIRA (pointing angle).
- B transverse momentum.
- B IP χ^2.

For the BDT training truth-matched Monte Carlo $B^0 \to \rho K^{*0}$ events from the MC11 generation fulfilling the same stripping requiremens as the data were considered as signal. The background sample is constructed from stripped $B^0 \to \rho K^{*0}$ candidates from 2012 data with an invariant mass $M(K\pi\pi\pi) > 5430$ MeV/c^2.

Once this sample of $B^0 \to \rho K^{*0}$ is obtained, the mass hypothesis of one of the pions coming from the ρ decay is changed into a kaon hypothesis. Then the cuts in Table 6.2 are applied, except for the GL cut. The invariant mass of the remaining candidates in the hypothesis $K^+\pi^-K^-\pi^+$ is used to extract a parameterisation of the $B^0 \to \rho K^{*0}$ contribution.

Table B.1: Cuts used to select the $B^0 \to \rho K^{*0}$ sample.

	Selection cuts
All tracks p	< 100000 MeV
All tracks p_T	> 100 MeV
All tracks IPØ^2	> 5
All tracks Ghost Prob	< 0.5
All tracks is Muon	$= 0$
$K^{\pm}$ PID$_{K-\pi}$	> 5
$K^{\pm}$ PID$_{p-K}$	< 0
$\pi^{\pm}$ PID$_{K-\pi}$	< 0
K^{*0} mass window	± 100 MeV
ρ mass window	± 225 MeV
K^{*0} and ρ p_T	> 200 MeV
K^{*0} and ρ vertex χ^2	< 20
B p_T	> 2500 MeV
B vertex χ^2/ndof	< 20
B flight distance χ^2	> 20
B IPØ^2	< 30
B DIRA	> 0.999

APPENDIX C

S–wave propagator in the K–matrix formalism

In the alternative model for the *S–wave* propagator, the $K_0^*(1430)$ is combined with a nonresonant term using the K–matrix formalism. First, a $K_0^*(1430)$ K element is considered

$$K_{K_0^*(1430)} = \frac{m_0 \Gamma_0(m)}{m_0^2 - m^2}, \tag{C.1}$$

which has a corresponding invariant $\hat{K}$ element:

$$\hat{K}_{K_0^*(1430)} \propto \frac{1}{m_0^2 - m^2} \tag{C.2}$$

A (real) constant term is added to this element to account for nonresonant background, (see formula 84 in [119]):

$$\hat{K}_S = \hat{K}_{K_0^*(1430)} + \kappa_S \tag{C.3}$$

The mass propagator can then be written as

$$T_S \propto \frac{\hat{K}_S}{1 - i(K_{K_0^*(1430)} + \kappa_S \rho_K)} = \frac{\hat{K}_S}{1 - i(\frac{m_0 \Gamma_0(m)}{m_0^2 - m^2} + \kappa_S \rho_{K^*})} \tag{C.4}$$

where $\rho_{K^{*0}} = 2\left(\frac{q}{m_{K\pi}}\right)$ and represents the phase space factor for the $K\pi$ final state.

APPENDIX D

Systematic studies

D.1 Fit bias

Fig. D.1 shows the pulls for the different angular parameters obtained from 500 toy experiments performed asuming the same statistics and parameter values observed in data.

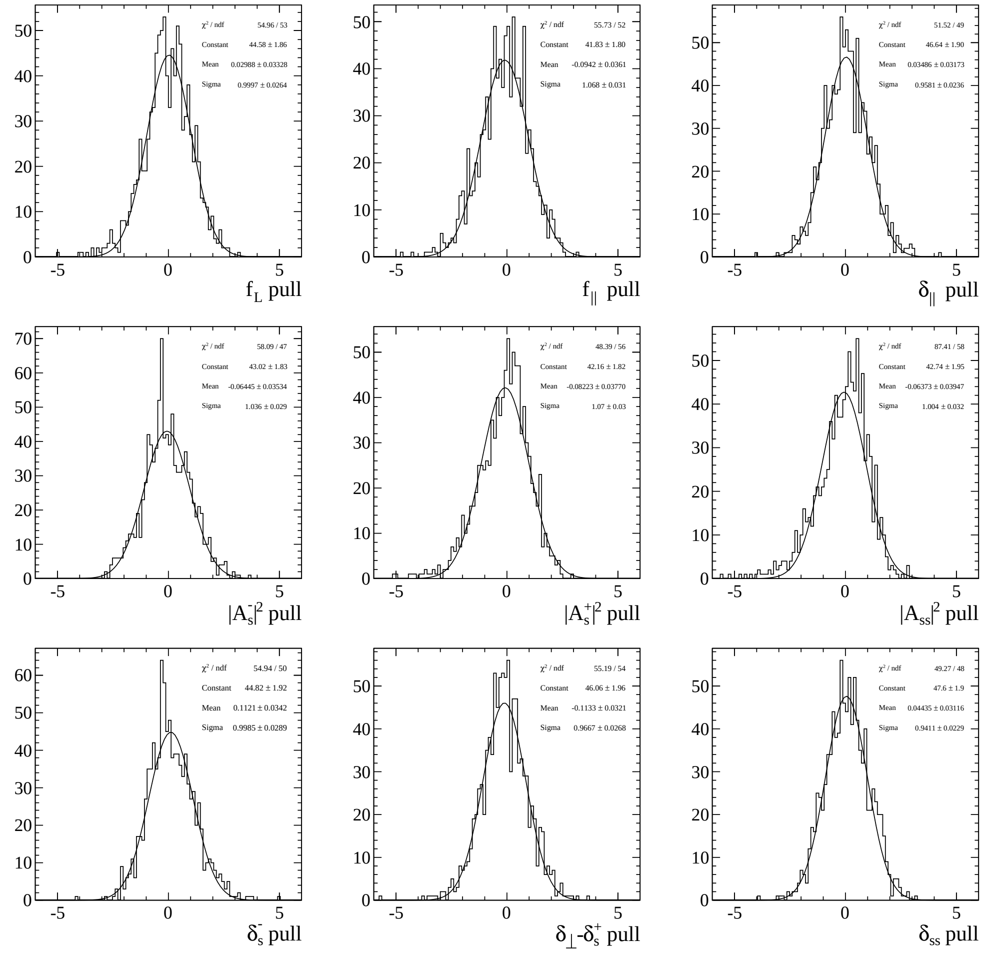

Figure D.1: Pull distributions of the parameters in the fit obtained from toy experiments simulating data used for the final result.

D.2 Monte Carlo statistics

To estimate the systematic error in the angular parameters induced by the limited statisctic available in the MC for the calculation of the angular acceptance, the fit was repeated one thousand times using different angular acceptance. In each iteration, the 2D angular acceptance is modified according to its statistical error in each acceptance bin. The pulls obtained for the fitted parameters are shown in Fig. D.2. The width of a gaussian fit to these pulls was taken as the systematic uncertainty for each of the parameters, see Table D.1.

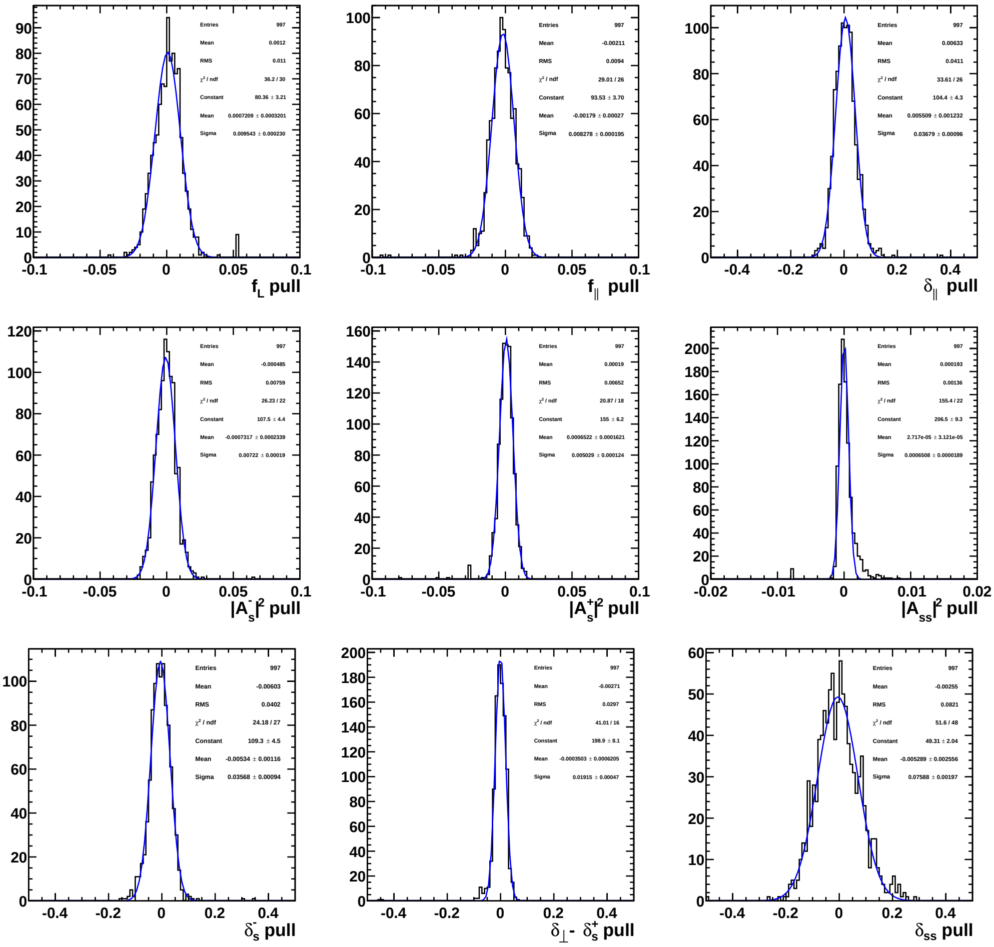

Figure D.2: Pulls for the different angular parameters obtained by fitting the data with an acceptance function modified acording to its statistical error.

D.3 Comparison Data / Monte Carlo

In this section, the main selection variables of the B_s^0 meson and its daughters are compared between MC and data. The data distributions have been obtained using *SPlot* technique [121], using as control variable the four-body invariant mass.

Table D.1: Variation of the different fit parameters induced by the statistical error in the determination of the angular acceptance. The mean and width of a gaussian fit to each parameter values distribution is quoted.

Parameter	Pull mean ($\times 10^{-3}$)	Pull width ($\times 10^{-3}$)
f_L	0.72 $\pm$ 0.32	9.54 $\pm$ 0.23
$f_{\parallel}$	-1.79 $\pm$ 0.27	8.28 $\pm$ 0.20
$\lvert A_s^-\rvert^2$	-0.73 $\pm$ 0.23	7.22 $\pm$ 0.19
$\lvert A_s^+\rvert^2$	0.65 $\pm$ 0.16	5.03 $\pm$ 0.12
$\lvert A_{ss}\rvert^2$	0.027 $\pm$ 0.031	0.651 $\pm$ 0.020
$\delta_{\parallel}$	5.5 $\pm$ 1.2	36.79 $\pm$ 0.96
$\delta_{\perp} - \delta_s^+$	-0.35 $\pm$ 0.62	19.15 $\pm$ 0.47
δ_s^-	-5.3 $\pm$ 1.2	35.68 $\pm$ 0.94
δ_{ss}	-5.3 $\pm$ 2.6	75.9 $\pm$ 2.0

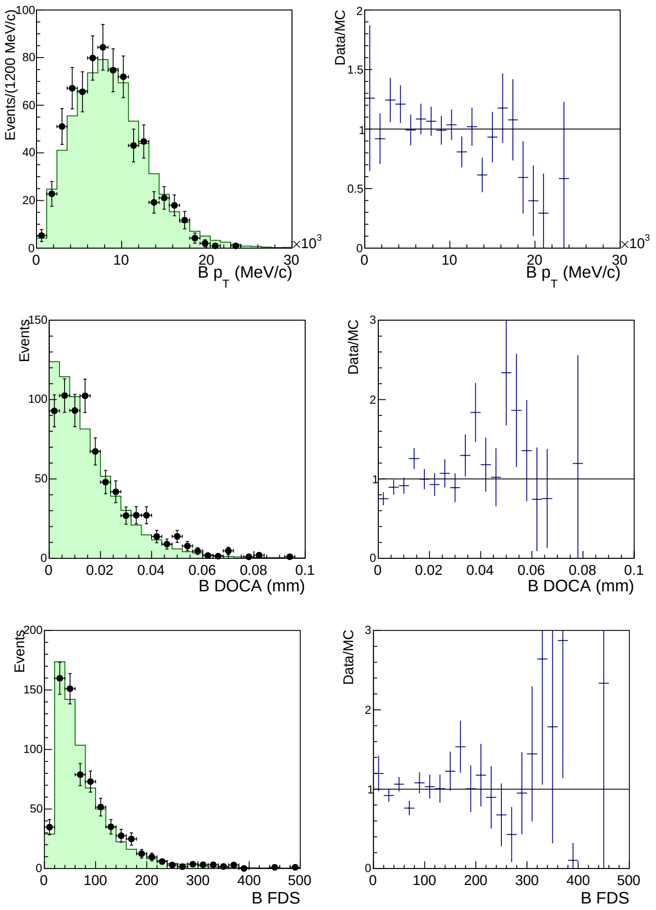

Figure D.3: Left: Comparison of the B_s^0 p_{T} (top), DOCA (middle) and flight distance significance (bottom) distributions in data (points) and MC simulation (solid green). Right: Ratio between data and MC.

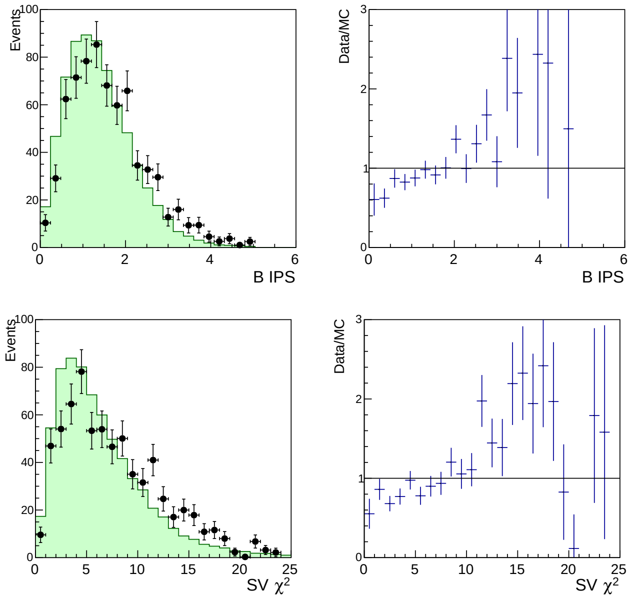

Figure D.4: Left: Comparison of the B_s^0 IP significance (top) and secondary vertex χ^2 (bottom) distributions in data (points) and MC simulation (solid green). Right: Ratio between data and MC.

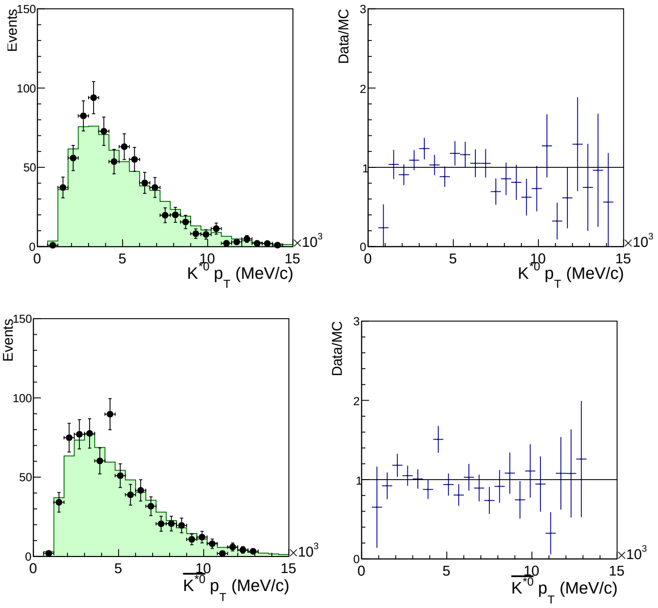

Figure D.5: Left: Comparison of the K^{*0} (top) and $\overline{K}^{*0}$ (bottom) p_{T} spectra in data (points) and MC simulation (solid green). Right: Ratio between data and MC.

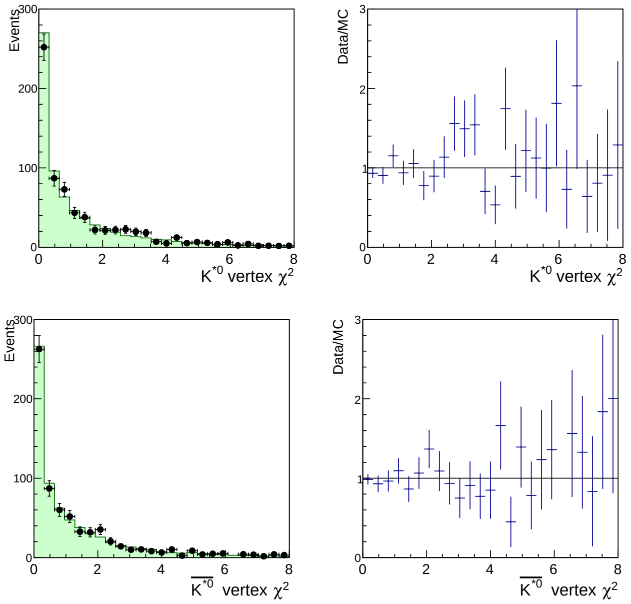

Figure D.6: Left: Comparison of the K^{*0} (top) and $\overline{K}^{*0}$ (bottom) vertex χ^2 distributions in data (points) and MC simulation (solid green). Right: Ratio between data and MC.

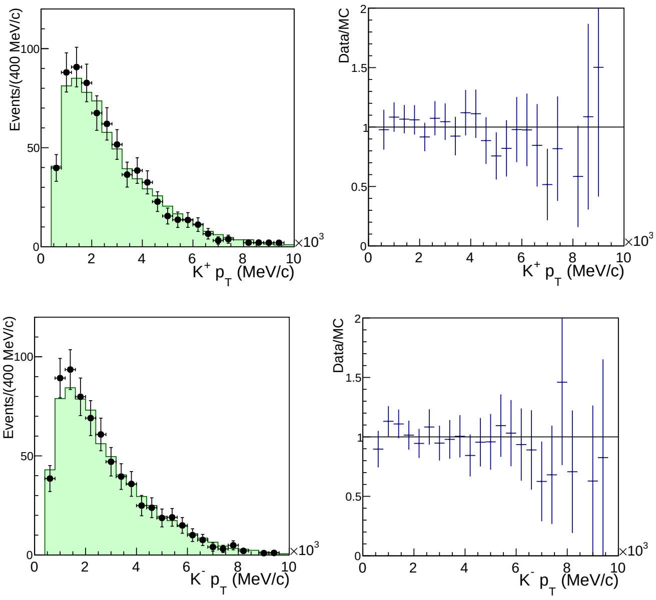

Figure D.7: Left: Comparison of the K^+ (top) and K^+ (bottom) p_T spectra in data (points) and MC simulation (solid green). Right: Ratio between data and MC.

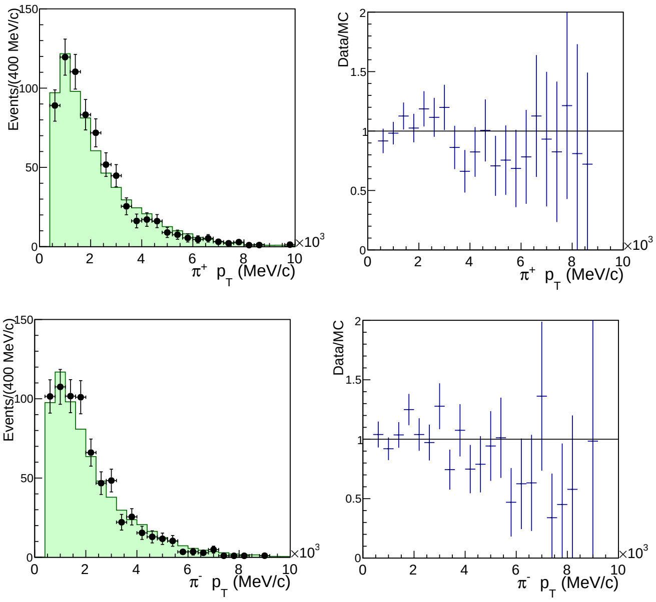

Figure D.8: Left: Comparison of the π^+ (top) and π^- (bottom) p_T spectrum in data (points) and MC simulation (solid green). Right: Ratio between data and MC.

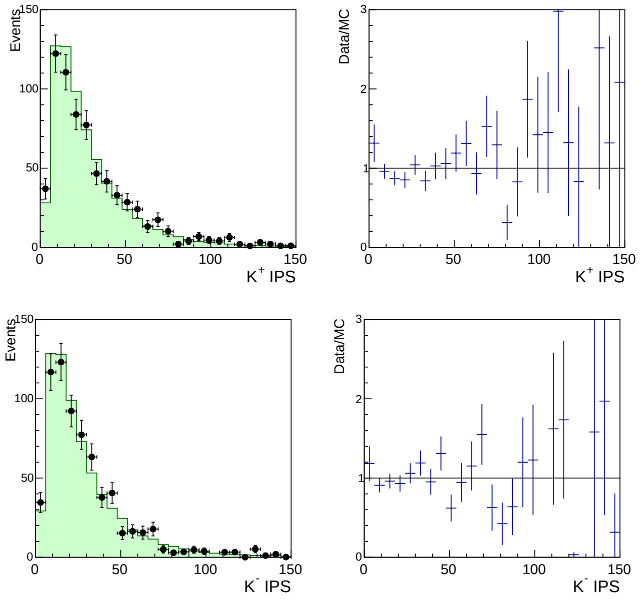

Figure D.9: Left: Comparison of the K^+ (top) and K^+ (bottom) IP significance spectra in data (points) and MC simulation (solid green). Right: Ratio between data and MC.

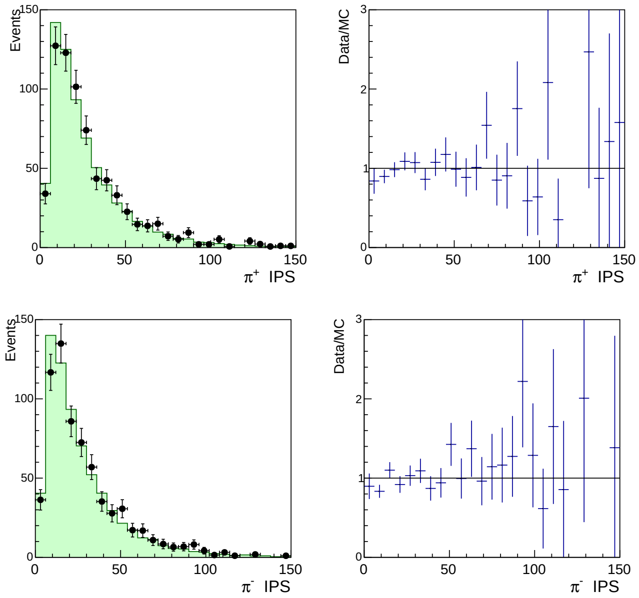

Figure D.10: Left: Comparison of the π^+ (top) and π^- (bottom) IP significance spectrum in data (points) and MC simulation (solid green). Right: Ratio between data and MC.

D.4 $M(K\pi)$ resolution

The $M(K\pi)$ resolution was estimated from Monte Carlo simulated data. The difference between the reconstructed and generated invariant mass of the $K\pi$ pairs was parameterised using three gaussian distributions with a common mean. The result of the fit is shown in Fig. D.11. From this result an effective resolution of $\sigma = 3.202 \pm 0.048$ MeV/c^2 was obtained. A single gaussian model with a effective width of $\sigma = 5$ MeV/c^2 was used for the systematic checks described in Sect. 6.5.4.5.

D.5 Time acceptance

In order to estimate the efficiency as a function of the lifetime of the B_s^0 meson, $B_s^0 \to K^{*0}\overline{K}^{*0}$ MC simulated events have been used. In this case, the sample was generated assuming CP-conservation ($\phi_s^{B_s^0 \to K^{*0}\overline{K}^{*0}} = 0$) and with the following set of values for the three polarisation amplitudes:

$$\begin{aligned} |A_0| = |A_{\parallel}| = |A_{\perp}| = 1 \\ \delta_0 = \delta_{\parallel} = \delta_{\perp} = 0 \end{aligned} \tag{D.1}$$

The generated lifetime distribution for that sample can be written as [98]

$$\frac{d\Gamma}{dt} \propto \frac{2}{3} e^{-\Gamma_L t} + \frac{1}{3} e^{-\Gamma_H t} \tag{D.2}$$

where Γ_H and Γ_L are the lifetime of the "heavy" and "light" mass eigenstates of the B_s^0-system, that can be expressed in terms of the usual parameters Γ_s (B_s^0 lifetime) and

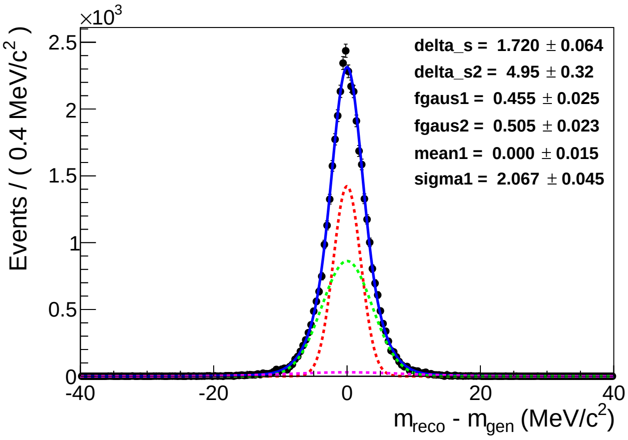

Figure D.11: Resolution in the measurement of the invariant mass of the $K\pi$ pairs. Points represent the difference between reconstructed and generated mass for MC simulated data. The blue solid line is the triple gaussian model fitted to the data. The dashed lines correspond to the contribution of each of the three gaussians.

$\Delta\Gamma_s$ (width difference between the two mass eigenstates) as

$$\begin{aligned} \Gamma_H &= \Gamma_s - \frac{\Delta\Gamma}{2} \\ \Gamma_L &= \Gamma_s + \frac{\Delta\Gamma}{2} \end{aligned} \tag{D.3}$$

The ratio between the lifetime distribution of the reconstructed and selected events and the generated PDF given above is shown in Fig. D.12. This ratio has been parameterised using the analytical function

$$\varepsilon(t) = \frac{t^3}{p_1 + t^3} \times (1 - p_2 t). \tag{D.4}$$

and the values of the parameters p_1 and p_2 have been estimated from a fit to the data.

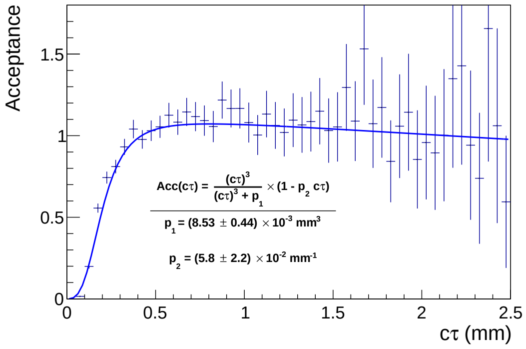

Figure D.12: Time acceptance calculated from MC simulated $B_s^0 \to K^{*0}\bar{K}^{*0}$ events. The solid line represents the fit of the model described in the text to the data.

APPENDIX E

TISTOS technique

In order to apply the TISTOS technique to calculate the L0 trigger efficiency from data, the number of $L0TIS$, $L0TOS$ and $L0TIS\&L0TOS$ events need to be determined. The L0 efficiency is calculated as

$$\varepsilon^{L0} = \varepsilon^{L0TIS} \frac{N^{L0}}{N^{L0TIS}} \tag{E.1}$$

where ε^{L0TIS} is approximated by

$$\varepsilon^{L0,TIS} = \frac{N^{L0TOS\&L0TIS}}{N^{L0TIS}} \tag{E.2}$$

just for the computation of the ratio of efficencies between $B_s^0 \to K^{*0}\overline{K}^{*0}$ and $B^0 \to \phi K^{*0}$. The determination of the signal events in each of the categories for signal and normalisation channel is obtained from a fit to the four body invariant mass spectrum. The models used to describe the $B_s^0 \to K^{*0}\overline{K}^{*0}$ and $B^0 \to \phi K^{*0}$ spectra are those explained in Sect. 6.3.3 and Sect. 6.6.1 respectively. Fig. E.1 shows the result of the fit in each category for both channels. The number of signal events in each category and the calculation of the L0TIS and L0 efficiencies are detailed in Table E.1.

Table E.1: Number of $B_s^0 \to K^{*0}\overline{K}^{*0}$ and $B^0 \to \phi K^{*0}$ signal candidates in each trigger category and determination of their L0 trigger efficiency.

Channel	$L0TOS$	$L0TIS$	$L0TOS\&L0TIS$	ε^{L0TIS}	ε^{L0}
$B^0 \to \phi K^{*0}$	520 ± 23	685 ± 27	157 ± 13	30.3 ± 2.0	46.4 ± 3.9
$B_s^0 \to K^{*0}\overline{K}^{*0}$	360 ± 20	448 ± 24	111 ± 11	30.8 ± 2.4	47.8 ± 5.0
ratio	-	-	-	-	0.97 ± 0.13

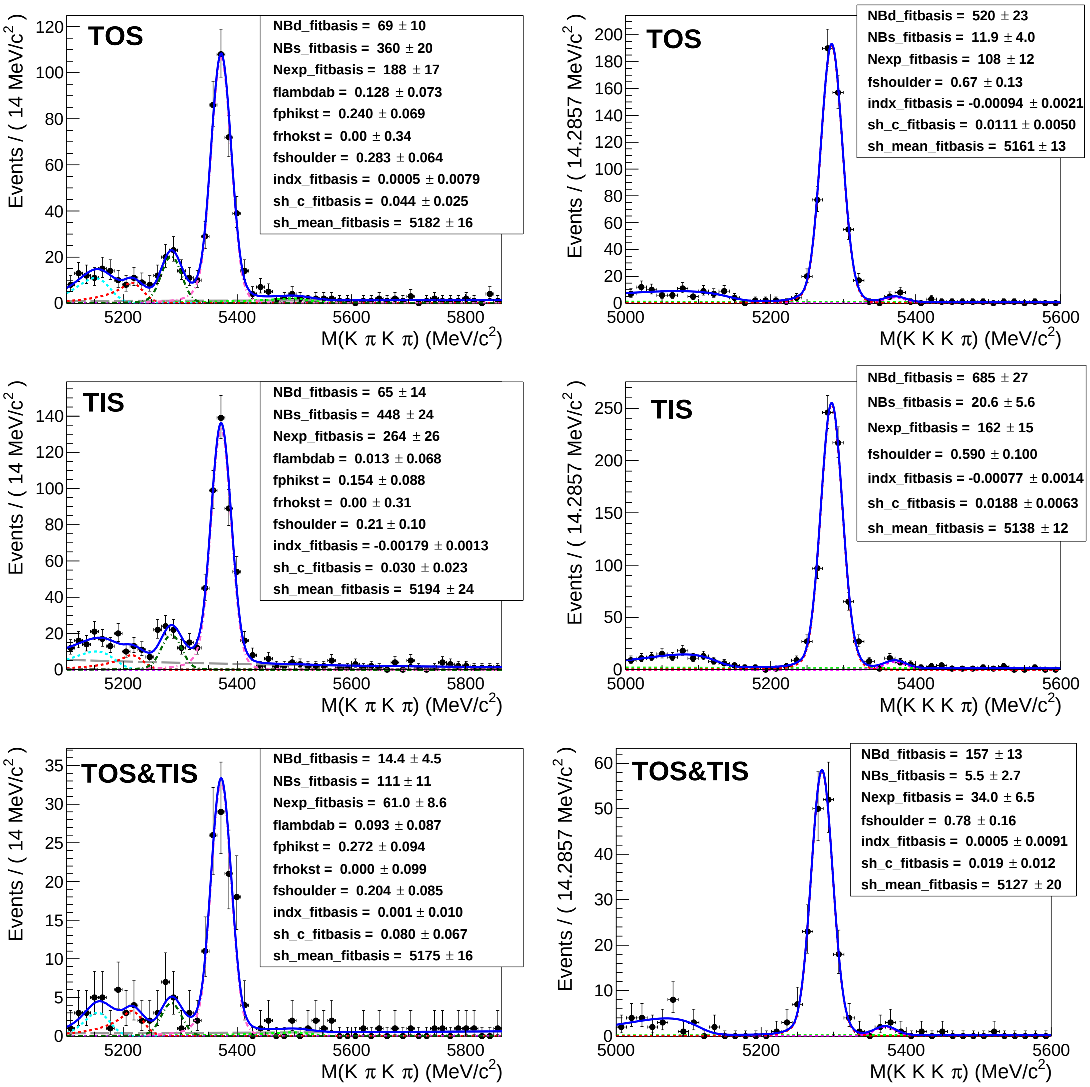

Figure E.1: Result of the fits to the four body invariant mass for $B_s^0 \to K^{*0}\bar{K}^{*0}$ (left) and $B^0 \to \phi K^{*0}$ (right), for each of the trigger categories: $L0TOS$ (top), $L0TIS$ (middle) and $L0TOS\&L0TIS$ (bottom).

Bibliography

[1] G. Bertone, D. Hooper, and J. Silk, *Particle dark matter: evidence, candidates and constraints*, Physics Reports **405** (2005) 279 , `arXiv:hep-ph/0404175`. [Cited in page 1].

[2] M. Beneke, J. Rohrer, and D. Yang, *Branching fractions, polarisation and asymmetries of $B \to VV$ decays*, Nucl. Phys. B **774** (2007) `arXiv:hep-ph/0612290`. [Cited in pages 2, 21, 23, 24, 141, 144, and 170].

[3] R. Fleischer, *Extracting CKM phases from angular distributions of $B_{d,s}$ decays into admixtures of CP eigenstates*, Phys. Rev. D **60** (1999) 073008, `arXiv:hep-ph/9903540`. [Cited in pages 2, 19, and 25].

[4] S. Descotes-Genon, J. Matias, and J. Virto, *Penguin–mediated $B_{d,s} \to VV$ decays and the $B_s^0 - \overline{B}_s^0$ mixing angle*, Phys. Rev. D **76** (2007) 074005, `arXiv:hep-ph/0705.0477v2`. [Cited in pages 2, 21, 25, 26, and 82].

[5] M. Ciuchini, M. Pierini, and L. Silvestrini, *$B_s^0 \to K^{*0}\overline{K}^{*0}$ decays: the golden channels for new physics searches*, Phys. Rev. Lett. **100** (2008) 031802, `arXiv:hep-ph/0703137`. [Cited in pages 2, 19, 21, 24, 25, 26, and 82].

[6] R. Fleischer and M. Gronau, *Studying new physics amplitudes in charmless B_s decays*, Phys. Lett. B **660** (2008) `arXiv:hep-ph/0709.4013`. [Cited in pages 2, 25, and 82].

[7] P. Álvarez Cartelle, *Study of the decay channel $B_s^0 \to K^{*0}\overline{K}^{*0}$ in LHCb.* 2010. "Diploma de Estudios Avanzados" project, University of Santiago de Compostela. [Cited in page 2].

[8] B. Bhattacharya, A. Datta, M. Duraisamy, and D. London, *Searching for new physics with $\bar{b} \to \bar{s}$ $B_s^0 \to V_1V_2$ penguin decays*, Phys. Rev. D **88** (2013) 016007, `arXiv:hep-ph/1306.1911`. [Cited in pages 2, 25, 27, 29, 51, and 81].

[9] D. Griffiths, *Introduction to Elementary Particles.* Physics textbook. Wiley, 2008. [Cited in page 3].

[10] A. Pich, *The Standard Model of Electroweak Interactions.* (2005) arXiv:hep-ph/0502010. [Cited in page 3].

[11] D. Martínez Santos, *Study of the very rare decay $B_s^0 \to \mu^+\mu^-$ in LHCb*. PhD thesis, University of Santiago de Compostela, Santiago de Compostela, 2010. [Cited in pages 3 and 68].

[12] ATLAS collaboration, *Observation of a new particle in the search for the Standard Model Higgs boson with the ATLAS detector at the LHC* , Phys. Lett. B **716** (2012) 1 . [Cited in pages 5 and 31].

[13] CMS collaboration, *Observation of a new boson at a mass of 125 GeV with the CMS experiment at the LHC*, Phys. Lett. B **716** (2012) 30 . [Cited in pages 5 and 31].

[14] N. Cabibbo, *Unitary Symmetry and Leptonic Decays*, Phys. Lett. **10** (1963). [Cited in pages 5 and 16].

[15] M. Kobayashi and T. Maskawa, *CP-Violation in the Renormalizable Theory of Weak Interaction*, Prog. Theor. Phys. **49** (1973). [Cited in page 5].

[16] Particle Data Group, K. Nakamura *et al.*, *Review of particle physics*, J. Phys. G **37** (2010) 075021. [Cited in pages 5, 17, 63, 68, 71, 73, 75, 77, 86, 106, 122, 126, and 136].

[17] J. H. Christenson, J. W. Cronin, V. L. Fitch, and R. Turlay, *Evidence for the* 2π *decay of the* K_2^0 *Meson*, Phys. Rev. Lett. **13** (1964). [Cited in page 7].

[18] BaBar Collaboration, *Observation of direct CP violation in* $B^0 \to K^+\pi^-$ *decays*, Phys. Rev. Lett. **93** (2004) `arXiv:hep-ex/0407057`. [Cited in page 7].

[19] Belle collaboration, *Observation of large CP violation and evidence for direct CP violation in* $B^0 \to \pi^+\pi^-$ *decays*, Phys. Rev. Lett. **93** (2004) `arXiv:hep-ex/0401029`. [Cited in page 7].

[20] LHCb collaboration, *First observation of* CP *violation in the decays of* B_s^0 *mesons*, Phys. Rev. Lett. **110** (2013) 221601., `arXiv:hep-ex/1304.6173`. [Cited in pages 7 and 39].

[21] A. D. Sakharov, *Violation of CP invariance, C asymmetry, and baryon asymmetry of the universe*, Pisma Zh. Eksp. Teor. Fiz. **5** (1967), [Translated in JETP Lett. 5, 24 (1967)]. [Cited in page 7].

[22] M. B. Gavela, P. Hernández, J. Orloff, and O. Péne, *Standard Model* CP*-violation and baryon asymmetry*, Modern Physics Letters A **09** (1994), no. 09 795. [Cited in page 7].

[23] A. J. Buras, *Searching for New Physics with rare decays and CP violation*, Journal of Physics: Conference Series **171** (2009), no. 1 012004. [Cited in page 7].

[24] G. C. Branco, L. Lavoura, and J. P. Silva, *CP Violation*. Int.Ser.Monogr.Phys. 103. 1999. [Cited in page 8].

[25] U. Nierste, *Three Lectures on Meson Mixing and CKM phenomenology*. TTP09-07, (2009) arXiv:hep-ph/0904.1869. [Cited in page 9].

[26] I. I. Bigi and A. I. Sanda, *CP Violation in heavy flavor decays : Predictions and search strategies* , Nucl. Phys. B **281** (1987). [Cited in page 13].

[27] R. Aleksan, I. Dunietz, B. Kayser, and F. L. Diberder, *CP Violation using non CP eigenstate decays of neutral B mesons*, Nucl. Phys. **B361** (1991). [Cited in page 13].

[28] LHCb Collaboration, *Measurement of the* B^0–$\bar{B}^0$ *oscillation frequency* Δm_d *with the decays* $B^0 \to D^-\pi^+$ *and* $B^0 \to J\,\psi K^{*0}$, Phys. Lett. B **719** (2013) 318, `arXiv:hep-ex/1210.6750`. [Cited in page 14].

[29] LHCb Collaboration, *Measurement of the* $B_s^0 - \bar{B}_s^0$ *oscillation frequency* Δm_s *in* $B_s^0 \to D_s^-(3)\pi$ *decays*, Phys. Lett. B **709** (2012) 177, `arXiv:hep-ex/1112.4311`. [Cited in page 14].

[30] Particle Data Group, J. Beringer *et al.*, *Review of Particle Physics*, Phys. Rev. D **86** (2012). [Cited in pages 15 and 61].

[31] Heavy Flavor Averaging Group (HFAG), *Averages of b-hadron, c-hadron, and* τ*-lepton properties as of early 2012*. (2013) `arXiv:hep-ex/1207.1158`. Online updates available at http://www.slac.stanford.edu/xorg/hfag. [Cited in pages 15 and 58].

[32] (D0 collaboration), *Study of* cp*-violating charge asymmetries of single muons and like-sign dimuons in* $p\overline{p}$ *collisions*, Phys. Rev. D **89** (2014) 012002. [Cited in page 15].

[33] LHCb collaboration, *Measurement of the flavour-specific* CP*-violating asymmetry* $a_{\rm sl}^s$ *in* B_s^0 *decays*, Phys. Lett. B **728** (2013) 607. [Cited in page 15].

[34] (LHCb collaboration), *Measurement of the semileptonic* cp *asymmetry in* B^0-$\overline{b}^0$ *mixing*, Phys. Rev. Lett. **114** (2015) 041601. [Cited in page 15].

[35] CKMfitter Group, *CP violation and the CKM matrix: Assessing the impact of the asymmetric B factories*, Eur. Phys. J. C **41** (2005), Updated results and plots available at: http://ckmfitter.in2p3.fr. [Cited in page 17].

[36] Belle Collaboration, *Measuremet of Polarization and Triple-Product Correlations in* $B \to \phi K^{*0} Decays$, Phys. Rev. Lett. **94** (2005). [Cited in page 19].

[37] Babar Collaboration, *Time-dependent and time-integrated angular analysis of the* $B \to \phi {K_S}^0\pi^0$ *and* $\phi K^{\pm}\pi^{\mp}$, Phys. Rev. D **78** (2008) 092008. [Cited in pages 19, 61, 62, 63, and 120].

[38] M. Neubert, *Heavy-quark symmetry*, Physics Reports **245** (1994) 259 . [Cited in pages 20 and 21].

[39] A. Pich, *Effective field theory.* Lectures at Les Houches Summer School (1998) arXiv:hep-ph/9806303. [Cited in pages 20 and 21].

[40] Javier Virto, *Topics in hadronic B decays.* PhD thesis, Universitat Autònoma de Barcelona, Barcelona, 2007, `arXiv:hep-ph/0712.3367`. [Cited in pages 21, 24, and 29].

[41] M. Gronau and J. Rosner, *Triple Product Asymmetries in* K, $D_{(s)}$ *and* $B_{(s)}$ *decays*, Phys. Rev. D **84** (2011) 096013, `arXiv:hep-ph/1107.1232`. [Cited in pages 22, 26, and 64].

[42] M. Beneke and M. Neubert, *QCD factorization for $B \to PP$ and $B \to PV$ decays* , Nuclear Physics B **675** (2003) 333 . [Cited in pages 23 and 24].

[43] B. Bhattacharya, A. Datta, M. Imbeault, and D. London, *Measuring β_s with $B_s^0 \to K^{*0}\overline{K}^{*0}$ – a Reappraisal*, Phys. Lett. **B717** (2012) 403, `arXiv:hep-ph/1203.3435`. [Cited in page 25].

[44] S. Descotes-Genon, J. Matias, and J. Virto, *Analysis of $B_{d,s}$ mixing angles in the presence of new physics and an update of $B_s^0 \to K^{*0}\overline{K}^{*0}$*, Phys. Rev. **D 85** (2012) 034010. [Cited in pages 26 and 82].

[45] A. Datta and D. London, *Triple-Product Correlations in $B \to V_1V_2$ Decays and New Physics*, Int. J. Mod. Phys. A **19** (2004) 2505. [Cited in page 26].

[46] S. P. Martin, *A SuperSymmetry primer.* (1997) arXiv:hep-ph/9709356. [Cited in page 29].

[47] Y. Shimizu, M. Tanimoto, and K. Yamamoto, *Supersymmetry contributions to CP violations in $b \to s$ and $b \to d$ transitions taking account of new data*, Phys. Rev. D **87** (2013) 056004. [Cited in page 29].

[48] `www.cern.ch`. [Cited in page 31].

[49] L. Evans and P. Bryant, *LHC Machine*, JINST **3** (2008). [Cited in page 31].

[50] `www.nobelprize.org`. [Cited in page 31].

[51] ATLAS collaboration, *ATLAS: technical proposal for a general-purpose pp experiment at the Large Hadron Collider at CERN.* CERN-LHCC/94-43. (1994). [Cited in page 31].

[52] CMS collaboration, *Technical Proposal.* CERN-LHCC/94-38. (1994). [Cited in page 31].

[53] ALICE collaboration, *ALICE: Technical proposal for a Large Ion collider Experiment at the CERN LHC.* CERN-LHCC/95-71. (1995). [Cited in page 31].

[54] LHCb Collaboration, *LHCb : Technical Proposal.* CERN-LHCC/98-004. (1998). [Cited in page 31].

[55] LHCb Collaboration, *Road map for selected key measurements from LHCb*, LHCb-PUB-2009-029. (2010). [Cited in page 33].

[56] LHCb collaboration, *The LHCb detector at the LHC*, JINST **3** (2008) S08005. [Cited in pages 33 and 47].

[57] LHCb collaboration, *LHCb VELO: Technical Design Report*, CERN-LHCC-2001-011. (2001). [Cited in page 35].

[58] LHCb collaboration, *LHCb inner tracker: Technical Design Report*, CERN-LHCC-2002-029. (2002). [Cited in page 36].

[59] LHCb collaboration, *LHCb outer tracker: Technical Design Report*, CERN-LHCC-2001-024. (2001). [Cited in page 36].

[60] LHCb collaboration, *Lhcb magnet technical design report*, CERN-LHCC-2000-007. [Cited in page 37].

[61] E. Bos, *Reconstruction of charged particles in the LHCb experiment*. PhD thesis, Amsterdam University, Amsterdam, 2010. [Cited in page 38].

[62] R. Frühwirth, *Application of kalman filtering to track and vertex fitting*, Nuclear Instruments and Methods in Physics Research Section A **262** (1987) 444 . [Cited in page 38].

[63] M. De Cian, *Track Reconstruction Efficiency and Analysis of $B^0 \to K^{*0}\mu^+\mu^-$ at the LHCb Experiment*. PhD thesis, Zurich University, Zurich, 2013. [Cited in page 38].

[64] A. Jaeger, P. Seyfert, M. De Cian, J. van Tilburg, and S. Hansmann-Menzemer, *Measurement of the track finding efficiency*, LHCb-PUB-2011-025. [Cited in page 38].

[65] LHCb collaboration, *First observation of the decay $B_s^0 \to \phi\bar{K}^{*0}$*, JHEP **2013** (2013) 92, `arXiv:hep-ex/1306.2239`. [Cited in page 39].

[66] M. Krasowski, M. Kucharczyk, W. Männer, G. Polok, and M. Witek, *Primary vertex reconstruction*, LHCb-2007-011. [Cited in page 39].

[67] LHCb collaboration, *Precision measurement of the $B_s^0 - \bar{B}_s^0$ oscillation frequency with the decay $B_s^0 \to D_s^-\pi^+$*, New J. Phys. **15** (2013) 053021, `arXiv:hep-ex/1304.4741`. [Cited in page 40].

[68] M. Adinolfi *et al.*, *Performance of the LHCb RICH detector at LHC*, Eur. Phys. J. C **73** (2012) 2431, `arXiv:physics.ins-det/1211.6759`. [Cited in pages 43 and 95].

[69] H. Terrier and I. Belyaev, *Particle identification with LHCb calorimeters*, LHCb-2003-092. (2003). [Cited in page 44].

[70] O. Deschamps, F. P. Machefert, M. H. Schune, G. Pakhlova, and I. Belyaev, *Photon and neutral pion reconstruction*, LHCb-2003-091. (2003). [Cited in page 44].

[71] D. Golubkov and V. Egorychev, *Electron particle identification with LHCb calorimeter system for 2011 data taking period*, LHCb-INT-2011-052. (2011). [Cited in page 44].

[72] V. Belyaev, V. Egorychev, and D. Golubkov, *Study of π^0/γ reconstruction efficiency with 2011 data*, LHCb-INT-2012-001. (2012). [Cited in page 45].

[73] G. Lanfranchi *et al.*, *The Muon Identification Procedure of the LHCb Experiment for the First Data*, LHCb-PUB-2009-013. (2009). [Cited in page 45].

[74] E. Polycarpo Macedo *et al.*, *Performance of the Muon Identification in LHCb with 2011 data*, LHCb-INT-2012-016. CERN-LHCb-INT-2012-016. [Cited in page 45].

[75] LHCb collaboration, *LHCb computing: Technical Design Report*, CERN-LHCC-2005-019. (2005). [Cited in page 46].

[76] LHCb Collaboration, L. collaboration, *LHCb trigger system: Technical Design Report*, LHCb-TDR-10. [Cited in page 46].

[77] A. Martin Sanchez, P. Robbe, and M.-H. Schune, *Performances of the LHCb L0 Calorimeter Trigger*, LHCb-PUB-2011-026. (2012). [Cited in page 47].

[78] R. Aaij and J. Albrecht, *Muon triggers in the High Level Trigger of LHCb*, LHCb-PUB-2011-017. CERN-LHCb-PUB-2011-017. (2011). [Cited in page 47].

[79] V. Gligorov, C. Thomas, and M. Williams, *The HLT inclusive B triggers*, LHCb-PUB-2011-016. (2011). [Cited in page 47].

[80] R. Aaij *et al.*, *The LHCb Trigger and its Performance in 2011*, J. Instrum. **8** (2012) P04022, `arXiv:hep-ex/1211.3055`. [Cited in page 48].

[81] LHCb collaboration, *Letter of Intent for the LHCb Upgrade*, CERN-LHCC-2011-001. (2011). [Cited in page 48].

[82] LHCb collaboration, *Framework TDR for the LHCb Upgrade: Technical Design Report*, CERN-LHCC-2012-007. (2012). [Cited in page 48].

[83] S. Stone and L. Zhang, *S-waves and the measurement of CP violating phases in B_s^0 decays*, Phys. Rev. D **79** (2009) 074024. [Cited in page 51].

[84] Y. Xie, P. Clarke, G. Cowan, and F. Muheim, *Determination of $2\beta_s$ in $B_s^0 \to J/\psi K^+K^-$ decays in the presence of a K^+K^- S-wave contribution*, Journal of High Energy Physics **2009** (2009) 074. [Cited in page 51].

[85] J. Richman, *An Experimenter's Guide to the Helicity Formalism*, Tech. Rep. CALT-68-1148, California Institute of Technology, 1984. [Cited in page 51].

[86] M. Calvo, M. Grabalosa, and M. Musy, *Combination of same-side with opposite-side flavour tagging*, LHCb-PUB-2009-027. (2010). [Cited in page 58].

[87] LHCb Collaboration, *Measurement of $\sigma(pp \to b\bar{b}X)$ at $\sqrt{s}$=7 TeV in the forward region*, Phys. Lett. B **694** (2010) 209. [Cited in page 58].

[88] LASS collaboration, *A study of $K^-\pi^+$ scattering in the reaction $K^-p \to K^-\pi^+n$ at 11 GeV/c*, Nuclear Physics B **296** (1988) 493. [Cited in page 61].

[89] LHCb collaboration, *Observation of the resonant character of the $Z(4430)^-$ state*, Phys. Rev. Lett. **112** (2014) 222002. [Cited in page 62].

[90] E. Klempt and A. Zaitsev, *Glueballs, hybrids, multiquarks. experimental facts versus qcd inspired concepts.*, Phys. Rep. **454** (2007) 1. [Cited in pages 62 and 122].

[91] S. Descotes and B. Moussallam, *The $K_0^*(800)$ scalar resonance from Roy-Steiner representations of πK scattering*, Eur. Phys. J. C **48** (2006). [Cited in pages 62 and 122].

[92] S. T'Jampens, *Etude de la violation de la symetrie CP dans les canaux charmonium-K*(892) par une analyse angulaire complete dependante du temps (experience BaBar)*. PhD thesis, Université Paris XI, Orsay, 2002. [Cited in page 63].

[93] SLD collaboration, *Search for charmless hadronic decays of B mesons with the SLAC SLD detector*, Phys. Rev. D **62** (2000) 071101. [Cited in page 67].

[94] BABAR Collaboration, *Observation of* $B^0 \to K^{*0}\overline{K}^{*0}$ *and Search for* $B^0 \to K^{*0}K^{*0}$, Phys. Rev. Lett. **100** (2008) 081801. [Cited in pages 67, 71, and 79].

[95] The Belle Collaboration, *Search for* $B^0 \to K^{*0}\overline{K}^{*0}$, $B^0 \to K^{*0}K^{*0}$ *and* $B^0 \to K^+\pi^-K^\mp\pi^\pm$ *decays*, Phys. Rev. D **81** (2010) 071101. [Cited in page 67].

[96] http://lhcb-release-area.web.cern.ch/LHCb-release-area/DOC/brunel. [Cited in page 68].

[97] http://lhcb-release-area.web.cern.ch/LHCb-release-area/DOC/davinci. [Cited in page 68].

[98] D. J. Lange, *The EvtGen particle decay simulation package*, Nucl. Instrum. Meth. A **462** (2001) 152. [Cited in pages 68, 129, and 193].

[99] http://lhcb-release-area.web.cern.ch/LHCb-release-area/DOC/gauss. [Cited in page 68].

[100] GEANT4 collaboration, S. Agostinelli *et al.*, *GEANT4: A simulation toolkit*, Nucl. Instrum. Meth. A **506** (2003) 250. [Cited in page 68].

[101] http://lhcb-release-area.web.cern.ch/LHCb-release-area/DOC/boole. [Cited in page 68].

[102] D. Karlen, *Using projections and correlations to approximate probability distributions*, Comput. Phys. **12** (1998) 380, `arXiv:physics.data-an/9805018`. [Cited in page 68].

[103] S. S. Wilks, *The large-sample distribution of the likelihood ratio for testing composite hypotheses*, The Annals of Mathematical Statistics **9** (1938) 60. [Cited in page 70].

[104] K. Abe *et al.*, *Measurements of branching fractions and decay amplitudes in* $B^0 \to J/\psi K^{*0}$ *decays*, Physics Letters B **538** (2002) 11 . [Cited in page 73].

[105] BABAR Collaboration, *Measurement of decay amplitudes of* $B \to J/\psi K^*$, $\psi(2S)K^*$, *and* $\chi_{c1}K^*$ *with an angular analysis*, Phys. Rev. D **76** (2007) 031102. [Cited in pages 73, 78, 143, and 169].

[106] T. Skwarnicki, *A study of the radiative cascade transitions between the Upsilon-prime and Upsilon resonances*. PhD thesis, Institute of Nuclear Physics, Krakow, 1986, DESY-F31-86-02. [Cited in pages 76 and 86].

[107] J. Podolanski and R. Armenteros. Phil. Mag. **45** (1954) 13. [Cited in page 77].

[108] P. Koppenburg, *Contribution to the Development of the LHCb Vertex Locator and Study of Rare Semileptonic Decays*. PhD thesis, Université de Lausanne, Lausanne, 2002. [Cited in page 77].

[109] LHCb Collaboration, *Determination of* f_s/f_d *for 7 TeV pp collisions and measurement of the* $B^0 \to D^- K^+$ *branching fraction*, Phys. Rev. Lett. **107** (2011) 211801. [Cited in page 77].

[110] LHCb collaboration, *Search for the rare decays* $B_s^0 \to \mu^+\mu^-$ *and* $B^0 \to \mu^+\mu^-$, Phys. Lett. B **699** (2011) 330 . [Cited in page 78].

[111] LHCb collaboration, *Measurement of* J/ψ *production in pp collisions at* $\sqrt{s} = 7$ *TeV*, Eur. Phys. J. C **71** (2011) 1645. [Cited in page 78].

[112] J. A. Hernando Morata, E. Lopez Asamar, D. Martinez Santos, H. Ruiz-Pérez, and F. Teubert, *Measurement of trigger efficiencies and biases*, LHCb-2008-073. (2010). [Cited in pages 78 and 131].

[113] LHCb Collaboration, *Flavor-untagged angular analysis of* $B_d^0 \to J/\psi K^*$ *and* $B_s^0 \to J/\psi\phi$ *decays*, LHCb-CONF-2011-002. (2011). [Cited in page 78].

[114] X. Liu, Z. Xiao, and Z. Zou, *Branching ratios and CP violation of* $B_s^0 \to K_0^*(1430)K^*$ *decays in the perturbative QCD approach.*, Phys. Rev. **D 88** (2013) 094003. [Cited in page 82].

[115] R. Brun and F. Rademakers, *ROOT - An Object Oriented Data Analysis Framework*, Nucl. Inst. & Meth. in Phys. Res. A **389** (1997) 81, Proceedings AIHENP'96 Workshop, Lausanne. [Cited in page 87].

[116] ARGUS collaboration, *Exclusive hadronic decays of B mesons*, Zeitschrift für Physik C: Particles and Fields **48** (1990) 543. [Cited in page 87].

[117] LHCb Collaboration, *First measurement of the* CP*-violating phase in* $B_s^0 \to \phi\phi$ *decays*, Phys. Rev. Lett. **110** (2013) 241802. [Cited in page 104].

[118] LHCb collaboration, *Measurement of polarization amplitudes and* CP *asymmetries in* $B^0 \to \phi K^*(892)^0$, J. High Energy Phys. **05** (2014) 069. [Cited in pages 104, 125, 132, and 133].

[119] S. Chung *et al.*, *Partial wave analysis in K matrix formalism*, Annalen Phys. **4** (1995) 404. [Cited in pages 104 and 185].

[120] BABAR Collaboration, *Search for the* $Z(4430)^-$ *at BABAR*, Phys. Rev. **D79** (2009) 112001, `arXiv:hep-ex/0811.0564`. [Cited in page 106].

[121] M. Pivk and F. L. Diberder, *sPlot: A statistical tool to unfold data distributions* , Nucl. Instrum. Meth. A **555** (2005) 356 . [Cited in pages 111 and 188].

[122] Y. Xie, *sFit: A method for background subtraction in maximum likelihood fit.* (2009) `arXiv:physics.data-an/0905.0724`. [Cited in page 111].

[123] LHCb Collaboration, *Updated average* f_s/f_d *b-hadron production fraction ratio for 7 TeV pp collisions*, LHCb-CONF-2013-011. (2013). [Cited in page 136].